The Structure and Dynamics of Fundamental Glasses by Neutron Scattering Techniques

Whittaker, Dean

Award date:
2012

Awarding institution:
University of Bath

The Structure and Dynamics of Fundamental Glasses by Neutron Scattering Techniques

submitted by

Dean A. J. Whittaker

for the degree of Doctor of Philosophy

of the

University of Bath

Department of Physics

December 17, 2012

For Nan White (1905 - 2011), fare thee well

Abstract

The method of isotope substitution in neutron spectroscopy is introduced to measure for the first time the partial vibrational density of states of two network glass forming systems, namely $GeSe_2$ at temperatures of 5, 20 and 292 K and GeO_2 at a temperature of 10 K. This work included the development of a new data analysis procedure involving corrections for e.g. beam attenuation, multiple scattering and multiple phonon scattering. The measurements were made using the MARI and MERLIN spectrometers at the ISIS pulsed neutron source where measurements of the elastic lines were used to help deduce the mean squared atomic displacements and Debye-Waller factors. In the case of $GeSe_2$, the latter were found as a function of temperature between 10 and 280 K. The results for $GeSe_2$ glass at temperatures of 5, 20, and 292 K were found to be in good agreement, proving the efficacy of the data correction procedure. For both $GeSe_2$ and GeO_2, the results were interpreted with the aid of molecular dynamics simulations to identify the energies corresponding to rocking, bending and stretching motions.

The method of *in situ* high pressure neutron diffraction was developed using double toroid sintered diamond anvils in a Paris-Edinburgh press to measure, for the first time, reliable diffraction patterns for GeO_2, SiO_2 and B_2O_3 glasses at pressures up to 17.5 GPa. The total pair distribution functions were obtained, allowing the nearest neighbour Ge-O, Si-O or B-O coordination numbers and bond distances to be calculated. The glass networks collapse by two principal mechanisms. The first mechanism, at lower pressures, involves a rearrangement of the structural motifs on an intermediate range length scale. The second mechanism, above thresholds in pressure of 5, 20 and 9 GPa for GeO_2, SiO_2 and B_2O_3, respectively, involves a change in the nature of the structural motifs.

Acknowledgements

I thank my main supervisor Phil Salmon and STFC supervisor Steve Bennington for their advice and support during my PhD. In particular, I thank Phil for providing excellent support during my writing phase. I also acknowledge the financial support of the EPSRC and STFC for the projects I have been involved with. I would like to thank the Institute of Physics for funding some travel to events and for funding schemes set up through the physics society.

From the university of Bath I would like to thank the LAM group: Anita Zeidler, James Drewitt, Kamil Wezka, Keiron Pizzey and Prae Chirawatkul for useful discussions, data, training, help and friendship; and Harry Bone, Paul Reddish, Adrian Hooper, Wendy Lambson and Phil Jones for help and support with our equipment.

For the work on inelastic neutron scattering I would like to thank: Ross Stewart, Jon Taylor, Devashibhai Adroja, Tatiana Guidi and Rob Bewley who gave fantastic support during experiments; Luigi Giacomazzi and Alfredo Pascquarello provided valuable simulation data; Gavin Mountjoy provided data on SiO_2 to compare with my GeO_2 data. Spencer Howells, Nigel Rhodes, Toby Perring, Russell Ewings and Freddy Akeroyd helped with software and practicalities in the data analysis.

For my work with X-rays not presented here, I would like to thank: Chris Benmore, Simon Billinge and Eugene Bychkov for help with our experiments and my data analysis procedures.

For my work on the Pearl instrument at ISIS I would like to thank: Matt Tucker, Craig Bull, Chris Barry, Stefan Klotz, Chris Goodway, Rob Done and PAW Engineering for experimental support; Martin Wilding for making the silica sample; Vadim Brazhkin and Mark Wilson for some data to compare mine with; and Malcolm Guthrie for support with creating the calibration curves. I would particularly like to thank Matt and Craig for fantastic instrument support during stressful experiments.

I would also like to thank Henry Fischer and Adrian Barnes for useful discussions; Alex Hannon for discussions, help, images, and writing the units conversion program that I find so helpful; Alan Soper and Rowan Hargreeves for support and discussions; and Paul Bingham, Emma Cruddace, Adrian Wright and others at the society of glass technology for positive encouragement and awarding me the Paul prize. I would like to thank all of the contributors to the ISIS neutron training course and ISIS neutron

school for the training provided.

With regards to my outreach / extra-curricular work I would like to thank the contributors to the Ask a Postgrad scheme: Mischa Stocklin (IOP), Tom Fowler, Fran Laughton, Gary Mathlin, James Beard, Caitlin Rice, Michael Grogan, Lucy Hooper, Melanie Keogh and Alexis Kallis; the organisers of I'm a Scientist, get me out of here including Rosie Schultz and Sophia Collins; and for various activities: Alison Rivett (IoP), Bob Draper (Bath), Claire Dimond (STEM / Graphic Science) and Katy Glazer (STFC / Graphic Science). I would like to acknowledge the University of Bath Students' Union for their support beyond expectation to help get projects off the ground.

Finally, I thank Jodie, mum and dad for putting up with me during my writing phase. It can't have been an easy task.

Contents

1. Introduction

Glassy materials are used for a variety of applications from advanced optical fibres [1] to windows and bottles and are of great interest, both fundamentally and for technological applications [2–6]. Despite their wide spread use, the theory of glasses is still not fully understood. In particular, the nature of the glass transition temperature and its variation between materials is still a mystery [7]. The ability to accurately model glass behaviour allows materials to be designed with tunable properties [8]. For example, molecular dynamics (MD) models can be used to find the microscopic and macroscopic properties of a material by considering the interactions between atoms. The structural and dynamical properties thus predicted can then be compared to experiments to test the validity of the model.

Unlike crystalline materials, glasses do not exhibit regular long range ordering and so their structure cannot be reduced to a series of repeating unit cells easily measured by diffraction techniques [9, 10]. Neither do their vibrational modes reduce to a small set of degenerate allowed states, easily measured by spectroscopic techniques [11]. Instead, glasses can be thought of as a liquid, frozen in time with a range of interatomic distances and a full set of $3N$ allowed vibrational modes. [1]

The structure of multicomponent glasses can be described by a set of partial pair-correlation functions $g_{\alpha\beta}(r)$, which are related to the probability of finding an atom of one chemical species β a distance r away from an atom of another chemical species α. Similarly, the dynamics of a glass can be described by a series of partial vibrational density of states $Z_\alpha(E)$, which are related to the energy E of the motions of atom α.

Many glasses, such as those described in this thesis ($GeSe_2$, GeO_2, SiO_2 and B_2O_3), form network-like structures [12] first described by Zachariasen [13]. In this picture, chemically ordered structural motifs are connected either at their corners or edges to form intermediate range ordering [14, 15]. Therefore, the $g_{\alpha\beta}(r)$ functions will feature sharp peaks at small r due to the presence of the structural motifs and peaks at larger

[1] Technically, there are $3N$-6 modes, where 6 of the $3N$ modes originate from translations and rotations of the entire bulk material and so do not contribute to the vibrational density of states. These modes are often ignored when counting the total number of modes due to the large number of atoms in real samples.

values of r that arise from intermediate range ordering. The vibrational modes can be attributed to local motions within the structural motifs or motions between the structural motifs. Both the structure and dynamics of a glass can change under different external conditions such as increased pressure [16]. A successful MD model should be able to predict the microscopic structure and dynamics of the glass under as many conditions as possible and experiments are needed to test such models.

Several MD approaches exist for modelling a glass. In so-called classical MD models, potentials between nuclei are used to describe their interactions and Newton's laws of motions are solved for a large system of atoms [17, 18]. Another simulation method uses the quantum mechanical *ab initio* approach [19], wherein the electronic structure is properly taken into account using density functional theory [20–23]. There are currently three well known classes of approximations to the functionals that are used in *ab initio* MD simulations [24]; the local density approximation (LDA) [25], the generalised gradient approximation (GGA) [26] and hybrid functionals [27, 28] such as the popular B3LYP functional [29, 30]. In the LDA, the true energy density is approximated by a local constant electron density, while in the GGA the gradient of the electron density is used in the approximation to account for non-uniform charge distributions. Hybrid functionals mix the exact (but computationally intensive) exchange part of Hartree-Fock theory together with the LDA or GGA approach to further improve the accuracy of the result. While these models are more sophisticated than classical models, they are far more computationally intensive and are therefore restricted in the number of particles that can be simulated. Current results for glasses [31] including $GeSe_2$ [32], show that the various MD models often require improvements to fully reproduce the experimental data.

Neutrons are a useful probe to study the structure and dynamics of materials. Neutrons scatter mostly from the nuclei of atoms, but can also scatter from electrons with a non-zero spin. In a diffraction experiment, the interference pattern thus produced can be used to obtain the sum of the partial pair correlation functions. The nearest-neighbour bond distances and coordination numbers can be calculated if the correlation functions do not overlap in a particular region. In a spectroscopy experiment, the transfer of energy between the neutron and the system is measured and a total vibrational density of states can be obtained as a sum of contributions from all of the chemical species in the system.

Different isotopes of the same chemical species can have different cross sections for neutrons. This fact can be employed to use the method of isotope substitution, first exploited by Enderby *et al.* in 1966 for diffraction studies [33]. In this technique, the partial pair correlation functions can be separated by measuring several isotopically enriched (but otherwise identical) samples and using a method akin to solving

simultaneous equations. This gives a much more detailed view of the structure of a glass.

As will be described in this thesis, the method of isotope substitution can also be used to separate the full set of partial vibrational density of states. This offers complementary information to that obtained by infrared and Raman light scattering techniques, where selection rules mean that only certain modes are accessible [11]. The full set of partial vibrational density of states provides a good test of MD simulations but this type of experiment has not yet been made. The development of neutron diffraction under high pressure provides another test for MD simulations. High quality neutron diffraction experiments at pressures above 9 GPa are currently lacking and new measurements are needed.

Thesis Outline

In this thesis, the dynamics of glasses under ambient pressure and the structure of glasses under high pressures are measured using neutron scattering techniques and, where possible, compared to MD simulations. The technique of isotope substitution in neutron spectroscopy is developed and the technique of *in situ* neutron diffraction under high pressure conditions is extended to a higher range of pressures than previously achieved.

In chapter 2, the essential theory for the method of isotope substitution in neutron spectroscopy and the method of neutron diffraction is presented. The large-scale facilities and instruments that are required to perform the experiments are presented in chapter 3, while the necessary data analysis procedures are given in chapter 4.

The first ever isotope substitution in neutron spectroscopy experiment is presented in chapter 5, where measurements were made on $GeSe_2$ glass using the MARI spectrometer at the ISIS pulsed neutron source. This material was chosen due to its favourable properties for the technique and the fact that it is a difficult material to model. The results are compared to classical MD simulations [34, 35]. In chapter 6, a further isotope substitution in neutron spectroscopy experiment on $GeSe_2$ glass is presented, made using the MERLIN spectrometer at the ISIS pulsed neutron source. Here, there was a significant increase in detected neutron flux and measurements were made at a variety of temperatures to provide a fuller survey of the dynamics of $GeSe_2$. All of the measurements are compared and the validity of the technique, along with the various approximations involved, are assessed.

In section 7 the method of isotope substitution in neutron spectroscopy is applied to GeO_2 glass using the MARI spectrometer. The results are compared with classical and *ab initio* MD simulations [36–38] and conclusions are drawn. The results for GeO_2 are

also compared with approximate measurements made for SiO_2, a structural analogue for which it is difficult to use the method of isotopic substitution in neutron spectroscopy.

In chapters 8 and 9, neutron diffraction measurements made under pressures up to 17.5 GPa using the PEARL diffractometer at the ISIS pulsed neutron source are presented. The technique and semi empirical data analysis procedure, based on that given by Drewitt [39], was further developed using GeO_2 glass, and was then applied to SiO_2 and B_2O_3 glasses. The measurements are compared to existing measurements made on different instruments at lower pressures to assess the validity of the semi empirical data correction procedure. The results are also compared to MD simulations, where possible. These are the highest pressures for which reliable neutron diffraction patterns have been measured. This extends previous work, where the maximum pressure was restricted to ≈ 9 GPa [40].

2. Theory

In this chapter, the relevant theory for the neutron spectroscopy and diffraction experiments presented in this thesis is described. Firstly the method of neutron spectroscopy to measure the partial vibrational density of states in various approximations is discussed. Then, the method of neutron diffraction to measure the structure of a glass is described. The formalism follows references [11, 41, 42] for neutron spectroscopy and reference [5] for neutron diffraction.

2.1 The Double Differential Scattering Cross Section

Figure 2-1 shows the scattering geometry for a spectroscopy experiment. A collimated beam of incident neutrons (in principle this could be any probe, e.g. photons or electrons) of flux Φ, incident wavevector $\mathbf{k}_i$ and incident energy E_i is scattered by a small sample to give a beam described by final wavevector $\mathbf{k}_f$ and final energy E_f.

A detector of small surface area $\mathrm{d}S$ is situated a distance R away from the system of scattering centres in a direction $\hat{\mathbf{k}}_f$ and subtends a solid angle $\mathrm{d}\Omega = \mathrm{d}S/R^2$. The double differential cross section is given by

$$\frac{\mathrm{d}^2\sigma}{\mathrm{d}\Omega \mathrm{d}E_f} = (\text{Number of neutrons scattered per second into } \mathrm{d}\Omega \text{ with final energy between } E_f \text{ and } E_f + \mathrm{d}E_f) / (\Phi \mathrm{d}\Omega \mathrm{d}E_f) \quad . \tag{2.1}$$

For each scattering event, the energy transferred from a neutron to the system is $E = E_i - E_f$ and the scattering vector, defined by the triangle in figure 2-2, is $\mathbf{Q} = \mathbf{k}_i - \mathbf{k}_f$ which has a magnitude $Q = |\mathbf{Q}|$ given by the cosine rule of

$$Q = \sqrt{k_i^2 + k_f^2 - 2k_i k_f \cos(2\theta)} \quad , \tag{2.2}$$

where 2θ is the scattering angle between $\mathbf{k}_i$ and $\mathbf{k}_f$. The incident and final energies

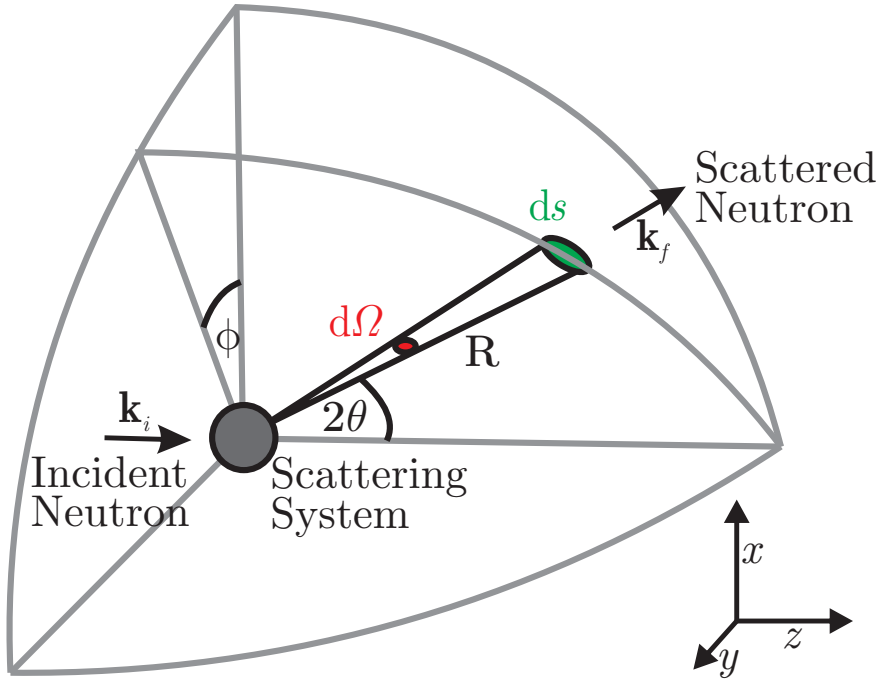

Figure 2-1: A neutron with wavevector $\mathbf{k}_i$ in a direction parallel to the z axis is incident on a system of scattering centres. The neutron scatters into a detector of surface area $\mathrm{d}S$ which subtends a solid angle $\mathrm{d}\Omega$ and has a final wavevector $\mathbf{k}_f$. The angle between the incident wavevector and the scattered wavevector is 2θ, the angle between the $x-z$ plane and the scattered wavevector is ϕ.

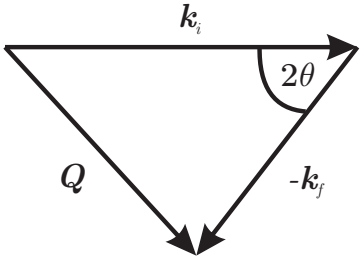

Figure 2-2: The scattering triangle formed by the vectors $\mathbf{k}_i$, $\mathbf{k}_f$ and $\mathbf{Q} = \mathbf{k}_i - \mathbf{k}_f$.

for a neutron are given by

$$E_i = \frac{\hbar^2 k_i^2}{2m_n} \quad , \quad E_f = \frac{\hbar^2 k_f^2}{2m_n} \quad , \tag{2.3}$$

where m_n is the mass of a neutron, while k_i and k_f are the magnitudes of $\mathbf{k}_i$ and $\mathbf{k}_f$, respectively.

2.2 Neutron Spectroscopy

Neutrons are a useful probe of the structure and dynamics of materials. They scatter directly from atomic nuclei via the strong interaction. The wavelength of thermal neutrons is of the order of the inter-atomic spacings and their energy is of the order of vibrational excitations. Therefore, the structure and dynamics of materials can be probed directly by experiment. The neutron scattering length, b, is a measure of the probability that a given atomic nucleus will scatter a neutron which is incident upon it. The value of b is not correlated to the atomic number or atomic mass of an element, but depends on the isotope and nuclear spin state. Therefore, different isotopes of the same element can have very different scattering lengths (see figure 2-3).

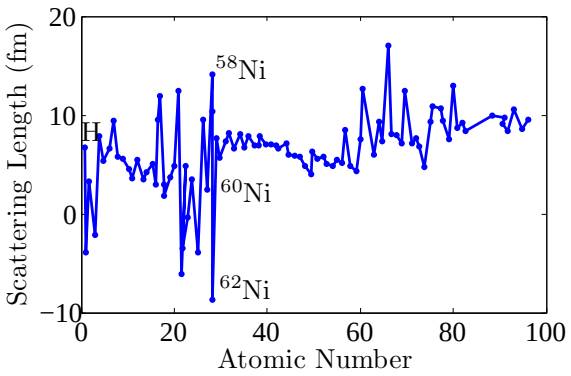

Figure 2-3: Neutron scattering lengths of common isotopes shown as a function of atomic number [43].

The double differential scattering cross section for a system of N scattering centres is given by [9]

$$\frac{1}{N}\frac{\mathrm{d}^2\sigma}{\mathrm{d}\Omega \mathrm{d}E_f} = \frac{1}{N}\frac{k_f}{k_i}\frac{1}{2\pi\hbar}\int_{-\infty}^{\infty} \mathrm{d}t e^{-i\omega t} \sum_{\mathrm{i}=1}^{N}\sum_{\mathrm{j}=1}^{N} \overline{b_\mathrm{i} b_\mathrm{j}} \left\langle e^{-i\mathbf{Q}\cdot\mathbf{R}_\mathrm{i}(0)} e^{i\mathbf{Q}\cdot\mathbf{R}_\mathrm{j}(t)} \right\rangle \quad , \tag{2.4}$$

where the brackets $\langle \cdots \rangle$ denote a thermal average, the quantity $\overline{b_\mathrm{i} b_\mathrm{j}}$ is the value of

$b_\mathrm{i}b_\mathrm{j}$ averaged over random nuclear spin orientations and isotope distributions, while b_i and b_j are the scattering lengths of nuclei i and j, respectively. $\mathbf{R}_\mathrm{i}(0)$ and $\mathbf{R}_\mathrm{j}(t)$ are the positions of particles i at time $t = 0$ and j at time t, respectively. $\omega = E/\hbar$ is an angular frequency where E is the energy transfer in a scattering event.

It is often convenient to separate incoherent from coherent scattering such that

$$\frac{1}{N}\frac{\mathrm{d}^2\sigma}{\mathrm{d}\Omega \mathrm{d}E_f} = \frac{1}{N}\left.\frac{\mathrm{d}^2\sigma}{\mathrm{d}\Omega \mathrm{d}E_f}\right|_\mathrm{c} + \frac{1}{N}\left.\frac{\mathrm{d}^2\sigma}{\mathrm{d}\Omega \mathrm{d}E_f}\right|_\mathrm{inc} = \frac{k_f}{k_i}\left(S_\mathrm{c}(\mathbf{Q},E) + S_\mathrm{inc}(\mathbf{Q},E)\right) \quad , \tag{2.5}$$

where $S_\mathrm{c}(\mathbf{Q},E)$ and $S_\mathrm{inc}(\mathbf{Q},E)$ are the coherent and incoherent total dynamical structure factors, respectively, given by [41]

$$S_\mathrm{c}(\mathbf{Q},E) = \frac{1}{N}\frac{1}{2\pi\hbar}\int_{-\infty}^{\infty}\mathrm{d}t\, e^{-i\omega t}\sum_{\mathrm{i}=1}^{N}\sum_{\mathrm{j}=1}^{N}\overline{b}_\mathrm{i}\overline{b}_\mathrm{j}\left\langle e^{-i\mathbf{Q}\cdot\mathbf{R}_\mathrm{i}(0)}e^{i\mathbf{Q}\cdot\mathbf{R}_\mathrm{j}(t)}\right\rangle \tag{2.6}$$

and

$$S_\mathrm{inc}(\mathbf{Q},E) = \frac{1}{N}\frac{1}{2\pi\hbar}\int_{-\infty}^{\infty}\mathrm{d}t\, e^{-i\omega t}\sum_{\mathrm{i}=1}^{N}\left(\overline{b_\mathrm{i}^2} - \overline{b}_\mathrm{i}^2\right)\left\langle e^{-i\mathbf{Q}\cdot\mathbf{R}_\mathrm{i}(0)}e^{i\mathbf{Q}\cdot\mathbf{R}_\mathrm{i}(t)}\right\rangle \quad . \tag{2.7}$$

The bar above $\overline{b}_\mathrm{i}$ and $\overline{b}_\mathrm{j}$ denotes the mean scattering length of the chemical species to which the nuclei i and j belong, respectively. $\overline{b_\mathrm{i}^2}$ is the mean of the squared scattering length of the chemical species to which atom i belongs. The means are taken over all isotopes and spin states of that chemical species. It is often convenient to define a coherent scattering cross section $\sigma_\mathrm{coh} = 4\pi b_\mathrm{coh}^2 = 4\pi\overline{b}^2$ and an incoherent scattering cross section $\sigma_\mathrm{inc} = 4\pi b_\mathrm{inc}^2 = 4\pi\left(\overline{b^2} - \overline{b}^2\right)$ for a given chemical species, where b_coh and b_inc are the coherent and incoherent scattering lengths, respectively.

Coherent scattering involves the correlations between the positions of the same nucleus at different times, and pairs of different nuclei at different times [9]. Coherent scattering, therefore, gives rise to interference effects. It can be interpreted as the scattering which would be seen if all nuclei of a particular chemical species had the same mean scattering length. Incoherent scattering arises from deviations of the scattering lengths from their mean values.

In a solid, nuclei move around well defined equilibrium positions, $\mathbf{R}_\mathrm{i}$, such that $\mathbf{R}_\mathrm{i}(t) = \mathbf{R}_\mathrm{i} + \mathbf{u}_\mathrm{i}(t)$, where $\mathbf{u}_\mathrm{i}(t)$ is a displacement. If the displacements are small, then

the harmonic approximation can be used and equation (2.6) is re-written as [41][1]

$$S_{\mathrm{c}}(\mathbf{Q},E) = \frac{1}{N}\sum_{\mathrm{i}=1}^{N}\sum_{\mathrm{j}=1}^{N}\overline{b}_{\mathrm{i}}\overline{b}_{\mathrm{j}}\left\langle e^{\left(-i\mathbf{Q}\cdot(\mathbf{R}_{\mathrm{i}}-\mathbf{R}_{\mathrm{j}})\right)}\right\rangle e^{-(W_{\mathrm{i}}(Q)+W_{\mathrm{j}}(Q))} \times \frac{1}{2\pi\hbar}\int_{-\infty}^{\infty}\mathrm{d}t\, e^{-i\omega t}e^{\left\langle(\mathbf{Q}\cdot\mathbf{u}_{\mathrm{i}}(0))(\mathbf{Q}\cdot\mathbf{u}_{\mathrm{j}}(t))\right\rangle} \quad , \tag{2.8}$$

where $W_{\mathrm{i}}(Q) = \frac{1}{6}\left\langle u_{\mathrm{i}}^2\right\rangle Q^2$ and $W_{\mathrm{j}}(Q) = \frac{1}{6}\left\langle u_{\mathrm{j}}^2\right\rangle Q^2$ are the Debye-Waller factors for nuclei i and j while $\left\langle u_{\mathrm{i}}^2\right\rangle$ and $\left\langle u_{\mathrm{j}}^2\right\rangle$ are the mean square displacements of nuclei i and j, respectively. The final term in equation (2.8) can be Taylor expanded as a power series such that

$$e^{\left\langle(\mathbf{Q}\cdot\mathbf{u}_{\mathrm{i}}(0))(\mathbf{Q}\cdot\mathbf{u}_{\mathrm{j}}(t))\right\rangle} = \sum_{p=0}^{\infty}\frac{1}{p!}\left\langle(\mathbf{Q}\cdot\mathbf{u}_{\mathrm{i}}(0))(\mathbf{Q}\cdot\mathbf{u}_{\mathrm{j}}(t))\right\rangle^{p} \quad , \tag{2.9}$$

where $p = 0, 1, 2, \ldots$. Substituting equation (2.9) into equation (2.8) gives

$$S_{\mathrm{c}}(\mathbf{Q},E) = \frac{1}{N}\sum_{\mathrm{i}=1}^{N}\sum_{\mathrm{j}=1}^{N}\overline{b}_{\mathrm{i}}\overline{b}_{\mathrm{j}}\left\langle e^{\left(-i\mathbf{Q}\cdot(\mathbf{R}_{\mathrm{i}}-\mathbf{R}_{\mathrm{j}})\right)}\right\rangle e^{-(W_{\mathrm{i}}(Q)+W_{\mathrm{j}}(Q))} \times \frac{1}{2\pi\hbar}\int_{-\infty}^{\infty}\mathrm{d}t\, e^{-i\omega t}\sum_{p=0}^{\infty}\frac{1}{p!}\left\langle(\mathbf{Q}\cdot\mathbf{u}_{\mathrm{i}}(0))(\mathbf{Q}\cdot\mathbf{u}_{\mathrm{j}}(t))\right\rangle^{p} \quad . \tag{2.10}$$

In this series, $p = 0$ represents the cross section for elastic scattering, $p = 1$ represents the cross section for all of the one phonon processes while $p > 2$ represents the cross section for p phonon (multiple phonon) processes.

2.2.1 Single Phonon Scattering

The single phonon contribution to the coherent dynamical structure factor (the case when $p = 1$ in equation (2.10)) is given by the sum of contributions from events that create phonons, $S_{\mathrm{c}+1}(\mathbf{Q},E)$, and from events that annihilate phonons $S_{\mathrm{c}-1}(\mathbf{Q},E)$, so that $S_1(\mathbf{Q},E) = S_{\mathrm{c}+1}(\mathbf{Q},E)+S_{\mathrm{c}-1}(\mathbf{Q},E)$, where $S_1(\mathbf{Q},E)$ is the single phonon coherent total dynamical structure factor. The general motion of each of N quantised simple harmonic oscillators in 3 dimensions due to single phonon processes can be described by the superposition of $3N$ allowed normal modes [11, pp. 139] such that for the case

[1] Only coherent scattering is considered in this thesis, but incoherent scattering can be included (see appendix A.1)

when $E = E_i - E_f > 0$

$$S_{\mathrm{c},+1}(\mathbf{Q},E) = \frac{1}{N}\frac{\hbar^2}{2}\sum_{\mathrm{i}=1}^{N}\sum_{\mathrm{j}=1}^{N}\bar{b}_{\mathrm{i}}\bar{b}_{\mathrm{j}}\left\langle e^{-i\mathbf{Q}\cdot(\mathbf{R}_{\mathrm{i}}-\mathbf{R}_{\mathrm{j}})}\right\rangle e^{-(W_{\mathrm{i}}(Q)+W_{\mathrm{j}}(Q))} \times\sum_{\nu=1}^{3N}\frac{(\mathbf{Q}\cdot\mathbf{e}_{\mathrm{i}}^{\nu})^{*}(\mathbf{Q}\cdot\mathbf{e}_{\mathrm{j}}^{\nu})}{(M_{\mathrm{i}}M_{\mathrm{j}})^{1/2}E_{\nu}}\left\langle n(E_{\nu})+1\right\rangle\delta(E-E_{\nu}) \tag{2.11}$$

and for the case when $E = E_i - E_f < 0$

$$S_{\mathrm{c},-1}(\mathbf{Q},E) = \frac{1}{N}\frac{\hbar^2}{2}\sum_{\mathrm{i}=1}^{N}\sum_{\mathrm{j}=1}^{N}\bar{b}_{\mathrm{i}}\bar{b}_{\mathrm{j}}e^{-i\mathbf{Q}\cdot(\mathbf{R}_{\mathrm{i}}-\mathbf{R}_{\mathrm{j}})}e^{-(W_{\mathrm{i}}(Q)+W_{\mathrm{j}}(Q))} \times\sum_{\nu=1}^{3N}\frac{(\mathbf{Q}\cdot\mathbf{e}_{\mathrm{i}}^{\nu})^{*}(\mathbf{Q}\cdot\mathbf{e}_{\mathrm{j}}^{\nu})}{(M_{\mathrm{i}}M_{\mathrm{j}})^{1/2}E_{\nu}}\left\langle n(E_{\nu})\right\rangle\delta(E+E_{\nu}) \quad , \tag{2.12}$$

where M_{i} and M_{j} are the masses of nuclei i and j respectively. $\mathbf{e}_{\mathrm{i}}^{\nu}$ and $\mathbf{e}_{\mathrm{j}}^{\nu}$ are the displacement vectors of the i^{th} and j^{th} nucleus in the ν^{th} normal mode , respectively, $E_\nu = \hbar\omega_\nu$ is the energy of mode ν, $\langle n_\nu(E)\rangle$ and $\langle n_\nu(E)+1\rangle$ are the Bose-Einstein occupation factors given by

$$\langle n(E_\nu)\rangle = \frac{1}{e^{E_\nu/(k_BT)}-1} \tag{2.13}$$

and

$$\langle n(E_\nu)+1\rangle = \frac{e^{E_\nu/(k_BT)}}{e^{E_\nu/(k_BT)}-1} \quad , \tag{2.14}$$

where k_B is Boltzmann's constant and T is the absolute temperature. The delta functions ensure that the only contributions to the summations in equations (2.11) and (2.12) are when $E = E_\nu$ and $E = -E_\nu$, respectively. Also, for the case when $E < 0$, using the symmetry of the delta function it follows that $\delta(E+E_\nu) = \delta(-(E+E_\nu)) = \delta(|E|-E_\nu)$. In addition

$$\langle n(-E)\rangle = \frac{1}{e^{-E/(k_BT)}-1} = \frac{e^{E/(k_BT)}}{1-e^{E/(k_BT)}} = -\left\langle n(E)+1\right\rangle \ , \tag{2.15}$$

such that $\langle n(-E)\rangle/(-E) = \langle n(E)+1\rangle/E$. Hence it follows that equation (2.12) can be re-written as

$$S_{\mathrm{c},-1}(\mathbf{Q},E) = \frac{1}{N}\frac{\hbar^2}{2}\sum_{\mathrm{i}=1}^{N}\sum_{\mathrm{j}=1}^{N}\overline{b}_{\mathrm{i}}\overline{b}_{\mathrm{j}}e^{-i\mathbf{Q}\cdot(\mathbf{R}_{\mathrm{i}}-\mathbf{R}_{\mathrm{j}})}e^{-(W_{\mathrm{i}}(Q)+W_{\mathrm{j}}(Q))} \times \sum_{\nu=1}^{3N}\frac{(\mathbf{Q}\cdot\mathbf{e}_{\mathrm{i}}^{\nu})^*(\mathbf{Q}\cdot\mathbf{e}_{\mathrm{j}}^{\nu})}{(M_{\mathrm{i}}M_{\mathrm{j}})^{1/2}E}\langle n(E)+1\rangle\,\delta(|E|-E_\nu) \quad . \tag{2.16}$$

Since $E > 0$ (thus $E = |E|$) in equation (2.11), equations (2.11) and (2.16) can both be expressed in the same equation valid for all $E \neq 0$ such that

$$S_1(\mathbf{Q},E) = \frac{1}{N}\frac{\hbar^2Q^2}{2}\sum_{\mathrm{i}=1}^{N}\sum_{\mathrm{j}=1}^{N}\overline{b}_{\mathrm{i}}\overline{b}_{\mathrm{j}}\left\langle e^{-i\mathbf{Q}\cdot(\mathbf{R}_{\mathrm{i}}-\mathbf{R}_{\mathrm{j}})}\right\rangle e^{-(W_{\mathrm{i}}(Q)+W_{\mathrm{j}}(Q))} \times \frac{\langle n(E)+1\rangle}{E}\sum_{\nu=1}^{3N}\frac{(\hat{\mathbf{Q}}\cdot\mathbf{e}_{\mathrm{i}}^{\nu})^*(\hat{\mathbf{Q}}\cdot\mathbf{e}_{\mathrm{j}}^{\nu})}{(M_{\mathrm{i}}M_{\mathrm{j}})^{1/2}}\delta(|E|-E_\nu)\,, \tag{2.17}$$

where $Q = |\mathbf{Q}|$ and $\hat{\mathbf{Q}} = \mathbf{Q}/(|\mathbf{Q}|)$. Equation (2.11) is recovered from equation (2.17) when $E > 0$ and equation (2.12) is recovered from equation (2.17) when $E < 0$.

2.2.2 The Extreme Incoherent Approximation

In the extreme incoherent approximation, no distinction is made between (e.g. the chemical) identity of the nuclei such that equation (2.17) becomes

$$S_1(\mathbf{Q},E) = \frac{1}{N}\frac{\hbar^2Q^2}{2\overline{M}}\left\langle\overline{b}^2\right\rangle e^{-2\overline{W}(Q)}\sum_{\mathrm{i}=1}^{N}\sum_{\mathrm{j}=1}^{N}\left\langle e^{-i\mathbf{Q}\cdot(\mathbf{R}_{\mathrm{i}}-\mathbf{R}_{\mathrm{j}})}\right\rangle \times \frac{\langle n(E)+1\rangle}{E}\sum_{\nu=1}^{3N}(\hat{\mathbf{Q}}\cdot\mathbf{e}_{\mathrm{i}}^{\nu})^*(\hat{\mathbf{Q}}\cdot\mathbf{e}_{\mathrm{j}}^{\nu})\delta(|E|-E_\nu) \quad . \tag{2.18}$$

All nuclei are described by the same mean square scattering length, which is taken to be

$$\left\langle\overline{b}^2\right\rangle = \sum_{\alpha=1}^{n}c_\alpha\overline{b}_\alpha^2\,, \tag{2.19}$$

the same mass, which is taken to be

$$\overline{M} = \sum_{\alpha=1}^{n}c_\alpha M_\alpha\,, \tag{2.20}$$

and the same Debye-Waller factor, which is taken to be

$$\overline{W}(Q) = \sum_{\alpha=1}^{n} c_\alpha W_\alpha(Q)\,. \tag{2.21}$$

In equations (2.19), (2.20) and (2.21), α denotes a chemical species, n denotes the number of chemical species while c_α, $\overline{b}_\alpha$, M_α and $W_\alpha(Q)$ are the atomic fraction, mean scattering length, mean mass and mean Debye-Waller factor for chemical species α, respectively.

The incoherent approximation is then made, whereby only the contribution from terms where i = j (i.e. terms involving the same nucleus) within the sum made in equation (2.18) are considered such that

$$S_1(\mathbf{Q},E) = \frac{1}{N}\frac{\hbar^2Q^2}{2\overline{M}}\left\langle \overline{b}^2\right\rangle e^{-2\overline{W}(Q)}\frac{\langle n(E)+1\rangle}{E}\sum_{\mathrm{i}=1}^{N}\sum_{\nu=1}^{3N}|\hat{\mathbf{Q}}\cdot\mathbf{e}_{\mathrm{i}}^{\nu}|^2\delta(|E|-E_\nu) \quad . \tag{2.22}$$

If $\hat{\mathbf{Q}}$ is averaged over all directions (which is the case for an homogeneous, isotropic solid such as most glasses) then

$$\left\langle|\hat{\mathbf{Q}}\cdot\mathbf{e}_{\mathrm{i}}^{\nu}|^2\right\rangle = \frac{1}{3}\left\langle|\mathbf{e}_{\mathrm{i}}^{\nu}|^2\right\rangle \quad . \tag{2.23}$$

If the *total* vibrational density of states, $Z(E)$, is defined to be the fraction of states between E and $E+\mathrm{d}E$ then

$$Z(E) = \frac{1}{3N}\sum_{\mathrm{i}=1}^{N}\sum_{\nu=1}^{3N}\left\langle|\mathbf{e}_{\mathrm{i}}^{\nu}|^2\right\rangle\delta(|E|-E_\nu) = \frac{1}{3N}\sum_{\nu=1}^{3N}\delta(|E|-E_\nu) \quad . \tag{2.24}$$

It follows that $Z(E)$ is an even function, $\int Z(E)\mathrm{d}E = 1$ for $E > 0$, and that equation (2.22) can be expressed in the extreme incoherent approximation as

$$S_1(Q,E) = \frac{\hbar^2Q^2}{2\overline{M}}\left\langle \overline{b}^2\right\rangle e^{-2\overline{W}(Q)}\frac{\langle n(E)+1\rangle}{E}Z(E) \quad . \tag{2.25}$$

2.2.3 The Incoherent Approximation

For a two component system of chemical species A and X, equation (2.17) can be rewritten as the sum of partial dynamical structure factors $S_{\alpha\beta}(\mathbf{Q},E)$ ($\alpha = A,X$, $\beta = A,X$, such that

$$S_1(\mathbf{Q},E) = \overline{b}_A^2 S_{AA}(\mathbf{Q},E) + \overline{b}_X^2 S_{XX}(\mathbf{Q},E) + 2\overline{b}_A\overline{b}_X S_{AX}(\mathbf{Q},E) \quad , \tag{2.26}$$

where $\overline{b}_\alpha$ is the mean scattering length of chemical species α. $S_{\alpha\beta}(\mathbf{Q},E)$ represents the correlations between nuclei of chemical species α and nuclei of chemical species β and is given by

$$S_{\alpha\beta}(\mathbf{Q},E) = \frac{1}{N}\frac{\hbar^2Q^2}{2}\sum_{\alpha\mathrm{i}=1}^{N_\alpha}\sum_{\beta\mathrm{j}=1}^{N_\beta} e^{-(W_{\alpha\mathrm{i}}(Q)+W_{\beta\mathrm{j}}(Q))}\left\langle e^{-i\mathbf{Q}\cdot(\mathbf{R}_{\alpha\mathrm{i}}-\mathbf{R}_{\beta\mathrm{j}})}\right\rangle \times \frac{\langle n(E)+1\rangle}{E}\sum_{\nu=1}^{3N}\frac{(\hat{\mathbf{Q}}\cdot\mathbf{e}^\nu_{\alpha\mathrm{i}})^*(\hat{\mathbf{Q}}\cdot\mathbf{e}^\nu_{\beta\mathrm{j}})}{(M_{\alpha\mathrm{i}}M_{\beta\mathrm{i}})^{1/2}}\delta(|E|-E_\nu) \quad , \tag{2.27}$$

where N_α and N_β are the number of nuclei in the system of chemical species α and β, while $\alpha\mathrm{i}$ and $\beta\mathrm{j}$ denote nuclei of chemical species α and β, respectively.

The incoherent approximation is then made, whereby only terms involving $\alpha\mathrm{i}=\beta\mathrm{j}$ (i.e. terms involving the same nuclei) contribute to the sum in equation (2.27) such that $S_{\alpha\beta}(Q,E)=0$ for $\alpha\neq\beta$ and

$$S_{\alpha\alpha}(\mathbf{Q},E) = \frac{1}{N}\frac{\hbar^2Q^2}{2M_\alpha}e^{-2W_\alpha(Q)}\frac{\langle n(E)+1\rangle}{E}\sum_{\alpha\mathrm{i}=1}^{N_\alpha}\sum_{\nu=1}^{3N}|\hat{\mathbf{Q}}\cdot\mathbf{e}^\nu_{\alpha\mathrm{i}}|^2\delta(|E|-E_\nu) \quad , \tag{2.28}$$

where M_α and $W_\alpha(Q)$ are the mean mass and Debye-Waller factor for atoms of chemical species α, respectively. If $\hat{\mathbf{Q}}$ is averaged over all directions (which is the case for an homogeneous, isotropic solid such as most glasses) then

$$\left\langle|\hat{\mathbf{Q}}\cdot\mathbf{e}^\nu_{\alpha\mathrm{i}}|^2\right\rangle = \frac{1}{3}\left\langle|\mathbf{e}^\nu_{\alpha\mathrm{i}}|^2\right\rangle \quad . \tag{2.29}$$

The partial vibrational density of states for a given chemical species α is defined as the fraction of modes with energy between E and $E+\mathrm{d}E$ such that

$$Z_\alpha(E) = \frac{1}{3N}\sum_{\alpha\mathrm{i}=1}^{N_\alpha}\sum_{\nu=1}^{3N}\left\langle|\mathbf{e}^\nu_{\alpha\mathrm{i}}|^2\right\rangle\delta(|E|-E_\nu) \quad , \tag{2.30}$$

where $Z_\alpha(E)$ is the partial vibrational density of states, defined such that $\int Z_\alpha(E)\mathrm{d}E = c_\alpha$. Therefore equation (2.28) becomes

$$S_{\alpha\alpha}(Q,E) = \frac{\hbar^2Q^2}{2M_\alpha}e^{-2W_\alpha(Q)}\frac{\langle n(E)+1\rangle}{E}Z_\alpha(E) \quad . \tag{2.31}$$

The total vibrational density of states is given by $Z(E)=Z_\mathrm{A}(E)+Z_\mathrm{X}(E)$.

2.2.4 Isotopic Substitution in Neutron Spectroscopy

If the incoherent scattering cross section is small enough to be ignored then equation (2.5) for an homogeneous, isotropic system, becomes

$$\frac{1}{N}\frac{\mathrm{d}^2\sigma}{\mathrm{d}\Omega \mathrm{d}E_f} = \frac{1}{N}\left.\frac{\mathrm{d}^2\sigma}{\mathrm{d}\Omega \mathrm{d}E_f}\right|_{\mathrm{c}} = \frac{k_f}{k_i} S_{\mathrm{c}}(Q,E) \quad . \tag{2.32}$$

The"Gold Medal" Result

If the multiple phonon contribution to the scattering can be ignored then $S_{\mathrm{c}}(Q,E) = S_1(Q,E)$ and, for a glass, it is convenient to re-write equation (2.26) in the form

$$S_1(Q,E) = \frac{\bar{b}_A^2}{M_A} S'_{AA}(Q,E) + \frac{\bar{b}_X^2}{M_X} S'_{XX}(Q,E) + 2\frac{\bar{b}_A \bar{b}_X}{\sqrt{M_A M_X}} S'_{AX}(Q,E)\,, \tag{2.33}$$

where the revised partial dynamical structure factors are defined by $S'_{\alpha\beta}(Q,E) \equiv \sqrt{M_\alpha M_\beta} S_{\alpha\beta}(Q,E)$. To measure the $S'_{\alpha\beta}(Q,E)$ functions, three neutron scattering experiments are necessary using samples that are identical in every respect except for their isotopic enrichments. Three functions ${}^{A1}_{X1}S_1(Q,E)$, ${}^{A2}_{X2}S_1(Q,E)$ and ${}^{A3}_{X3}S_1(Q,E)$ are then measured, where $A1, A2$ and $A3$ represent different isotopic enrichments of chemical species A and, similarly, $X1, X2$ and $X3$ represent different isotopic enrichments of chemical species X. A matrix $\mathbf{B}$ can be defined by

$$\mathbf{B} = \begin{pmatrix} \frac{\bar{b}_{A1}^2}{M_{A1}} & \frac{\bar{b}_{X1}^2}{M_{X1}} & 2\frac{\bar{b}_{A1}\bar{b}_{X1}}{\sqrt{M_{A1}M_{X1}}} \\ \frac{\bar{b}_{A2}^2}{M_{A2}} & \frac{\bar{b}_{X2}^2}{M_{X2}} & 2\frac{\bar{b}_{A1}\bar{b}_{X2}}{\sqrt{M_{A2}M_{X2}}} \\ \frac{\bar{b}_{A3}^2}{M_{A3}} & \frac{\bar{b}_{X3}^2}{M_{X3}} & 2\frac{\bar{b}_{A3}\bar{b}_{X3}}{\sqrt{M_{A3}M_{X3}}} \end{pmatrix}, \tag{2.34}$$

such that

$$\begin{pmatrix} {}^{A1}_{X1}S_1(Q,E) \\ {}^{A2}_{X2}S_1(Q,E) \\ {}^{A3}_{X3}S_1(Q,E) \end{pmatrix} = \mathbf{B} \begin{pmatrix} S'_{AA}(Q,E) \\ S'_{XX}(Q,E) \\ S'_{AX}(Q,E) \end{pmatrix} \tag{2.35}$$

and thus

$$\begin{pmatrix} S'_{AA}(Q,E) \\ S'_{XX}(Q,E) \\ S'_{AX}(Q,E) \end{pmatrix} = \mathbf{B}^{-1} \begin{pmatrix} {}^{A1}_{X1}S_1(Q,E) \\ {}^{A2}_{X2}S_1(Q,E) \\ {}^{A3}_{X3}S_1(Q,E) \end{pmatrix}. \tag{2.36}$$

The partial dynamical structure factors are then found by using

$$S_{\alpha\beta}(Q,E) = \frac{1}{\sqrt{M_\alpha M_\beta}} S'_{\alpha\beta}(Q,E)\,. \tag{2.37}$$

Equation (2.31) can be re-written to allow for deviations from the incoherent approximation by replacing $Z_\alpha(E)$ with the generalised one phonon partial vibrational density of states $G_\alpha(Q,E)$ so that

$$G_\alpha(Q,E) = \frac{2M_\alpha}{\hbar^2 Q^2} e^{2W_\alpha(Q)} \frac{E}{\langle n(E)+1\rangle} S_{\alpha\alpha}(Q,E)\ . \tag{2.38}$$

The effective partial vibrational density of states $G(E)$ is then obtained by taking the mean of $G_\alpha(Q,E)$ over Q such that

$$G_\alpha(E) = \frac{1}{Q_{\max} - Q_{\min}} \int_{Q_{\min}}^{Q_{\max}} G_\alpha(Q,E)\, dQ\,, \tag{2.39}$$

where $Q_{\max}$ and $Q_{\min}$ are the maximum and minimum values of Q over which $S_1(Q,E)$ is measured reliably. When the $S'_{\alpha\alpha}(Q,E)$ functions are separated by using equation (2.36) and $G_\alpha(Q,E)$ and $G_\alpha(E)$ are calculated from $S'_{\alpha\alpha}(Q,E)$ by using equations (2.37), (2.38) and (2.39), the effective partial vibrational density of states thus calculated are referred to as the "gold medal" results. Molecular dynamics simulations (e.g. [35, 44, 45]) have shown that $G_\alpha(E)$ is an excellent approximation to the true partial vibrational density of states $Z_\alpha(E)$.

The "Silver Medal" Result

If the contribution to $S_1(Q,E)$ from $S_{AX}(Q,E)$ is ignored (i.e. the incoherent approximation is made to $S_1(Q,E)$, before separation of the full set of partial dynamical structure factors), then equation (2.33) can be re-written as

$$S_1(Q,E) = \frac{\bar{b}_A^2}{M_A} S'_{AA}(Q,E) + \frac{\bar{b}_X^2}{M_X} S'_{XX}(Q,E)\,. \tag{2.40}$$

The functions ${}^{A1}_{X1}S_1(Q,E)$ and ${}^{A2}_{X2}S_1(Q,E)$ are then measured as in the previous section. A matrix $\mathbf{C}$ can be defined as

$$\mathbf{C} = \begin{pmatrix} \frac{\bar{b}_{A1}^2}{M_{A1}} & \frac{\bar{b}_{X1}^2}{M_{X1}} \\ \frac{\bar{b}_{A2}^2}{M_{A2}} & \frac{\bar{b}_{X2}^2}{M_{X2}} \end{pmatrix}\,, \tag{2.41}$$

such that

$$\begin{pmatrix} {}^{A1}_{X1}S_1(Q,E) \\ {}^{A2}_{X2}S_1(Q,E) \end{pmatrix} = \mathbf{C} \begin{pmatrix} S'_{AA}(Q,E) \\ S'_{XX}(Q,E) \end{pmatrix} \tag{2.42}$$

and thus

$$\begin{pmatrix} S'_{AA}(Q,E) \\ S'_{XX}(Q,E) \end{pmatrix} = \mathbf{C}^{-1} \begin{pmatrix} {}^{A1}_{X1}S_1(Q,E) \\ {}^{A2}_{X2}S_1(Q,E) \end{pmatrix}\,. \tag{2.43}$$

The generalised partial vibrational density of states are again extracted by using equations (2.37) and (2.38). When the $S'_{\alpha\alpha}(Q,E)$ functions are separated by using equation (2.43) and $G_\alpha(Q,E)$ and $G_\alpha(E)$ are calculated from $S'_{\alpha\alpha}(Q,E)$ by using equations (2.37), (2.38) and (2.39), the effective partial vibrational density of states thus calculated are referred to as the "silver medal" results. This method is mathematically equivalent to the first order difference method (see appendix A.2.

The "Bronze Medal" Result

Equation (2.25) can be re-written to allow for deviations from the extreme incoherent approximation by replacing $Z(E)$ with the generalised one phonon partial vibrational density of states $G(Q,E)$ so that

$$G(Q,E) = \frac{1}{\left\langle \bar{b}^2 \right\rangle} \frac{2\overline{M}}{\hbar^2 Q^2} e^{2\overline{W}(Q)} \frac{E}{\langle n(E)+1 \rangle} S_1(Q,E)\,. \tag{2.44}$$

Similar to equation (2.39), the effective *total* vibrational density of states $G(E)$ is obtained by taking the mean of $G(Q,E)$ over Q such that

$$G(E) = \frac{1}{Q_{\max} - Q_{\min}} \int_{Q_{\min}}^{Q_{\max}} G(Q,E)\, dQ\,. \tag{2.45}$$

The use of equations (2.44) and (2.45) is well established [42, 46] (see reference [41] for a detailed explanation) and we refer to equation (2.45) as the "bronze medal" result. $G(E)$ will be a good approximation to the true vibrational density of states $Z(E)$ when $\bar{b}_{\mathrm{A}} \simeq \bar{b}_{\mathrm{X}}$ and $M_{\mathrm{A}} \simeq M_{\mathrm{X}}$.

2.3 Differential Scattering Cross Section

In section 2.1 the *double* differential scattering cross section was introduced in equation (2.1). If the final energy of the neutrons is not distinguished and all particles scattered into a solid angle Ω are counted, then the differential scattering cross section is measured where

$$\frac{\mathrm{d}\sigma}{\mathrm{d}\Omega} = (\text{Number of neutrons scattered per second into } \mathrm{d}\Omega)/(\Phi \mathrm{d}\Omega) \quad . \tag{2.46}$$

Here, the double differential and differential cross sections are related by

$$\frac{\mathrm{d}\sigma}{\mathrm{d}\Omega} = \int_0^\infty \left(\frac{\mathrm{d}^2\sigma}{\mathrm{d}\Omega \mathrm{d}E_f} \right) \mathrm{d}E_f \quad . \tag{2.47}$$

In the static approximation, a condition that is met when E_i is much larger than any energy transfer to/from the system, $k_i \approx k_f$ so that equation (2.2) becomes

$$Q = \frac{4\pi}{\lambda}\sin(\theta) \quad , \tag{2.48}$$

where $\lambda = 2\pi/k_i$ is the wavelength of the incident neutron.

2.4 Neutron Diffraction

In neutron diffraction, within the static approximation the differential scattering cross section is given by [9]

$$\frac{1}{N}\frac{\mathrm{d}\sigma}{\mathrm{d}\Omega} = \frac{1}{N}\sum_{\mathrm{i}=1}^{N}\sum_{\mathrm{j}=1}^{N}\overline{b_{\mathrm{i}}b_{\mathrm{j}}}\left\langle e^{-i\mathbf{Q}\cdot\mathbf{R}_{\mathrm{i}}(0)}e^{i\mathbf{Q}\cdot\mathbf{R}_{\mathrm{j}}(0)}\right\rangle \quad , \tag{2.49}$$

where the brackets $\langle\cdots\rangle$ denote a thermal average, the quantity $\overline{b_{\mathrm{i}}b_{\mathrm{j}}}$ is the value of $b_{\mathrm{i}}b_{\mathrm{j}}$ averaged over random nuclear spin orientations and isotope distributions, while b_{i} and b_{j} are the scattering lengths of nuclei i and j, respectively. $\mathbf{R}_{\mathrm{i}}(0)$ and $\mathbf{R}_{\mathrm{j}}(0)$ are the positions of nuclei i and j at a time $t = 0$, respectively.

For an isotropic, homogeneous system of scattering centres with n chemical species, the differential scattering cross section can be expressed in the form of a total structure factor, $F(Q)$, and a self term such that [5, 47]

$$\frac{1}{N}\frac{\mathrm{d}\sigma}{\mathrm{d}\Omega} = F(Q) + \frac{\sigma_{\mathrm{self}}}{4\pi} \quad , \tag{2.50}$$

and

$$\frac{\sigma_{\mathrm{self}}}{4\pi} = \sum_{\alpha=1}^{n} c_\alpha(\bar{b}_\alpha^2 + b_{\mathrm{inc},\alpha}^2)(1 + P_\alpha(Q)) \quad , \tag{2.51}$$

where $b_{\mathrm{inc},\alpha} = \overline{b_\alpha^2} - \bar{b}_\alpha^2$, while $\overline{b_\alpha^2}$ and $\bar{b}_\alpha$ are the mean of the square of the scattering length and the mean of the scattering length of chemical species α, respectively. $P_\alpha(Q)$ is the so-called Placzek correction for chemical species α that arises from a departure from the static approximation (originally derived by Placzek [48] with an explanation of different methods used for its calculation given in reference [49]). $F(Q)$ corresponds to the sum of the terms in equation (2.49) when i $\neq$ j, less the forward scattering, i.e. it represents the interference pattern produced from neutrons scattered from pairs of different nuclei. σ_{self} is the self scattering cross section, corresponding to i = j in equation (2.49), i.e. it represents scattering from the same nucleus.

The total structure factor can be expressed in terms of a sum of so-called Faber-

Ziman partial structure factors $S_{\alpha\beta}(Q)$ which describe the correlations between pairs of nuclei of chemical species α and β by the expression [50]

$$F(Q) = \sum_{\alpha=1}^{n}\sum_{\beta=1}^{n} c_\alpha c_\beta \bar{b}_\alpha \bar{b}_\beta \left[S_{\alpha\beta}(Q) - 1\right] \quad , \tag{2.52}$$

where c_α and c_β are the atomic fractions of chemical species α and β, respectively and $\langle \bar{b} \rangle = \sum_\alpha^n c_\alpha \bar{b}_\alpha$. The total pair distribution function, $G(r)$, is given by the sine Fourier transform of $F(Q)$ such that

$$\begin{aligned} G(r) &= \frac{1}{2\pi^2 r\rho} \int_0^\infty Q F(Q) \sin(Qr)\, \mathrm{d}Q \\ &= \sum_{\alpha=1}^{n}\sum_{\beta=1}^{n} c_\alpha c_\beta \bar{b}_\alpha \bar{b}_\beta \left[g_{\alpha\beta}(r) - 1\right] \quad , \end{aligned} \tag{2.53}$$

where ρ is the atomic number density of the system and the partial pair distribution function, $g_{\alpha\beta}(r)$, is related to the probability of finding a nucleus of chemical species β in a shell between r and $r + \mathrm{d}r$ centred on a nucleus of chemical species α. $g_{\alpha\beta}(r)$ and $S_{\alpha\beta}(Q)$ are related by the Fourier transform relation

$$S_{\alpha\beta}(Q) - 1 = \frac{4\pi\rho}{Q} \int_0^\infty r \left(g_{\alpha\beta}(r) - 1\right) \sin(Qr)\ \mathrm{d}r \quad . \tag{2.54}$$

The function $g_{\alpha\beta}(r)$ is used to find the coordination number, $\overline{n}_\alpha^\beta$, which is the mean number of nuclei of chemical species β in a shell of radius between $r = r_1$ and $r = r_2$ centred on a nucleus of chemical species α, by the equation

$$\overline{n}_\alpha^\beta = 4\pi\rho c_\beta \int_{r_1}^{r_2} g_{\alpha\beta}(r) r^2\, \mathrm{d}r \quad . \tag{2.55}$$

In the low r limit, $g_{\alpha\beta}(r) = 0$ such that

$$G(0) = -\sum_{\alpha=1}^{n}\sum_{\beta=1}^{n} c_\alpha c_\beta \bar{b}_\alpha \bar{b}_\beta = -\left\langle b \right\rangle^2 \quad . \tag{2.56}$$

2.5 Elastic and Total Scattering

In the case where $p = 0$, equation (2.10) can be re-written as

$$S_{\mathrm{c}}^{\mathrm{el}}(\mathbf{Q}, E) = \frac{1}{N} \sum_{\mathrm{i}=1}^{N} \sum_{\mathrm{j}=1}^{N} \overline{b}_{\mathrm{i}} \overline{b}_{\mathrm{j}} \left\langle e^{\left(-i\mathbf{Q}\cdot(\mathbf{R}_{\mathrm{i}} - \mathbf{R}_{\mathrm{j}})\right)} \right\rangle e^{-(W_{\mathrm{i}}(Q) + W_{\mathrm{j}}(Q))} \times \frac{1}{2\pi\hbar} \int_{-\infty}^{\infty} \mathrm{d}t \, e^{-i\omega t} \tag{2.57}$$

and, since $\int_{-\infty}^{\infty} \mathrm{d}t \, e^{-i\omega t} = 2\pi\hbar\delta(\hbar\omega) = 2\pi\hbar\delta(E)$, equation (2.57) can be re-written as

$$S_{\mathrm{c}}^{\mathrm{el}}(\mathbf{Q}, E) = \frac{1}{N} \sum_{\mathrm{i}=1}^{N} \sum_{\mathrm{j}=1}^{N} \overline{b}_{\mathrm{i}} \overline{b}_{\mathrm{j}} \left\langle e^{-i\mathbf{Q}\cdot(\mathbf{R}_{\mathrm{i}} - \mathbf{R}_{\mathrm{j}})} \right\rangle e^{-(W_{\mathrm{i}}(Q) + W_{\mathrm{j}}(Q))} \delta(E) \quad . \tag{2.58}$$

It can be shown that the coherent elastic structure factor for a homogeneous, isotropic system is given by [51, 52]

$$S_{\mathrm{c}}^{\mathrm{el}}(Q) = \int_{-\infty}^{\infty} S_{\mathrm{c}}^{\mathrm{el}}(Q, E) \, \mathrm{d}E = F(Q) + \sum_{\alpha=1}^{n} c_\alpha \overline{b}_\alpha^2 e^{-2W_\alpha(Q)}, \tag{2.59}$$

It can also be shown that the incoherent elastic structure factor for a homogeneous, isotropic system is given by [52]

$$S_{\mathrm{inc}}^{\mathrm{el}}(Q) = \int_{-\infty}^{\infty} S_{\mathrm{inc}}^{\mathrm{el}}(Q, E) \, \mathrm{d}E = \sum_{\alpha=1}^{n} c_\alpha b_{\mathrm{inc},\alpha}^2 e^{-2W_\alpha(Q)} \ , \tag{2.60}$$

where $b_{\mathrm{inc},\alpha}$ is the incoherent scattering length of chemical species α. Using equation (2.5) with equations (2.59) and (2.60), the elastic differential cross section is then defined as

$$\frac{1}{N} \frac{\mathrm{d}\sigma}{\mathrm{d}\Omega}\bigg|_{\mathrm{el}} = S_{\mathrm{inc}}^{\mathrm{el}}(Q) + S_{\mathrm{c}}^{\mathrm{el}}(Q) = F(Q) + \sum_{\alpha=1}^{n} c_\alpha \left(\overline{b}_\alpha^2 + \overline{b}_{\mathrm{inc},\alpha}^2 \right) e^{-2W_\alpha(Q)} \ . \tag{2.61}$$

In the approximation where $W_\alpha(Q) = \overline{W}(Q)$ for all α,

$$\frac{1}{N} \frac{\mathrm{d}\sigma}{\mathrm{d}\Omega}\bigg|_{\mathrm{el}} = F(Q) + e^{-2\overline{W}(Q)} \sum_{\alpha=1}^{n} c_\alpha \left(\overline{b}_\alpha^2 + b_{\mathrm{inc},\alpha}^2 \right) \ . \tag{2.62}$$

3. Instrumentation

In this chapter, the instruments that have been used for the experiments reported in this thesis are presented. The ISIS pulsed neutron source at the Rutherford Appleton Laboratory in the UK and three neutron instruments, the MARI and MERLIN spectrometers and the PEARL high pressure diffractometer, are described. The design and implementation of the Paris-Edinburgh press, which is used to apply pressure to samples *in situ*, are then given.

3.1 The ISIS Pulsed Neutron Source

The ISIS pulsed neutron source (figure 3-1) at the Rutherford Appleton Laboratory in Didcot, UK provides short pulses of neutrons with a range of wavelengths for use in experiments. At ISIS a tantalum target is bombarded with a high energy (800 MeV)

Figure 3-1: ISIS at the Rutherford Appleton Laboratory in Didcot, UK [53].

proton beam at a rate of 50 Hz to trigger a spallation process in which the target nuclei are broken into smaller pieces, releasing neutrons [54]. There are ≈ 17 neutrons produced for every proton collision which gives about 4.8 x 10^{14} neutrons per pulse. The overall neutron flux is inferred from the proton beam current, which at ISIS is

approximately 200 μA [53]. The proton pulse is ≈ 0.3 μs long and produces a neutron pulse with the same width in time. The neutrons travel down channels (beam lines) and are slowed down from energies of order MeV to energies of order meV for experiments. These energies are comparable to those of atomic excitations. The slowing of the neutrons is achieved by collisions in a hydrogen based moderator which also broadens the pulse to around 5-50 μs. The result is a "white beam" that contains a distribution of neutron energies between 0 and 1 eV. The exact distribution of neutron energies depends on the moderator type and temperature. The intensity distributions produced by three different moderators are given in figure 3-2. The neutrons pass through beam-

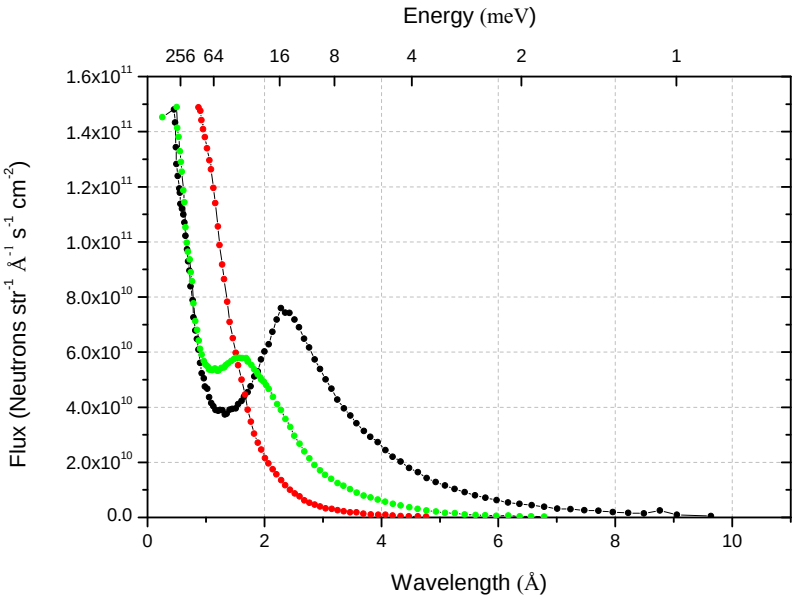

Figure 3-2: The wavelength/energy distribution of neutrons from methane (red line), water (green line) and hydrogen (black line) moderators at the ISIS pulsed neutron source.

guides to instruments as shown in figure 3-3; each instrument is designed for a specific type of experiment.

3.2 Direct Geometry time-of-flight Chopper Spectrometers

One instrument type that is used to measure the double differential scattering cross section in the energy range relevant to phonon scattering is a direct geometry time-of-flight chopper spectrometer. In this type of spectrometer (figure 3-4), neutrons with a specified incident velocity $\mathbf{v}_i$ are selected from the white beam pulse from the

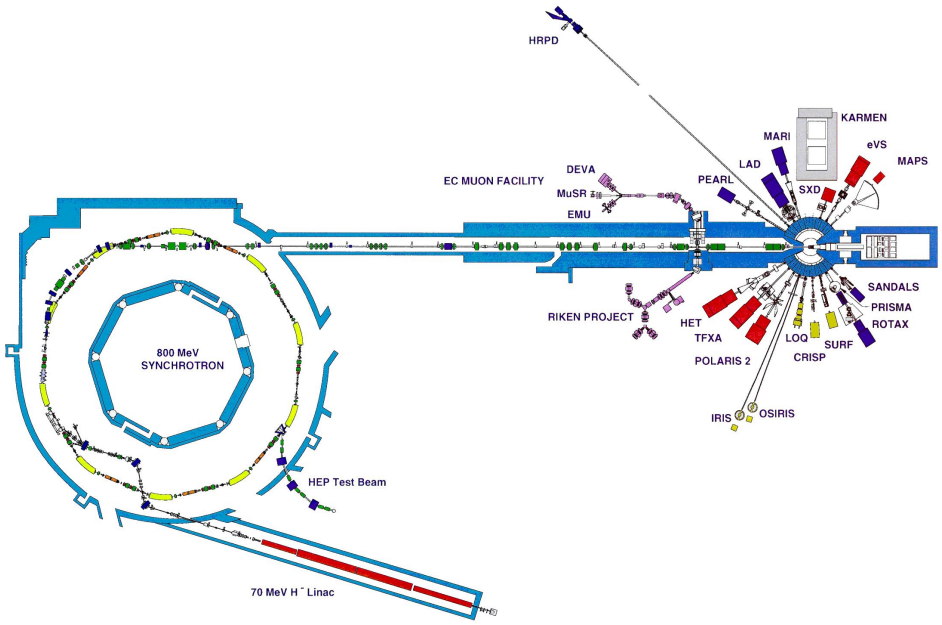

Figure 3-3: A schematic view of the ISIS pulsed neutron source (target station 1 only) showing around 20 instruments [53].

moderator using a series of choppers. First, the nimonic chopper[1], which is closest to the moderator, closes the neutron beam channel between pulses to reduce background noise and to block very high energy neutrons. Next, the disc chopper (figure 3-5a) spins at the same frequency as the source (50 Hz) and is used to narrow the range of incident neutron velocities that continue through the neutron beam channel. Finally a Fermi chopper (figure 3-5b), designed to allow a close-to Gaussian distribution of neutron velocities through to the sample position (as explained in refs. [55, 56]), opens a path for the beam for a short time centred on a time t_{Fermi} after each pulse leaves the moderator. This chopper usually spins at a frequency that is a multiple of the source frequency and opens the neutron beam channel several times during each pulse from the moderator. The Fermi and disc choppers are only open at the same time once per pulse, allowing a narrow pulse of nearly monochromatic neutrons with velocities centred on the chosen incident velocity of $\mathbf{v}_i$ ($|\mathbf{v}_i| = v_i = L_{Fermi}/t_{Fermi}$, where L_{Fermi} is the path length from the moderator to the Fermi chopper), to continue through to the sample position, a path length of L_1 from the moderator. For a given $\mathbf{v}_i$, a faster Fermi chopper frequency will result in a narrower range of transmitted velocities, but at the cost of transmitted flux. Neutrons interact with the sample and emerge with a final velocity of $\mathbf{v}_f$. The scattered neutron intensity is measured as a function of time-of-flight by a detector at a known position, a path length of L_2 from the sample

[1]The nimonic chopper is named after the nickel-molybdenum allow from which it is made.

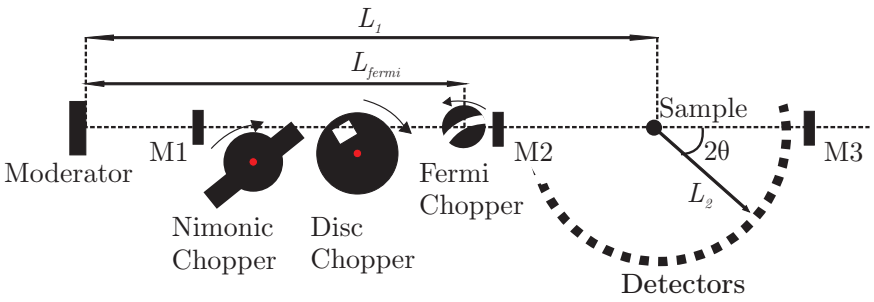

Figure 3-4: Direct geometry time-of-flight chopper spectrometer schematic. Monitors are denoted by M1, M2 and M3. A "white beam" of neutrons from the moderator is chopped so that only neutrons with a chosen velocity are incident on the sample, where they are scattered and are detected at an angle 2θ. The path length between the moderator and Fermi chopper is L_{Fermi}, the path length between the moderator and sample is L_1 and the path length between the sample and detectors is L_2. The time that a neutron takes to traverse the path length $(L_1 + L_2)$ is recorded in order to calculate $\mathbf{k}_f$. The nimonic and disc choppers help to reduce background noise by blocking high energy neutrons and shape the neutron pulse, respectively.

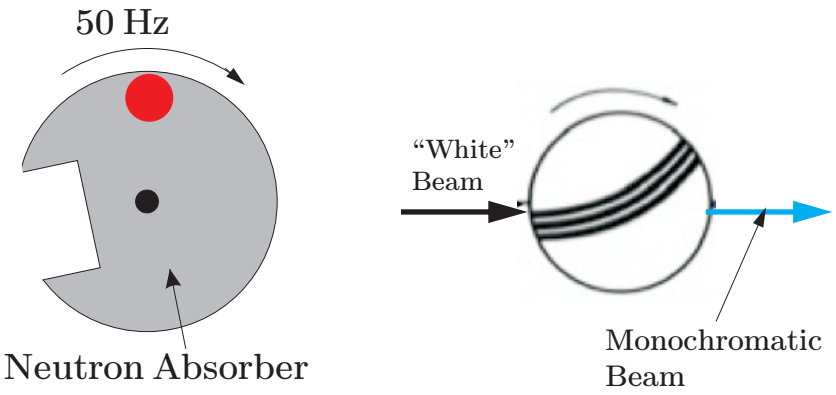

Figure 3-5: (a) A disc chopper, made of neutron absorbing material, spins at 50 Hz and opens the channel once per pulse for a short time to allow a range of neutron energies through. The chopper spins around an axis perpendicular to the plane of the page, parallel to the incident neutron beam marked in red. (b) A Fermi chopper spins with a frequency that is a multiple of 50 Hz. The curved slits drawn in black are transparent to neutrons, with a curvature that allows a narrow roughly Gaussian distribution of energies through to the sample position at a time t_{Fermi} after the pulse leaves the moderator.

position as illustrated in figure 3-6. The position of the detector relative to the sample

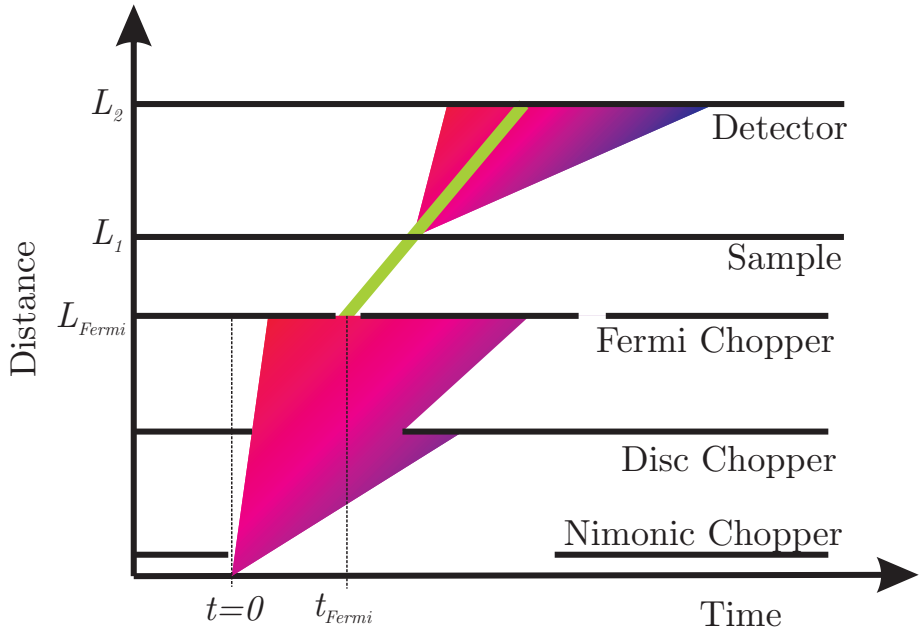

Figure 3-6: Distance-time illustration of the neutron pulse propagation from a direct geometry time-of-flight chopper spectrometer. A "white" pulse is generated at the moderator at time $t = 0$. A nimonic chopper is used to eliminate background, a disc chopper narrows the range of velocities and a Fermi chopper selects a narrow range of nearly monochromatic velocities shown by the solid green line at a time $t = t_{Fermi}$. The incident neutrons interact with the sample and gain or lose energy. A detector then records the scattered neutron intensity as a function of time. This is an illustration only.

gives the direction of $\mathbf{v}_f$ and the time-of-flight technique [9, 56] allows the magnitude of $\mathbf{v}_f$ to be measured where $|\mathbf{v}_f| = v_f = L_2/t_2$, $t_2 = t - L_1 v_i$ is the time taken for a neutron to traverse a path between the sample and detector and t is the total time-of-flight between the moderator and detector. The incident and final wavevectors $\mathbf{k}_i$ and $\mathbf{k}_f$ are related to the incident and final velocities by the de Broglie relation such that

$$\mathbf{k}_i = \frac{m_n}{\hbar}\mathbf{v}_i \quad , \quad \mathbf{k}_f = \frac{m_n}{\hbar}\mathbf{v}_f \,. \tag{3.1}$$

$\mathbf{k}_i$ and $\mathbf{k}_f$ are used to obtain the double differential scattering cross section as a function of the scattering vector Q and energy transferred from the neutron to the system E as described in section 2.1. In practice, a choice of incident neutron energy, E_i, is made and this is converted to the appropriate t_{Fermi} by control software. The choice of incident neutron energy and scattering angle provides a constraint on the range of

Q and E a detector measures, given by using equations (2.2) and (2.3) as

$$Q = \sqrt{\frac{2m_n}{\hbar^2}\left(2E_i - E - 2\sqrt{E_i\left(E_i - E\right)}\cos(2\theta)\right)} \quad , \tag{3.2}$$

which defines the path in (Q, E) space over which the scattered neutron intensity is measured for a detector at an angle 2θ to the incident beam. This so-called kinematically allowed region is plotted in figure 3-7 for an incident energy of 60 meV. Therefore,

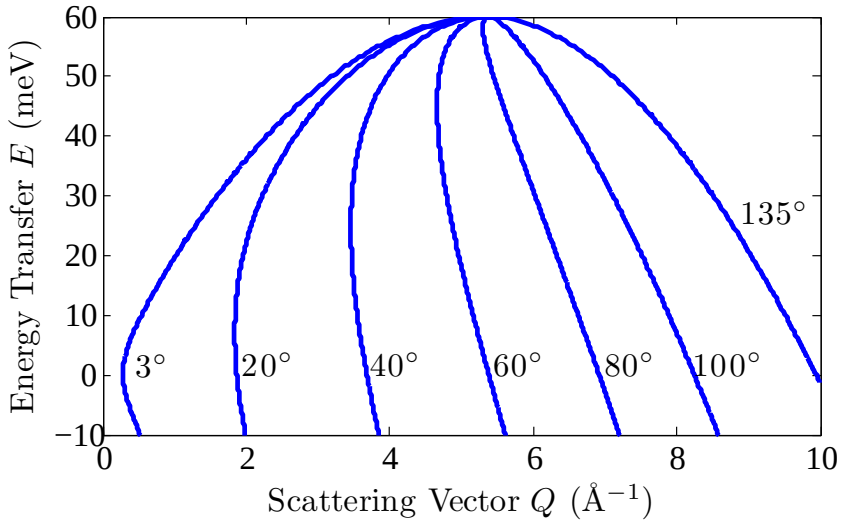

Figure 3-7: Example of the region over which the scattered neutron intensity is measured by each detector for neutrons of incident energy 60 meV. Each curve represents a single detector at an angle to the incident beam 2θ in the range from 3 ° to 135 °.

to cover a wide range of Q and E, many detectors are required over a range of scattering angles.

3.2.1 The MARI Spectrometer

The MARI spectrometer [57] views the ISIS methane moderator and incorporates an array of detectors that covers a nearly continuous range of 2θ angles from $\approx$ 3 ° to $\approx$ 135 ° (see figure 3-8). The detector arrangement features some small gaps in coverage because the detectors are arranged in 8 banks of around 100 detectors each, separated by collimating vanes. The vanes help to prevent scattering that originates away from the sample position from reaching the detectors. The moderator to sample path length L_1 is 11.739 m and the sample to detector path length L_2 is 4.020 m. Each detector is a tube made from $\approx$ 0.4 mm thick Al with an outer diameter of 25.4 mm and height of 300 mm, filled with ^{3}He gas to a pressure of 10 bar. The detector efficiency

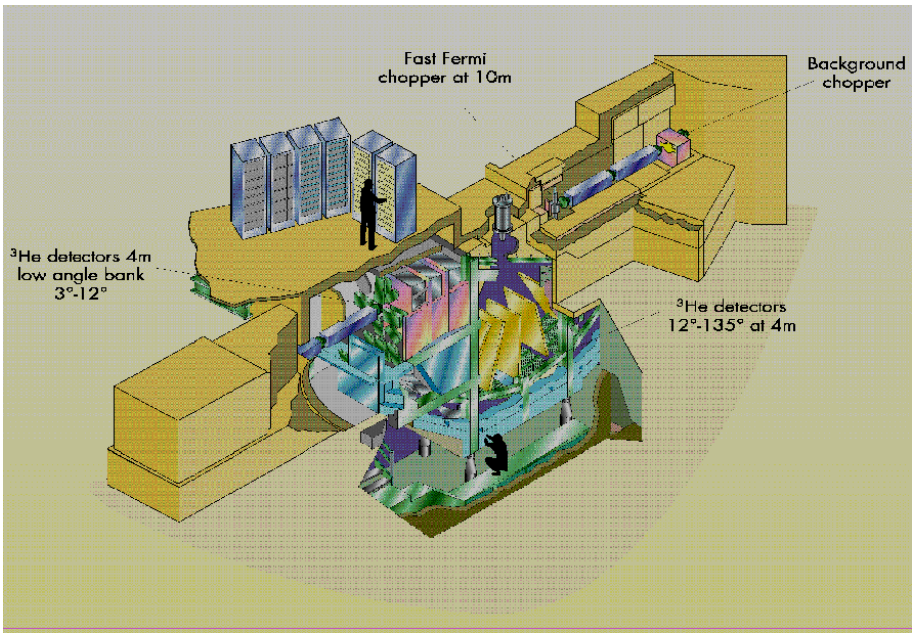

Figure 3-8: The MARI spectrometer at the ISIS pulsed neutron source [58]. Neutrons scatter from a sample into a detector array, which is separated into 8 banks of around 100 detectors each.

(figure 3-9) is 70-100 % depending on the neutron energy [59]. A three dimensional

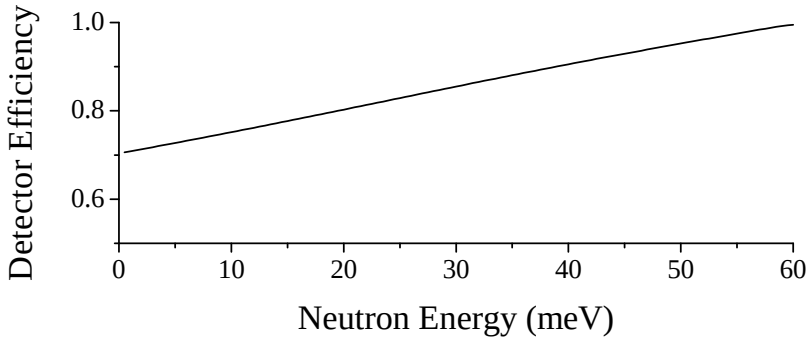

Figure 3-9: The efficiency of ^{3}He detectors used on MARI and MERLIN instruments as a function of the energy of a neutron [59].

(3D) representation of the measured spectra is presented in figure 3-10 where the gaps between detector banks can be seen.

The sample to be measured is loaded into a can, usually of annular geometry to reduce the sample attenuation and multiple scattering, and attached to the end of a "candle stick" (figure 3-11) that is lowered into position at the centre of the detectors and is usually cooled by a closed cycle refrigerator (CCR). The path between the CCR

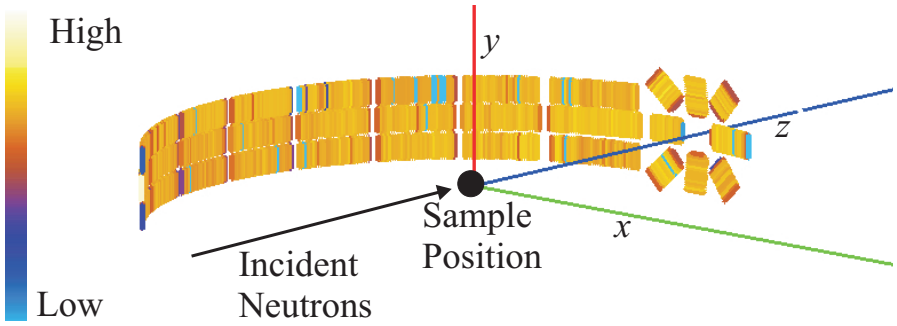

Figure 3-10: The intensity measured on MARI for a sample of vanadium shown in a 3D representation. There are ≈ 900 detector elements arranged in 8 banks. Each tube shown is at a distance of 4.020 m from the sample and is 30 cm high. Here, the measured intensity as a function of position and time-of-flight has been integrated over all time-of-flights. The light blue colour marks some faulty detectors.

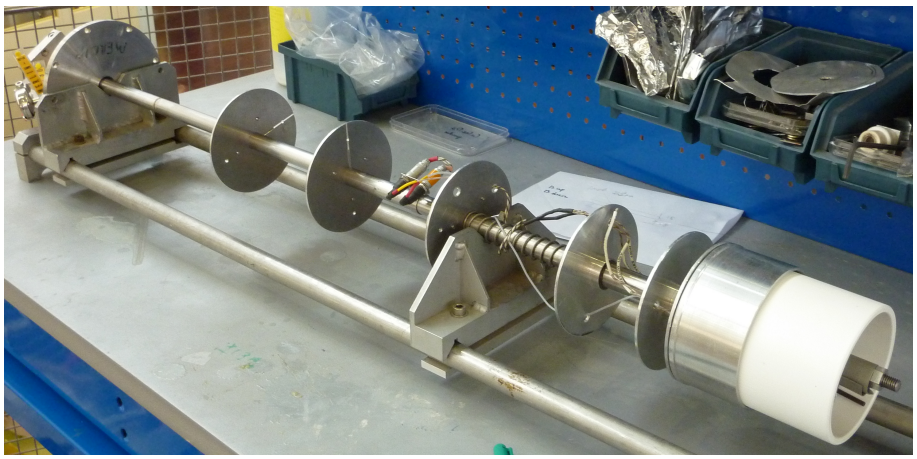

Figure 3-11: A "candle stick" used on MARI to lower the sample into position inside a CCR. The sample can is attached to the bottom of the stick with a screw, seen to the bottom right.

tail and the detectors is under vacuum. The CCR tail is evacuated and then filled with a low pressure of He gas. This acts to prevent condensation of air during cooling, eliminates background scattering from air, and promotes uniform heat exchange between the CCR and sample.

The MERLIN Spectrometer

The MERLIN spectrometer [60] views the methane moderator and provides a continuous coverage of scattering angles by incorporating a large array of two dimensional (2D) position sensitive detector tubes (figure 3-12). The detector tubes (otherwise identical

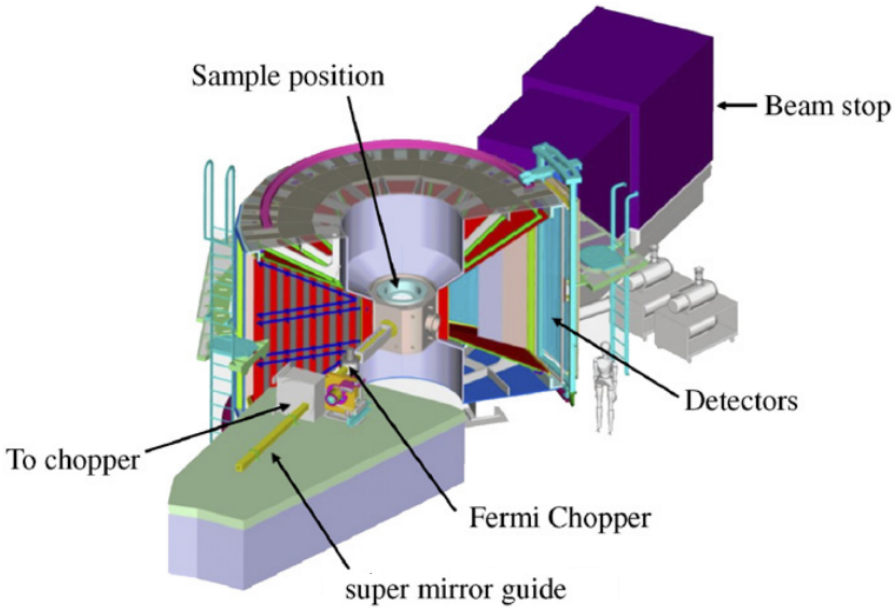

Figure 3-12: Merlin spectrometer schematic from ref. [60]. The MERLIN spectrometer incorporates a supermirror guide and a large 2-dimensional array of position sensitive detectors.

to those used on MARI) are 3 m long and are able to record the position of incidence of a neutron along the tube to a precision of 2.1 cm. The moderator to sample path length L_1 is 11.8 m and the sample to detector path length L_2, as measured to the centre of the detector array, is 2.5 m. The detectors cover a range of scattering angles from ≈-45° to ≈135° in the horizontal plane and ≈ ±30° in the vertical plane [60]. The scattered neutron intensity is measured as a function of time-of-flight over 69,632 individual detector pixels of known position. In addition to the large solid angle coverage (3.1 sr), the MERLIN spectrometer incorporates a supermirror guide, which gives a factor of ≈ 5 gain in incident flux over MARI. The effect of these differences is that MERLIN gives a gain in the detected neutron flux of a factor of approximately 35 over

MARI. The gain in flux comes at the cost of resolution in both energy transfer E and scattering vector Q due to the shorter sample to detector path length and divergence of the supermirror guide. For the same choice of Fermi chopper, incident energy and Fermi chopper spinning frequency, the energy resolution of the MERLIN spectrometer is $\approx 25\%$ worse than that of MARI. Figure 3-13 demonstrates the spatial coverage of the MERLIN detectors. Samples are loaded in a similar way to MARI. The geometry of the sample assembly means that it is possible to load powder samples without a rigid container.

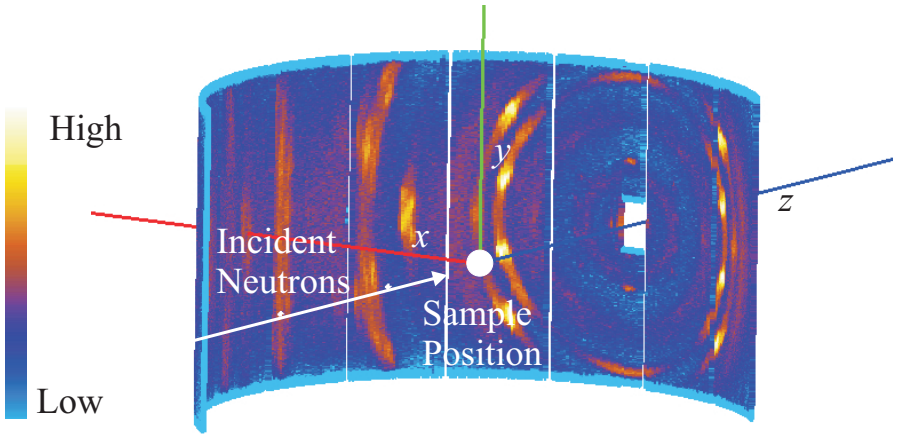

Figure 3-13: The intensity measured for an empty can using the MERLIN instrument shown in a 3D representation. The Debye-Scherrer rings for aluminium diffraction peaks are seen, along with the effect of preferred orientation of the Al crystallites (bright spots within the rings). There are 69,632 detector pixels. The centre of each position sensitive detector tube is at a distance of 2.5 m from the sample and is 3 m high. Here, the measured intensity as a function of position and time-of-flight has been integrated over all time-of-flights.

3.3 Time-of-Flight Neutron Diffraction Instrumentation for High Pressure Studies

In a time-of-flight neutron diffraction experiment, a large fraction of the moderated white beam of neutrons produced by the source is used. The intensity of neutrons is measured as a function of time-of-flight for a detector at an angle of 2θ to the incident beam as shown in figure 3-14. If the scattering from a sample is assumed to be elastic, then the wavelength of the neutron is determined using the de Broglie relationship which can be written as

$$\lambda = \frac{ht}{m_n \left(L_1 + L_2\right)} \,, \tag{3.3}$$

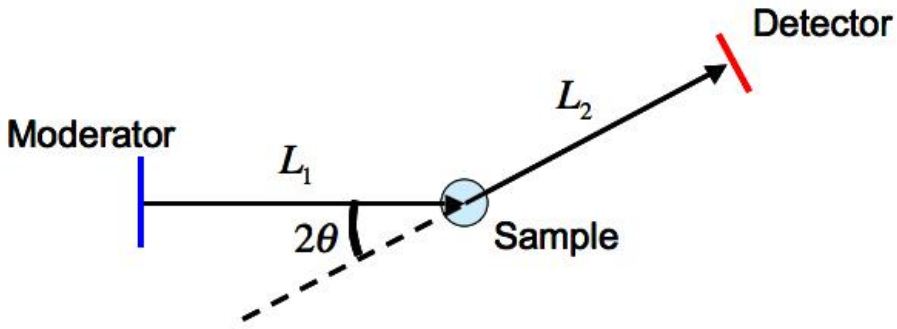

Figure 3-14: Schematic of a diffraction experiment at a time-of-flight spallation source. A detector is placed at an angle of 2θ to the incident beam, L_1 is the path length from the moderator to the sample and L_2 is the path length from the sample to the detector. The scattered intensity is measured as a function of time-of-flight.

where m_n is the mass of a neutron, t is the time-of-flight, L_1 is the path length between the moderator and the sample, L_2 is the path length between the sample and the detector and h is Planck's constant. As described in section 2.3, the scattering vector Q is given by equation (2.2).

3.3.1 PEARL

The PEARL High Pressure (HiPr) time-of-flight neutron diffraction instrument (figure 3-15) views the methane moderator at the ISIS pulsed neutron source and features an array of nine detector modules, each with 120 ^{6}Li ZnS scintillator detector elements covering scattering angles between 83 and 97 °. The scattering angle of ≈ 90 ° limits

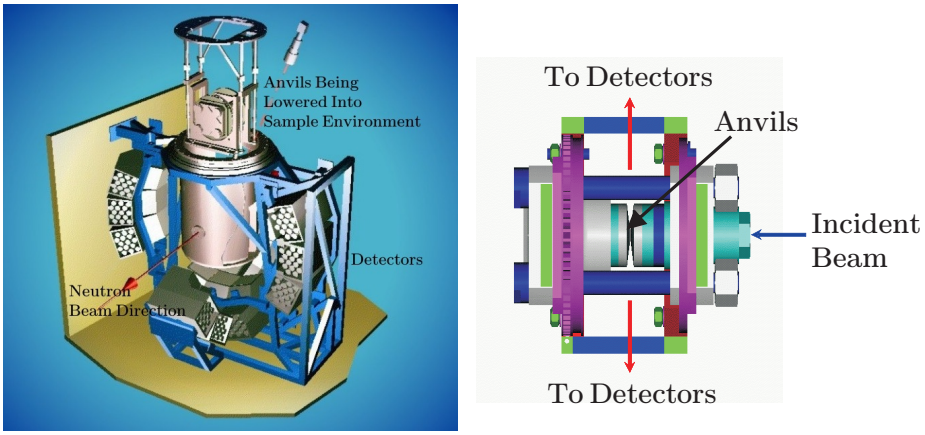

(a) *(b)*

Figure 3-15: The PEARL diffractometer. (a) The full pressure assembly in the beam and (b) the Paris-Edinburgh press [61].

the range of scattering vectors that can be measured to $1.55 \leq Q \leq 19.6$ Å^{-1}. Pressure is applied to a sample using a Paris-Edinburgh press as described in section 3.4. The instrument is used in transverse geometry, meaning that the incident beam travels through a hole in the breach and the detected neutrons are in a plane perpendicular to the incident beam as shown in figure 3-15b. There are two additional detector banks, one covering scattering angles between 60 ° and 20 ° and the other covering scattering angles between 100 ° and 120 °. However, these banks are inaccessible during a high pressure experiment because the path of any neutron scattered in their direction is blocked by the anvils.

The restricted range at low Q, which does not extend below 1.55 Å^{-1}, provides a challenge for measurements on amorphous materials. Often, there is a first sharp diffraction peak (FSDP) [62, 63] in this region that cannot be excluded when performing the Fourier transform into real space (equation (2.53)) if accurate real space functions are to be obtained. The FSDP is associated with intermediate range ordering in a system.

3.4 The Paris-Edinburgh Press

In neutron scattering experiments, the Paris-Edinburgh press [64, 65] is often used to apply pressure to samples. The current press designs are based on a toroidal design first made in the 1960's, the history of the press designs is summarised by Khvostantsev *et al.* [66, 67]. This innovative press design allows for the larger sample volumes demanded by neutron scattering experiments, which is necessary because of the limited flux of neutron sources. Many types of anvil and gasket assembly may be used in the press. In our experiments either single toroid sintered diamond anvils with single toroid Ti-Zr gaskets (figure 3-16a) were used to reach pressures of up to ≈ 10 GPa [68–70] or double toroid sintered diamond anvils with double toroid Ti-Zr gaskets (figure 3-16b) were used to reach pressures up to ≈ 20 GPa [71, 72]. In both cases the inner die of the anvils, formed by the spark erosion of sintered diamond, is held in a tungsten carbide seat supported by a steel binding ring [64]. The steel part of each anvil is covered in a Cd jacket to reduce any secondary scattering of neutrons by the anvil. The inner die features an indentation in the shape of a spherical cap to accommodate a sample pellet and grooves to accommodate the Ti-Zr gaskets. A sample pellet is placed between two opposing anvils and encapsulated by the gasket assembly. The gaskets are made from an alloy of $Ti_{0.676}Zr_{0.324}$, a composition chosen such that the mean coherent scattering length of the gasket is zero. Pressure is applied to the anvils using a hydraulic pump. As pressure is applied, the gasket assembly deforms into the grooves of the anvils and holds the sample in place radially. The grooves in the anvil act to provide inward

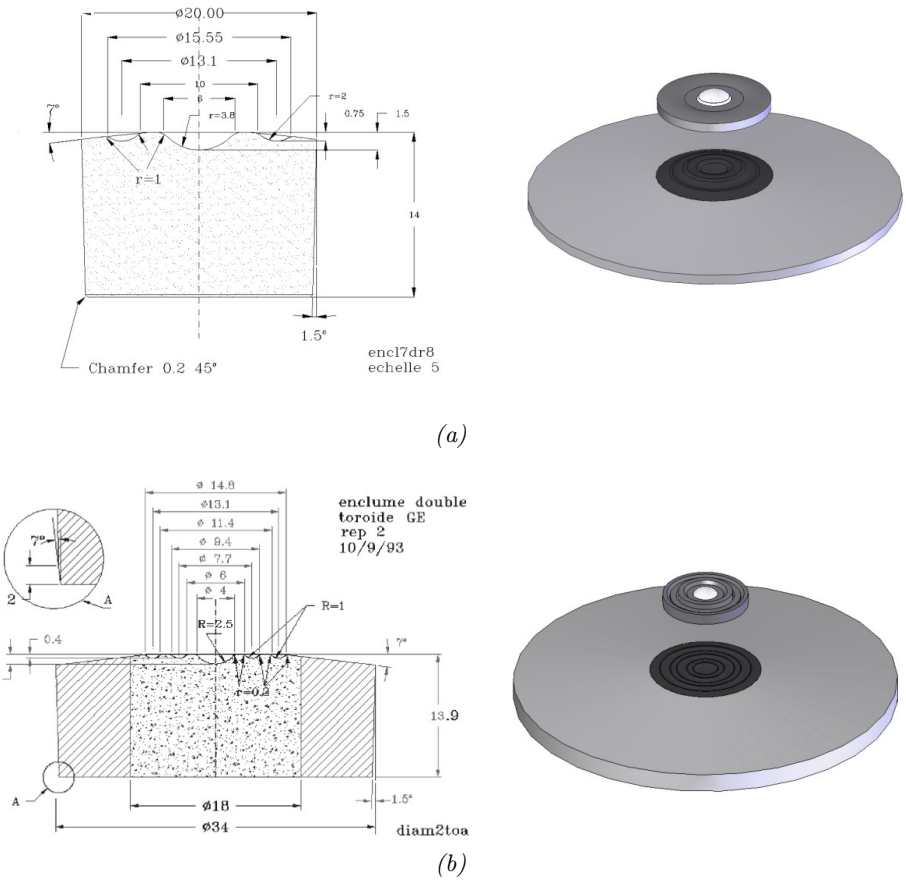

Figure 3-16: (a) Single toroid anvils and gasket and (b) double toroid anvils and gasket, drawn by Drewitt [39] using information from Klotz [73].

support for the gasket and provide a more favourable pressure distribution across the anvils [69] to prevent cracking. Single toroid anvils can achieve pressures of up to 15 GPa. In the case of double toroid anvils, a combination of smaller sample size (thus a higher pressure for the same applied load) and better gasket support, through having two grooves in the anvils to support the gasket assembly, allows pressures of up to 30 GPa to be achieved. The use of diamond adds particularly strong Bragg peaks and Bragg edges to the measured neutron diffraction patterns that are difficult to subtract. However, the diamond anvil cells can reach higher pressures than their boron-nitride counterparts without breaking.

4. Data Treatment

In this chapter, the data analysis methods used for inelastic neutron scattering experiments (section 4.1) and high pressure neutron diffraction experiments (section 4.2) are described.

4.1 Inelastic Neutron Scattering Experiments

4.1.1 Introduction

The aim of the inelastic neutron scattering experiments presented in this thesis (made using either the MARI or MERLIN spectrometers) is to measure the single phonon dynamical structure factor $S_1(Q, E)$. To achieve this, the scattered neutron intensity has to be corrected for background scattering, attenuation of the neutron beam, multiple scattering and multiple phonon scattering using the approaches described below.

In the inelastic neutron scattering experiments described in this thesis an annular geometry was used, whereby powder samples were held in annular aluminium cans as illustrated in figure 4-1. The intensity of single scattered neutrons from the sample and by the can are denoted by $I_{\mathrm{s}}(Q, E)$ and $I_{\mathrm{c}}(Q, E)$, respectively. The attenuation of $I_{\mathrm{s}}(Q, E)$ by the presence of the sample and can is represented by the coefficient $A_{\mathrm{s,sc}}(Q, E)$ such that the overall sample scattered intensity is given by $A_{\mathrm{s,sc}}(Q, E)I_{\mathrm{s}}(Q, E)$. Similarly, the attenuation of $I_{\mathrm{c}}(Q, E)$ by the presence of the sample and can is represented by the coefficient $A_{\mathrm{c,sc}}(Q, E)$ such that the overall can scattered intensity is given by $A_{\mathrm{c,sc}}(Q, E)I_{\mathrm{c}}(Q, E)$. Neutrons also scatter from other sources, such as the CCR, with an intensity $I_{\mathrm{b}}(Q, E)$ which, to a good approximation, is not attenuated by the presence of the sample and/or the can. Neutrons can also scatter multiple times to give an intensity denoted by $I_{\mathrm{ms,sc}}(Q, E)$.

This section is organised as follows. In section 4.1.2 the initial measurements, normalisation and correction for the background scattering are presented in the approximation that multiple scattering is small. In section 4.1.3 a correction for the multiple scattering contribution to $I_{\mathrm{s}}(Q, E)$ is described. Finally, in section 4.1.4 the method used to calculate the multiple phonon correction within the extreme incoherent

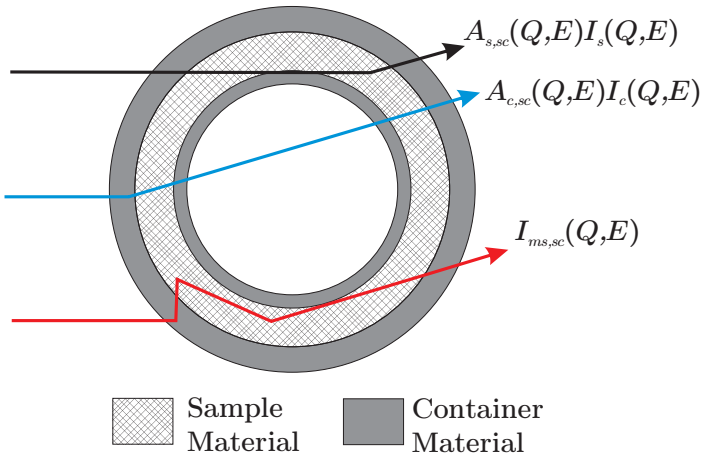

Figure 4-1: The annular geometry for the inelastic neutron scattering experiments described in this thesis where a powdered sample is contained in an Al can. Examples of the path of a neutron in three different scattering events are given; a neutron that has scattered once in the sample which gives a contribution $A_{\mathrm{s,sc}}(Q,E)I_{\mathrm{s}}(Q,E)$ to the measured intensity (black arrow), a neutron that has scattered once in the can which gives a contribution $A_{\mathrm{c,sc}}(Q,E)I_{\mathrm{c}}(Q,E)$ to the measured intensity (blue arrow) and a neutron that has scattered three times which gives a contribution $I_{\mathrm{ms,sc}}(Q,E)$ to the measured intensity (red arrow).

approximation is given. The data analysis procedure is summarised in figure 4-2.

4.1.2 Normalisation and Correction for Scattering from the Can

For the inelastic neutron scattering experiments described in this thesis, three measurements were made under identical conditions as a function of the scattering angle, 2θ, and time-of-flight, t, using a monochromatic beam of neutrons. The intensity was measured for the sample in a can $I_{\mathrm{sc}}^{\mathrm{meas}}(2\theta,t)$, for the empty can with no sample $I_{\mathrm{c}}^{\mathrm{meas}}(2\theta,t)$ and for an annular shaped piece of solid vanadium $I_{\mathrm{v}}^{\mathrm{meas}}(2\theta,t)$. The scattered intensity $I_{\mathrm{wb}}^{\mathrm{meas}}(2\theta,t)$ was also measured for an annular shaped piece of solid vanadium using a so-called "white beam" of neutrons for which there is a wide range of neutron energies. This white beam measurement is used to identify and remove faulty detectors and to calibrate the efficiency of the detectors as discussed in refs. [55, 74–76]. In the case when several samples were measured in a single experiment, $I_{\mathrm{c}}^{\mathrm{meas}}(2\theta,t)$, $I_{\mathrm{v}}^{\mathrm{meas}}(2\theta,t)$ and $I_{\mathrm{wb}}^{\mathrm{meas}}(2\theta,t)$ were measured only once.

Using the Libisis data analysis software [77], a standard vanadium normalisation method involving $I_{\mathrm{wb}}^{\mathrm{meas}}(2\theta,t)$ and $I_{\mathrm{v}}^{\mathrm{meas}}(2\theta,t)$ was used to convert $I_{\mathrm{sc}}^{\mathrm{meas}}(2\theta,t)$ and $I_{\mathrm{c}}^{\mathrm{meas}}(2\theta,t)$ to the normalised measured intensities, $I_{\mathrm{sc}}^{\mathrm{E}}(Q,E)$ and $I_{\mathrm{c}}^{\mathrm{E}}(Q,E)$ for the sample-in-can and empty can, respectively. This method is described by Perring [74] and is given in the "HET manual" [78]. The validity of using vanadium as a scattering

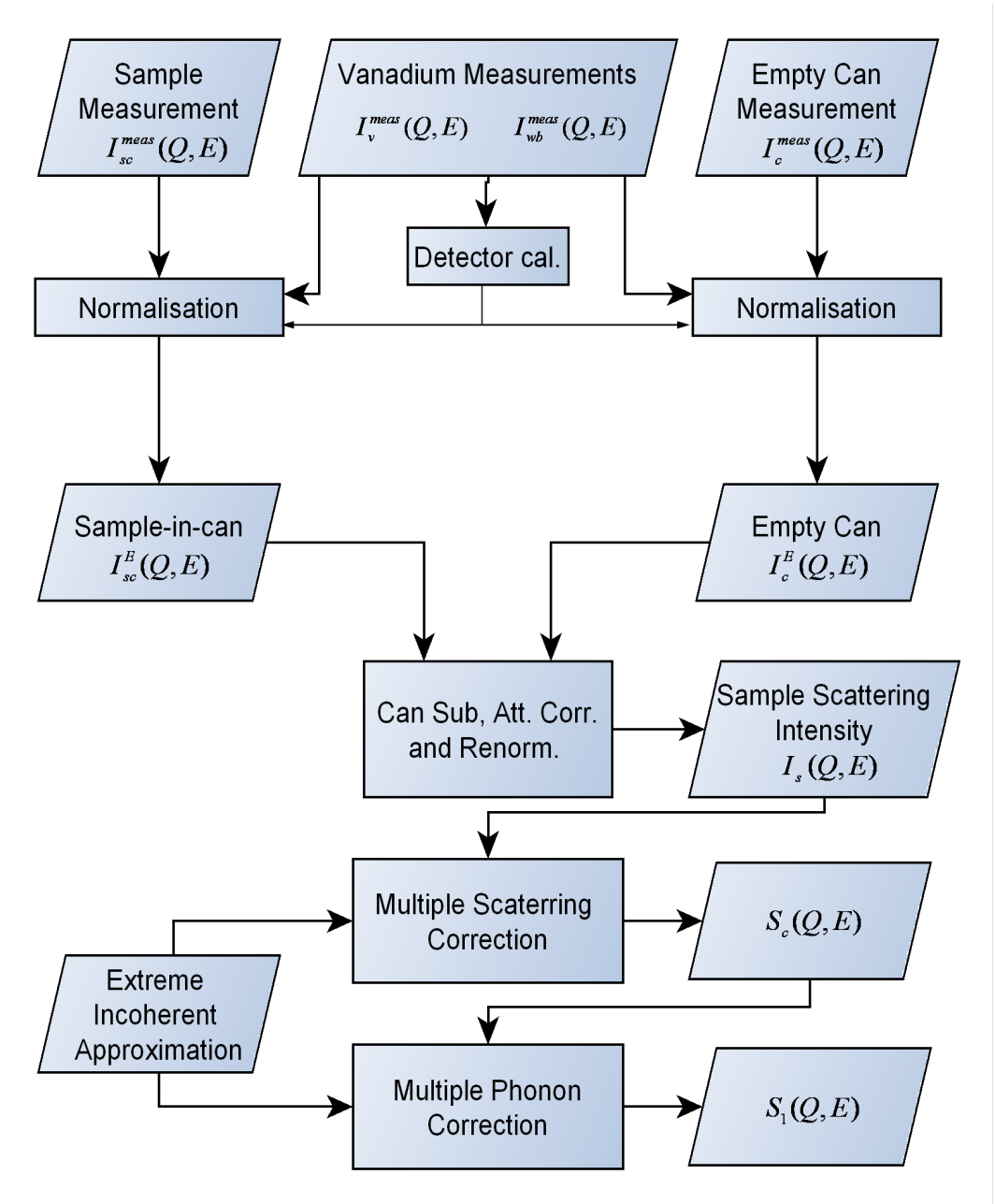

Figure 4-2: The data analysis procedure for inelastic neutron scattering experiments. Here "Can Sub.", "Att. Corr." and "Renorm." represent the empty can subtraction, attenuation correction and renormalisation. Cal. stands for calibration.

standard is discussed by Mayers [75, 76].

The incident and scattered beams are attenuated by the sample and empty can such that [79]

$$I^{\mathrm{E}}_{\mathrm{sc}}(Q,E) = A_{\mathrm{s,sc}}(Q,E)I_{\mathrm{s}}(Q,E) + A_{\mathrm{c,sc}}(Q,E)I_{\mathrm{c}}(Q,E) + I_{\mathrm{b}}(Q,E) + I_{\mathrm{ms,sc}}(Q,E) \quad (4.1)$$

and

$$I^{\mathrm{E}}_{c}(Q,E) = A_{\mathrm{c,c}}(Q,E)I_{\mathrm{c}}(Q,E) + I_{\mathrm{b}}(Q,E) + I_{\mathrm{ms,c}}(Q,E)\,, \quad (4.2)$$

where $I_{\mathrm{ms,sc}}(Q,E)$ and $I_{\mathrm{ms,c}}(Q,E)$ are the multiple scattering intensities for the sample-in-can and empty can, respectively. $A_{x,y}(Q,E)$ is the attenuation coefficient for neutrons scattered in region x and attenuated by region y, where the regions are denoted by s for the sample, c for the can and sc for the sample and can. The attenuation coefficients take values between 0 (0 % transmission) and 1 (100 % transmission). In the approximation that there is no multiple scattering so that $I_{\mathrm{ms,sc}}(Q,E) = I_{\mathrm{ms,c}}(Q,E) = 0$, equations (4.1) and (4.2) can be combined to give the attenuation corrected sample scattered intensity

$$I_{\mathrm{s}}(Q,E) = \frac{1}{A_{\mathrm{s,sc}}(Q,E)}\left[\left(I^{\mathrm{E}}_{\mathrm{sc}}(Q,E) - I_{\mathrm{b}}(Q,E)\right) - \frac{A_{\mathrm{c,sc}}(Q,E)}{A_{\mathrm{c,c}}(Q,E)}\left(I^{\mathrm{E}}_{\mathrm{c}}(Q,E) - I_{\mathrm{b}}(Q,E)\right)\right]. \quad (4.3)$$

The attenuation coefficients have been derived for cylindrical geometry (see ref. [80] for elastic scattering and ref. [81] for inelastic scattering) or flat plate geometry (see refs. [82, 83]). They cannot, at present, be calculated analytically for multiple annuli (i.e. an annular sample inside an annular can). The attenuation coefficients can, however, be calculated for two concentric cylinders by a method developed by Poncet [81] using the formalism of Paalman and Pings [79]. By treating the outer cylinder as a sample and the inner cylinder as transparent to neutrons, it is possible to calculate the attenuation coefficient for a single annulus. For example, a coefficient $A_{\mathrm{sc,sc}}(Q,E)$ can be calculated and the approximation made where $A_{\mathrm{s,sc}}(Q,E) \simeq A_{\mathrm{c,sc}}(Q,E) \simeq A_{\mathrm{sc,sc}}(Q,E)$ such that equation (4.3) becomes

$$\begin{aligned} I_{\mathrm{s}}(Q,E) \;\simeq\; & \frac{1}{A_{\mathrm{sc,sc}}(Q,E)}\left(I^{\mathrm{E}}_{\mathrm{sc}}(Q,E) - I_{\mathrm{b}}(Q,E)\right) \\ & - \frac{1}{A_{\mathrm{c,c}}(Q,E)}\left(I^{\mathrm{E}}_{\mathrm{c}}(Q,E) - I_{\mathrm{b}}(Q,E)\right). \end{aligned} \quad (4.4)$$

$A_{\mathrm{sc,sc}}(Q,E)$ is calculated for a 'pseudo sample' for which the atoms of the Al can and sample have been mixed such that the fraction of sample atoms is $f = N_{\mathrm{sample}}/\left(N_{\mathrm{Al}} + N_{\mathrm{sample}}\right)$, where N_{sample} and N_{Al} are the numbers of sample and Al atoms in the beam, respectively. An effective density $\langle n \rangle = f n_{\mathrm{sample}} + (1-f) n_{\mathrm{Al}}$,

an effective total scattering cross section $\langle\sigma\rangle = f\sigma_{\text{sample}} + (1-f)\sigma_{\text{Al}}$ and an average absorption cross section $\langle\sigma_{\text{abs}}\rangle = f\sigma_{\text{abs,sample}} + (1-f)\sigma_{\text{abs,Al}}$ are then assigned to each atom of the pseudo sample.

In the ideal case, a measurement of the empty instrument would be taken such that the full attenuation correction described above can be made. However, in practice the measurement of the empty instrument (including any CCR tail) is not usually made. Most of the scattering in the measurement of the empty can is from sources other than the can and therefore the approximation is made wherein $I_{\text{b}}(Q,E) \simeq I_{\text{c}}^{\text{E}}(Q,E)$ and equation (4.4) reduces to

$$I_{\text{s}}(Q,E) \simeq \frac{1}{A_{\text{sc,sc}}(Q,E)} \left(I_{\text{sc}}^{\text{E}}(Q,E) - I_{\text{c}}^{\text{E}}(Q,E)\right) , \tag{4.5}$$

where $A_{\text{sc,sc}}(Q,E)$ is calculated as above for a pseudo sample.

Furthermore, the absolute normalisation described in section 4.1.2 is, in practice, difficult to achieve for inelastic experiments. A renormalisation factor, m, is used so that equation (4.5) becomes

$$I_{\text{s}}(Q,E) = \frac{m}{A_{\text{sc,sc}}(Q,E)} \left(I_{\text{sc}}^{\text{E}}(Q,E) - I_{\text{c}}^{\text{E}}(Q,E)\right) \tag{4.6}$$

and m is chosen such that the differential scattering cross section with an implicit Plackzek correction $\mathrm{d}\sigma/\mathrm{d}\Omega = \int I_{\text{s}}(Q,E)\,\mathrm{d}E$ is in agreement with the neutron diffraction pattern measured for the same sample.

4.1.3 The Multiple Scattering Contribution to Inelastic Scattering

Multiple scattering occurs when a single neutron is involved in two or more distinct scattering events [84] as illustrated in figure 4-3. For most geometries, it is not possible

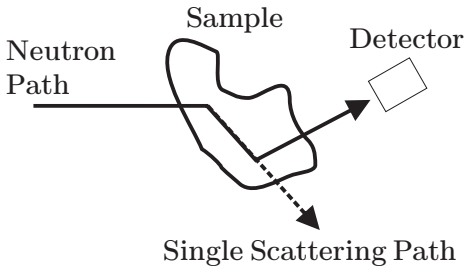

Figure 4-3: Example of a neutron undergoing two scattering events in a sample of arbitrary geometry.

to calculate multiple scattering analytically. However, approximations for calculating

the multiple scattering in the case of slab, spherical and cylindrical geometries are summarised by Sears [85]. An effective method of calculating multiple scattering is by Monte Carlo simulation as described in refs. [80, 86–88]. The treatment of multiple *elastic* scattering has been done using computer programs such as Gudrun [89]. In the case of inelastic scattering, computer software such as Discus [90] and MScatt [86, 91–93] have been written. Software for calculating multiple scattering for inelastic neutron experiments using annular geometry on instruments such as MARI and MERLIN was not, however, readily available during the work described in this thesis.

However, a crude approximation can be used to find the multiple scattering in an inelastic neutron scattering experiment by assuming that the multiple scattering for an annulus has equal probability at all angles (thus, for measured point in E, all Q) [94, 95] as illustrated in figure 4-4. Monte Carlo simulations [96] and approximate

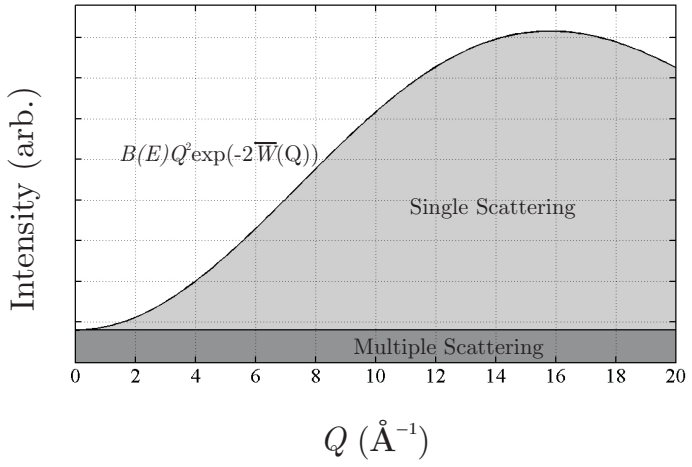

Figure 4-4: Example of the multiple scattering contribution to the intensity measured for a given energy transfer.

calculations [85] show that this is a good estimate for flat plate geometry. The technique has been used successfully by others such as Hannon *et al.* [97] and Fabiani *et al.* [46] for annular geometry. Using this approximation and the extreme incoherent approximation as in equation (2.25), the attenuation corrected sample scattered intensity is given in the high Q regime by [98]

$$I_{\mathrm{s}}(Q,E) = I_{\mathrm{ms}}(E) + B(E)Q^2 \exp(-2\overline{W}(Q)) \;, \tag{4.7}$$

where $B(E)$ is a fitted coefficient, $I_{\mathrm{ms}}(E)$ is the remaining multiple scattering contribution to $I_{\mathrm{s}}(Q,E)$ after subtraction of the empty can and attenuation correction. For each measured energy transfer E, equation (4.7) is fitted to measured data by varying

the values of $I_{\rm ms}(E)$ and $B(E)$. The estimate for $I_{\rm ms}(E)$ thus obtained is subtracted from $I_{\rm s}(Q,E)$ to correct for multiple scattering.

If there is a significant amount of multiple phonon scattering, then equation (4.7) must be altered to take into account higher phonon terms given by equation (4.10) below such that

$$I_{\rm s}(Q,E) = I_{\rm ms}(E) + \sum_{p=1}^{N_p} B_p(E) Q^{2p} \exp(-2\overline{W}(Q)) \; , \tag{4.8}$$

where p denotes the number of phonons, $B_p(E)$ are fitted coefficients and N_p is the number of phonon terms included. By making the assumption that the scattering from the sample is fully coherent, the total coherent dynamical structure factor for the sample is then given by

$$S_{\rm c}(Q,E) = I_{\rm s}(Q,E) - I_{\rm ms}(E) \; . \tag{4.9}$$

4.1.4 The Multiple Phonon Correction

Multiple phonon scattering occurs when more than one vibrational mode is involved in a single neutron scattering event. The formalism for multiple phonon scattering given here follows that of Suck [99, 100] and Sjölander [101], and has been used by Dawidowski *et al.* [88, 102, 103].

Equation (2.10) can be expressed more conveniently in the extreme incoherent approximation by [52, 99]

$$S_{\rm c}(Q,E) = S_1(Q,E) + S_{\rm mp}(Q,E) = \left\langle \bar{b}^2 \right\rangle \exp(-2\overline{W}(Q)) \sum_{p=1}^{\infty} \frac{1}{p!} \left(\frac{\hbar^2 Q^2}{2\overline{M}} \right)^p u_p(E) \; , \tag{4.10}$$

where $S_1(Q,E)$ is, within the extreme incoherent approximation, the dynamical structure factor for single phonon scattering ($p = 1$) given by

$$S_1(Q,E) = \left\langle \bar{b}^2 \right\rangle \exp(-2\overline{W}(Q)) \frac{\hbar^2 Q^2}{2\overline{M}} u_1(E) \; , \tag{4.11}$$

where, using equation (2.25),

$$u_1(E) = \frac{Z(E)}{E} \left\langle n(E) + 1 \right\rangle \tag{4.12}$$

and $Z(E)$ is the *one phonon* vibrational density of states. $S_{\rm mp}(Q,E)$ is, within the extreme incoherent approximation, the dynamical structure factor for multiple phonon

scattering ($p > 1$) given by

$$S_{\mathrm{mp}}(Q,E) = \left\langle \bar{b}^2 \right\rangle \exp(-2\overline{W}(Q)) \sum_{p=2}^{\infty} \frac{1}{p!} \left(\frac{\hbar^2 Q^2}{2\overline{M}} \right)^p u_p(E) \,, \tag{4.13}$$

where $u_p(E)$ is the p-phonon function, given for $p > 1$, by the convolution relation [99]

$$u_p(E) = \int_{-\infty}^{\infty} u_{p-1}(E) u_1(E - E') \mathrm{d}E' \,. \tag{4.14}$$

The generalised vibrational density of states from equation (2.44) is then given by the sum of single and multiple phonon contributions $G(Q,E) = G_1(Q,E) + G_{\mathrm{mp}}(Q,E)$, such that by substituting equation (4.10) into equation (2.44) it follows that in the extreme incoherent approximation

$$G(Q,E) = \frac{E}{\langle n(E) + 1 \rangle} \sum_{p=1}^{\infty} \frac{1}{p!} \left(\frac{\hbar^2 Q^2}{2\overline{M}} \right)^{p-1} u_p(E) \,, \tag{4.15}$$

where the one phonon term ($p = 1$), $G_1(Q,E)$, is given by

$$G_1(Q,E) = \frac{E}{\langle n(E) + 1 \rangle} u_1(E) \tag{4.16}$$

and the multiple phonon term ($p > 1$), $G_{\mathrm{mp}}(Q,E)$, is given by

$$G_{\mathrm{mp}}(Q,E) = \frac{E}{\langle n(E) + 1 \rangle} \sum_{p=2}^{\infty} \frac{1}{p!} \left(\frac{\hbar^2 Q^2}{2\overline{M}} \right)^{p-1} u_p(E) \,. \tag{4.17}$$

$G(E)$ in equation (2.45) will also have contributions from one phonon and multiple phonon processes such that

$$G(E) = G_1(E) + G_{\mathrm{mp}}(E) \,, \tag{4.18}$$

where the one phonon contribution is

$$G_1(E) \approx Z(E) = \frac{1}{Q_{\max} - Q_{\min}} \int_{Q_{\min}}^{Q_{\max}} G_1(Q,E) \, dQ \tag{4.19}$$

and the multiple phonon contribution is

$$G_{\mathrm{mp}}(E) = \frac{1}{Q_{\max} - Q_{\min}} \int_{Q_{\min}}^{Q_{\max}} G_{\mathrm{mp}}(Q, E)\, \mathrm{d}Q \tag{4.20}$$

To find $G_1(E)$, an iterative procedure was developed whereby

$$G_1^{(\mathrm{i}+1)}(E) = G(E) - G_{\mathrm{mp}}^{(\mathrm{i})}(E)\ , \tag{4.21}$$

where i (i = 1, 2, 3, $\cdots$) represents the i^{th} iteration and $G(E)$ is calculated using the measured dataset. $G_{\mathrm{mp}}^{(\mathrm{i})}(E)$ is calculated by assuming that $Z(E) = G_1^{(\mathrm{i})}(E)$ in equation (4.12), which is used to calculate $u_p^{(\mathrm{i})}(E)$ by using equation (4.14) and $G_{\mathrm{mp}}^{(\mathrm{i})}(E)$ by using equations (4.17) and (4.20). For the first iteration, $G_1^{(1)}(E) = G(E)$ and in subsequent iterations, $G^{(\mathrm{i})}(E)$ (i > 1) is obtained from equation (4.21). The procedure is re-iterated until convergence is achieved whereby $G_1^{(\mathrm{i}+1)}(E) = G_1^{(\mathrm{i})}(E)$. In the extreme incoherent approximation, the multiple phonon contribution $S_{\mathrm{mp}}(Q, E)$ to the coherent dynamical structure factor is then calculated by using equation (4.13) and the single phonon dynamical structure factor is given by

$$S_1(Q, E) = S_{\mathrm{c}}(Q, E) - S_{\mathrm{mp}}(Q, E) \quad . \tag{4.22}$$

The multiple phonon correction procedure was tested using a model density of states with three peaks as shown in figure 4-5. The single phonon density of states was normalised such that the integral over all energies was unity. Then the following procedure was implemented:

1. $u_1(E)$ was calculated using equation (4.12) with a temperature of 200 K.
2. The multiple phonon terms $u_p(E)$ were calculated up to the 5^{th} phonon term using equation (4.14).
3. $G_{\mathrm{mp}}(Q, E)$ was calculated using equation (4.17) with a Debye-Waller factor corresponding to $\langle u^2 \rangle / 3 = 0.0125$ Å.
4. $G_{\mathrm{mp}}(E)$ was calculated by using equation (4.20)
5. $G(E)$ was calculated using equation (4.18).
6. The correction procedure was used with $G(E)$ as the input to recover $G_1(E)$ and $G_{\mathrm{mp}}(E)$. The results after each iteration are given in figure 4-5.

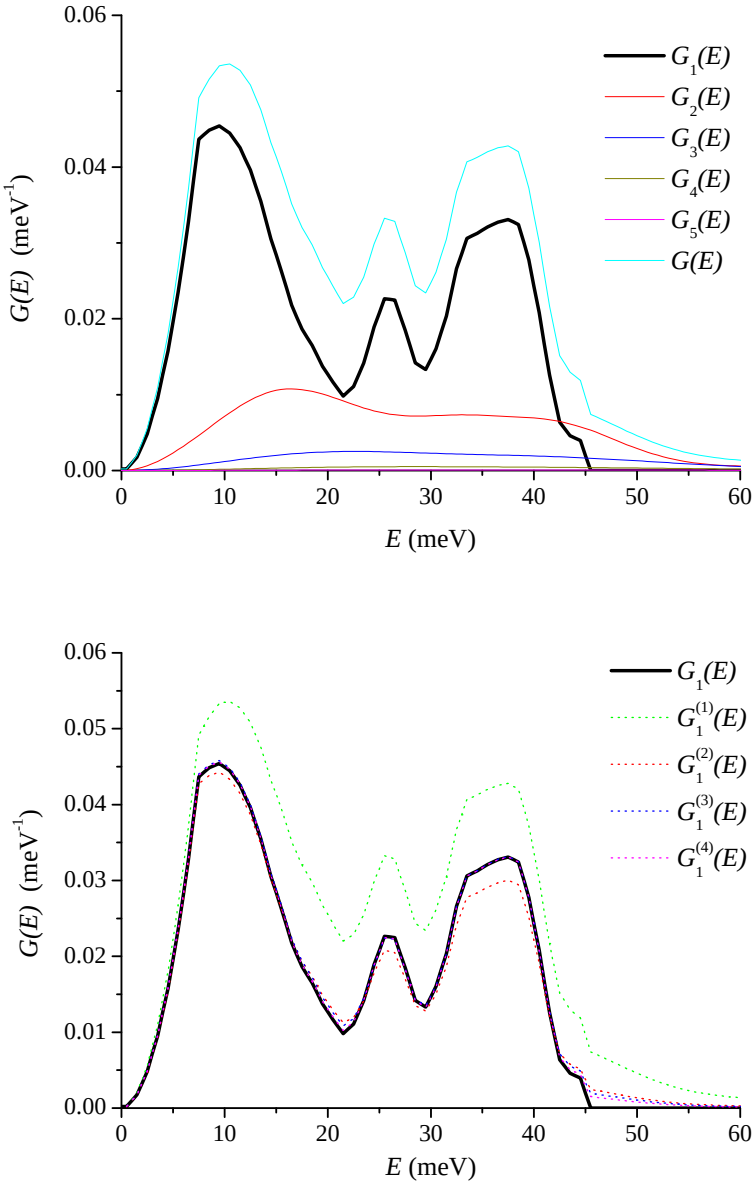

Figure 4-5: (top) The phonon terms calculated for a $G_1(E)$ function with three peaks, where $G_p(E)$ represents the p^{th} phonon term calculated by using the method described in the text and $G(E) = \sum_{p}^{5} G_p(E)$. (bottom) The single phonon term $G_1^{(\text{i})}(E)$ calculated after i iterations by the correction program using $G(E)$ as the input dataset. $G_1(E)$ is the true single phonon scattering as given in the top figure. A temperature of 200 K and Debye-Waller factor of $\langle u^2 \rangle / 3 = 0.0125$ Å^2 were used in the calculations. After each iteration, the calculated $G_1^{(\text{i})}(E)$ function from the program approaches $G_1(E)$ where convergence is more-or-less achieved when i = 3

4.2 High Pressure Experiments on the PEARL Diffractometer

4.2.1 Introduction

The data analysis procedure used for glasses measured on the PEARL diffractometer (see section 3.3.1) is reported by Salmon *et al.* [104]. The procedure is an extension of that developed by Drewitt [39]. Due to the complicated scattering geometry, large background scattering and lack of low Q data associated with such experiments, a semi-empirical data analysis procedure was required. Three measurements are made; for the sample at pressure, $I^{\mathrm{E}}_{\mathrm{sc}}(Q)$, for a vanadium pellet compressed to a pressure such that its geometry is the same as that of the sample, $I^{\mathrm{E}}_{\mathrm{vc}}(Q)$, and for an empty Ti-Zr gasket at ambient pressure, $I^{\mathrm{E}}_{\mathrm{c}}(Q)$. These latter datasets are used for normalisation and background subtraction. In section 4.2.2 the pressure calibration is presented, while in section 4.2.3 the ideal correction procedure is given, together with examples of the correction factors. In section 4.2.5 practical considerations are made and the semi-empirical data correction procedure is presented, wherein the data are normalised, a residual slope in $F(Q)$ is removed and a Lorentzian line shape is used for $F(Q)$ in the low Q region that is not accessible by experiment. The correction and normalisation procedure is summarised in figure 4-6.

4.2.2 Pressure Calibration

The pressure at the sample position is determined from the load L applied to the anvils through calibration curves based on many neutron diffraction experiments using systems with a known equation of state in an otherwise identical setup. In the case of single toroid anvils it was found that the calibration curve (figure 4-7) depends on whether the samples are held in standard or encapsulated [105] Ti-Zr gaskets and so only experiments done using standard gaskets are presented here. For this anvil profile, the calibration curve for samples contained in standard Ti-Zr gaskets was deduced from (i) a calibration run in which a pellet made from a 1:3 mixture of NaCl and glassy $GeSe_2$ was compressed in cubic BN anvils, a Rietveld refinement was made of the NaCl Bragg peaks, and the pressure was obtained from the NaCl equation of state [106]; (ii) applying the procedure described by Drewitt *et al.* [40] where various samples were compressed by different loads using cubic BN anvils and the dimensions of the recovered gaskets were measured; and (iii) compression of GeO_2 glass pellets using sintered diamond anvils where a Rietveld refinement was made to the diamond Bragg peaks and the unit cell volume to pressure conversion was made on the basis of previous experiments on crystalline ice VII [107]. In the case of double toroid anvils, the available data indicates

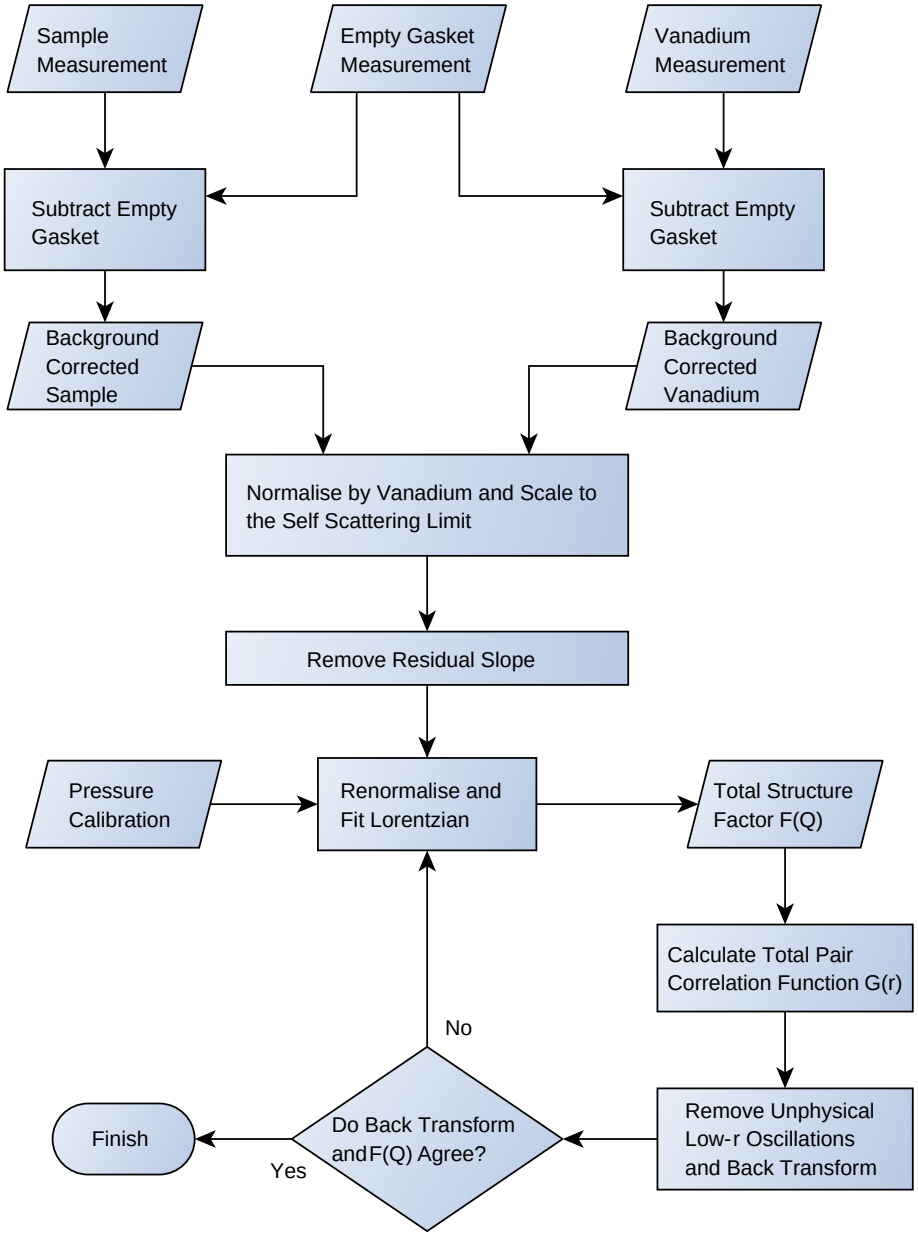

Figure 4-6: The data analysis procedure for the PEARL neutron diffraction experiments.

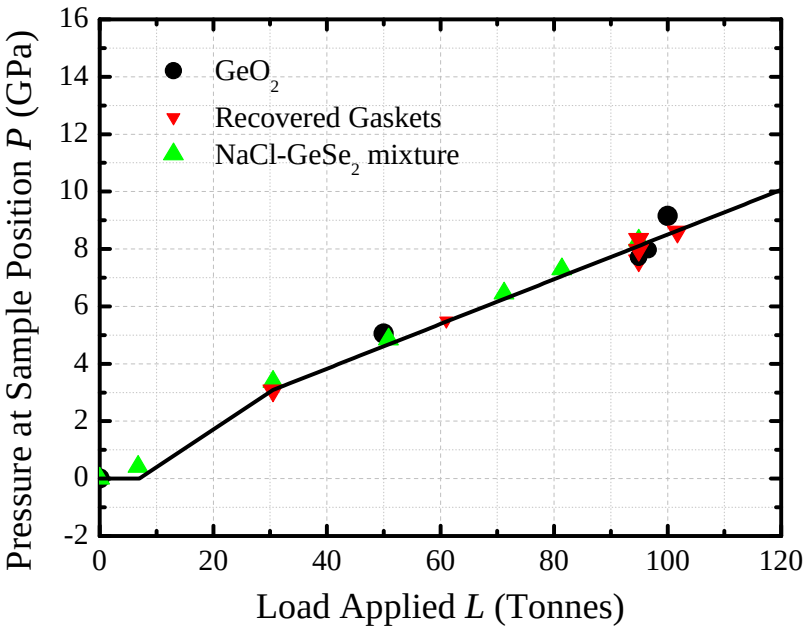

Figure 4-7: Calibration curve for the load L applied to the piston of a V4 or VX5 variant Paris-Edinburgh press versus the pressure P at the sample position for single toroid anvils at a temperature of 300 K. The calibration was made using standard Ti-Zr gaskets and the data points correspond to a calibration run using a mixture of NaCl and glassy $GeSe_2$ (▲); measurement of the dimensions of recovered gaskets after various samples were compressed using different loads (▼); or consideration of the diamond Bragg peaks measured when various GeO_2 glass pellets were compressed in sintered diamond anvils (●). The solid black curve was used to give the pressure at the sample position.

similar calibration curves for standard and encapsulated Ti-Zr gaskets (figure 4-8). For

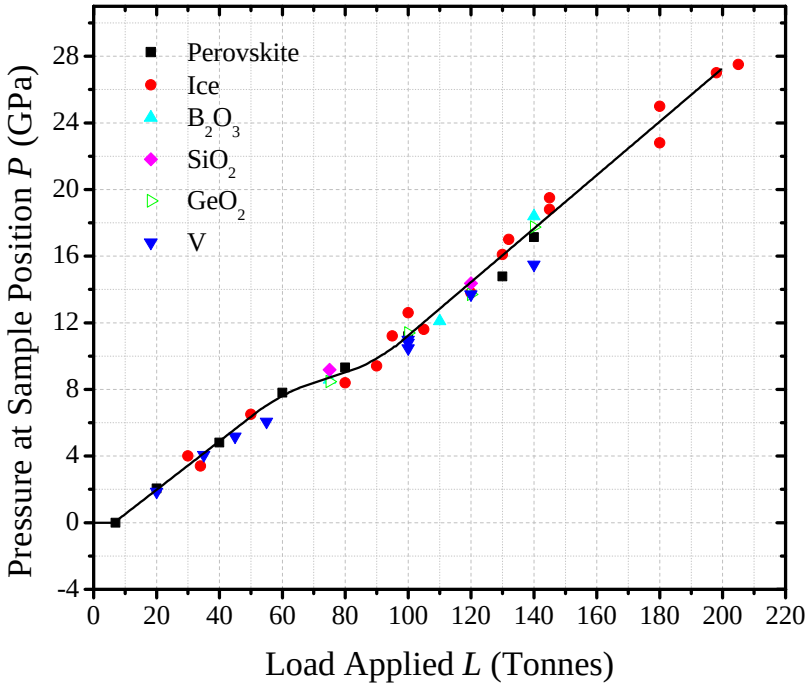

Figure 4-8: Load L applied to the piston of a V3 variant Paris-Edinburgh press versus the pressure P at the sample position for double toroid sintered diamond anvils. The calibration curve was deduced from (i) the diffraction patterns measured for a perovskite held in encapsulated Ti-Zr gaskets with a methanol-ethanol-water pressure transmitting medium and a MgO pressure marker (■); (ii) the diffraction patterns measured for crystalline ice held in encapsulated Ti-Zr gaskets (●); and (iii) a Le Bail analysis of the Bragg peaks measured for sintered diamond anvils at different pressure points when various samples, contained in standard gaskets, were compressed. For the latter, the unit cell volume to pressure conversion was made on the basis of the perovskite experiment and the data points correspond to samples of GeO_2 (▷), SiO_2 (◆) or B_2O_3 (▲) glass and crystalline vanadium (▼). These data points have been shifted downwards by 2 GPa but show the same P versus L behaviour as for the perovskite and ice samples i.e. although there is an uncertainty in the absolute values of the diamond Bragg peak data points from study (iii) (e.g. the anvils in standard and encapsulated gasket experiments may not be at the same position for the same applied load) their relative values are the same as for studies (i) and (ii).

this anvil profile, the calibration curve was deduced from (i) the diffraction patterns measured for the perovskite $CaSnO_3$ held in encapsulated Ti-Zr gaskets with a MgO pressure marker [108] in a 16:3:1 mixture of deuterated methanol:ethanol:water; (ii) the diffraction patterns measured for crystalline ice held in encapsulated Ti-Zr gaskets; and (iii) a Le Bail analysis [109] of the Bragg peaks measured for sintered diamond anvils at different pressure points when various samples, contained in standard gaskets,

were compressed. For the latter, the unit cell volume to pressure conversion was made on the basis of the perovskite experiment.

4.2.3 Background Subtraction and Vanadium Normalisation

The measured sample and vanadium measured intensities, corrected for background scattering, are given by [104]

$$I_{\mathrm{sc}}(Q) = I^{\mathrm{E}}_{\mathrm{sc}}(Q) - I^{\mathrm{E}}_{\mathrm{bs}}(Q) = a(Q)N_{\mathrm{s}}A_{\mathrm{s,sc}}(Q)\left.\frac{d\sigma}{d\Omega}\right|_{\mathrm{s}} + a(Q)M_{\mathrm{sc}}(Q) \quad , \tag{4.23}$$

$$I_{\mathrm{Vc}}(Q) = I^{\mathrm{E}}_{\mathrm{vc}}(Q) - I^{\mathrm{E}}_{\mathrm{bV}}(Q) = a(Q)N_{\mathrm{V}}A_{\mathrm{V,Vc}}(Q)\left.\frac{d\sigma}{d\Omega}\right|_{\mathrm{V}} + a(Q)M_{\mathrm{Vc}}(Q) \quad , \tag{4.24}$$

where, for the sample of interest ($\alpha = \mathrm{s}$) or vanadium ($\alpha = \mathrm{V}$), $I^{\mathrm{E}}_{\alpha\mathrm{c}}(Q)$ is the measured intensity, $I_{\alpha\mathrm{c}}(Q)$ is the background corrected intensity, $I_{\mathrm{b}\alpha}(Q)$ is the background intensity, $\mathrm{d}\sigma/\mathrm{d}\Omega|_{\alpha}$ is the differential cross section per atom and $M_{\alpha\mathrm{c}}(Q)$ is the multiple scattering cross section for sample α in the gasket, $A_{\alpha,\alpha\mathrm{c}}(Q)$ is the attenuation coefficient for scattering by the sample or vanadium and attenuation by the sample or vanadium and gasket, N_{α} is the total number of atoms illuminated by the incident beam, and $a(Q)$ is a normalisation coefficient that transforms measured intensities into neutron scattering cross sections.

The scattering from vanadium is mostly incoherent i.e. its coherent scattering length $\bar{b}_{\mathrm{V}} \approx 0$ such that $F(Q) \approx 0$ and $d\sigma/d\Omega|_{\mathrm{V}} = \sigma_{\mathrm{self}}/4\pi = b^2_{\mathrm{inc,V}}(1 + P_{\mathrm{V}}(Q))$ (cf. equation (2.50)), where $b^2_{\mathrm{inc},V}$ is the incoherent neutron scattering length for vanadium and $P_{\mathrm{V}}(Q)$ is the Placzek correction for vanadium. Equation (4.24) is then solved to give $a(Q) = I_{\mathrm{Vc}}(Q)/\left[N_{\mathrm{V}}A_{\mathrm{V,Vc}}(Q)b^2_{\mathrm{inc,V}}(1 + P_{\mathrm{V}}(Q)) + M_{\mathrm{Vc}}(Q)\right]$ and by substituting $a(Q)$ into equation (4.23) the differential scattering cross section for the sample is given by

$$\left.\frac{\mathrm{d}\sigma}{\mathrm{d}\Omega}\right|_{\mathrm{s}} = F(Q) + \frac{\sigma_{\mathrm{self}}}{4\pi} = W(Q)\frac{I_{\mathrm{sc}}(Q)}{I_{\mathrm{vc}}(Q)} + X(Q) \quad , \tag{4.25}$$

where

$$W(Q) = \frac{1}{N_{\mathrm{s}}A_{\mathrm{s,sc}}(Q)}\left[N_{\mathrm{V}}A_{\mathrm{V,Vc}}(Q)b^2_{\mathrm{inc,V}}\left(1 + P_{\mathrm{V}}(Q)\right) + M_{\mathrm{Vc}}(Q)\right] \tag{4.26}$$

and

$$X(Q) = \frac{M_{\mathrm{sc}}(Q)}{N_{\mathrm{s}}A_{\mathrm{s,sc}}(Q)} \quad . \tag{4.27}$$

	Single Toroid		Double Toroid	
	Ambient	8.5 GPa	Ambient	11.5 GPa
R_s (cm)	0.3	0.3	0.2	0.2
R_c (cm)	0.7335	0.9438	0.69	0.895
h (cm)	0.16	0.532	0.16	0.55
ρ GeO_2 ($Å^{-3}$) [110]	0.0629	0.0868	0.0629	0.1031
ρ V ($Å^{-3}$) [111]	0.0721	0.0757	0.0721	0.0794
ρ $Ti_{0.676}Zr_{0.324}$ ($Å^{-3}$) [40]	0.0511	0.0536	0.0511	0.0579

Table 4.1: The variables used in the calculation of the attenuation coefficients for samples of GeO_2 in either single or double toroid anvils at the pressures indicated. The gasket dimensions for the high pressure experiments were found from measurements of the recovered gaskets.

4.2.4 Attenuation, Multiple Scattering and Placzek Correction Factors

A simplified geometry for the diffraction experiments is given in figure 4-9. The atten-

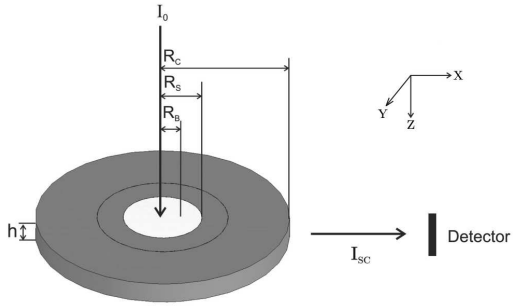

Figure 4-9: Schematic showing the idealised transverse scattering geometry for a high pressure neutron diffraction experiment on the PEARL diffractometer [104], where a sample of radius R_s and height h, contained within an annular gasket of outer radius R_c and height h, is illuminated by a beam of intensity I_0 with a circular profile of radius R_B. The incident beam lies parallel to the Z axis and the scattered beam, of intensity I_{sc}^{E}, is observed in the $X-Y$ plane.

uation coefficients for this geometry for a sample of GeO_2 were calculated by Salmon *et al.* [104] using the dimensions given in table 4.1. The Placzek corrections for the sample and vanadium were calculated using the method described by Howe *et al.* [112].

The order of magnitude of the multiple scattering correction was also calculated by using the procedure described by Soper *et al.* [80]. The multiple scattering gives a contribution of around 1 % or 2 % to $W(Q)$ and its contribution to $X(Q)$ is $<< \sigma_{self}/4\pi$, which means that equation (4.25) can be re-written as

$$F(Q) \simeq W(Q)I_{sc}(Q)/I_{vc}(Q) - \sigma_{self}/4\pi. \tag{4.28}$$

For comparable sample and vanadium volumes it follows that

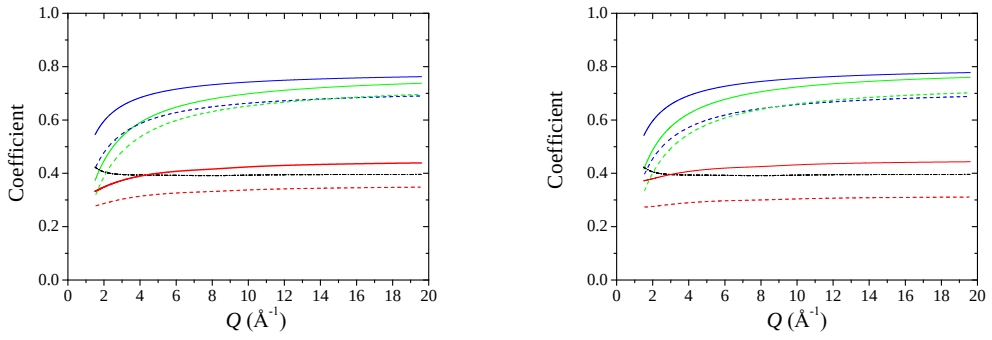

Figure 4-10: The coefficients $A_{\mathrm{s,sc}}(Q)$ (blue), $A_{\mathrm{V,Vc}}(Q)$ (green), and $W(Q)$ (in units of barn) (red) as calculated for a sample of GeO_2 with (a) single toroid anvil geometry at ambient pressure (solid curves) and a pressure of 8.5 GPa (dashed curves) or (b) double toroid anvil geometry at ambient pressure (solid curves) and a pressure of 17.5 GPa (dashed curves). Each panel also shows $b^2_{\mathrm{inc,V}}[1 + P_{\mathrm{V}}(Q)]$ (barn) (black chained curve). The coefficients $A_{\mathrm{s,sc}}(Q)$, $A_{\mathrm{V,Vc}}(Q)$ and $W(Q)$ were calculated using the dimensions of either the initial or recovered gaskets given in table 4.1 and an incident beam of radius $R_{\mathrm{B}} = 0.169$ cm. The chosen high pressure gasket densities are overestimates since they correspond to the pressure of the sample and not to a pressure between that of the sample and ambient. The scattering and absorption cross-sections used in the calculations were taken from Sears [113].

$$W(Q) \simeq \frac{1}{\rho_{\mathrm{s}} A_{\mathrm{s,sc}}(Q)} \rho_{\mathrm{V}} A_{\mathrm{V,Vc}}(Q) b^2_{\mathrm{inc,V}} (1 + P_{\mathrm{V}}(Q)) \quad , \tag{4.29}$$

where ρ_v and ρ_{s} are the atomic number densities for vanadium and the sample of interest, respectively. Examples of the $A_{\mathrm{s,sc}}(Q)$, $A_{\mathrm{V,Vc}}(Q)$ and $W(Q)$ functions are shown in figure 4-10 for ambient and high pressure conditions. The results show that $W(Q)$ is a relatively flat and weakly varying function at high Q.

4.2.5 Data Reduction in Practice

In practice, the background intensity for each pressure cannot be measured and the background scattering changes with pressure, as the material in the anvils compresses. Therefore, an approximation was made that, for a given pressure and sample, $I^{\mathrm{E}}_{\mathrm{b}\alpha}(Q) = C_\alpha I^{\mathrm{E}}_{\mathrm{c}}(Q)$ where $I^{\mathrm{E}}_{\mathrm{c}}(Q)$ is the intensity measured with an empty gasket at ambient pressure and C_α is a constant chosen such that the diamond Bragg peaks in the ratio $I_{\mathrm{sc}}(Q)/I_{\mathrm{Vc}}(Q)$ are minimised (figure 4-11(b)). Also, the dimensions of the gasket and sample at pressure are not certain and the sample geometry is not cylindrical so there is an error in the calculated $W(Q)$ functions. In practice, the $W(Q)$ function used in the

data analysis procedure was taken to be a constant independent of Q, chosen so that the differential scattering cross section initially calculated oscillates around $\sigma_{\rm self}/4\pi$ at high Q as expected (figure 4-11(c)). An initial $F(Q)$ function is then calculated by using equation (4.28) such that $F^{(0)}(Q) = W(Q)I_{\rm sc}(Q)/I_{\rm Vc}(Q) - \sigma_{\rm self}/4\pi$.

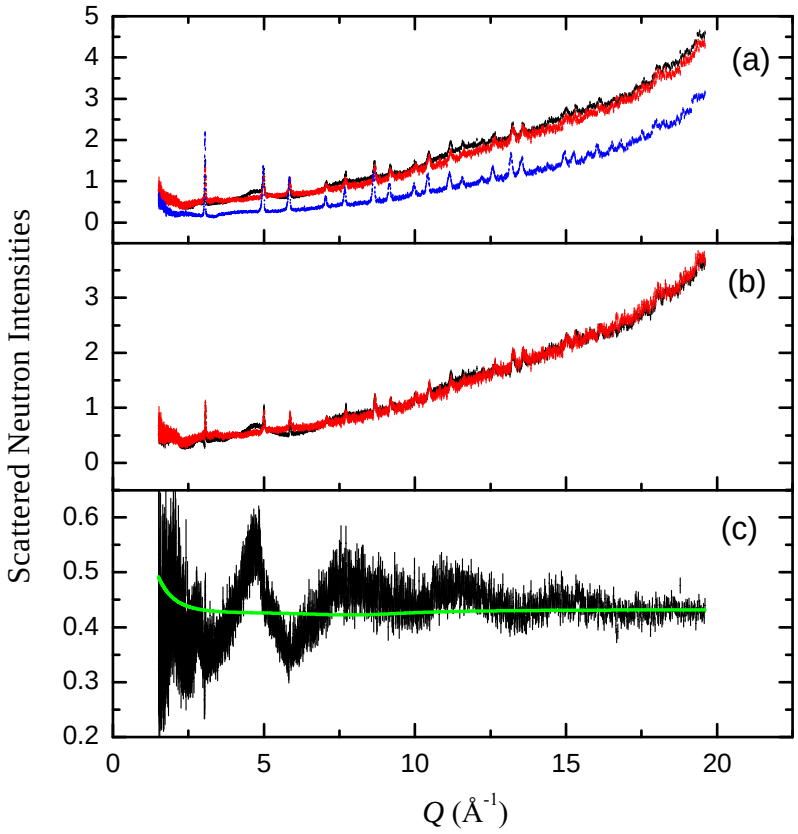

Figure 4-11: Example of the background correction procedure for a sample of GeO_2 at a pressure of 8.5(5) GPa using double-toroid sintered diamond anvils. The sample load was 75 tns, the vanadium load was 35 tns and the empty gasket load was 2 tns. (a) The measured intensity for the sample $I^{\rm E}_{\rm sc}(Q)$ (solid black curve), vanadium $I^{\rm E}_{\rm Vc}(Q)$ (solid red) and empty gasket $I^{\rm E}_{\rm c}(Q)$ (solid blue curve). (b) $I_{\rm sc}(Q) = I^{\rm E}_{\rm sc}(Q) - C_{\rm s}I^{\rm E}_{\rm c}(Q)$ (solid black curve) and $I_{\rm Vc}(Q) = I^{\rm E}_{\rm Vc}(Q) - C_{\rm V}I^{\rm E}_{\rm c}(Q)$ (solid red curve), where $C_{\rm s} = 0.2$ and $C_{\rm V} = 0.2$. (c) The ratio $W(Q)I_{\rm sc}(Q)/I_{\rm Vc}(Q)$ (solid black curve) and $\sigma_{\rm self}/4\pi$ (solid red curve), where $W(Q)$ is taken to be a constant equal to 0.44.

In the absence of experimental data, the region in $F^{(0)}(Q)$ for $Q \leq 1.55$ Å^{-1} is first set to the $Q = 0$ limit as estimated e.g. from the sample compressibility [39]. The corresponding total pair distribution function $G^{(0)}(r)$ is found by using equation (2.53) and large amplitude features in $G^{(0)}(r)$ at low r, well below the distance of closest approach between two atoms, are set to the calculated $r = 0$ limit (equation

(2.56)). The resultant data set is then back Fourier transformed to give a revised slope-corrected total structure factor $F^{(1)}(Q)$ as shown in figure 4-12. The low Q region of

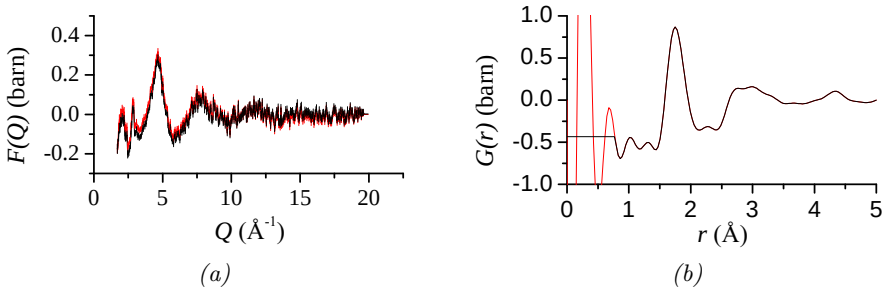

Figure 4-12: Example of the slope correction procedure for a sample of GeO_2 at a pressure of 8.5(5) GPa using double-toroid sintered diamond anvils. The zeroth approximation to the total structure factor $F^{(0)}(Q)$ (solid red curve in (a)) is Fourier transformed to give $G^{(0)}(r)$ (solid red curve in (b)). The large amplitude features in $G^{(0)}(r)$ at small r are set to the $G(0)$ limit (solid black curve in (b)) and this is back Fourier transformed to give the revised total structure factor $F^{(1)}(Q)$ (solid black curve in (a)).

$F^{(1)}(Q)$ is fitted with a Lorentzian function, since this often gives a good account of the FSDP [114, 115], such that the fitted function passes through the expected $Q = 0$ limit. The revised $F^{(1)}(Q)$ function is then Fourier transformed to give $G^{(1)}(r)$, the lowest r oscillations in $G^{(1)}(r)$ below the distance of closest approach between two atoms are set to the calculated $r = 0$ limit, and the resultant data set is back Fourier transformed to give a revised total structure factor $F^{(2)}(Q)$. $F^{(2)}(Q)$ is then scaled, the small Q region is refitted with a Lorentzian shape and the entire procedure is re-iterated until, as far as possible, (i) the small r oscillations in the final $G(r)$ function are of minimal amplitude and are symmetrical about the calculated limit $G(0)$ limit and (ii) there is agreement between the $F(Q)$ function and the back Fourier transform of the $G(r)$ function after the lowest r oscillations below the distance of closest approach between two atoms are set to the calculated $G(0)$ limit. The procedure is demonstrated in figure 4-13.

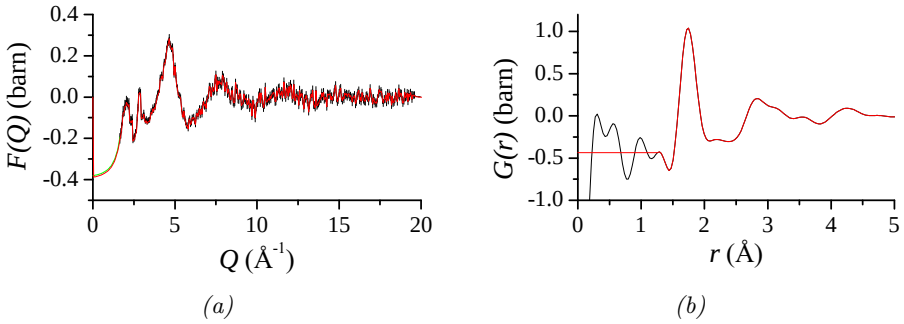

Figure 4-13: Example of the back Fourier transform and Lorentzian fitting procedure for a sample of GeO_2 at a pressure of 8.5(5) GPa using double-toroid sintered diamond anvils. The scaled total structure factor $F^{(1)}(Q)$ (solid black curve in (a)) is fitted with a Lorentzian shape at low Q (the solid green curve in (a)) and Fourier transformed to give $G^{(1)}(r)$ (the solid black curve in (b)). The low r oscillations in $G^{(1)}(r)$ are set to the $G(0)$ limit as indicated by the solid red curve in (b) and this is back Fourier transformed to compare to $F^{(1)}(Q)$ (solid red curve in (a)). The correction procedure is re-iterated until the conditions mentioned in the text are met.

5. Vibrational Density of States of $GeSe_2$ Glass Using the MARI Spectrometer

5.1 Introduction

The ability to model materials is important in order to predict their properties over a wide range of compositions [8], temperatures and pressures [19, 24, 116–125]. Molecular dynamics (MD) is an atomistic modelling approach [126]. MD models for key systems are tested and refined against experimental data from e.g. diffraction and spectroscopy experiments (examples relevant to the glasses studied here include refs. [35, 37, 44, 45, 127–133]).

A good example of a test for the MD approach is represented by the $GeSe_2$ system. $GeSe_2$ is a prototypical chalcogenide glass (a family of glasses that are of both scientific and technological interest [3, 134, 135]) where the structure under ambient conditions is formed from a network of corner and edge sharing $GeSe_4$ tetrahedra [136–152]. The similar electronegativities of Ge and Se also leads to the formation of homopolar bonds, which makes $GeSe_2$ challenging to study by MD simulations.

Great effort has been undertaken to understand the dynamics of $GeSe_2$ using light (e.g. Raman and infrared) scattering techniques [153–162]. However, extracting a full density of states using these techniques is difficult due to selection rules and experimental constraints [99, 163]. While it is a flux-limited technique, neutron spectroscopy does not suffer from many of these limitations [11, pp. 132]. The total vibrational density of states in the extreme incoherent approximation has been measured for $GeSe_2$ [51, 130, 164] but no experiments have been aimed at giving the full partial vibrational density of states for this or any other binary network forming glass.

$GeSe_2$ also has properties that make it a good candidate to develop the technique of isotope substitution in neutron spectroscopy. The natural isotopic abundances of Ge and Se have similar scattering cross sections [113] and atomic masses [165] so that the

extreme incoherent approximation should hold well. Isotopically enriched samples of $^{\mathrm{N}}\mathrm{Ge}^{\mathrm{N}}\mathrm{Se}_2$, $^{70}\mathrm{Ge}^{\mathrm{N}}\mathrm{Se}_2$ and $^{73}\mathrm{Ge}^{76}\mathrm{Se}_2$ can be made, where N represents the natural isotopic abundance, and there is a large contrast between the neutron scattering lengths of the different isotopes ($^{\mathrm{N}}$Ge, ^{70}Ge and ^{73}Ge have coherent scattering lengths of 8.185(20), 10.0(1) and 5.09(4) fm, while $^{\mathrm{N}}$Se and ^{76}Se have coherent scattering lengths of 7.790(9) and 12.2(1) fm, respectively). The incoherent scattering cross sections for all of the isotopes of Ge and Se are also small in comparison with the coherent scattering cross sections [113], the largest being for ^{73}Ge which has an incoherent scattering length of 3.40(31) fm. The purpose of the present investigation is to develop the method of isotope substitution in neutron spectroscopy to measure the partial vibrational density of states of $GeSe_2$ in order to compare to MD simulations. An experiment was done on the MARI spectrometer (see section 3.2.1) using samples of $^{\mathrm{N}}\mathrm{Ge}^{\mathrm{N}}\mathrm{Se}_2$, $^{70}\mathrm{Ge}^{\mathrm{N}}\mathrm{Se}_2$ and $^{73}\mathrm{Ge}^{76}\mathrm{Se}_2$. Giacomazzi *et al.* have produced *ab initio* MD models for $GeSe_2$ using a GGA gradient functional (model 1 in ref. [35]) and a BLYP function [45]. However, the classical MD results of Giacomazzi *et al.* (model 4 in ref. [35]) using potentials from Vashishta *et al.* [141, 166] were found to best match experimental data.

This chapter is organised as follows. In section 5.2 the experimental procedure is presented. In section 5.3 the data analysis procedure is shown, where at each stage the total vibrational density of states $G(E)$ is calculated within the extreme incoherent ("bronze medal") approximation and the results are presented before and after each correction to show their effect. In section 5.3.3 the subtraction of the empty can scattering, including an account of the attenuation and renormalisation corrections, is presented. The multiple scattering is calculated to give the total coherent dynamical structure factor $S_{\mathrm{c}}(Q, E)$ for each sample in section 5.3.4. The multiple phonon corrections are calculated in section 5.3.4. In section 5.4 the matrices used to calculate the single phonon partial dynamical structure factors within the "silver medal" approximation are given.

Results are presented in section 5.5. First, the single phonon generalised vibrational density of states calculated in the "bronze medal" approximation $G_1(Q, E)$ is given together with corresponding single phonon effective vibrational density of states $G_1(E)$ for each sample. The single phonon partial generalised vibrational density of states $G_{\mathrm{Ge}}(Q, E)$ and $G_{\mathrm{Se}}(Q, E)$ calculated in the "silver medal" approximation are then given together with the corresponding single phonon effective partial vibrational density of states $G_{\mathrm{Ge}}(E)$ and $G_{\mathrm{Se}}(E)$. The experimental data are compared to the results obtained from classical MD simulations made by Giacomazzi *et al.* [35] using the potentials of Vashishta *et al.* [141, 166] and the results obtained from previous experiments reported in refs. [51, 130, 164].

Finally the efficacy of the experimental and data analysis procedures is discussed

in section 5.6 and conclusions are drawn in section 5.7. Throughout this chapter, a Debye-Waller factor corresponding to $\langle u^2 \rangle / 3 = 0.002$ Å^2 has been used for $\overline{W}(Q)$, $W_{\mathrm{Ge}}(Q)$ and $W_{\mathrm{Se}}(Q)$ in the calculations where required. This value was found from an experiment which is described in chapter 6 (see table 6.4).

5.2 Experimental Procedure

5.2.1 Glass Preparation

Three isotopically enriched glasses were prepared for a previous experiment by Salmon and Petri [136] in an identical way with a stoichiometry, determined by mass, of 0.3333(2)Ge : 0.6667(2)Se. $^{\mathrm{N}}$Ge (99.9999 %, Aldrich) or ^{70}Ge (99.8 % ^{70}Ge, 0.2 % ^{72}Ge) or ^{73}Ge (98 % ^{73}Ge, 0.3 % ^{70}Ge, 0.8 % ^{72}Ge, 0.8 % ^{74}Ge, 0.1 % ^{76}Ge) were loaded into silica ampoules (1 mm wall thickness, 4.8 mm internal diameter) together with $^{\mathrm{N}}$Se (99.999 %, Johnson Matthey) or ^{76}Se (99.75 % ^{76}Se, 0.2 % ^{74}Se, 0.05 % ^{77}Se) in a high purity argon filled glovebox ($\approx$ 0.1 ppm oxygen, $<$ 10 ppm water).

Before loading, the ampoules were cleaned with chromic acid and etched using a 40 % solution of hydrofluoric acid so that the inside surface of the ampoules was atomically smooth. After loading, the ampoules were purged three times with He gas and evacuated to a pressure of $\approx$ 10.5 torr. After $\approx$ 48 hours the ampoules were sealed, loaded into a rocking furnace and heated at 1 °C min^{-1} to 1000 °C, pausing for 1 hour at both the melting and boiling points of Se (221 °C and 685 °C [165] respectively) and the melting point of Ge (938.3 °C). After $\approx$ 48 hours the ampoules were slowly cooled to 850 °C, where they were equilibrated for $\approx$ 4 hours and quenched in an ice/salt water mixture at a temperature of ≈ -5 °C. The glasses were separated cleanly from the silica in an argon filled glovebox. For each experiment described below, the samples were loaded into or unloaded from aluminium foil packets in a He filled glovebox. After use in each experiment (where all experiments were done under vacuum or a He atmosphere), the samples were sealed in glass bottles in an argon filled glovebox and placed inside a bomb. Any contamination by oxygen or water could lead to a change in the diffraction pattern that is detectable by experiment but no such changes were found. The properties of the isotopically enriched samples that are relevant to the present neutron scattering experiments are given in table 5.1. It is assumed that the samples have a number density equal to the room temperature value for the $^{\mathrm{N}}$Ge$^{\mathrm{N}}$Se$_2$ sample, which is 0.0334(1) Å^{-3} [167].

	$^{N}Ge^{N}Se_2$	$^{70}Ge^{N}Se_2$	$^{73}Ge^{76}Se_2$
$\overline{M}$ (g)	76.83666	75.9494153	74.9162907
M_{Ge} (g)	72.5900	69.9355	72.2501
M_{Se} (g)	78.9600	78.9600	75.9157
$\left\langle \overline{b}^2 \right\rangle$ (barn)	0.647(1)	0.757(7)	1.07(2)
$\overline{b}_{Ge}$ (fm)	8.185(20)	10.0(1)	5.09(4)
$\overline{b}_{Se}$ (fm)	7.970(9)	7.970(9)	12.2(1)

Table 5.1: Specific parameters for the isotopically enriched samples that were measured using the MARI spectrometer at the ISIS pulsed neutron source where $\overline{M}$ is the average atomic mass of the sample, M_α is the average atomic mass of an atom of chemical species α, $\overline{b}_\alpha$ is the average coherent scattering length of chemical species α and $\left\langle \overline{b}^2 \right\rangle = \sum c_\alpha b_\alpha^2$ is the mean square coherent scattering length. The scattering lengths were calculated using the values from reference [113]. N denotes the natural isotopic abundance.

5.2.2 Neutron Spectroscopy Measurements

Measurements were made on the MARI spectrometer at the ISIS Pulsed Neutron Source in Didcot (see section 3.2.1). A "sloppy" type Fermi chopper, which transmits a high intensity of neutrons with low energy resolution, spinning with a frequency of 250 Hz was used to select an almost monochromatic incident beam of neutrons centred on an energy of 60.35(5) meV. For this configuration, the MCHOP software [168] was used to give an estimated incident neutron flux of 7435 neutrons s^{-1} with a full width at half maximum (FWHM) in energy at the elastic line ($E = 0$) of 2.46 meV. The energy resolution and detector coverage of the spectrometer under these conditions is shown in figure 5-1.

The samples (where the masses that were used are given in table 5.2) were loaded into packets made from 0.013(1) mm thick aluminium foil in a He filled glovebox. Each loaded sample was wrapped around the inside surface of a cylindrical aluminium can of thickness 0.10(1) mm and diameter of 42 mm to form an annular sample geometry. A 1 mm thick cadmium plate was used to cover the top of the can and provide shielding as shown in figure 5-2. The assembly was placed into a CCR in the neutron beam and the CCR was purged with He gas three times. A pressure of 26 mbar of He gas was let into the sample chamber for heat exchange with the CCR. The samples were cooled to 20(1) K. The incident beam profile was square with a height of 35.0 mm and width of 50.0 mm centred on the foil packet such that the entire sample was illuminated.

Four measurements were taken under identical conditions for samples of $^{N}Ge^{N}Se_2$, $^{70}Ge^{N}Se_2$, $^{73}Ge^{76}Se_2$ in an aluminium foil packet and for an empty aluminium foil packet. Two further measurements were made using a solid annular vanadium sample at room temperature for detector calibration and absolute normalisation; one under

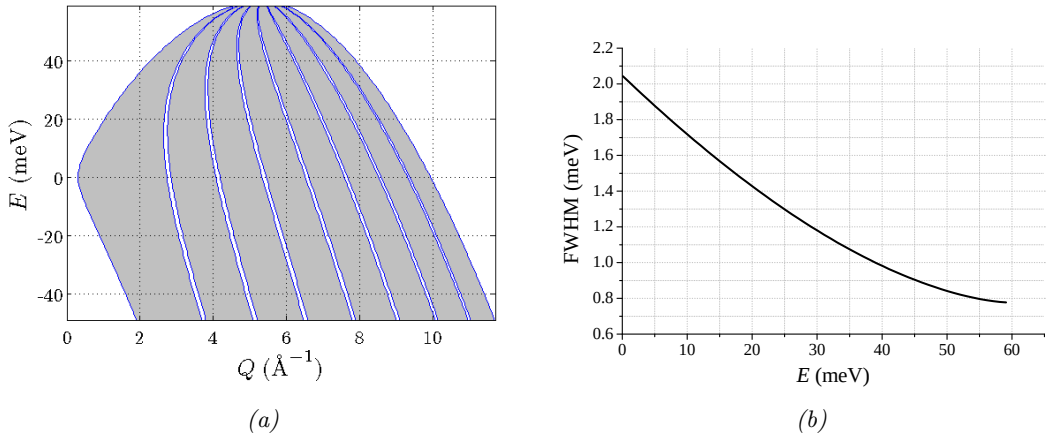

(a) (b)

Figure 5-1: (a) The kinematically allowed region and (b) the energy resolution full width at half maximum (FWHM) calculated using the MCHOP program [168] for the $GeSe_2$ experiment done using the MARI spectrometer using an incident energy of 60.35(5) meV and Fermi chopper frequency of 250 Hz. In (a), the accessible Q-E space is shaded in grey i.e. there are gaps between the different detector groups (see section 3.2.1).

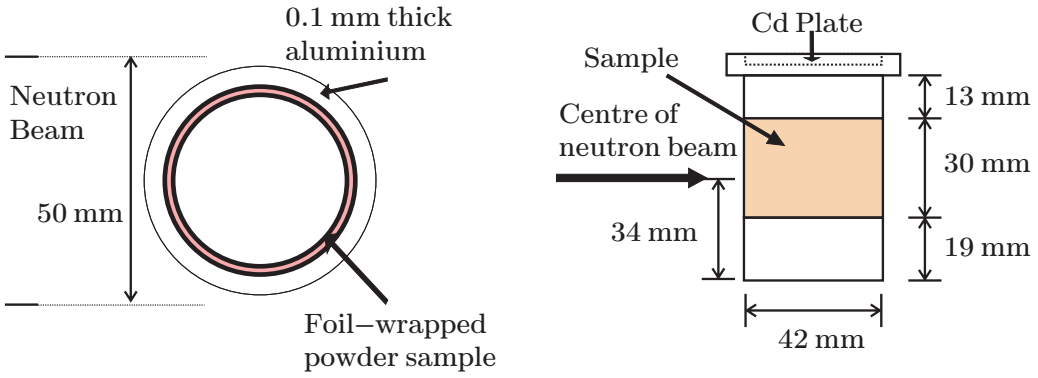

(a) (b)

Figure 5-2: The sample in an Al foil packet loaded into the middle of a 0.10(1) mm thick Al can. (a) Top view and (b) side view.

Sample	Sample Mass (g)	Proton Charge (μA h)
$^{N}Ge^{N}Se_2$	5.027(1)	7196.2
$^{70}Ge^{N}Se_2$	2.084(1)	9316.6
$^{73}Ge^{76}Se_2$	1.958(1)	12687.7
Empty Can	N/A	8389.0

Table 5.2: The mass of sample used together with the charge of protons that was incident on the spallation target during each measurement. The latter is proportional to the number of neutrons that were incident on the sample during that measurement.

identical conditions to the sample measurements and one using an incident beam containing a wide range of neutron energies (i.e. a so-called white beam).

5.3 Data Treatment

The data analysis procedure for the measurements taken on the MARI spectrometer follows the general correction procedure described in section 4.1.

5.3.1 Width of the Elastic Line

The elastic peak centred on $I_{\mathrm{s}}(Q, E = 0)$ is broadened by the energy resolution of the spectrometer and must be taken into account. The energy resolution of a time-of-flight chopper spectrometer instrument has a complicated, asymmetric shape determined by the target, moderator and chopper properties. Theoretical calculations exist [9, 55, 169] but, for practical use, the moderator pulse must be measured [170, 171] and approximations are made. The elastic scattered intensity is significantly larger than the inelastic scattered intensity, so it is usually sufficient to define the limits of the elastic peak in E by eye using e.g. the measured intensity for vanadium ($I_{\mathrm{V}}^{\mathrm{E}}(Q, E)$). Any scattered intensity that is within these limits will be dominated by the elastic contribution, although some contribution from inelastic scattering will also be present. Any scattering that is outside of these limits will be fully inelastic. The extent of the elastic peak therefore defines the lowest energy transfer for which the dynamics can be reliably measured.

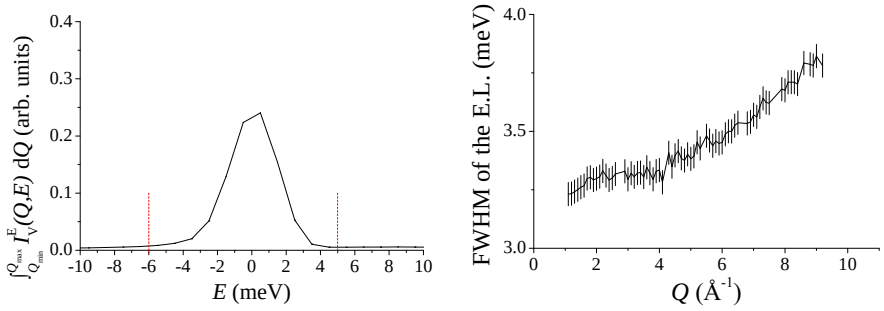

(a) *(b)*

Figure 5-3: (a) The width due to energy resolution broadening of the elastic peak from the monochromatic vanadium measurement, as represented by the function $\int_{Q_{\mathrm{min}}}^{Q_{\mathrm{max}}} I_{\mathrm{V}}^{\mathrm{E}}(Q, E)\,\mathrm{d}Q$, where for each value of E, Q_{min} and Q_{max} are the minimum and maximum Q values that can be measured. Dotted lines indicate the energy transfer range for which the measured intensity is mostly elastic. Data have been normalised such that the integral under the curve is unity.(b) The Q dependence of the FWHM of the elastic line (E.L.) found empirically from the monochromatic vanadium measurement.

Figure 5-3a shows, for a vanadium sample, the broadening of the elastic line due to the effect of the energy resolution of the instrument. A range of $-6 \leq E \leq 5$ meV was selected by eye to define the extent of the elastic line where the limits are shown in figure 5-3a as dotted lines. Outside of this range, scattering is deemed to be fully inelastic.

The range over which the elastic line is broadened is dependent on Q. The FWHM of the elastic line found empirically using the measurement on the vanadium sample is shown in figure 5-3b. The FWHM increases from 3.23(5) to 3.78(5) meV over the range in Q from 1.1 to 9.2 Å^{-1}. The advantages of using high Q data, where the intensity is higher and the effect of the multiple scattering is lower, outweighs the advantages gained in resolution at low Q. For all Q values, the FWHM found empirically differs significantly from the estimated value of 2.46 meV using the MCHOP program (see figure 5-1).

5.3.2 Bose-Einstein Occupation Factor

The Bose-Einstein occupation factor was calculated using equation (2.14) for the experimental temperature of 20 K and is given in figure 5-4. The plot shows that inelastic scattering for $E < 0$ will be very small such that only inelastic scattering for $E > 0$ will be considered.

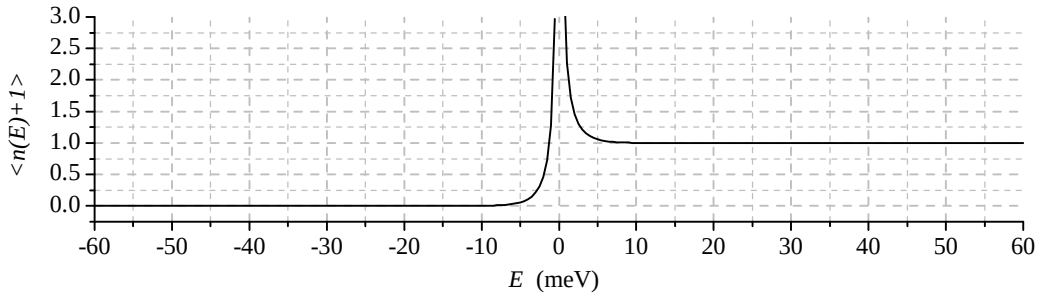

Figure 5-4: The Bose-Einstein occupation factor calculated using equation (2.14) for a temperature of 20 K.

5.3.3 Background Subtraction with Attenuation Corrections and Renormalisation

The normalised sample-in-can scattered intensity, $I_{\text{sc}}(Q, E)$, and empty can scattered intensity, $I_{\text{c}}(Q, E)$, were measured for each sample. The background and attenuation corrected intensity, $I_{\text{s}}(Q, E)$, for each sample was found by using equation (4.6) which,

for convenience, is re-written here:

$$I_{\mathrm{s}}(Q,E) = \frac{m}{A_{\mathrm{sc,sc}}(Q,E)}\left(I^{\mathrm{E}}_{\mathrm{sc}}(Q,E) - I^{\mathrm{E}}_{\mathrm{c}}(Q,E)\right) , \tag{5.1}$$

where $A_{\mathrm{sc,sc}}(Q,E)$ is the attenuation coefficient (figure 5-5), found by treating the sample-in-can as a single annular sample with effective parameters given in table 5.3, and m is a renormalisation constant found to be 0.87, 0.82 or 1.34 for the measurements made on $^{\mathrm{N}}\mathrm{Ge}^{\mathrm{N}}\mathrm{Se}_2$, $^{70}\mathrm{Ge}^{\mathrm{N}}\mathrm{Se}_2$ and $^{73}\mathrm{Ge}^{76}\mathrm{Se}_2$, respectively. In figure 5-6 integrals are

	$^{\mathrm{N}}\mathrm{Ge}^{\mathrm{N}}\mathrm{Se}_2$	$^{70}\mathrm{Ge}^{\mathrm{N}}\mathrm{Se}_2$	$^{73}\mathrm{Ge}^{76}\mathrm{Se}_2$
Inner Radius (cm)	2.0369	2.0664	2.0673
Outer Radius (cm)	2.1000	2.1000	2.1000
Eff. Number Density ($\mathrm{Å}^{-3}$)	0.0389	0.0473	0.0477
Eff. Total Scattering Cross Section (barn)	5.16(2)	4.15(3)	5.40(7)
Eff. Abs. Cross Section at 2200 ms^{-1} (barn)	4.64(7)	2.98(5)	24.5(15)

Table 5.3: Parameters used to calculate $A_{\mathrm{sc,sc}}(Q,E)$. The parameters for each pseudo sample were calculated using the neutron scattering and absorption cross sections from ref. [113], a GeSe_2 number density of 0.0334 $\mathrm{Å}^{-3}$ [167] and an Al number density of 0.06026 $\mathrm{Å}^{-3}$ [165].

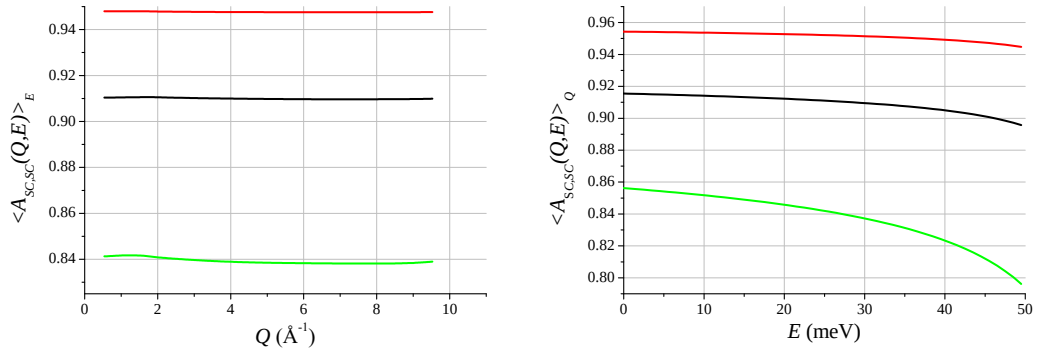

(a) Q Dependence *(b)* E Dependence

Figure 5-5: The attenuation coefficients $A_{\mathrm{sc,sc}}(Q,E)$ for samples of $^{\mathrm{N}}\mathrm{Ge}^{\mathrm{N}}\mathrm{Se}_2$ (solid black curve), $^{70}\mathrm{Ge}^{\mathrm{N}}\mathrm{Se}_2$ (solid red curve) and $^{73}\mathrm{Ge}^{76}\mathrm{Se}_2$ (solid green curve) averaged (a) over energies between 0 and 40 meV or (b) over all Q values. The coefficients were calculated using the parameters given in table 5.3. The maximum energy for the vibrational density of states is $\sim$ 45 meV (see e.g. figure 5-9)

given of the intensities for the sample-in-can measurement, $\int_{E_{\mathrm{min}}}^{E_{\mathrm{max}}} I^{\mathrm{E}}_{\mathrm{sc}}(Q,E)\mathrm{d}E$, empty can measurement, $\int_{E_{\mathrm{min}}}^{E_{\mathrm{max}}} I^{\mathrm{E}}_{\mathrm{c}}(Q,E)\mathrm{d}E$, and corrected sample, $\int_{E_{\mathrm{min}}}^{E_{\mathrm{max}}} I_{\mathrm{s}}(Q,E)\mathrm{d}E$, where E_{min} and E_{max} are the minimum (≥ -50 meV) and maximum (≤ 50 meV) energies

measured at a given Q value, respectively. These integrals represent differential scattering cross sections and are presented to show the effect that scattering from the can has on the sample-in-can measurement. The differential scattering cross section from Salmon *et al.* [136] that was used to find m is also plotted in figure 5-6. The effect

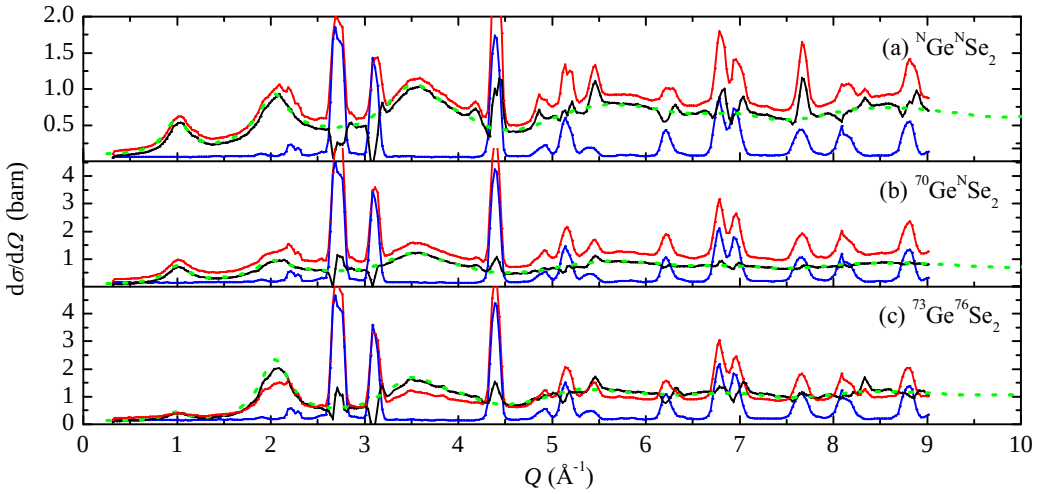

Figure 5-6: The differential scattering cross section $\mathrm{d}\sigma/\mathrm{d}\Omega$ samples of (a) $^{\mathrm{N}}\mathrm{Ge}^{\mathrm{N}}\mathrm{Se}_2$, (b) $^{70}\mathrm{Ge}^{\mathrm{N}}\mathrm{Se}_2$ and (c) $^{73}\mathrm{Ge}^{76}\mathrm{Se}_2$ calculated using the sample-in-can, $\int_{E_{\min}}^{E_{\max}} I_{\mathrm{sc}}^{\mathrm{E}}(Q,E)\mathrm{d}E$ (solid red curve) empty can $\int_{E_{\min}}^{E_{\max}} I_{\mathrm{c}}^{\mathrm{E}}(Q,E)\mathrm{d}E$ (solid blue curve) and corrected sample ($\int_{E_{\min}}^{E_{\max}} I_{\mathrm{s}}(Q,E)\mathrm{d}E$) (solid black curve) intensities, where $E_{\min}$ and $E_{\max}$ are the minimum (≥ -50 meV) and maximum (≤ 50 meV) energies measured at a given Q value, respectively. Also plotted are $\mathrm{d}\sigma/\mathrm{d}\Omega = F(Q)+\sigma_{\mathrm{self}}/4\pi$ from the diffraction experiment by Salmon *et al.* [136] (broken green curve).

of the background, attenuation and renormalisation correction on the $G(E)$ function is shown in figure 5-7 for the $^{\mathrm{N}}\mathrm{Ge}^{\mathrm{N}}\mathrm{Se}_2$ sample where the appropriate values for $^{\mathrm{N}}\mathrm{Ge}^{\mathrm{N}}\mathrm{Se}_2$ used in equation (2.45) are listed in table 5.1.

5.3.4 Multiple Scattering Correction

The approximate method used to calculate the inelastic multiple scattering contributions to the $I_{\mathrm{s}}(Q,E)$ functions is given in section 4.1.3. The incoherent approximation given by $I_{\mathrm{s}}(Q,E) = I_{\mathrm{ms}}(E) + B(E)Q^2\exp(-2\overline{W}(Q))$ (equation (4.7)) could not be fitted directly to the measured $I_{\mathrm{s}}(Q,E)$ functions at each measured E value due to a large statistical error. As will be explained in section 6.4.4, the multiple scattering contribution to $G(E)$ for cold samples roughly follows the density of states. Therefore, for the multiple scattering contribution, $I_{\mathrm{ms}}(E)$ was estimated from the expression (cf.

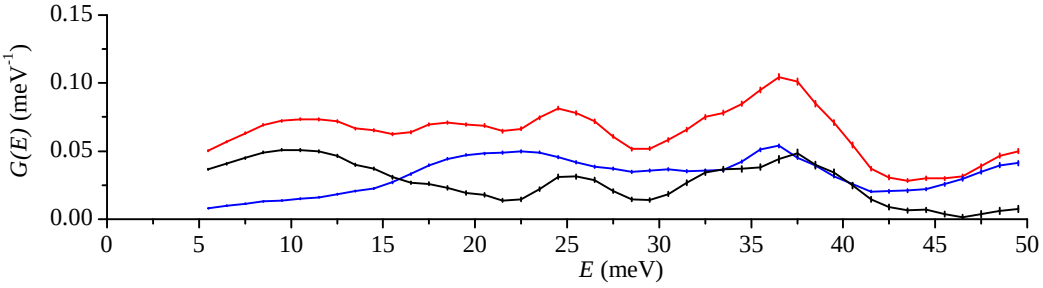

Figure 5-7: $G(E)$ calculated in the "bronze medal" approximation for the $^{\mathrm{N}}\mathrm{Ge}^{\mathrm{N}}\mathrm{Se}_2$ sample from $I_{\mathrm{sc}}^{\mathrm{E}}(Q,E)$ for the sample-in-can (solid red curve), from $I_{\mathrm{c}}^{\mathrm{E}}(Q,E)$ for the empty can (solid green curve), and from $I_{\mathrm{s}}(Q,E)$ for the sample after correction for the empty can scattering, attenuation and renormalisation (solid black curve). No correction for multiple scattering or multiple phonon scattering has been applied.

equation (2.25))

$$I_{\mathrm{ms}}(E) = C_{\mathrm{ms}} G_{\mathrm{uncor}}(E) \frac{\langle n(E)+1 \rangle}{E} \,, \tag{5.2}$$

where $G_{\mathrm{uncor}}(E)$ is the density of states calculated without the correction for multiple scattering or multiple phonon scattering and C_{ms} is a constant which is selected by the following method:

1. Choose a value for C_{ms} and calculate $I_{\mathrm{ms}}(E)$ using equation (5.2).
2. Fit $I_{\mathrm{s}}(Q,E)$ to the measured function given by equation (4.7) by varying $B(E)$.
3. Compare the fitted and measured functions by taking integrals over several broad ranges in E and comparing the results (two such integrals are presented in figure 5-8).
4. Change C_{ms} and re-iterate the procedure.
5. The final C_{ms} value corresponds to the case when the measured function oscillates in Q around the fitted function (i.e. the two functions are in the best agreement possible) by eye.

The coherent dynamical structure factor is then $S_{\mathrm{c}}(Q,E) = I_{\mathrm{s}}(Q,E) - I_{\mathrm{ms}}(E)$ (see equation (4.9)). Using equations (2.44) and (2.45) (i.e. the "bronze medal" approximation), the $G(E)$ functions that were calculated for the three samples from $I_{\mathrm{s}}(Q,E)$, $S_{\mathrm{c}}(Q,E)$ or $I_{\mathrm{ms}}(E)$ using the appropriate values from table 5.1 are given in figure 5-9.

5.3.5 Multiple Phonon Correction

To assist in the calculation of the multiple phonon corrections, $G(E)$ was calculated from $S_{\mathrm{c}}(Q,E)$ using equations (2.44) and (2.45) with the appropriate values given in

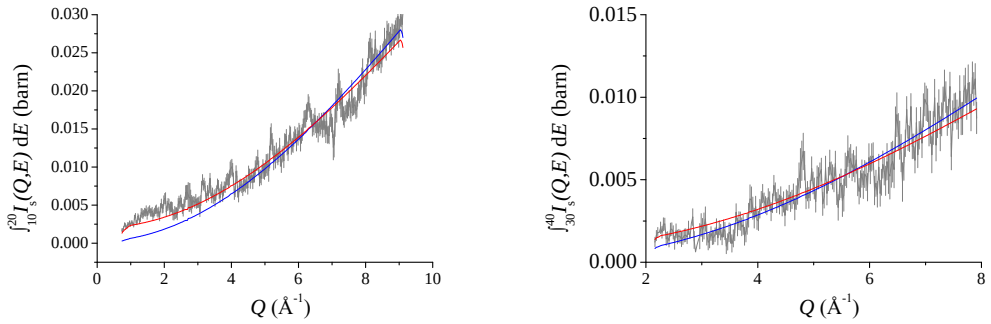

(a) 10 to 20 meV *(b)* 30 to 40 meV

Figure 5-8: $I_s(Q,E)$ for the $^{N}Ge^{N}Se_2$ sample (solid grey curve), an example of a bad fit to the data using $I_s(Q,E) = I_{ms}(E) + B(E)Q^2\exp\left(-2\overline{W}(Q)\right)$ (solid blue curve) and an example of a good fit to the data using $I_s(Q,E) = I_{ms}(E) + B(E)Q^2\exp\left(-2\overline{W}(Q)\right)$ (solid red curve), where $I_{ms}(E)$ is defined by equation (5.2). To improve the statistics, the functions have been integrated over the range of energy transfers from (a) 10 to 20 meV or (b) 30 to 40 meV.

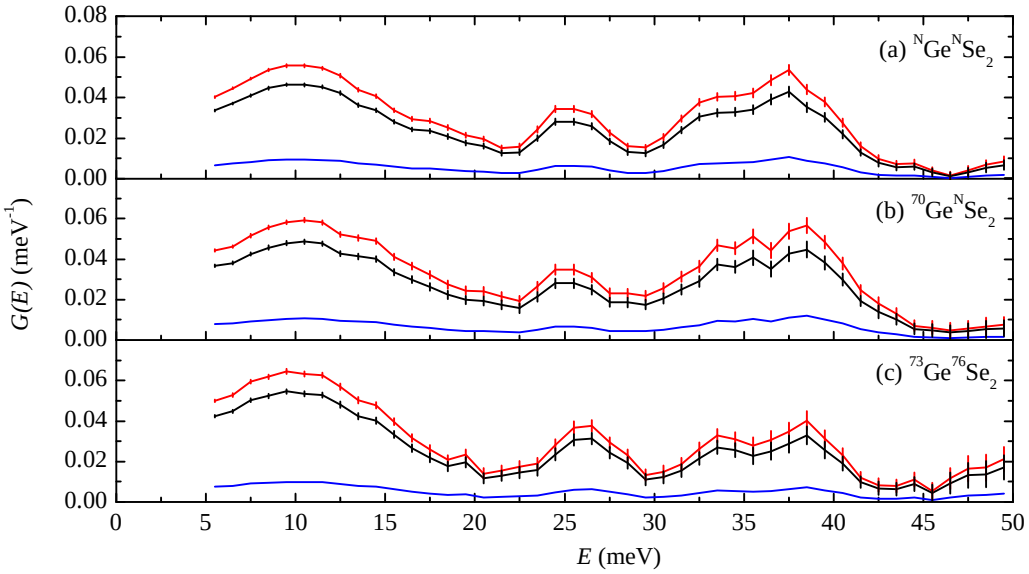

Figure 5-9: $G(E)$ calculated in the "bronze medal" approximation using $I_s(Q,E)$ (solid red curve), $I_{ms}(E)$ (solid blue curve), or $S_c(Q,E) = I_s(Q,E) - I_{ms}(E)$ (solid black curve) and the values given in table 5.1 for samples of (a) $^{N}Ge^{N}Se_2$, (b) $^{70}Ge^{N}Se_2$ and (c) $^{73}Ge^{76}Se_2$.

table 5.1. The Debye model [172] was used in the region which could not be measured (below 5 meV) due to resolution function broadening of the elastic scattered intensity. In the Debye model, $G(E) \propto E^2$ and the constant of proportionality was chosen such that the Debye model coincides with the first measured data point beyond the region of the elastic peak.

The multiple phonon correction, $S_{\mathrm{mp}}(Q,E)$, was then calculated up to the 5^{th} phonon term using the method described in section 4.1.4. The vibrational density of states $G(E)$ without the multiple phonon correction calculated from $S_{\mathrm{c}}(Q,E)$, the multiple phonon contribution to the vibrational density of states $G_{\mathrm{mp}}(E)$, and the single phonon vibrational density of states $G_1(E) = G(E) - G_{\mathrm{mp}}(E)$ are plotted in figure 5-10. The single phonon dynamical structure factor was found by using $S_1(Q,E) =$

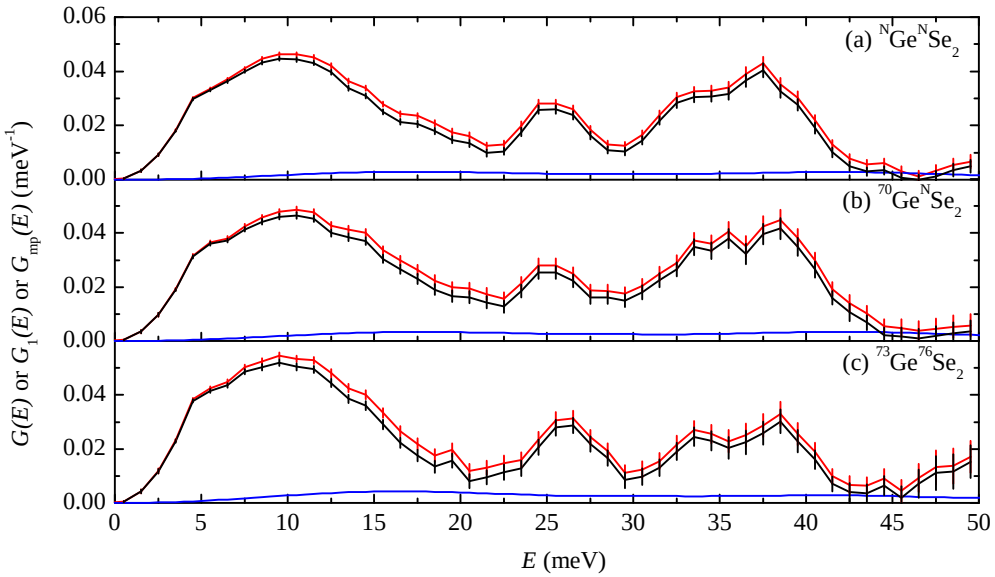

Figure 5-10: $G(E)$ calculated in the "bronze medal" approximation from $S_{\mathrm{c}}(Q,E)$ without the multiple phonon correction (solid red curve), the calculated multiple phonon correction to the vibrational density of states $G_{\mathrm{mp}}(E)$ (solid blue curve) and the single phonon vibrational density of states $G_1(E) = G(E) - G_{\mathrm{mp}}(E)$ (solid black curve) for samples of (a) $^{\mathrm{N}}\mathrm{Ge}^{\mathrm{N}}\mathrm{Se}_2$, (b) $^{70}\mathrm{Ge}^{\mathrm{N}}\mathrm{Se}_2$ and (c) $^{73}\mathrm{Ge}^{76}\mathrm{Se}_2$.

$S_{\mathrm{c}}(Q,E) - S_{\mathrm{mp}}(Q,E)$ (equation (4.22)). An example of the dynamical structure factors thus obtained is given in figure 5-11 for the $^{\mathrm{N}}\mathrm{Ge}^{\mathrm{N}}\mathrm{Se}_2$ sample, where $S_{\mathrm{c}}(Q,E)$, $S_1(Q,E)$ and the calculated $S_{\mathrm{mp}}(Q,E)$ are integrated over two energy transfer ranges of (a) 10 to 20 meV or (b) 30 to 40 meV. In this figure the empty can, attenuation, renormalisation and multiple scattering corrections have all been made.

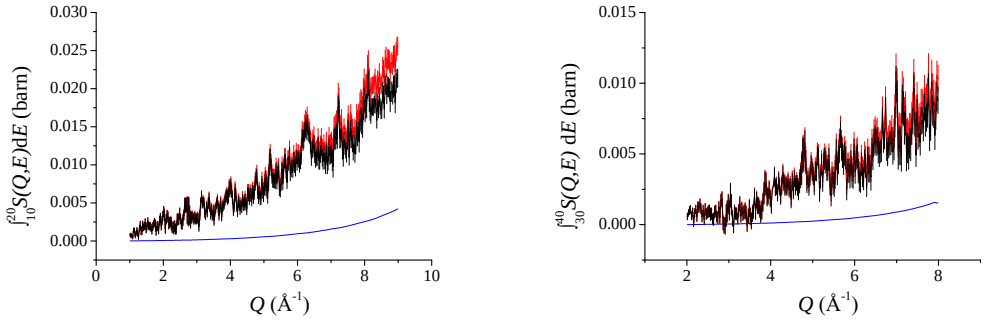

(a) 10 to 20 meV

(b) 30 to 40 meV

Figure 5-11: The $S_c(Q,E)$ function (solid red curve), the multiple phonon contribution $S_{mp}(Q,E)$ (solid blue curve) and the single phonon contribution calculated using $S_1(Q,E) = S_c(Q,E) - S_{mp}(Q,E)$ (solid black curve) for the $^{N}Ge^{N}Se_2$ sample, where each function has been integrated over an energy transfer range of (a) 10 to 20 meV or (b) 30 to 40 meV. In all cases the empty can, attenuation, renormalisation and multiple scattering corrections have been made.

5.4 "Silver Medal" Calculations

Once the data had been fully corrected, the "silver medal" results were calculated. Three different matrices were used as described in section 2.2.4 where, using the values given in table 5.1, for the $^{N}Ge^{N}Se_2$ and $^{70}Ge^{N}Se_2$ samples

$$\begin{pmatrix} S'_{\mathrm{GeGe}}(Q,E) \\ S'_{\mathrm{SeSe}}(Q,E) \end{pmatrix} = \begin{pmatrix} -197.5242 & 197.5242 \\ 350.9115 & -226.6060 \end{pmatrix} \begin{pmatrix} {}^{\mathrm{N}}_{\mathrm{N}}S_1(Q,E) \\ {}^{70}_{\mathrm{N}}S_1(Q,E) \end{pmatrix}, \tag{5.3}$$

for the $^{N}Ge^{N}Se_2$ and $^{73}Ge^{76}Se_2$ samples

$$\begin{pmatrix} S'_{\mathrm{GeGe}}(Q,E) \\ S'_{\mathrm{SeSe}}(Q,E) \end{pmatrix} = \begin{pmatrix} 128.9691 & -53.1341 \\ -23.6519 & 60.9571 \end{pmatrix} \begin{pmatrix} {}^{\mathrm{N}}_{\mathrm{N}}S_1(Q,E) \\ {}^{73}_{76}S_1(Q,E) \end{pmatrix} \tag{5.4}$$

and for the $^{70}Ge^{N}Se_2$ and $^{73}Ge^{76}Se_2$ samples

$$\begin{pmatrix} S'_{\mathrm{GeGe}}(Q,E) \\ S'_{\mathrm{SeSe}}(Q,E) \end{pmatrix} = \begin{pmatrix} 78.0246 & -32.1454 \\ -14.3091 & 57.1079 \end{pmatrix} \begin{pmatrix} {}^{70}_{\mathrm{N}}S_1(Q,E) \\ {}^{73}_{76}S_1(Q,E) \end{pmatrix}. \tag{5.5}$$

In these matrices, ${}^{y}_{x}S_1(Q,E)$ denotes the single phonon total dynamical structure factor, measured for a sample of $^{x}Ge^{y}Se_2$, where x denotes N, 70 or 73 and y denotes N or 76.

Using the method of singular value decomposition (SVD) [173], the following matrix for a set of "silver medal" results was also used, where the data taken from all three

isotopically enriched samples contribute to the final result

$$\begin{pmatrix} S'_{\mathrm{GeGe}}(Q,E) \\ S'_{\mathrm{SeSe}}(Q,E) \end{pmatrix} = \begin{pmatrix} 30.14196 & 59.78915 & -37.05076 \\ 0.457465 & -14.58586 & 57.03347 \end{pmatrix} \begin{pmatrix} {}^{\mathrm{N}}_{\mathrm{N}}S_1(Q,E) \\ {}^{70}_{\mathrm{N}}S_1(Q,E) \\ {}^{73}_{76}S_1(Q,E) \end{pmatrix}. \tag{5.6}$$

The partial vibrational density of states ($G_\alpha(E)$ functions) were calculated using equations (2.38) and (2.39) assuming Debye-Waller factors of $W_{\mathrm{Ge}}(Q) = W_{\mathrm{Se}}(Q) = \overline{W}(Q) = 0.002Q^2$. The results are given in figure 5-12.

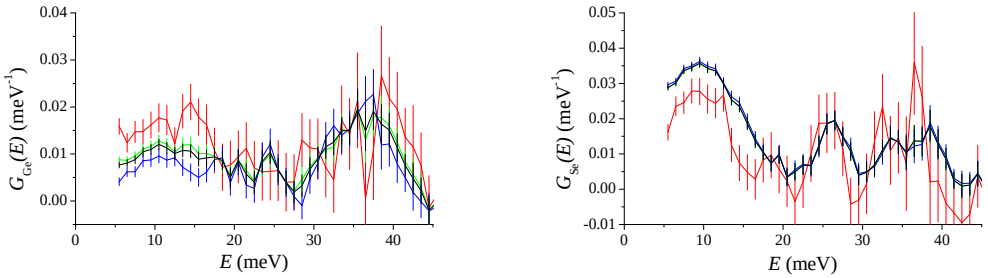

(a) $G_{\mathrm{Ge}}(E)$ *(b)* $G_{\mathrm{Se}}(E)$

Figure 5-12: The results for the partial vibrational density of states obtained by applying the "silver medal" approximation calculated using equation (5.3) (solid red line), equation (5.4) (solid green line), equation (5.5) (solid blue line) and equation (5.6) (solid black line) for (a) $G_{\mathrm{Ge}}(E)$ or (b) $G_{\mathrm{Se}}(E)$.

5.5 Results

5.5.1 Generalised Vibrational Density of States

The generalised single phonon vibrational density of states for each sample $G_1(Q,E)$ and the generalised single phonon partial vibrational density of states $G_\alpha(Q,E)$ were calculated by using equations (2.44) and (2.38), respectively. To improve the statistics, integrals of these functions were taken over three ranges in energy representing the three peaks in $G_1(E)$ (see e.g. figure 5-17). The results for the first peak, from 8 to 18 meV, are shown in figure 5-13, the results for the second peak, from 23 to 28 meV, are shown in figure 5-14, and the results for the third peak, from 32 to 40 meV, are shown in figure 5-15. The generalised vibrational density of states $G_1(Q,E)$ for a sample of ${}^{\mathrm{N}}\mathrm{Ge}^{\mathrm{N}}\mathrm{Se}_2$ and the generalised partial vibrational density of states $G_\alpha(Q,E)$ calculated by Giacomazzi *et al.* from classical MD simulations [34] are also plotted in figures 5-13 to 5-15. The integration ranges chosen for the simulation data are different to those

for the experimental data because there is a relative shift of the peaks in $G_1(E)$ as demonstrated in figure 5-17. Ranges that cover the same peaks were therefore used for the classical MD results, in this case 6 to 16 meV for the first peak, 20 to 25 meV for the second peak and 28 to 34 meV for the third peak.

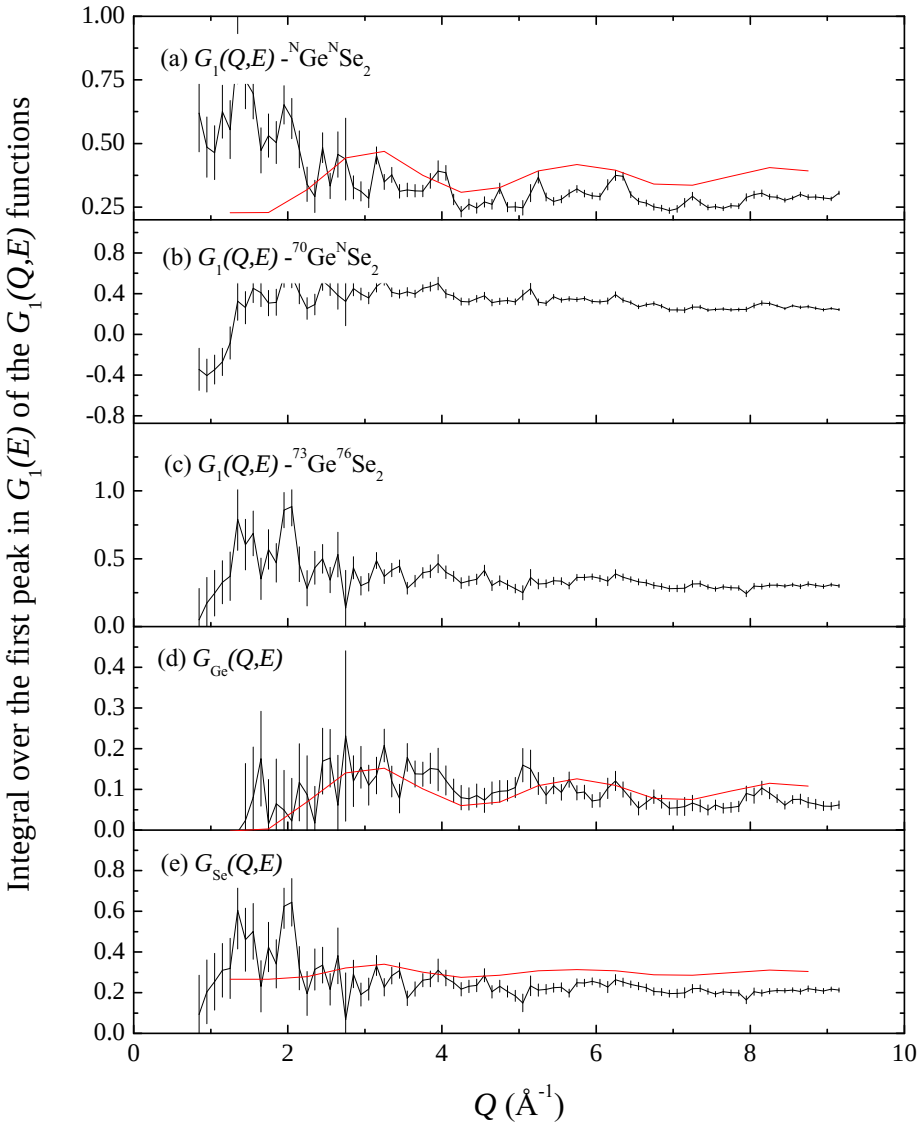

Figure 5-13: The results from the present experimental study (solid black curves) and from the classical MD simulations done by Giacomazzi *et al.* [35], when available, (solid red curves) for the integral of $G_1(Q,E)$ over the first peak in $G_1(E)$ for samples of (a) $^{N}Ge^{N}Se_2$, (b) $^{70}Ge^{N}Se_2$ and (c) $^{73}Ge^{76}Se_2$. Plotted in (d) and (e) are the integrals of $G_{Ge}(Q,E)$ and $G_{Se}(Q,E)$ over the first peak in $G_1(E)$, respectively, calculated in the "silver medal" approximation using the SVD matrix in equation (5.6). The limits for the integrals are given in the text.

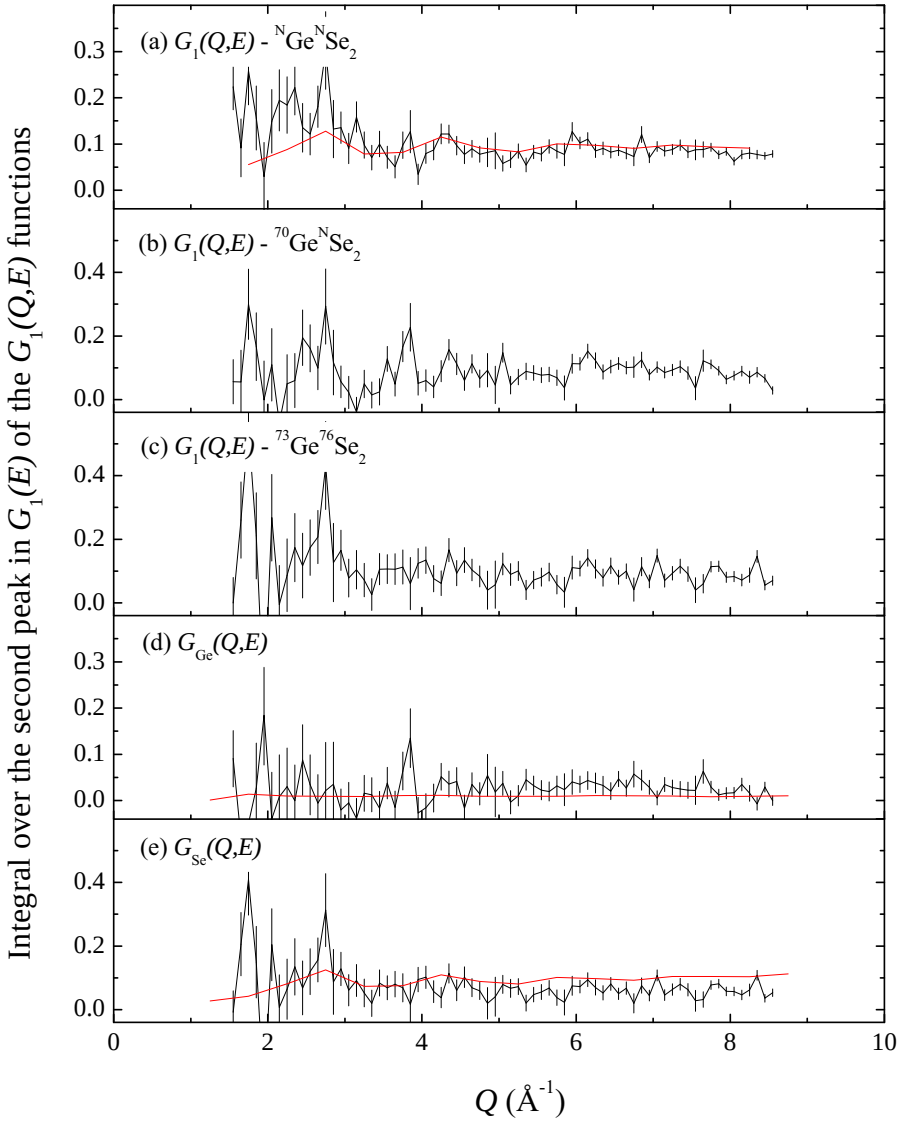

Figure 5-14: The results from the present experimental study (solid black curves) and from the classical MD simulations done by Giacomazzi *et al.* [35], when available, (solid red curves) for the integral of $G_1(Q,E)$ over the second peak in $G_1(E)$ for samples of (a) $^{N}Ge^{N}Se_2$, (b) $^{70}Ge^{N}Se_2$ and (c) $^{73}Ge^{76}Se_2$. Plotted in (d) and (e) are the integrals of $G_{Ge}(Q,E)$ and $G_{Se}(Q,E)$ over the second peak in $G_1(E)$, respectively, calculated in the "silver medal" approximation using the SVD matrix in equation (5.6). The limits for the integrals are given in the text.

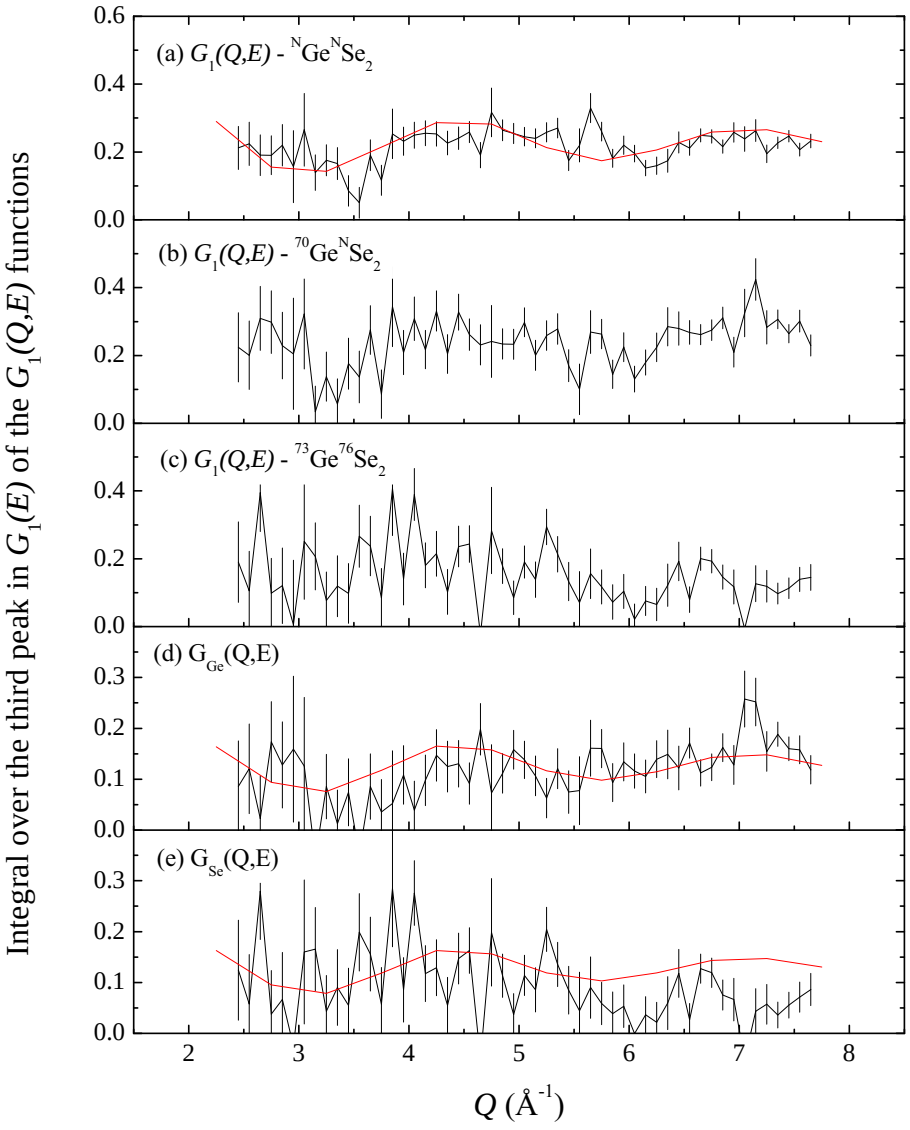

Figure 5-15: The results from the present experimental study (solid black curves) and from the classical MD simulations done by Giacomazzi *et al.* [35], when available, (solid red curves) for the integral of $G_1(Q,E)$ over the third peak in $G_1(E)$ for samples of (a) $^{N}Ge^{N}Se_2$, (b) $^{70}Ge^{N}Se_2$ and (c) $^{73}Ge^{76}Se_2$. Plotted in (d) and (e) are the integrals of $G_{Ge}(Q,E)$ and $G_{Se}(Q,E)$ over the third peak in $G_1(E)$, respectively, calculated in the "silver medal" approximation using the SVD matrix in equation (5.6). The limits for the integrals are given in the text.

5.5.2 Single Phonon Vibrational Density of States

The results in the "bronze medal" approximation for the samples of $^{N}Ge^{N}Se_2$, $^{70}Ge^{N}Se_2$ and $^{73}Ge^{76}Se_2$ are compared in figure 5-16. In figure 5-17 a comparison is made between

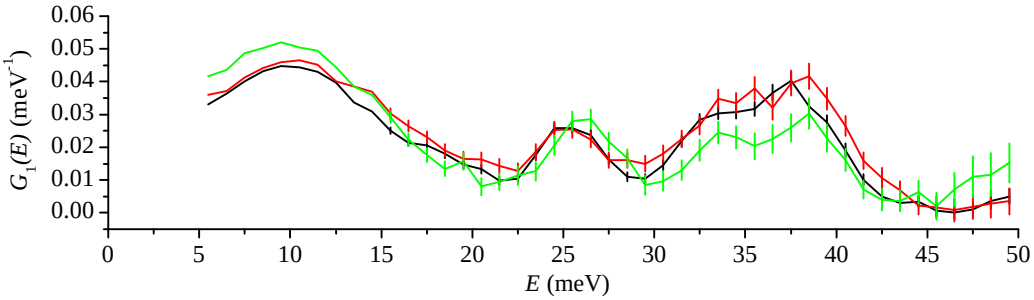

Figure 5-16: The fully corrected single phonon vibrational density of states $G_1(E)$ calculated using the "bronze medal" approximation for samples of $^{N}Ge^{N}Se_2$ (solid black curve), $^{70}Ge^{N}Se_2$ (solid red curve) and $^{73}Ge^{76}Se_2$ (solid green curve).

the $G(E)$ functions calculated for $^{N}Ge^{N}Se_2$ using the "bronze medal" approximation in the present work, the experimental results of Walter *et al.* [51] and Sinclair *et al.* [164], and the classical MD simulation results of Giacomazzi *et al.* [35]. The "silver medal"

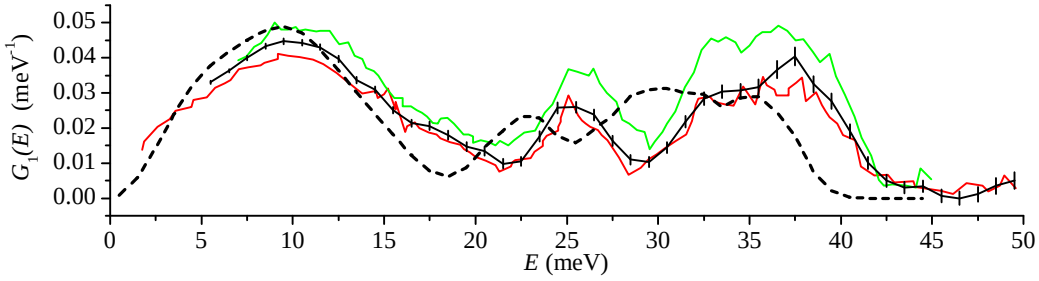

Figure 5-17: The single phonon density of states $G_1(E)$ calculated using the "bronze medal" approximation for a sample of $^{N}Ge^{N}Se_2$ as obtained in the present work (solid black curve), from a study using the LRMECS spectrometer at the Intense Pulsed Neutron Source for a temperature of 13(2) K with an incident neutron energy of 60.06 meV [51] (solid green curve), from a study using the MARI spectrometer for a temperature of 18(1) K and an incident neutron energy of 60 meV [164] (solid red curve) and from the classical MD simulations made by Giacomazzi *et al.* [35] (broken black curve).

results for $G_{Ge}(E)$ and $G_{Se}(E)$, obtained using the SVD method (equation (5.6)), are compared with those calculated from the classical MD simulations of Giacomazzi *et al.* [35] in figure 5-18.

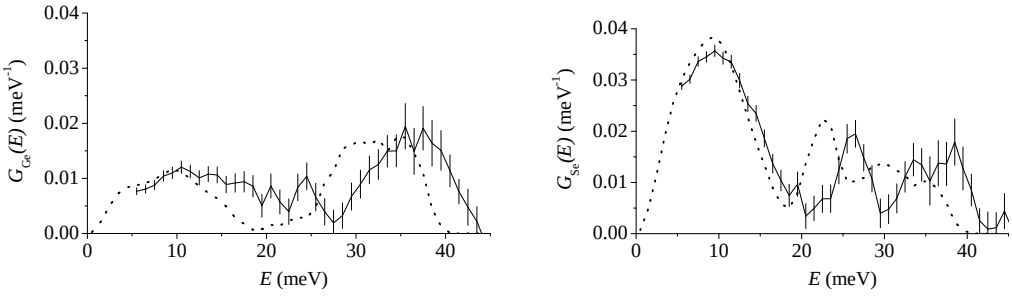

(a) $G_{\mathrm{Ge}}(E)$ *(b)* $G_{\mathrm{Se}}(E)$

Figure 5-18: Comparison of the partial vibrational density of states calculated in the "silver medal" approximation using the SVD matrix (equation 5.6) (solid black curves) with those calculated from the classical MD simulations made by Giacomazzi *et al.* [35] (broken black curves) for (a) $G_{\mathrm{Ge}}(E)$ and (b) $G_{\mathrm{Se}}(E)$.

5.6 Discussion

The subtraction of the measured intensity for the cryostat and empty can proved to be difficult as illustrated in figure 5-7. The Al Bragg peaks do not align in Q between the measurements for the sample-in-can and for the empty can. This results in a poor background subtraction since Al Bragg peaks are still present in $I_{\mathrm{s}}(Q, E)$.

Despite this difficulty, the single phonon vibrational density of states $G_1(E)$, calculated in the extreme incoherent approximation for a sample of $^{\mathrm{N}}\mathrm{Ge}^{\mathrm{N}}\mathrm{Se}_2$ at a temperature of $T = 20(1)$ K measured using the MARI instrument, is in good agreement with a similar experiment done on the same instrument at $T = 18(1)$ K by Sinclair *et al.* [164] and is in broad agreement, within a scaling factor, with the results obtained by Walter *et al.* at $T = 13(2)$ K using the LRMECS instrument [51]. There is a small disagreement in the position of the second peak in $G_1(E)$ at ≈ 25 meV between the measurements presented here (where the peak is at $E = 25.35(15)$ meV) and those made by Walter *et al.* (where the peak is at $E = 25.85(15)$ meV), whereas the value measured by Sinclair *et al.* (where the peak is at $E = 25.31(15)$ meV) is in almost exact agreement. $G_1(E)$ measured by Sinclair *et al.* exhibits the same features but has sharper peaks because the experiment was done using a higher resolution chopper arrangement (a "C" type chopper spinning at a frequency of 450 Hz). There is a small difference in the height of the first peak at ≈ 10 meV. In figure 5-18 the results in the present study are compared to the MD simulations of Giacomazzi *et al.* [35] made using the potentials of Vashishta *et al.* [141, 166]. The main features in the experimental data are reproduced in the simulation data, except for a systematic shift of the peaks in $G_1(E)$ and $G_\alpha(E)$ to lower E as shown in figures 5-17 and 5-18.

The largest scattering length contrast is between the $^{70}\mathrm{Ge}^{\mathrm{N}}\mathrm{Se}_2$ and $^{73}\mathrm{Ge}^{76}\mathrm{Se}_2$ sam-

ples. The isotope ^{76}Se has a significantly higher scattering length (12.2(1) fm) compared to ^{73}Ge (5.09(4) fm) and there is twice as much Se as Ge. Therefore, the scattering from the $^{73}Ge^{76}Se_2$ sample is dominated by scattering from Se atoms such that there is a big contrast between the intensities measured for this sample and the other samples. The "silver medal" results that were obtained by using the measurements made for the $^{70}Ge^{N}Se_2$ and $^{73}Ge^{76}Se_2$ samples (equation (5.4)) and the "silver medal" results obtained by using the SVD matrix (equation (5.6)) are in good agreement.

5.6.1 Validity of the "Silver Medal" Approximation

In the "silver medal" approximation, it is assumed that the cross term $S_{\mathrm{GeSe}}(Q,E)$ is zero. The "gold medal" approximation (where $S_{\mathrm{GeSe}}(Q,E)$ is taken into account) requires very accurate and precise neutron spectroscopy measurements. Due to the complexity of the corrections, stability of the MARI instrument and the very high levels of scattering that arise from the empty can measurement, it was not possible to obtain the "gold medal" result in the present work. However, for $GeSe_2$, the simulations made by Giacomazzi *et al.* [35, 45] have been used to calculate the contribution that $S_{\mathrm{GeSe}}(Q,E)$ makes to the final vibrational density of states, and it is found to be small. Plotted in figure 5-19 are the true partial vibrational density of states $Z_\alpha(E)$ and the vibrational density of states $G_\alpha(E)$ calculated in the "silver medal" approximation obtained from the simulations by Giacomazzi *et al.* [36].

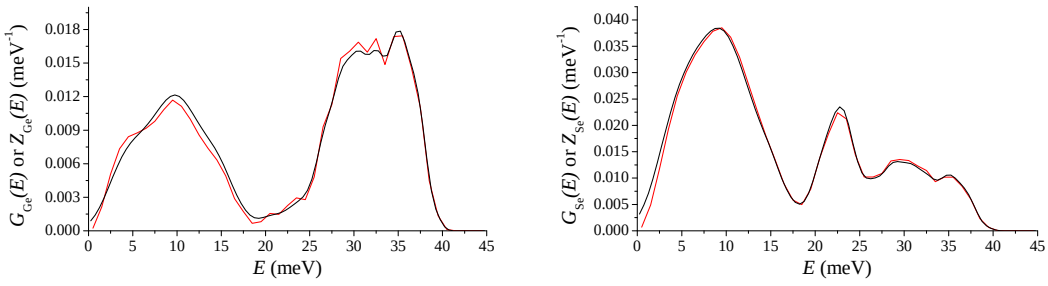

(a) $G_{\mathrm{Ge}}(E)$ or $Z_{\mathrm{Ge}}(E)$ *(b)* $G_{\mathrm{Se}}(E)$ or $Z_{\mathrm{Se}}(E)$

Figure 5-19: The true partial vibrational density of states $Z_\alpha(E)$ (solid black curve) and "silver medal" vibrational density of states $G_\alpha(E)$ at a temperature of 5 K (solid red curve) calculated from the MD simulations made by Giacomazzi *et al.* [36].

The quality of the measurements made using the MARI spectrometer is limited by the incident flux and detector coverage. The result is that the $G_{\mathrm{Ge}}(E)$ and $G_{\mathrm{Se}}(E)$ functions that have been calculated from these measurements have a large statistical error. It would therefore be advantageous to use a neutron spectrometer which gives

an increased count rate.

5.7 Conclusion

The single phonon partial vibrational density of states of a glass has been measured for the first time within the "silver medal" approximation using the method of isotope substitution in neutron spectroscopy, albeit with a high statistical error. This was achieved by measuring the total dynamical structure factors $S_c(Q, E)$ for samples of $^{\mathrm{N}}\mathrm{Ge}^{\mathrm{N}}\mathrm{Se}_2$, $^{70}\mathrm{Ge}^{\mathrm{N}}\mathrm{Se}_2$ and $^{73}\mathrm{Ge}^{76}\mathrm{Se}_2$. A data analysis procedure was devised to subtract the empty can scattering, normalise the data and correct for multiple scattering. The corrections for the multiple phonon scattering described in section 4.1.4 were successfully applied to the low temperature regime.

The measured single phonon vibrational density of states in the "bronze medal" approximation for the $^{\mathrm{N}}\mathrm{Ge}^{\mathrm{N}}\mathrm{Se}_2$ sample is in good agreement with the results obtained from refs. [51, 130, 164]. Both the "bronze medal" and "silver medal" results are in agreement, within the statistical error and a shift in E, with the classical MD simulations made by Giacomazzi *et al.* [35] made using the potentials of Vashishta *et al.* [141, 166].

All of this demonstrates that the method of isotopic substitution in neutron spectroscopy is a plausible way to measure the partial vibrational density of states of a glass to compare with e.g. classical MD simulations. However, an experiment with smaller statistical errors and better background subtraction is required. Further experiments using the MERLIN spectrometer were therefore undertaken to address these issues. These experiments are described in chapter 6.

6. Vibrational Density of States of $GeSe_2$ Glass Using the MERLIN Spectrometer

6.1 Introduction

In chapter 5, the method of isotopic substitution in neutron spectroscopy was used to calculate the partial vibrational density of states for $GeSe_2$ glass using the MARI spectrometer. The measurements were limited by a large statistical error and poor subtraction of scattering from the can and sample environment. In this chapter, measurements made on the MERLIN spectrometer are presented that complement and extend those made using MARI.

The MERLIN spectrometer (see section 3.2.1) has a gain in detected neutron flux of around 35 over the MARI spectrometer depending on the scattering angle and incident energy. Therefore, the spectra measured using the MERLIN spectrometer have a much lower statistical error. The geometry of the sample loading means that a self supporting, rigid sample can is not necessary. Instead, a thin foil packet can be suspended from a candlestick. This reduces scattering from the empty can. The gain in flux and measurement precision comes at the cost of resolution; the resolution in Q and E of the MERLIN spectrometer is worse than that of MARI by around 20 %.

The Debye-Waller factor is an important parameter used in calculating the density of states and, while some measurements have been made [51, 174], new measurements were needed. One approach is to measure the elastic scattering and compare it to the total scattering from a diffraction experiment. In order to achieve this, an experiment (herein referred to as experiment 1) was made using an incident beam of neutrons with an energy of 29.9 meV. Measurements were made using a sample of $^{N}Ge^{N}Se_2$ at temperatures between 10 and 280 K. By using a lower incident energy, better energy resolution around the elastic line at $E = 0$ was achieved and so the elastic scattering was more precisely measured.

Two other experiments (herein referred to as experiments 2 and 3) were made using samples of $^{N}Ge^{N}Se_2$, $^{70}Ge^{N}Se_2$ and $^{73}Ge^{76}Se_2$ and an incident beam of neutrons with an energy of ≈ 60 meV. These experiments were made with the sample held at a low temperature of 5 K or at room temperature, respectively.

This chapter is organised as follows. In section 6.2 the experimental method for all three experiments is presented. In section 6.3 the correction procedure is given for the first experiment and the Debye-Waller factor as a function of temperature is measured. In section 6.4, the corrections for experiments 2 and 3 are shown, where at each stage the total vibrational density of states $G(E)$ is calculated within the extreme incoherent ("bronze medal") approximation and the results are presented before and after each correction to show its effect. In section 6.6, the results found in the present study are compared to those obtained from the experiments done using the MARI spectrometer (see chapter 5) and the Molecular Dynamics (MD) simulations made by Giacomazzi *et al.* [35]. The results are discussed in section 6.7 and conclusions are drawn in section 6.8.

6.2 Experimental Method

All of the measurements were made on the MERLIN spectrometer at the ISIS Pulsed Neutron Source in Didcot (see section 3.2.1) using the samples of $^{N}Ge^{N}Se_2$, $^{70}Ge^{N}Se_2$ and $^{73}Ge^{76}Se_2$ described in section 5.2.1. The samples were loaded into packets of aluminium foil (≈ 0.013 mm thickness) in a helium filled glovebox. Each loaded packet was put into an aluminium foil can and rolled around a solid cylinder to form an approximately annular sample shape of diameter ≈ 40 mm. The can was then fixed using Al tape to the bottom of a boron-nitride disk and the tape covered with cadmium to shield it from neutrons (figure 6-1). The assembly was lowered into the instrument on the end of a shielded aluminium "candlestick". The beam profile was square with dimensions of 50 mm wide by 40 mm high centred on the foil packet such that the sample area was fully illuminated.

Three experiments, described in detail below, were done using the instrument configurations that are summarised in table 6.1. In all of the experiments, a "sloppy" type Fermi chopper was used. This transmits a high intensity of neutrons with low energy resolution and selects an almost monochromatic incident beam of neutrons centred on the chosen incident energy. For this configuration, the MCHOP software [168] was used to give the estimated incident neutron flux and full width at half maximum (FWHM) in energy of the elastic line (see table 6.1). The values obtained from MCHOP were calculated for a different instrument (HET) and then adjusted for MERLIN by multiplying by a factor of 1.2, which is the estimated difference in resolution and incident flux between the two instruments.

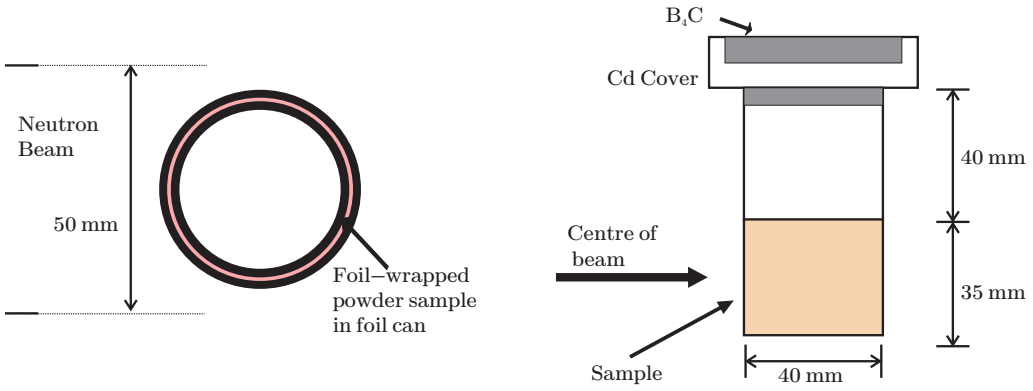

Figure 6-1: (a) Top view and (b) side view of the sample in an Al foil packet loaded into the middle of an Al foil can of 0.013(1) mm thickness, attached to the bottom of a neutron absorbing B_4C block.

	Experiment 1	Experiment 2	Experiment 3
Incident energy (meV)	29.9 (1)	59.5(1)	59.9(1)
Temperature (K)	Various	5	RT (292 K)
Fermi chopper freq. (Hz)	200	300	300
Est. incident flux (n s^{-1})	79930	86025	86025
FWHM of elastic line (meV)	1.59	3.65	3.65

Table 6.1: Instrument configurations for the MERLIN spectrometer used in three different experiments. RT stands for room temperature, taken to be 292 K. The FWHM of the elastic line and incident flux were estimated using the MCHOP software [168].

6.2.1 Neutron Spectroscopy Experiment 1

In the first experiment, an almost monochromatic incident beam of neutrons centred on an energy 29.9(1) meV and a Fermi chopper frequency of 200 Hz were used. The energy resolution and detector coverage for the MERLIN instrument under these conditions is given in figure 6-2. A $^{\mathrm{N}}\mathrm{Ge}^{\mathrm{N}}\mathrm{Se}_2$ sample of mass 4.607(1) g was loaded as described above, the candlestick was lowered into a fixed CCR in the neutron beam and the CCR was purged three times with He gas. A pressure of 23 mbar of He gas was let into the cryostat for heat exchange with the sample. Measurements were made at a

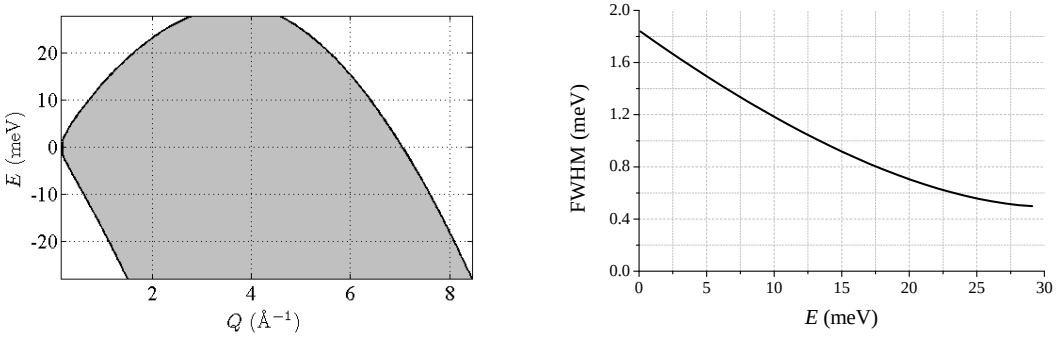

(a) *(b)*

Figure 6-2: (a) The kinematically allowed region and (b) the energy resolution full width at half maximum (FWHM) calculated using the MCHOP program [168] for experiment 1 done using the MERLIN spectrometer using an incident energy of 29.9(1) meV and Fermi chopper frequency of 200 Hz. In (a) the accessible Q-E space is shaded in grey.

series of temperatures. The measurements began while the sample temperature was still approaching the equilibrium temperature but this occurred quickly. The maximum, minimum and mean temperatures recorded at the sample position for each measurement are given in table 6.2. A series of empty foil can measurements were made under the same conditions. Each measurement was made for a period of time ($\approx$ 1 h) until a proton charge of 150 μA h was reached. A vanadium sample was measured at room temperature under the same conditions for absolute normalisation.

6.2.2 Neutron Spectroscopy Experiments 2 and 3

In experiment 2, for each measurement the candlestick was lowered into a CCR in the neutron beam and the CCR was purged three times with He gas. A pressure of 30 mbar of He gas was let into the CCR for heat exchange with the sample. The sample was then cooled to a temperature of 5 K. In the case of experiment 3, the CCR was completely removed to reduce scattering from sources other than the sample and

Nominal T (K)	Mean T (K)	Minimum T (K)	Maximum T (K)
10	11(1)	11(1)	11(1)
50	49(1)	49(1)	57(1)
100	98(1)	94(1)	117(1)
150	146(1)	141(1)	166(1)
200	194(1)	189(1)	214(1)
250	239(1)	236(1)	254(1)
280	278(1)	278(1)	280(1)

Table 6.2: The mean, minimum and maximum temperature (T) near the sample position for each of the measurements made in experiment 1.

measurements were taken under vacuum at room temperature. The temperature at the sample position was not measured directly but it is taken to be 292 K, as measured for the surroundings by placing a thermocouple on the top flange of the candlestick holder.

A Fermi chopper frequency of 300 Hz was used to select an almost monochromatic incident beam of neutrons centred on an energy 59.5(5) meV for experiment 1 and 59.9(5) meV for experiment 2. The energy resolution and the detector coverage of the MERLIN spectrometer for an incident energy of 60 meV is shown in 6-3.

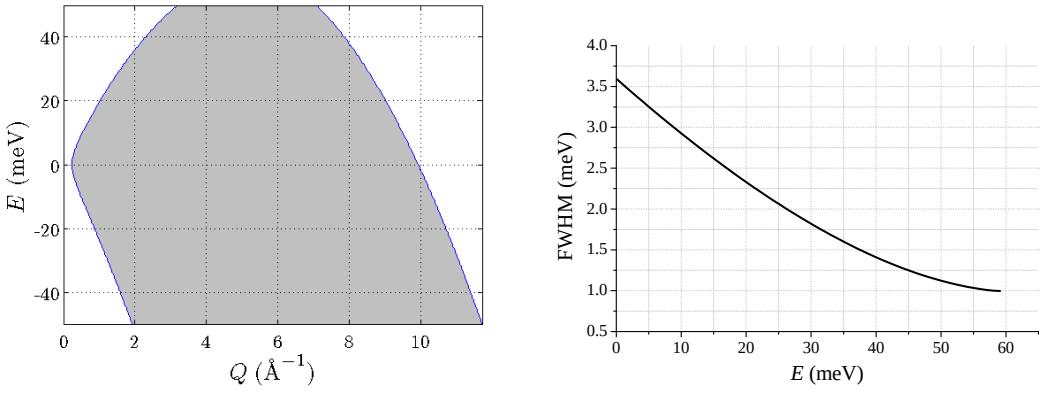

Figure 6-3: (a) The kinematically allowed region and (b) the energy resolution full width at half maximum (FWHM) calculated using the MCHOP program [168] for experiments 2 and 3 done using the MERLIN spectrometer with an incident energy of ≈ 60 meV and Fermi chopper frequency of 300 Hz. In (a) the accessible Q-E space is shaded in grey.

In both experiments four measurements were made under identical conditions, summarised in table 6.3. The intensities were measured for samples of $^{\mathrm{N}}\mathrm{Ge}^{\mathrm{N}}\mathrm{Se}_2$, $^{70}\mathrm{Ge}^{\mathrm{N}}\mathrm{Se}_2$ and $^{73}\mathrm{Ge}^{76}\mathrm{Se}_2$ in an aluminium foil packet in an Al foil can and an empty aluminium foil packet in an Al foil can. Two further measurements were made for each experiment using a solid annular vanadium sample at room temperature for detector calibration and

absolute normalisation; one under identical conditions to the sample measurements and one using an incident beam containing a wide range of neutron energies (i.e. a so-called white beam).

Sample	Sample Mass (g)	Proton Charge (μA h)
Experiment 2 (Low Temperature)		
$^{\mathrm{N}}\mathrm{Ge}^{\mathrm{N}}\mathrm{Se}_2$	4.607(1)	3175.78
$^{70}\mathrm{Ge}^{\mathrm{N}}\mathrm{Se}_2$	2.019(1)	3091.68
$^{73}\mathrm{Ge}^{76}\mathrm{Se}_2$	1.958(1)	3245.9
Empty Can	N/A	3453.826
Experiment 3 (Room Temperature)		
$^{\mathrm{N}}\mathrm{Ge}^{\mathrm{N}}\mathrm{Se}_2$	4.6310(1)	3009.2
$^{70}\mathrm{Ge}^{\mathrm{N}}\mathrm{Se}_2$	2.065(1)	2841.6
$^{73}\mathrm{Ge}^{76}\mathrm{Se}_2$	1.972(1)	3241.0
Empty Can	N/A	1925.5

Table 6.3: The mass of sample used together with the charge of protons that was incident on the spallation target during each measurement. The latter is proportional to the number of neutrons that were incident on the sample during that measurement.

6.3 The Debye-Waller Factor and Temperature Dependence of the Vibrational Density of States

The Debye-Waller factor was found from the measurements made during experiment 1 using an incident neutron energy of 29.9(1) meV. In these measurements, the resolution broadened elastic peak is sharper than for measurements made at the higher incident energy and thus there is a lower contribution from inelastic scattering under this peak. While the full vibrational density of states could not be obtained, the temperature dependence of the uncorrected first peak is given.

6.3.1 Width of the Elastic Line

The elastic line resolution broadening is described in section 5.3.1. Figure 6-4 shows, for the vanadium sample, the broadening of the elastic line due to the effect of the energy resolution of the instrument for an incident neutron energy of 29.9(1) meV. A range of $-4 \leq E \leq 4$ meV was selected by eye to define the extent of the elastic line where the limits are shown in figure 6-4 as dotted lines. An assumption was made

that all of the scattering inside this range is elastic such that an integral over this peak represents the elastic differential scattering cross section.

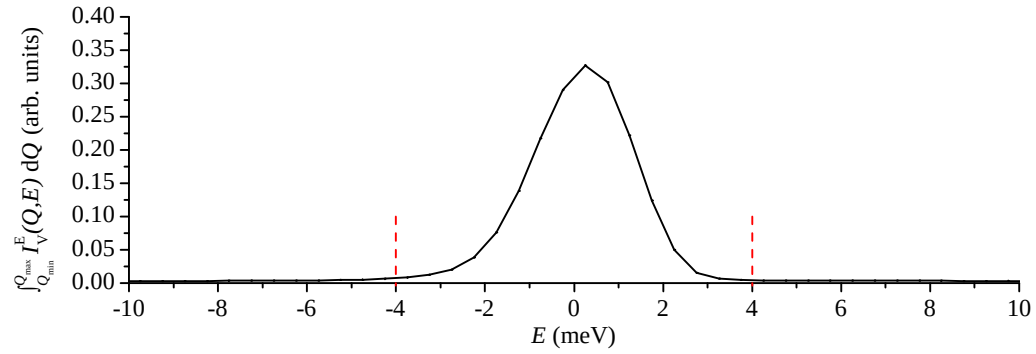

Figure 6-4: The width of the elastic peak due to energy resolution broadening from the monochromatic vanadium represented by $\int_{Q_{\min}}^{Q_{\max}} I_{\mathrm{V}}^{\mathrm{E}}(Q,E)\,\mathrm{d}Q$, where for each value of E, $Q_{\min}$ and $Q_{\max}$ are the minimum and maximum Q values that can be measured. Dotted lines indicate the energy transfer range for which the measured intensity is mostly elastic. Data have been normalised such that the integral under the curve is unity.

6.3.2 Bose-Einstein Occupation Factors

The Bose-Einstein occupation factors were calculated using equation (2.14) for the mean temperatures used in the experiment and are given in figure 6-5.

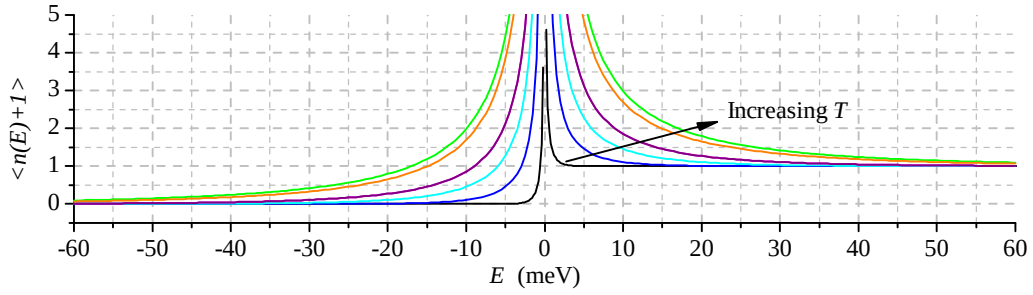

Figure 6-5: The Bose-Einstein occupation factors calculated from the mean temperatures given in table 6.2 using equation 2.14 where the nominal temperatures are 10 K (black), 50 K (dark blue), 100 K (cyan), 150 K (purple), 200 K (orange) and 280 K (green).

6.3.3 Background Subtraction with Attenuation Correction and Renormalisation

The normalised sample-in-can scattered intensity $I_{\mathrm{sc}}^{\mathrm{E}}(Q,E)$ and empty can scattered intensity $I_{\mathrm{c}}^{\mathrm{E}}(Q,E)$ were measured at each temperature. The scattered intensity $I_{\mathrm{s}}(Q,E)$

was found by using equation (4.6) which, for convenience is re-written here:

$$I_{\mathrm{s}}(Q,E) = \frac{m}{A_{\mathrm{sc,sc}}(Q,E)} \left(I_{\mathrm{sc}}^{\mathrm{E}}(Q,E) - I_{\mathrm{c}}^{\mathrm{E}}(Q,E) \right) , \tag{6.1}$$

where m is a renormalisation constant and $A_{\mathrm{sc,sc}}(Q,E)$ is the attenuation coefficient (figure 6-6) found by treating the sample-in-can as a single annular sample with an effective inner radius of 1.9531 cm, outer radius of 2 cm, effective number density of 0.0321 Å^{-3}, effective total scattering cross section of 6.33(31) barn and effective absorption cross section of 6.0(1) barn.

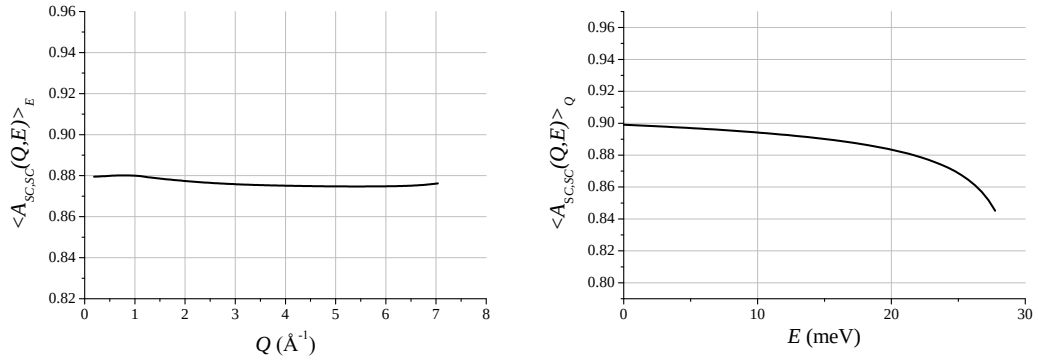

(a) Q Dependence *(b) E Dependence*

Figure 6-6: The attenuation coefficients $A_{\mathrm{sc,sc}}(Q,E)$ calculated for a sample of $^{\mathrm{N}}\mathrm{Ge}^{\mathrm{N}}\mathrm{Se}_2$ averaged (a) over energies between 0 and 25 meV and (b) over all Q values.

At low Q, the effect of the Debye-Waller factor is small and $\mathrm{d}\sigma/\mathrm{d}\Omega|_{\mathrm{el}} \approx \mathrm{d}\sigma/\mathrm{d}\Omega$. Therefore, m was chosen by eye such that the first and second peaks in $\mathrm{d}\sigma/\mathrm{d}\Omega|_{\mathrm{el}} = \int_{E_{\mathrm{min}}}^{E_{\mathrm{max}}} I_{\mathrm{s}}(Q,E)\mathrm{d}E$ at $Q \approx 1$ Å^{-1} and $Q \approx 2$ Å^{-1}, where E_{min} and E_{max} are -4 and 4 meV, respectively, agreed with $\mathrm{d}\sigma/\mathrm{d}\Omega$ from a diffraction experiment made on the D4C diffractometer at the Institut Laue-Langevin (ILL) by Salmon *et al.* [136]. The value of m thus obtained was 0.92 for every measurement. The $\mathrm{d}\sigma/\mathrm{d}\Omega|_{\mathrm{el}}$ functions obtained using $I_{\mathrm{sc}}^{\mathrm{E}}(Q,E)$ for the sample-in-can, $I_{\mathrm{c}}^{\mathrm{E}}(Q,E)$ for the empty can and $I_{\mathrm{s}}(Q,E)$ for the corrected sample scattering are presented for the 5 K measurement in figure 6-7.

6.3.4 Multiple Scattering and Multiple Phonon Scattering Corrections

In the case of the measurements made in experiment 1, the multiple scattering correction could not be applied effectively because there is a large statistical error. The multiple phonon correction could not be applied effectively because it requires that $G(E)$ is measured over its entire energy range.

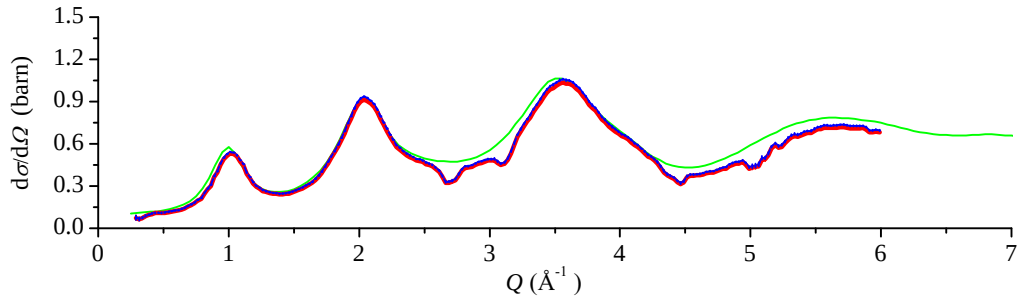

Figure 6-7: The elastic differential scattering cross section $\mathrm{d}\sigma/\mathrm{d}\Omega|_{\mathrm{el}}$ for a sample of $^{\mathrm{N}}\mathrm{Ge}^{\mathrm{N}}\mathrm{Se}_2$ calculated for the sample-in-can $\int_{E_{\min}}^{E_{\max}} I_{\mathrm{sc}}^{\mathrm{E}}(Q,E)\mathrm{d}E$ (solid red curve), the empty can $\int_{E_{\min}}^{E_{\max}} I_{\mathrm{c}}^{\mathrm{E}}(Q,E)\mathrm{d}E$ (solid blue curve) and the corrected sample $\int_{E_{\min}}^{E_{\max}} I_{\mathrm{s}}(Q,E)\mathrm{d}E$ (solid black curve) intensities, where $E_{\min}$ and $E_{\max}$ are -4 and 4 meV, respectively. The datasets are compared to the total differential scattering cross section $\mathrm{d}\sigma/\mathrm{d}\Omega$ from the diffraction experiment by Salmon *et al.* [175] where $\mathrm{d}\sigma/\mathrm{d}\Omega = F(Q) + \sigma_{\mathrm{self}}/4\pi$ (solid green curve).

6.3.5 Calculating The Debye-Waller Factors

In equation (2.62) the $F(Q)$ function corrected for self scattering can be written as

$$F(Q) = \left.\frac{\mathrm{d}\sigma}{\mathrm{d}\Omega}\right|_{\mathrm{el}} - e^{-2\overline{W}(Q)} \sum_{\alpha=1}^{n} c_\alpha(\bar{b}_\alpha^2 + b_{\mathrm{inc},\alpha}^2) \;, \tag{6.2}$$

where $\sum_{\alpha=1}^{n} c_\alpha(\bar{b}_\alpha^2 + b_{\mathrm{inc},\alpha}^2) = 0.6705$ barn is the self scattering limit. $\overline{W}(Q)$ was chosen for each measurement such that $F(Q)$ found by this method and $F(Q)$ from the diffraction experiment made by Salmon *et al.* [136] are in as close agreement as possible at all Q values (see figure 6-8). The values of $2\overline{W}(Q)/Q^2 = \langle u^2 \rangle /3$ thus obtained as a function of temperature are given in table 6.4 and are plotted in figure 6-9 alongside the values obtained from the MD simulations made by Giacomazzi *et al.* [34].

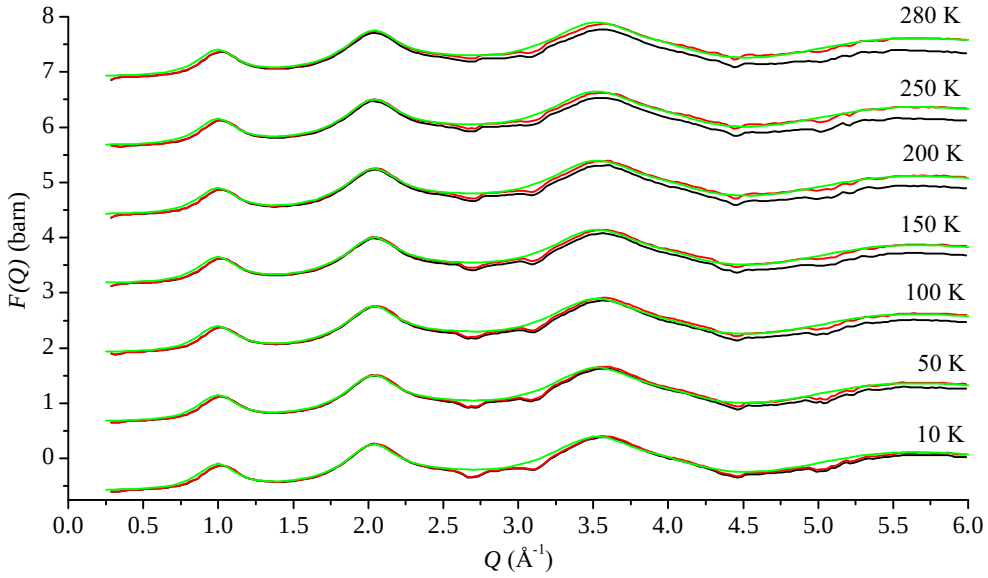

Figure 6-8: The $F(Q)$ functions calculated for $^{\mathrm{N}}\mathrm{Ge}^{\mathrm{N}}\mathrm{Se}_2$ using $F(Q) = \int_{E_{\min}}^{E_{\max}} I_{\mathrm{s}}(Q,E)\mathrm{d}E - \sum_{\alpha}^{n} c_{\alpha}(\bar{b}_{\alpha}^2 + b_{\mathrm{inc},\alpha}^2)$ (solid black curve), $F(Q) = \int_{E_{\min}}^{E_{\max}} I_{\mathrm{s}}(Q,E)\mathrm{d}E - \sum_{\alpha}^{n} c_{\alpha}(\bar{b}_{\alpha}^2 + b_{\mathrm{inc},\alpha}^2)\exp\left(-2\overline{W}(Q)\right)$ (solid red curve) and from the diffraction experiment by Salmon *et al.* [136] (solid green curve), where $E_{\min}$ and $E_{\max}$ are -4 and 4 meV, respectively, while $\overline{W}(Q) = Q^2\left\langle u^2\right\rangle/3$ with $\left\langle u^2\right\rangle/3$ values given in table 6.4. For temperatures greater than 10 K, each successive plot is displaced vertically by 1.25 barn. The mean temperature of the sample for each measurement is given in table 6.4.

Nominal T (K)	Actual T (K)	$\left\langle u^2\right\rangle/3$ (Å^2)
10	11(1)	0.002(1)
50	49(1)	0.004(1)
100	98(1)	0.006(1)
150	146(1)	0.008(1)
200	194(1)	0.010(1)
250	239(1)	0.0115(20)
280	278(1)	0.0125(20)

Table 6.4: The mean square displacement found by comparing the elastic scattering from experiment 1 with diffraction data from Salmon *et al.* [136]. The errors are estimated from the lowest and highest mean squared displacements for which a good fit can still be achieved between the $F(Q)$ functions found from the elastic scattering and from the diffraction experiment by Salmon *et al.* [136].

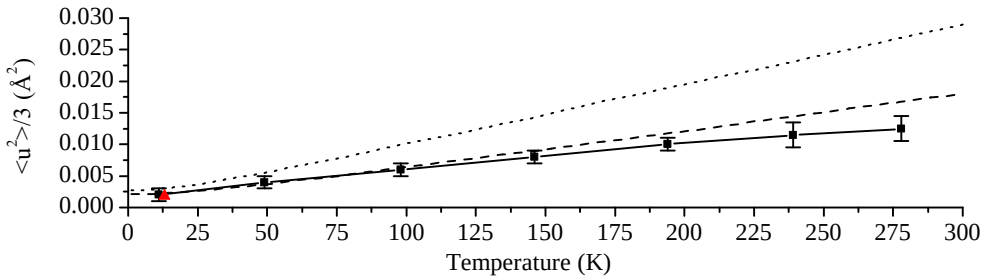

Figure 6-9: Temperature dependence of the mean square displacement $\langle u^2 \rangle /3$ found from experiment 1 (joined closed squares), from a similar experiment by Walter *et al.* [51] (red triangle) or the value for Ge (dashed line) and Se (dotted line) from simulations by Giacomazzi [34].

Total Vibrational Density of States

An "uncorrected" total vibrational density of states in the "bronze medal" approximation (figure 6-10) was calculated from $I_s(Q, E)$ by using equations (2.44) and (2.45).

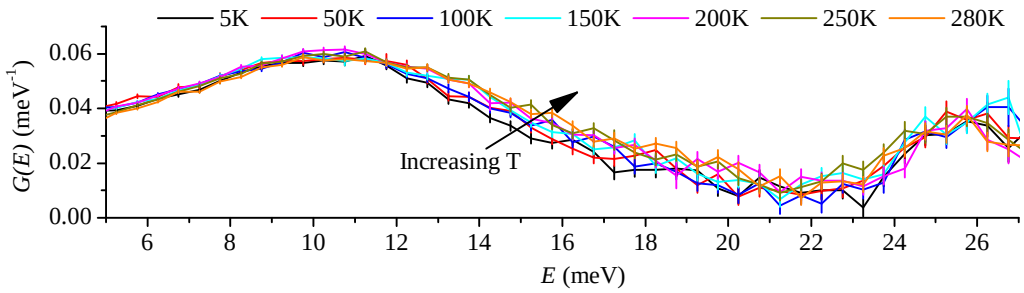

Figure 6-10: The uncorrected $G(E)$ functions calculated for the indicated nominal temperatures in the "bronze medal" approximation for $^{N}Ge^{N}Se_2$ using measurements made at an incident energy of 29.9(1) meV with the MERLIN spectrometer. No multiple scattering or multiple phonon corrections were made.

6.4 The Full Vibrational Density of States of $GeSe_2$

The data taken in experiments 2 and 3 using an incident neutron energy of ≈ 60 meV were used to find the vibrational density of states of GeO_2 at two different temperatures, namely 5 K and room temperature (292 K). The data analysis procedure for these experiments followed the general correction procedure described in section 4.1. The Debye-Waller factors were calculated using the closest values taken from table 6.4 such that $\langle u^2 \rangle /3 = 0.002$ and $\langle u^2 \rangle /3 = 0.0125$ Å^2 for experiments 2 and 3, respectively.

6.4.1 Width of the Elastic Line

The width of the elastic line is discussed in section 5.3.1. Figure 6-11a shows, for a monochromatic vanadium sample, the broadening of the elastic line due to the effect of the energy resolution of the instrument. A range of $-8 \leq E \leq 7$ meV was selected by eye to define the extent of the elastic line where the limits are shown in figure 6-11a as dotted lines. Outside of this range, scattering was deemed to be fully inelastic.

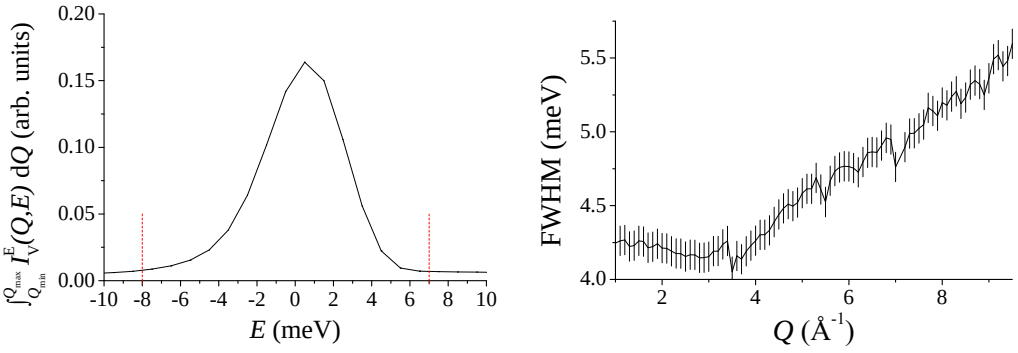

(a) *(b)*

Figure 6-11: (a) The width due to energy resolution broadening of the elastic peak from the monochromatic vanadium represented by $\int_{Q_{\min}}^{Q_{\max}} I_{\mathrm{V}}^{\mathrm{E}}(Q,E)\,\mathrm{d}Q$, where for each value of E, $Q_{\min}$ and $Q_{\max}$ are the minimum and maximum Q values that can be measured. Dotted lines indicate the energy transfer range for which the measured intensity is mostly elastic. Data have been normalised such that the integral under the curve is unity. (b) The Q dependence of the FWHM of the elastic line (E.L.) found empirically from the monochromatic vanadium measurement.

The range over which the elastic line is broadened is dependent on Q. The FWHM of the elastic line found empirically using the monochromatic vanadium measurement are shown in figure 7-8b. The FWHM increases from 4.25(10) to 5.60(10) meV over the range in Q from 1 to 9.5 $\mathrm{Å}^{-1}$. These values differ significantly from the value of 3.65 meV estimated using the MCHOP software [168], where the latter value was found by taking the value for the HET instrument and multiplying it by 1.2.

6.4.2 Bose-Einstein Occupation Factors

The Bose-Einstein occupation factors were calculated using equation (2.14) for the experimental temperatures of 5 and 292 K and are given in figure 6-12.

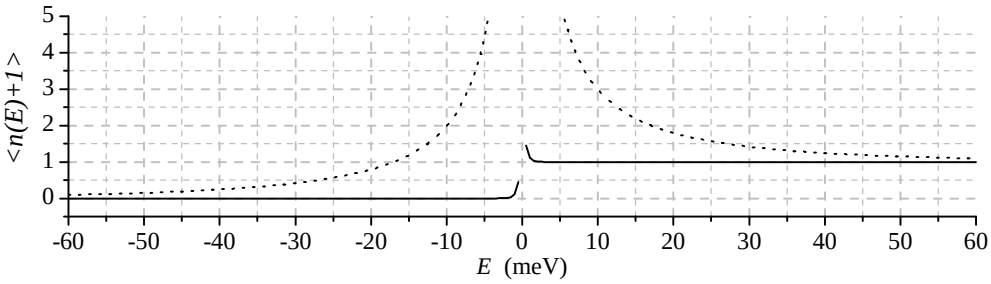

Figure 6-12: The Bose-Einstein occupation factors calculated using equation 2.14 for the sample measurements at temperatures of 5 K (solid curve) and 292 K (broken curve).

6.4.3 Background Subtraction with Attenuation Corrections and Renormalisation

The normalised sample-in-can scattered intensity $I_{\rm sc}^{\rm E}(Q,E)$ and empty can scattered intensity $I_{\rm c}^{\rm E}(Q,E)$ were measured for each sample. The sample scattered intensity $I_{\rm s}(Q,E)$ was found by using equation (6.1), where the attenuation coefficients $A_{\rm sc,sc}(Q,E)$ (figure 6-13) were found by treating the sample-in-can as a single annular sample with effective parameters given in table 6.5. The renormalisation constant m for the measurements on $^{\rm N}Ge^{\rm N}Se_2$, $^{70}Ge^{\rm N}Se_2$ and $^{73}Ge^{76}Se_2$ was found to be 0.90, 0.80 and 1.08 for experiment 2, and 1.09, 0.93 and 1.09 for experiment 3, respectively. In figure 6-

	$^{\rm N}Ge^{\rm N}Se_2$	$^{70}Ge^{\rm N}Se_2$	$^{73}Ge^{76}Se_2$
Experiment 2 (Low Temperature)			
Inner Radius (cm)	1.9450	1.9729	1.9732
Outer Radius (cm)	2	2	2
Eff. Number Density ($Å^{-3}$)	0.0368	0.0433	0.0434
Eff. Total Scattering Cross Section (barn)	6.33(3)	5.66(5)	7.80(11)
Eff. Abs. Cross Section at 2200 ms^{-1} (barn)	6.04(9)	4.56(8)	39.4(23)
Experiment 3 (Room Temperature)			
Inner Radius (cm)	1.9531	1.9761	1.9767
Outer Radius (cm)	2	2	2
Eff. Number Density ($Å^{-3}$)	0.0321	0.0397	0.0400
Eff. Total Scattering Cross Section (barn)	6.33(31)	5.71(55)	7.82(11)
Eff. Abs. Cross Section at 2200 ms^{-1} (barn)	6.0(1)	4.61(76)	39.5(24)

Table 6.5: Parameters used to calculate $A_{\rm sc,sc}(Q,E)$. The effective parameters were obtained using neutron scattering and absorption cross sections taken from ref. [113], a $GeSe_2$ number density of 0.0334 $Å^{-3}$ [167] and an Al number density of 0.06026 $Å^{-3}$ [165].

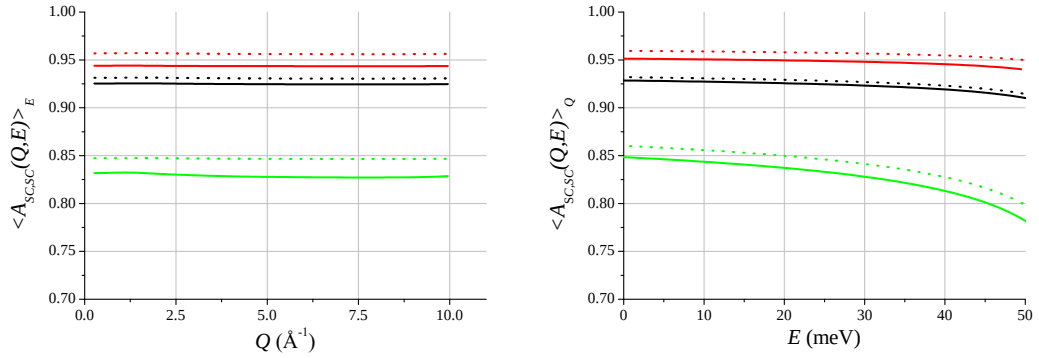

(a) Q Dependence *(b) E Dependence*

Figure 6-13: The attenuation coefficients $A_{\mathrm{sc,sc}}(Q,E)$ for experiments 2 (solid curves) and 3 (broken curves) for samples of $^{\mathrm{N}}Ge^{\mathrm{N}}Se_2$ (black) $^{70}Ge^{\mathrm{N}}Se_2$ (red) and $^{73}Ge^{76}Se_2$ (green) averaged (a) over energies between 0 and 140 meV or (b) over all Q values. The coefficients were calculated using the parameters taken from table 5.3. The maximum energy for the vibrational density of states is $\simeq$ 45 meV (see e.g. figure 5-9).

14, for each experiment the integrals of the intensities are given for the sample-in-can measurement, $\int_{E_{\min}}^{E_{\max}} I_{sc}^{E}(Q,E)\mathrm{d}E$, empty can measurement $\int_{E_{\min}}^{E_{\max}} I_{c}^{E}(Q,E)\mathrm{d}E$ and corrected sample scattering $\int_{E_{\min}}^{E_{\max}} I_{s}(Q,E)\mathrm{d}E$, where $E_{\min}$ and $E_{\max}$ are the minimum ($\geq$ -50 meV) and maximum ($\leq$ 50 meV) energies which were measured at a given Q value. These integrals represent the differential scattering cross sections and are presented to show the effect that the scattering from the can has on the sample-in-can measurement. The differential scattering cross sections from Salmon *et al.* [136] that were used to find m are also plotted in figure 6-14. The effect of the background, attenuation and renormalisation correction on the $G(E)$ function is shown for experiments 2 and 3 in figure 6-15 for the $^{\mathrm{N}}Ge^{\mathrm{N}}Se_2$ sample where the appropriate values for $^{\mathrm{N}}Ge^{\mathrm{N}}Se_2$ used in equation (2.45) are listed in table 5.1.

6.4.4 Multiple Scattering Correction

Experiment 2

In the case of experiment 2, made at a temperature of 5 K, the incoherent approximation given by equation 4.7 was used to calculate the multiple scattering contribution and is reproduced here for convenience

$$I_{\mathrm{s}}(Q,E) = I_{\mathrm{ms}}(E) + B(E)Q^2\exp(-2\overline{W}(Q)) \;, \tag{6.3}$$

where $B(E)$ is a fitted coefficient, $I_{\mathrm{ms}}(E)$ is the multiple scattering contribution to $I_{\mathrm{s}}(Q,E)$ that remains after subtraction of the empty can and attenuation correction.

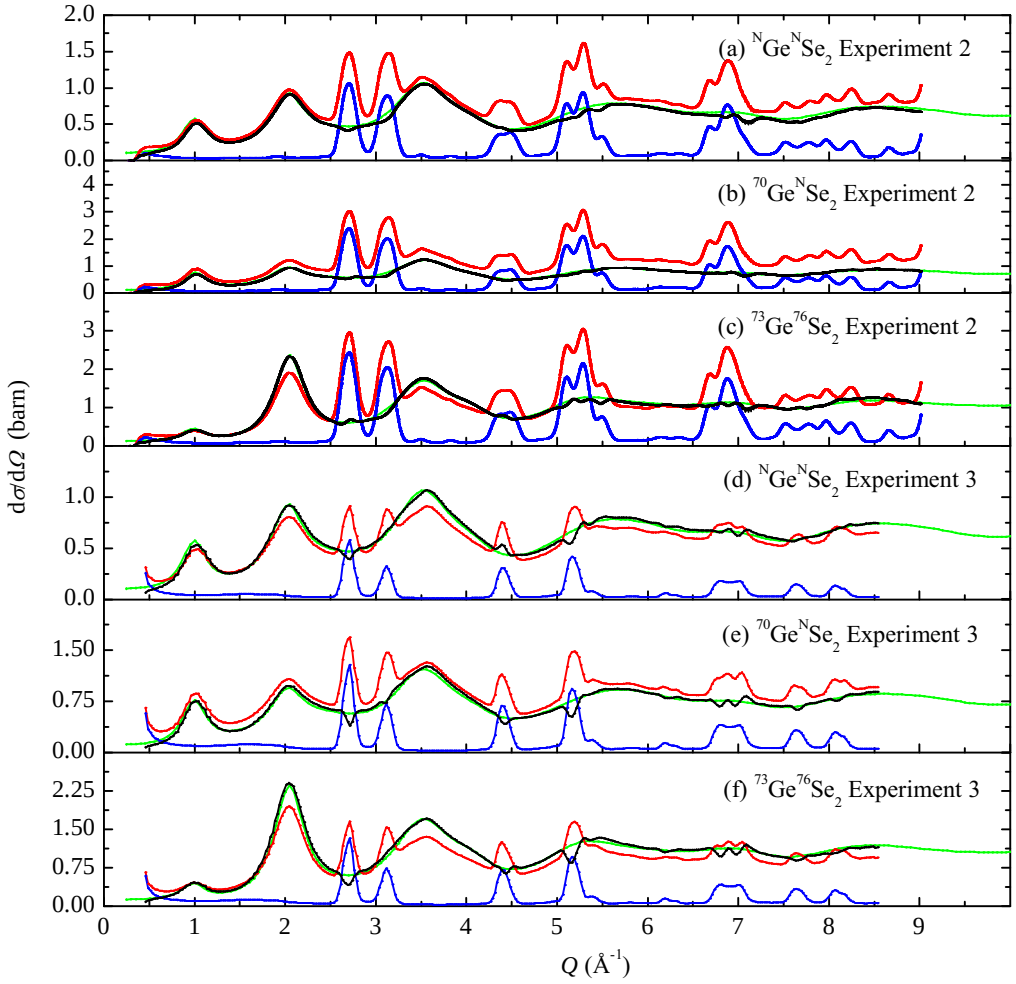

Figure 6-14: The differential scattering cross section $d\sigma/d\Omega$ from experiment 2 for samples of (a) $^{N}Ge^{N}Se_2$, (b) $^{70}Ge^{N}Se_2$ and (c) $^{73}Ge^{76}Se_2$; and for experiment 3 for samples of (d) $^{N}Ge^{N}Se_2$, (e) $^{70}Ge^{N}Se_2$ and (f) $^{73}Ge^{76}Se_2$ calculated using the sample-in-can $\int_{E_{min}}^{E_{max}} I_{sc}^{E}(Q,E)dE$ (solid red curve), empty can $\int_{E_{min}}^{E_{max}} I_{c}^{E}(Q,E)dE$ (solid blue curve) or sample after correction for the empty can, attenuation and renormalisation $\int_{E_{min}}^{E_{max}} I_{s}(Q,E)dE$ (solid black curve) intensities, where E_{min} and E_{max} are the minimum ($\geq$ -50 meV) and maximum ($\leq$ 50 meV) energies which were measured at a given Q value. Also plotted are $d\sigma/d\Omega = F(Q) + \sigma_{self}/4\pi$ from a diffraction experiment by Salmon *et al.* [136] (solid green curve).

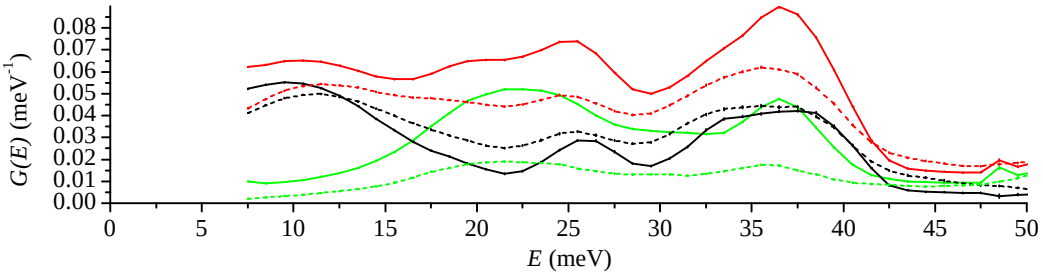

Figure 6-15: $G(E)$ calculated in the "bronze medal" approximation for experiments 2 (solid curves) or 3 (broken curves) for the $^{N}Ge^{N}Se_2$ sample using $I^{E}_{sc}(Q,E)$ for the sample-in-can (red), from $I^{E}_{c}(Q,E)$ for the empty can (green), and from $I_s(Q,E)$ for the sample after correction for empty can scattering, attenuation and renormalisation (black). No correction for multiple scattering or multiple phonon scattering has been applied.

For each measured value of E, a least squares fit of equation (6.3) was made to the measured $I_s(Q,E)$ functions by varying $I_{ms}(E)$ and $B(E)$. The coherent dynamical structure factor is then given by $S_c(Q,E) = I_s(Q,E) - I_{ms}(E)$ (see equation (4.9)).

An example of the fit to $I_s(Q,E)$ for the sample of $^{N}Ge^{N}Se_2$ is given in figure 6-16, where an integral is taken over an energy transfer range from 10 to 20 meV to improve the statistics. A fit to $I_s(Q,E)$ with $I_{ms}(E) = 0$ is also plotted in figure 6-16

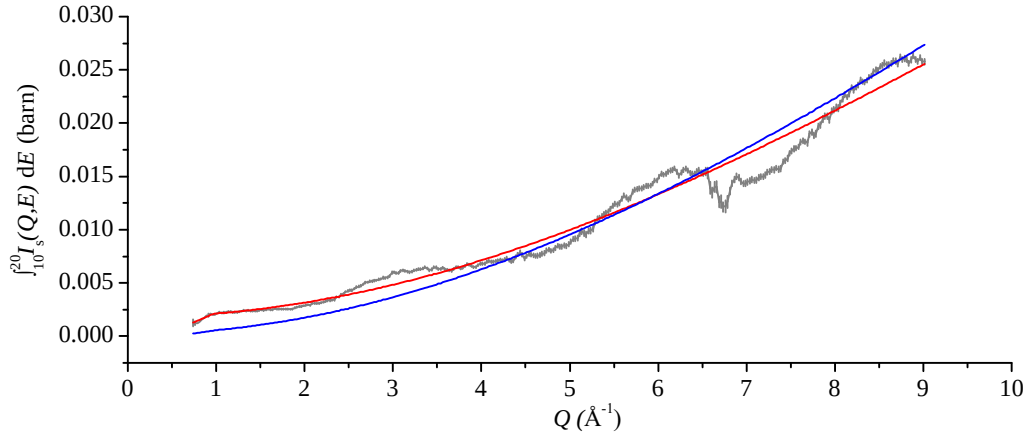

Figure 6-16: $I_s(Q,E)$ measured in experiment 2 (done at low temperature) for the $^{N}Ge^{N}Se_2$ sample (solid grey curve), an example of a poor fit to the data using equation (6.3) and fixing $I_{ms}(E) = 0$ (solid blue curve) and an example of a good fit to the data using equation (6.3) (solid red curve), where $I_{ms}(E)$ is defined in equation (5.2). To increase the statistics, the functions have been integrated over the range from 10 to 20 meV in energy transfer.

to show that the incoherent approximation does not fit well without the Q-independent multiple scattering term. Using equations (2.44) and (2.45) (i.e. the "bronze medal" approximation), the $G(E)$ functions that were calculated for the three samples using

the appropriate values from table 5.1 and either $I_s(Q,E)$, $S_c(Q,E)$ or $I_{ms}(E)$ are given for the low temperature experiment in figure 6-17. In the case of the low temperature measurements, the multiple scattering correction approximately follows the density of states. This is because the most likely 2-scattering events that give intensity in the inelastic region are those corresponding to elastic-inelastic scattering (in either order), due to the very large elastic differential scattering cross section in comparison with the inelastic differential cross section for neutrons. In these events, a neutron only changes energy once, with a probability distribution related to the vibrational density of states. Therefore, as long as the sample is cold enough such that there is a low probability of inelastic-inelastic 2-scattering events, one would expect multiple scattering to follow the density of states.

Experiment 3

In the case of experiment 3, made at room temperature, the model $I_s(Q,E)$ in the incoherent approximation for single phonon scattering (equation (6.3)) did not give a good fit to the measured $I_s(Q,E)$ functions because there is significant multiple phonon scattering. Therefore, the model $I_s(Q,E)$ function that includes higher phonon terms (equation (4.9)) was fitted to the measured $I_s(Q,E)$ functions and is reproduced here for convenience

$$I_s(Q,E) = I_{ms}(E) + \sum_{p=1}^{N_p} B_p(E) Q^{2p} \exp(-2\overline{W}(Q)) \,, \tag{6.4}$$

where p denotes the number of phonons, $B_p(E)$ are fitted coefficients and N_p is the number of phonon terms. In the fits, terms including $p = 1$, 2 and 3 were used.

An example of a fit to $I_s(Q,E)$ is given in figure 6-18, where the functions have been integrated in E between 10 and 20 meV to improve the statistics. A least squares fit to $I_s(Q,E)$ in the incoherent approximation that does not include multiple phonon terms (equation (6.3)) is also plotted in figure 6-18 and shows that, without the additional phonon terms, the incoherent approximation does not fit well. Using equations (2.44) and (2.45) (i.e. the "bronze medal" approximation), the $G(E)$ functions that were calculated for the three samples using the appropriate values from table 5.1 and either $I_s(Q,E)$, $S_c(Q,E)$ or $I_{ms}(E)$ are given for the room temperature experiment in figure 6-17.

In the case of the room temperature measurements, the multiple scattering does not follow the density of states. Inelastic-inelastic 2-scattering events have a significant probability of occurring at a temperature of 292 K.

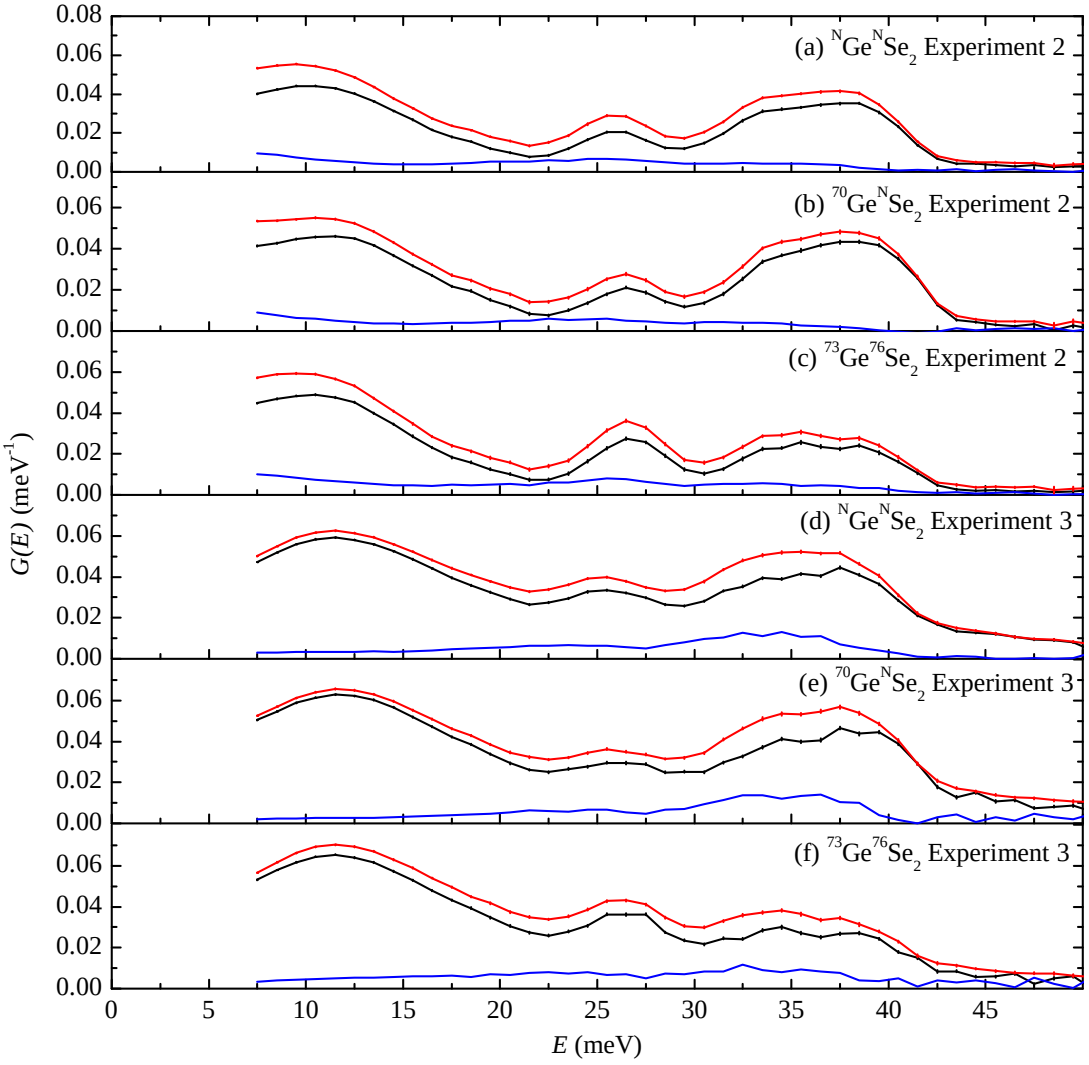

Figure 6-17: $G(E)$ calculated in the "bronze medal" approximation in experiment 2 (done at a low temperature) for samples of (a) $^{N}Ge^{N}Se_2$, (b) $^{70}Ge^{N}Se_2$ and (c) $^{73}Ge^{76}Se_2$ or experiment 3 (done at room temperature) for samples of (d) $^{N}Ge^{N}Se_2$, (e) $^{70}Ge^{N}Se_2$ and (f) $^{73}Ge^{76}Se_2$ using $I_s(Q,E)$ (solid red curve), $I_{ms}(E)$ (solid blue curve), or $S_c(Q,E) = I_s(Q,E) - I_{ms}(E)$ (solid black curve) and values taken from table 5.1.

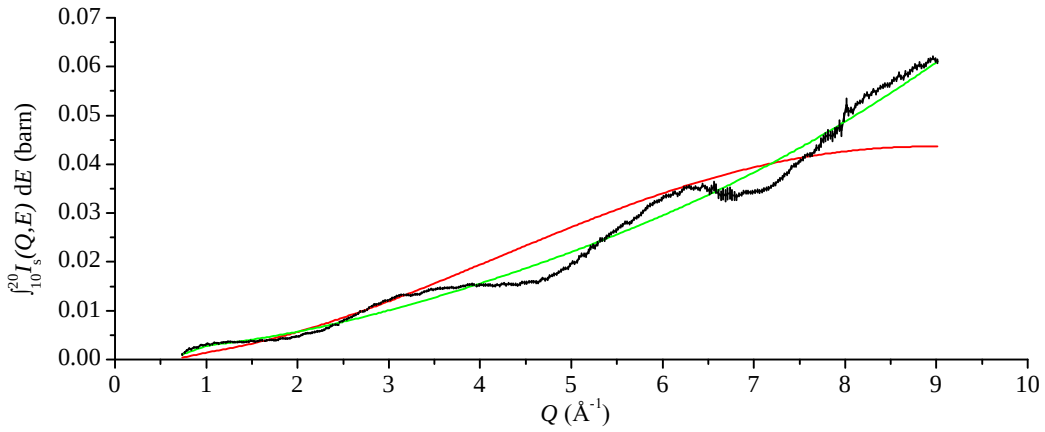

Figure 6-18: The $I_s(Q, E)$ function measured in experiment 3 (made at room temperature) for the $^{N}Ge^{N}Se_2$ sample (solid black curve), an example of a fit to the data within the incoherent approximation that does not include multiple phonon terms (equation (6.3)) (solid red curve) and a fit to the data within the incoherent approximation that does include multiple phonon terms (equation (6.4)) (solid green curve). To improve the statistics, the functions have been integrated over the energy transfer range from 10 to 20 meV.

6.4.5 Multiple Phonon Correction

To assist in the calculation of the multiple phonon corrections, $G(E)$ was calculated from $S_c(Q, E)$ using equations (2.44) and (2.45) with the appropriate values given in table 5.1. The Debye model [172] was used in the region which could not be measured (below 7 meV) due to resolution function broadening of the elastic scattered intensity. In the Debye model, $G(E) \propto E^2$ and the constant of proportionality was chosen such that the Debye model coincides with the first measured data point beyond the region of the elastic peak.

The multiple phonon correction, $S_{mp}(Q, E)$, was then calculated up to the 5^{th} phonon term using the method described in section 4.1.4. The vibrational density of states $G(E)$ without the multiple phonon correction calculated from $S_c(Q, E)$, the multiple phonon contribution to the vibrational density of states $G_{mp}(E)$, and the single phonon vibrational density of states $G_1(E) = G(E) - G_{mp}(E)$ are plotted in figure 6-20. The single phonon dynamical structure factors were found by using $S_1(Q, E) = S_c(Q, E) - S_{mp}(Q, E)$ (equation (4.22)). An example of the dynamical structure factors thus obtained are given in figure 6-19 using the $^{N}Ge^{N}Se_2$ sample in (a) experiment 2 made at low temperature or (b) experiment 3 made at room temperature, where $S_c(Q, E)$, $S_1(Q, E)$ and the calculated $S_{mp}(Q, E)$ are integrated over the energy transfer range from 10 to 20 meV to improve the statistics. In this figure the empty can, attenuation, renormalisation and multiple scattering corrections have all been made. Also plotted in figure 6-19b is a fit using the incoherent approximation without the

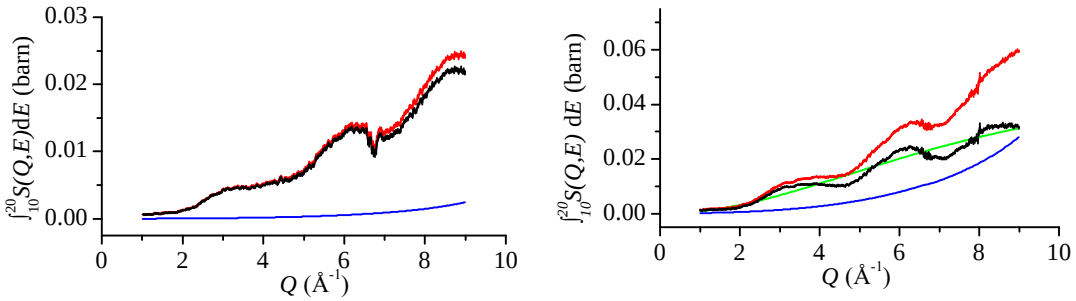

(a) Low Temperature

(b) Room Temperature

Figure 6-19: $S_c(Q,E)$(solid red curve), the multiple phonon contribution $S_{\rm mp}(Q,E)$ (solid blue curve) and the single phonon contribution calculated using $S_1(Q,E) = S_{\rm c}(Q,E) - S_{\rm mp}(Q,E)$ (solid black curve) for the $^{\rm N}Ge^{\rm N}Se_2$ sample as measured in (a) experiment 2 made at low temperature or (b) experiment 3 made at room temperature. Each function has been integrated over an energy transfer range from 10 to 20 meV. In (b) the single phonon incoherent approximation (equation (6.3)) is fitted to the fully corrected $S_c(Q,E)$ function (solid green line) to show that, after the multiple phonon correction has been made, the incoherent approximation for single phonon scattering gives a good fit to the measured data. In all cases the empty can, attenuation, renormalisation and multiple scattering corrections have been made.

multiple phonon or multiple scattering terms (equation (6.4)) to $S_1(Q,E)$ for the room temperature experiment. This shows that subtraction of the multiple phonon scattering brings the data into agreement with the incoherent approximation for single phonons.

6.5 "Silver Medal" Calculations

Once the data had been fully corrected, the "silver medal" results were calculated for experiment 2 (figure 6-21) and experiment 3 (figure 6-22) using the matrices given in section 5.4. The partial vibrational density of states ($G_\alpha(E)$ functions) were calculated using equations (2.38) and (2.39) assuming Debye-Waller factors of $W_{\rm Ge}(Q) = W_{\rm Se}(Q) = \overline{W}(Q)$.

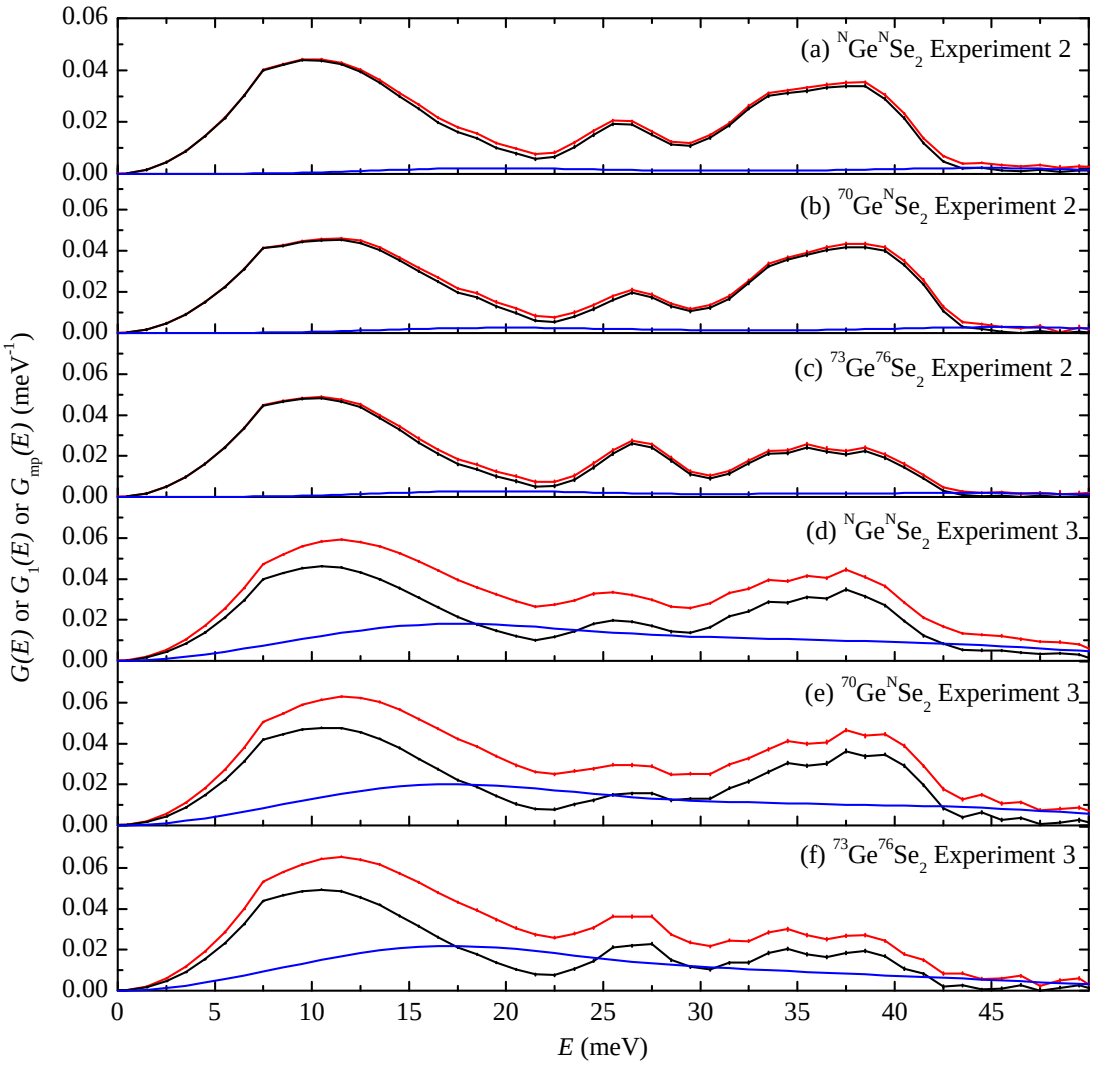

Figure 6-20: $G(E)$ calculated in the "bronze medal" approximation for experiment 2 (done at low temperature) for samples of (a) $^{N}Ge^{N}Se_2$, (b) $^{70}Ge^{N}Se_2$ and (c) $^{73}Ge^{76}Se_2$ or experiment 3 (done at room temperature) for samples of (d) $^{N}Ge^{N}Se_2$, (e) $^{70}Ge^{N}Se_2$ and (f) $^{73}Ge^{76}Se_2$ from $S_c(Q,E)$ without the multiple phonon correction (solid red curve), the calculated multiple phonon correction to the vibrational density of states $G_{mp}(E)$ (solid blue curve) and the single phonon vibrational density of states $G_1(E) = G(E) - G_{mp}(E)$ (solid black curve).

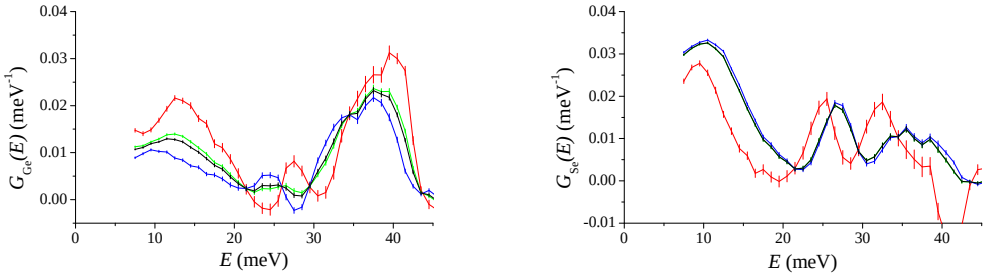

(a) $G_{\mathrm{Ge}}(E)$ *(b)* $G_{\mathrm{Se}}(E)$

Figure 6-21: The results for the partial vibrational density of states in the "silver medal" approximation from measurements made in experiment 2 (made at low temperature) for (a) $G_{\mathrm{Ge}}(E)$ or (b) $G_{\mathrm{Se}}(E)$ calculated using equation (5.3) (solid red line), equation (5.4) (solid green line), equation (5.5) (solid blue line) or equation (5.6) (solid black line).

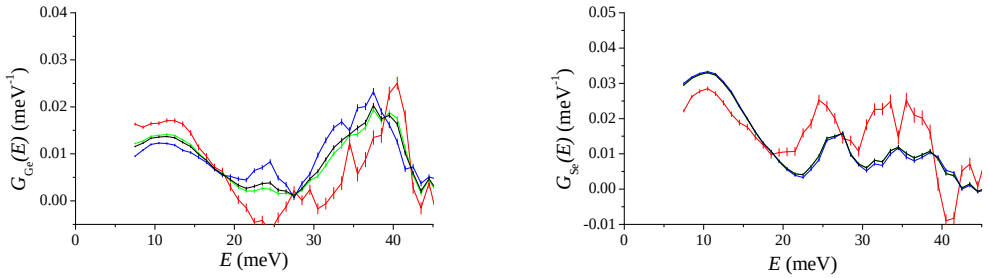

(a) $G_{\mathrm{Ge}}(E)$ *(b)* $G_{\mathrm{Se}}(E)$

Figure 6-22: The results for the partial vibrational density of states in the "silver medal" approximation from measurements made in experiment 3 (done at room temperature) for (a) $G_{\mathrm{Ge}}(E)$ or (b) $G_{\mathrm{Se}}(E)$ calculated using equation (5.3) (solid red line), equation (5.4) (solid green line), equation (5.5) (solid blue line) or equation (5.6) (solid black line).

.

6.6 Results

6.6.1 Generalised Vibrational Density of States

The generalised single phonon vibrational density of states for each sample $G_1(Q,E)$ (see figure 6-23) and the generalised single phonon partial vibrational density of states $G_\alpha(Q,E)$ were calculated for experiments 2 and 3 by using equations (2.44) and (2.38), respectively. To improve the statistics, integrals of these functions were taken over three ranges in energy representing the three peaks in $G_1(E)$ (see e.g. figure 6-29). The results for the first peak, from 8 to 18 meV, are shown in figure 6-24, the results for the second peak, from 23 to 28 meV, are shown in figure 6-25, and the results for the third peak, from 32 to 40 meV, are shown in figure 6-26. Also plotted in figures 6-24 to 6-26 are the MARI results described in chapter 5.

The generalised vibrational density of states $G_1(Q,E)$ for a sample of $^{\mathrm{N}}\mathrm{Ge}^{\mathrm{N}}\mathrm{Se}_2$ and the generalised partial vibrational density of states $G_\alpha(Q,E)$ were simulated using the MD method described by Giacomazzi *et al.* [34] for temperatures of 5 K and 292 K. The simulated and experimental data for $G_1(Q,E)$ (figure 6-27) and $G_\alpha(Q,E)$ (figure 6-28) are compared. The integration ranges chosen for the simulation data are different to those for the experimental data because there is a relative shift of the peaks in $G_1(E)$ as demonstrated in figure 6-34a. Ranges that cover the same peaks were therefore used for the MD results, in this case 6 to 16 meV for the first peak, 20 to 25 meV for the second peak and 28 to 34 meV for the third peak.

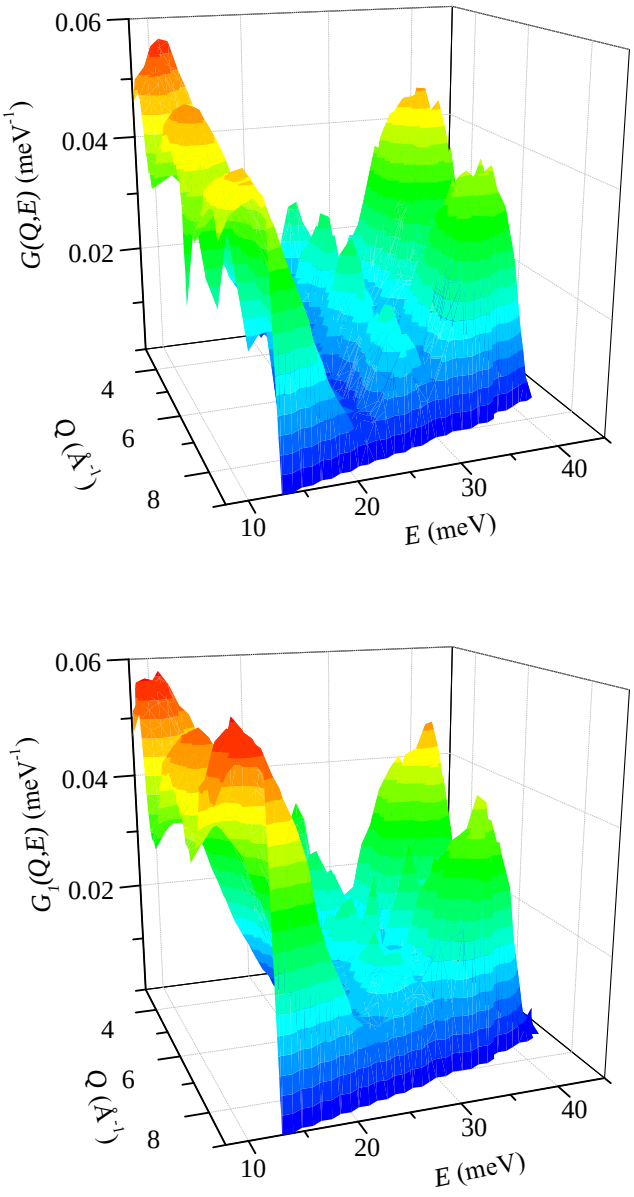

Figure 6-23: The $G_1(Q, E)$ function calculated in the "bronze medal" approximation found for a sample of $^{\mathrm{N}}\mathrm{Ge}^{\mathrm{N}}\mathrm{Se}_2$ in (top) experiment 2 made at a temperature of 5 K and (bottom) experiment 3 made at a temperature of 292 K.

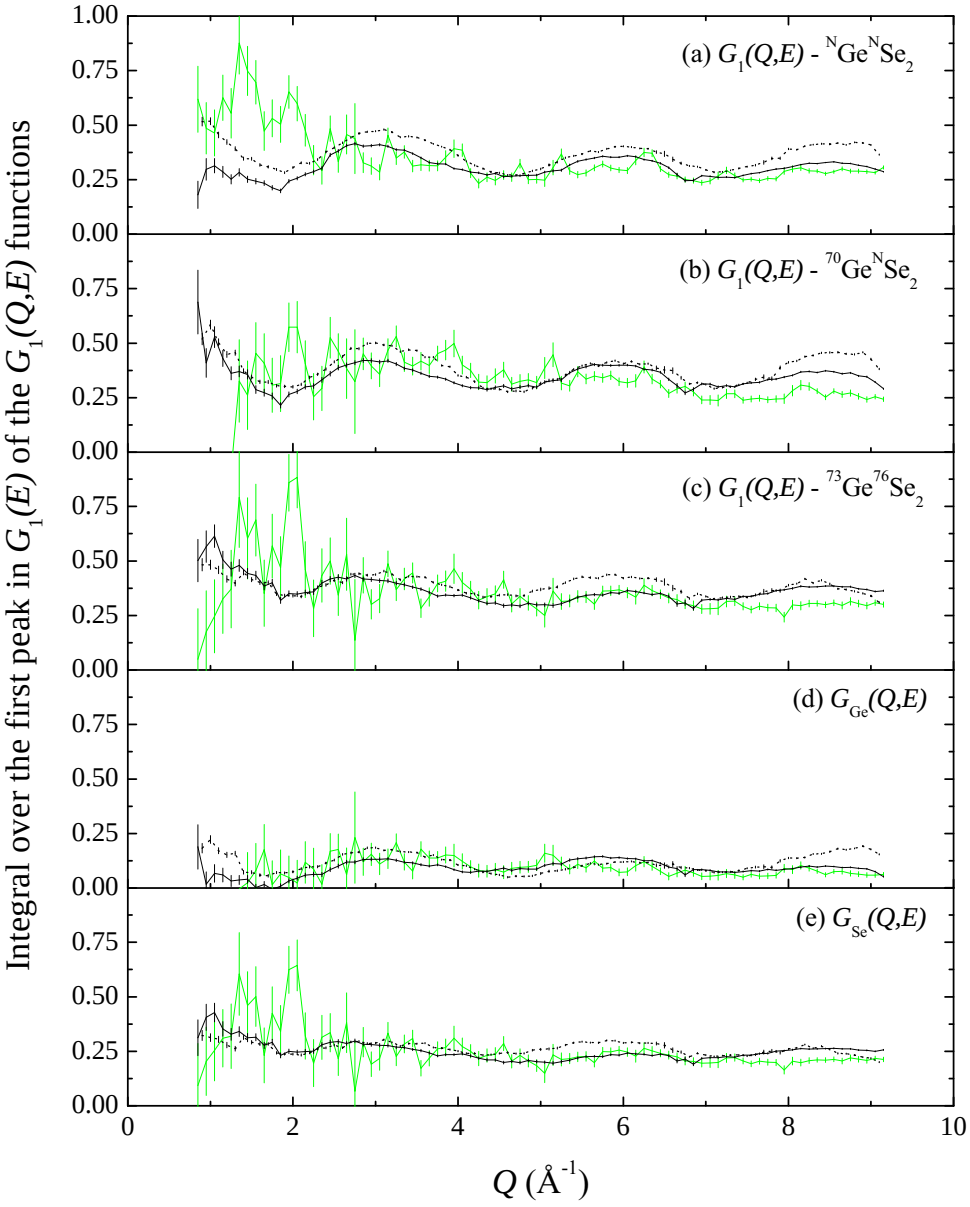

Figure 6-24: The integral over the first peak in $G_1(E)$ of $G_1(Q,E)$ as obtained in experiment 2 done at low temperature (solid black curves), experiment 3 done at room temperature (broken black curves) and from the MARI experiment done at low temperature described in chapter 5 (solid green curves) using samples of (a) $^{N}Ge^{N}Se_2$, (b) $^{70}Ge^{N}Se_2$ and (c) $^{73}Ge^{76}Se_2$. Plotted in (d) and (e) are the integrals of $G_{Ge}(Q,E)$ and $G_{Se}(Q,E)$ over the first peak in $G_1(E)$, respectively. The $G_\alpha(Q,E)$ functions were calculated using the SVD matrix (equation (5.6)) and the limits for the integrals are given in the text.

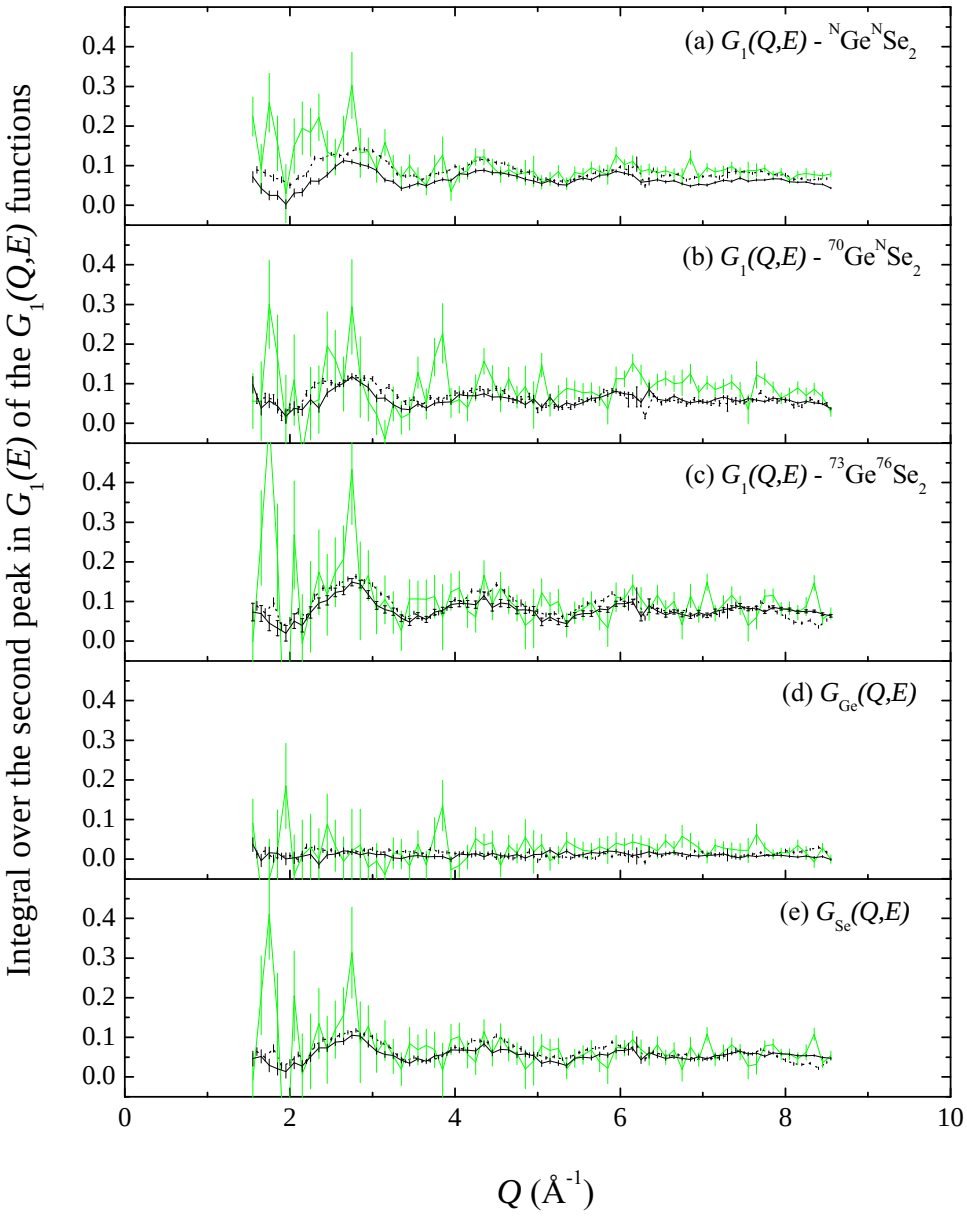

Figure 6-25: The integral over the second peak in $G_1(E)$ of $G_1(Q,E)$ as obtained in experiment 2 done at low temperature (solid black curves), experiment 3 done at room temperature (broken black curves) and from the MARI experiment done at low temperature described in chapter 5 (solid green curves) using samples of (a) $^{N}Ge^{N}Se_2$, (b) $^{70}Ge^{N}Se_2$ and (c) $^{73}Ge^{76}Se_2$. Plotted in (d) and (e) are the integrals of $G_{Ge}(Q,E)$ and $G_{Se}(Q,E)$ over the second peak in $G_1(E)$, respectively. The $G_\alpha(Q,E)$ functions were calculated using the SVD matrix (equation (5.6)) and the limits for the integrals are given in the text.

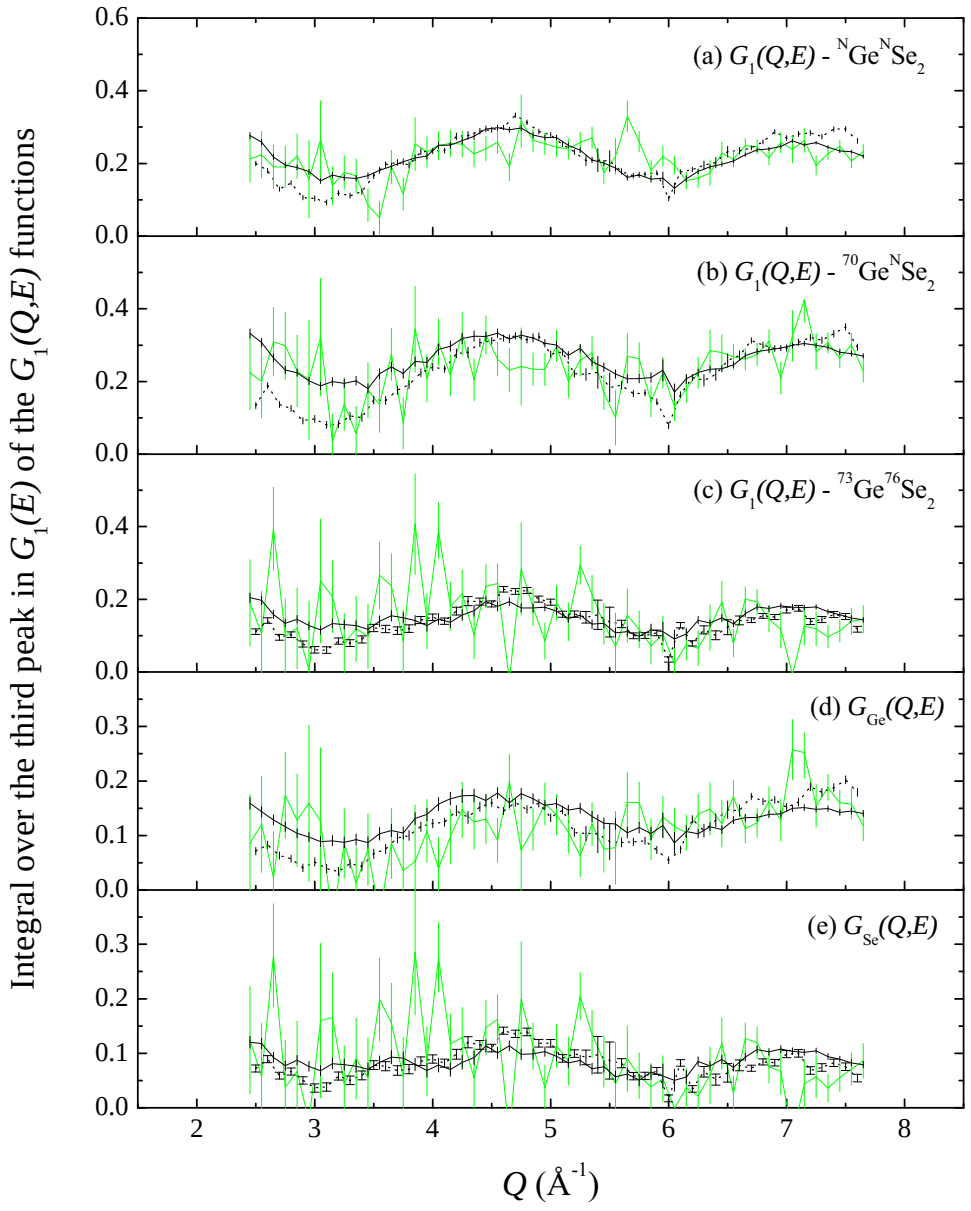

Figure 6-26: The integral over the third peak in $G_1(E)$ of $G_1(Q,E)$ as obtained in experiment 2 done at low temperature (solid black curves), experiment 3 done at room temperature (broken black curves) and from the MARI experiment done at low temperature described in chapter 5 (solid green curves) using samples of (a) $^{N}Ge^{N}Se_2$, (b) $^{70}Ge^{N}Se_2$ and (c) $^{73}Ge^{76}Se_2$. Plotted in (d) and (e) are the integrals of $G_{Ge}(Q,E)$ and $G_{Se}(Q,E)$ over the third peak in $G_1(E)$, respectively. The $G_\alpha(Q,E)$ functions were calculated using the SVD matrix (equation (5.6)) and the limits for the integrals are given in the text.

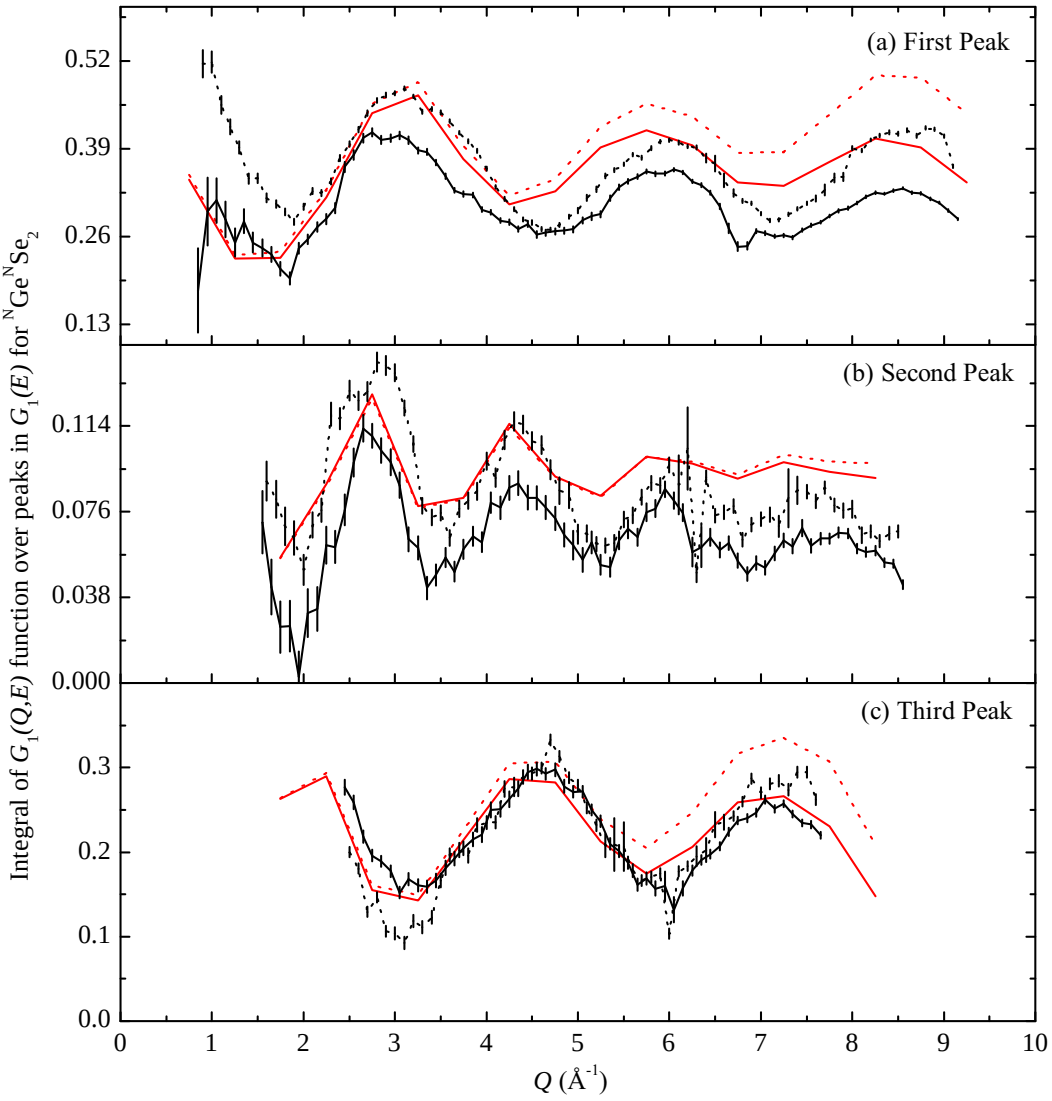

Figure 6-27: The results for a sample of $^{N}Ge^{N}Se_2$ at a temperature of 5 K (solid curves) or 292 K (broken curves) from experiments 2 and 3 (black) or from the *ab initio* MD simulations made by Giacomazzi *et al.* [34] (red) of the integral of $G_1(Q, E)$ over (a) the first peak, (b) the second peak, or (c) the third peak of $G_1(E)$. The limits for the integrals are given in the text.

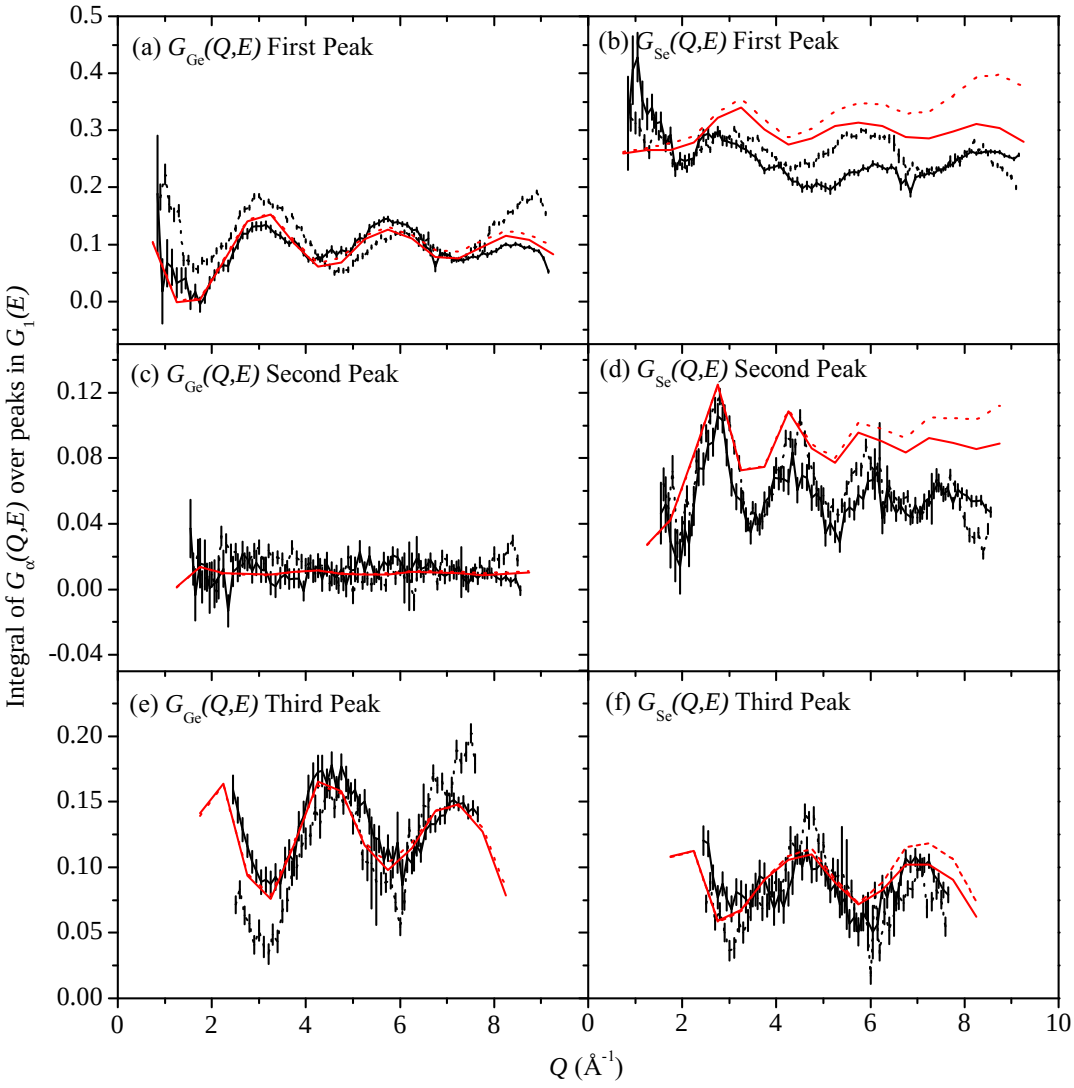

Figure 6-28: The integral of $G_{\mathrm{Ge}}(Q,E)$ over (a) the first peak, (c) the second peak, or (e) the third peak and the integral of $G_{\mathrm{Se}}(Q,E)$ over (b) the first peak, (d) the second peak, or (f) the third peak of $G_1(E)$. The datasets correspond to temperatures of 5 K (solid curves) or 292 K (broken curves) from experiments 2 and 3 (black) or from the *ab initio* MD simulations made by Giacomazzi *et al.* [34] (red). These results have been calculated in the "silver medal" approximation using the SVD matrix (equation (5.6)) and the limits for the integrals are given in the text.

6.6.2 The Single Phonon Vibrational Density of States

The results in the "bronze medal" approximation for samples of $^{N}Ge^{N}Se_2$, $^{70}Ge^{N}Se_2$ and $^{73}Ge^{76}Se_2$ are compared in figure 6-29. A comparison between the $G_1(E)$ functions for $^{N}Ge^{N}Se_2$ calculated in the "bronze medal approximation" in the present work and in the work by other authors is given in figure 6-30.

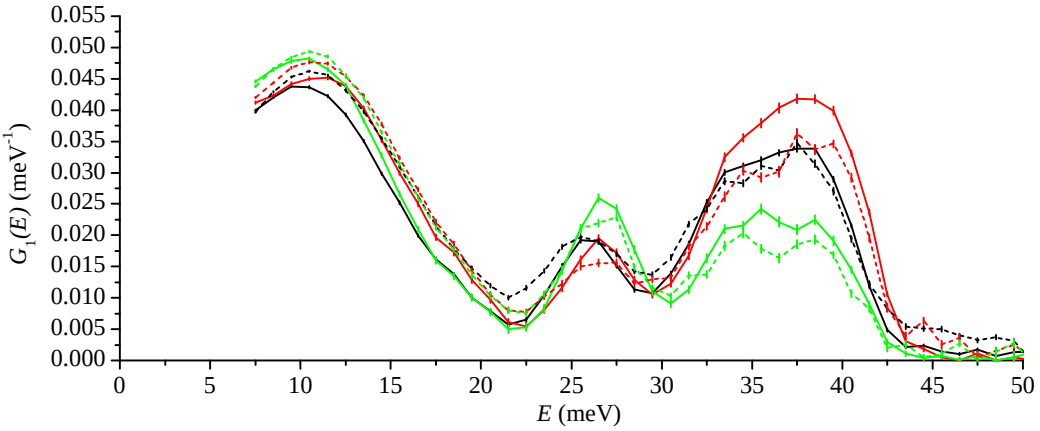

Figure 6-29: The fully corrected single phonon vibrational density of states $G_1(E)$ calculated for experiment 2 done at low temperature (solid curves) and experiment 3 done at room temperature (broken curves) using the "bronze medal" approximation for samples of $^{N}Ge^{N}Se_2$ (black), $^{70}Ge^{N}Se_2$ (red) and $^{73}Ge^{76}Se_2$ (green).

In figure 6-31 a comparison is made between the total vibrational density of states $G_1(E)$ in the "bronze medal" approximation and the partial vibrational density of states $G_\alpha(E)$ in the "silver medal" approximation as obtained from experiments 2 and 3, and from the MARI experiment described in chapter 5. In the case of $G_\alpha(E)$, the results from the SVD method (equation 5.6) are shown.

A comparison is made in figure 6-32 between the $G_1(E)$ functions calculated for $^{N}Ge^{N}Se_2$ in the "bronze medal" approximation from experiments 2 and 3, and from the MD simulations made by Giacomazzi *et al.* [35]. In figure 6-33 the $G_\alpha(E)$ functions calculated in the "silver medal" approximation using the SVD method (equation 5.6) are compared to the $G_\alpha(E)$ functions calculated in the "silver medal" approximation from the simulations. Finally, in figure 6-34, the sum of the "silver medal" results such that $G_1(E) = G_{Ge}(E) + G_{Se}(E)$ is compared to $G_1(E)$ calculated in the "bronze medal" approximation for temperatures of 5 K and 292 K from the present work and from the MD simulations of Giacomazzi *et al.* [35].

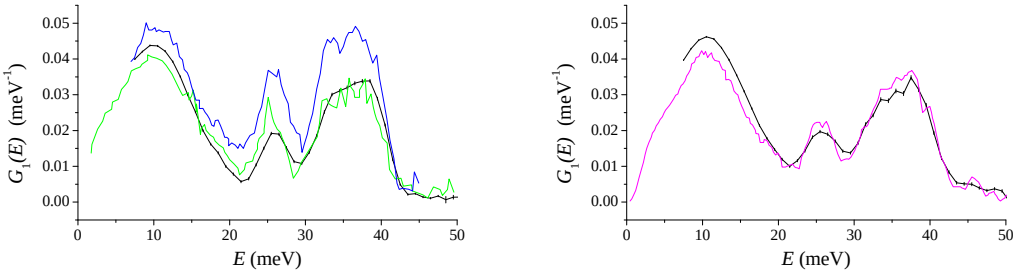

(a) Low Temperature

(b) Room Temperature

Figure 6-30: (a) The single phonon density of states $G_1(E)$ calculated using the "bronze medal" approximation for a sample of $^{N}Ge^{N}Se_2$ as obtained from experiment 2 done at low temperature (solid black curve), from a study using the LRMECS spectrometer at the Intense Pulsed Neutron Source at a temperature of 13(2) K with an incident neutron energy of 60.06 meV [51] (solid blue curve), and from a study using the MARI spectrometer at a temperature of 18(1) K and an incident neutron energy of 60 meV [164] (solid green curve). (b) The single phonon density of states $G_1(E)$ calculated using the "bronze medal" approximation for a sample of $^{N}Ge^{N}Se_2$ as obtained in experiment 3 done at room temperature (solid black curve) and from a study made at room temperature using the BT-4 instrument at the NIST facility in neutron energy gain mode by Cappelletti *et al.* [130] (solid magenta curve).

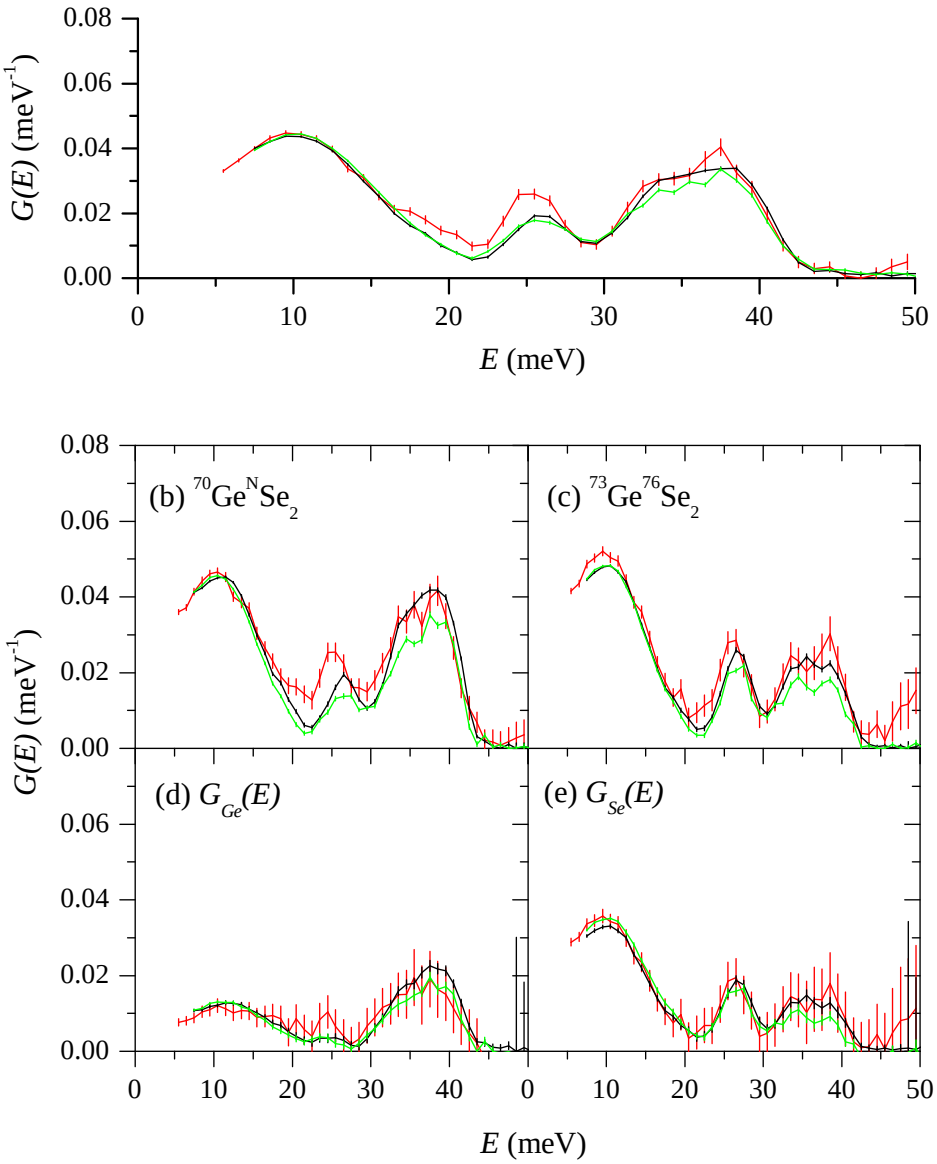

Figure 6-31: $G_1(E)$ calculated in the "bronze medal" approximation for experiment 2 done at low temperature (solid black curves), experiment 3 done at room temperature (broken black curves), and the low temperature experiments done using the MARI spectrometer described in chapter 5 (solid green curves) for samples of (a) $^{\mathrm{N}}\mathrm{Ge}^{\mathrm{N}}\mathrm{Se}_2$, (b) $^{70}\mathrm{Ge}^{\mathrm{N}}\mathrm{Se}_2$ or (c) $^{73}\mathrm{Ge}^{76}\mathrm{Se}_2$. In (d) and (e) the $G_{\mathrm{Ge}}(E)$ and $G_{\mathrm{Se}}(E)$ functions calculated in the "silver medal" approximation using the SVD method (equation (5.6)) are plotted, respectively.

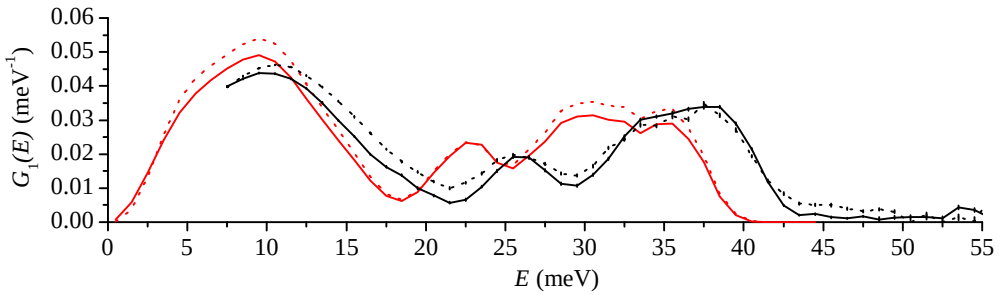

Figure 6-32: The $G_1(E)$ function obtained for $^{\mathrm{N}}\mathrm{Ge}^{\mathrm{N}}\mathrm{Se}_2$ in the "bronze medal" approximation at a temperature of 5 K (solid curves) or 292 K (broken curves) from experiments 2 and 3 (black) or from the MD simulations made by Giacomazzi *et al.* [35] (red).

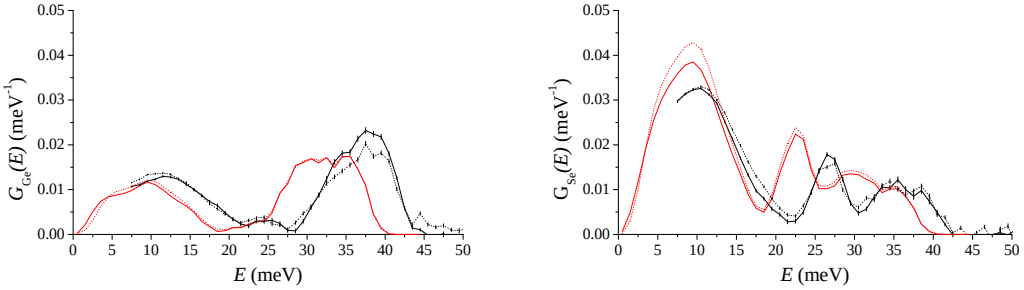

(a) $G_{\mathrm{Ge}}(E)$ *(b)* $G_{\mathrm{Se}}(E)$

Figure 6-33: Comparison of the partial vibrational density of states (a) $G_{\mathrm{Ge}}(E)$ or (b) $G_{\mathrm{Se}}(E)$ obtained in the "silver medal" approximation using the SVD matrix (equation (5.6)) at a temperature of 5 K (solid curves) or 292 K (broken curves) from experiments 2 and 3 (black) or from the MD simulations made by Giacomazzi *et al.* [35] (red).

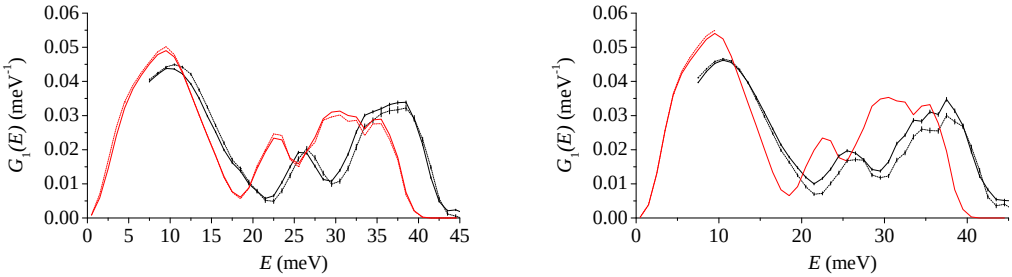

(a) Low Temperature *(b)* Room Temperature

Figure 6-34: $G_1(E)$ for temperatures of (a) 5 K and (b) 292 K obtained using either the "bronze medal" approximation for the $^{\mathrm{N}}\mathrm{Ge}^{\mathrm{N}}\mathrm{Se}_2$ sample (solid curves) or the expression $G_1(E) = G_{\mathrm{Ge}} + G_{\mathrm{Se}}(E)$ using the SVD matrix (equation 5.6) (broken curves) from experiments 2 and 3 (black) or from the MD simulations made by Giacomazzi *et al.* [35] (red).

6.7 Discussion

The partial vibrational density of states of $GeSe_2$ have been measured with a small statistical error within the "silver medal" approximation using the method of isotopic substitution in neutron spectroscopy. High quality datasets have been obtained from three experiments using the MERLIN spectrometer. In experiment 1, the Debye-Waller factor was found and the temperature dependence of the density of states at small energy transfers was measured. In experiment 2, the full set of partial vibrational density of states was obtained at a temperature of 5 K. In experiment 3, the full set of partial vibrational density of states was obtained at room temperature, providing a test for the multiple phonon corrections and a further set of data to compare with simulations.

The Debye-Waller Factor

The Debye-Waller factor is related to the mean squared displacement by $2\overline{W}(Q) = Q^2 \langle u^2 \rangle /3$. $\langle u^2 \rangle /3$ was calculated as a function of temperature using the procedure described in section 6.3. There is disagreement between the empirical values and $\langle u^2 \rangle /3$ calculated for Ge and Se from the MD simulations made by Giacomazzi *et al.* [35], although the datasets follow a similar trend with increasing temperature. The gradient for the experimental values is smaller than for the simulated values (see figure 6-9). The neutron spectroscopy experiment done by Walter *et al.* [51], where a similar technique was used at a temperature of 10 K, gave $\langle u^2 \rangle /3 = 0.00188$ Å^2, which is in better agreement with the present study than with the simulations. Other authors who have measured the vibrational density of states of $GeSe_2$ (e.g. refs. [130, 164]) do not quote Debye-Waller factors.

The Debye-Waller factors were used to approximate the Debye temperature θ_D [52, pp. 110], which within the Debye model is constant with temperature. At low temperatures, when $T \approx 0$, the Debye temperature is approximated by

$$\theta_D = \frac{3}{4k_B} \left(\frac{\hbar^2 Q^2}{2\overline{M}} \right) \left(\frac{1}{\overline{W}(Q)} \right) , \tag{6.5}$$

while at a high temperature, when $T >> \theta_D$,

$$\theta_D = \sqrt{\frac{3}{k_B} \left(\frac{\hbar^2 Q^2}{2\overline{M}} \right) \left(\frac{T}{\overline{W}(Q)} \right)} . \tag{6.6}$$

For the measurements made at temperatures of 10 and 292 K, corresponding to $\langle u^2 \rangle /3$ = 0.002(1) and 0.0125(20) Å^2, the calculated Debye temperatures are 157 and 172 K

using equations (6.5) and (6.6), respectively. For the mean squared displacements of $\langle u^2 \rangle /3 = 0.00252$ and 0.0230 Å^2 found from the simulations made by Giacomazzi *et al.* [34, 36], the Debye temperatures calculated from equations (6.5) and (6.6) were 125 and 127 K, respectively. The Debye temperature has been calculated using the measured heat capacity to be 152.01(23) K [174]. The Debye temperatures from the experimental data are in the better agreement than the values obtained from the simulations with the values calculated from thermodynamic measurements.

The values of the mean squared displacement obtained from the MD simulations made by Giacomazzi *et al.* [34] are highly sensitive to the nature of low energy modes and the shift in E of the vibrtional density of states (see e.g. figure 6-32). When the calculation takes this into account, different values are found for the MD simulation data, where for a temperature of 292 K $\langle u^2 \rangle /3 = 0.015$ Å^2 [34]. This is in better agreement with the experimental value of 0.0125(2) Å^2 and with the value of 0.01535 Å^2 obtained from *ab initio* MD simualtions using the BLYP model [45].

Temperature dependence of $G(E)$

The uncorrected vibrational density of states measured up to $E \approx 20$ meV in experiment 1 shows that there is a small change with temperature in the position of the first peak in $G_1(E)$ at $\approx$ 10 meV (figure 6-35). There is also a small broadening of the first peak with increasing temperature, probably due to an increase in multiple phonon scattering for which a correction was not made (figure 6-10). The position of the

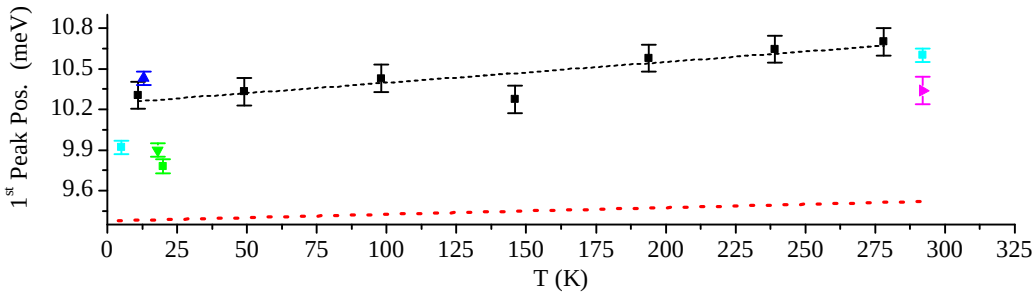

Figure 6-35: The position of the first peak in $G_1(E)$ calculated in the "bronze medal" approximation for the $^{\mathrm{N}}$Ge$^{\mathrm{N}}$Se$_2$ sample from MERLIN experiments 1 (■), 2 and 3 (■), the MARI experiment described in chapter 5 (■); the neutron spectroscopy studies of Walter *et al.* [51] (▲), Sinclair *et al.* [164] (▼) and Cappelletti *et al.* [130] (▶); and the MD simulations of Giacomazzi *et al.* [35] (broken red line). A linear fit to the (■) datapoints is given by the broken black line.

first peak in $G_1(E)$ for the $^{\mathrm{N}}$Ge$^{\mathrm{N}}$Se$_2$ sample was difficult to obtain from experiment 1 and for the measurements made by Cappelletti *et al.* [130] due to a large spread of the datapoints. A parabola was therefore fitted to the highest 6 datapoints in

the region of the first peak and the positions thus obtained are plotted in figure 6-35. Similarly, the highest 3 datapoints were fitted with a parabola to find the peak positions plotted in figure 6-35 for experiments 2 and 3, the MD simulations made by Giacomazzi *et al.* [35], the experiment made on the LRMECS spectrometer by Walter *et al.* [51] and the experiment made on the MARI spectrometer by Sinclair *et al.* [164]. Both the simulations and the experiments appear to indicate a small increase in the first peak position with temperature. The change in peak position is an artifact of the approximations used to calculate $G_1(E)$ and is caused by a deviation from the approximation that $W_{\mathrm{Ge}}(Q) = W_{\mathrm{Se}}(Q) = \overline{W}(Q)$ as used to obtain $G_1(E)$ in the experimental work [176]. It is worth noting that this small increase in peak position is of the same order as the discrepancy between experiments made on different spectrometers.

Comparison between the MARI and MERLIN experiments

In experiments 2 and 3 and the MARI experiment described in chapter 5, the vibrational density of states $G_1(E)$ found in the "bronze medal" approximation for samples of $^{\mathrm{N}}\mathrm{Ge}^{\mathrm{N}}\mathrm{Se}_2$, $^{70}\mathrm{Ge}^{\mathrm{N}}\mathrm{Se}_2$ and $^{73}\mathrm{Ge}^{76}\mathrm{Se}_2$ feature two peaks at ≈ 10 and ≈ 26 meV (exact positions are given in table 6.6) and a broad feature between 30 and 45 meV (see figure 6-31). While there is a small disagreement in the height of these features, the

	First Peak Position (meV)			Second Peak Position (meV)		
	Exp. 2	Exp. 3	MARI	Exp. 2	Exp. 3	MARI
$^{\mathrm{N}}\mathrm{Ge}^{\mathrm{N}}\mathrm{Se}_2$	9.92(15)	10.60(15)	9.78(15)	25.97(15)	25.74(15)	25.35(15)
$^{70}\mathrm{Ge}^{\mathrm{N}}\mathrm{Se}_2$	11.88 (15)	10.81(15)	10.44(15)	26.59(15)	27.08(15)	25.00(15)
$^{73}\mathrm{Ge}^{76}\mathrm{Se}_2$	10.22(15)	10.53(15)	10.04(15)	26.75(15)	26.54(15)	26.20(15)
"Silver Medal"	10.46(15)	10.57(15)	9.80(15)	26.55(15)	26.65(15)	25.57(15)

Table 6.6: The positions of the first two peaks in $G_1(E)$ calculated in the "bronze medal" approximation for samples of $^{\mathrm{N}}\mathrm{Ge}^{\mathrm{N}}\mathrm{Se}_2$,$^{70}\mathrm{Ge}^{\mathrm{N}}\mathrm{Se}_2$ and $^{73}\mathrm{Ge}^{76}\mathrm{Se}_2$ as well as for the sum of the silver medal results $G_1(E) = G_{\mathrm{Ge}}(E) + G_{\mathrm{Se}}(E)$ found using the SVD matrix. Values are given for experiments (exp.) 2 and 3 as well as for the MARI experiment described in chapter 5.

positions of the features from experiments 2 and 3 are in good agreement. The peaks in experiment 3, made at room temperature, appear broadened compared to experiment 2, made at low temperature. Both the small height difference and broadening may be due to remaining multiple phonon scattering intensity. The peak positions for the MARI experiment are somewhat different, with shifts in E of the order of 1 meV. These shifts are partly due to differences between the asymmetric resolution functions of the two instruments (see figure 6-36). By comparing the resolution functions of the

two instruments, a shift towards lower E is expected in the MARI experiment, as is observed in the data.

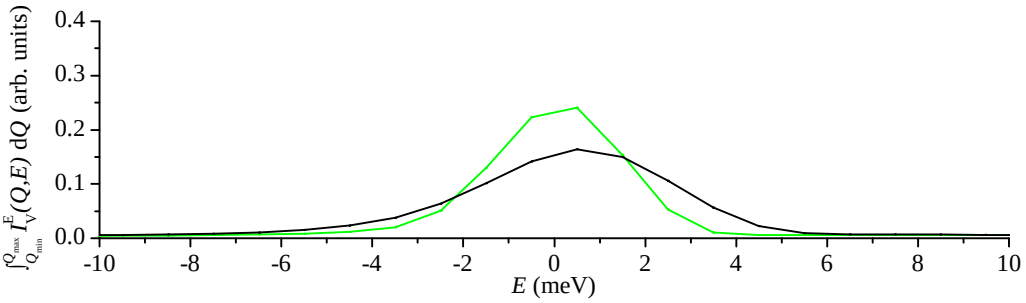

Figure 6-36: The width of the elastic peak due to energy resolution broadening from the intensity measured for the monochromatic vanadium represented by $\int_{Q_{\min}}^{Q_{\max}} I_{\mathrm{V}}^{\mathrm{E}}(Q,E)\,\mathrm{d}Q$ for MERLIN (solid black line) and MARI (solid green line) at an incident energy of ≈ 60 meV, where $Q_{\min}$ and $Q_{\max}$ are the minimum and maximum Q values that can be measured.

Furthermore, for experiment 3 made at room temperature and the MARI experiment made at low temperature the feature in $G_1(E)$ between 30 and 45 meV appears to be split into two peaks at $\simeq 34.36$ and $\simeq 38.4$ meV but this is not apparent in experiment 2 made at low temperature. There are two features at similar positions observed in the infra-red spectrum of $GeSe_2$ [155]. The MD simulations made by Giacomazzi *et al.* [35] indicate that this peak splitting may arise from a separation in energy of the stretching and bending type modes (see figure 6-39 and an explanation of the different modes below). The lack of this feature in the $G_1(E)$ functions found from experiment 2 may arise from intensity in this region from the can and cryostat that has not been fully subtracted. The intensity of this scattering is higher for experiment 2 compared to experiment 3 (see figure 6-15).

The $G_{\mathrm{Se}}(E)$ functions found in the "silver medal" approximation using the SVD matrix for all three experiments are in remarkably good agreement (figure 6-31 (e)), with the exception of the apparent peak splitting between 30 and 45 meV mentioned above. While there is good agreement between both results obtained using the MERLIN spectrometer, the $G_{\mathrm{Ge}}(E)$ functions found in the "silver medal" approximation using the SVD matrix for the MARI experiment has a much larger peak at ≈ 25 meV (see figure 6-31 (d)). This appears to result from an unknown systematic error.

As was expected from the fact that Ge and Se of natural isotopic abundance have similar masses and scattering lengths, there was not much difference between $G_1(E)$ calculated in the "bronze medal" approximation for the sample of $^{\mathrm{N}}\mathrm{Ge}^{\mathrm{N}}\mathrm{Se}_2$ and $G_1(E) = G_{\mathrm{Ge}}(E) + G_{\mathrm{Se}}(E)$ calculated in the "silver medal" approximation using the SVD matrix (see figure 6-34a).

The features in the generalised vibrational density of states, $G_1(Q,E)$, calculated in the "bronze medal approximation" for samples of $^{\mathrm{N}}\mathrm{Ge}^{\mathrm{N}}\mathrm{Se}_2$, $^{70}\mathrm{Ge}^{\mathrm{N}}\mathrm{Se}_2$ and $^{73}\mathrm{Ge}^{76}\mathrm{Se}_2$ and the generalised partial vibrational density of states, $G_\alpha(Q,E)$, calculated in the "silver medal" approximation using the SVD matrix from experiments 2 and 3 are in good agreement with each other (see figures 6-24 to 6-26). The functions from the MARI experiment agree with those from the MERLIN experiment at $Q > 3$ Å^{-1} within the experimental error.

Insights from the "silver medal" approximation

In the "silver medal" approximation, it is assumed that the cross term $S_{\mathrm{GeSe}}(Q,E)$ is zero (see section 2.2.4). In the "gold medal" approximation, where $S_{\mathrm{GeSe}}(Q,E)$ is taken into explicit account, very accurate neutron spectroscopy measurements are required. Due to the complexity of the corrections, stability of the instruments and the very high levels of scattering that arise from the empty can measurement, it was not possible to obtain reliable results using the "gold medal" approximation in the current work. However, for $^{\mathrm{N}}\mathrm{Ge}^{\mathrm{N}}\mathrm{Se}_2$ the simulations have calculated the contribution that $S_{\mathrm{GeSe}}(Q,E)$ makes to the final density of states, and it is found to be small [45] (see e.g. figure 5-19).

The results from the "silver medal" approximation show three bands of energy in the vibrational density of states (see figure 6-37). Below 21 meV the contributions

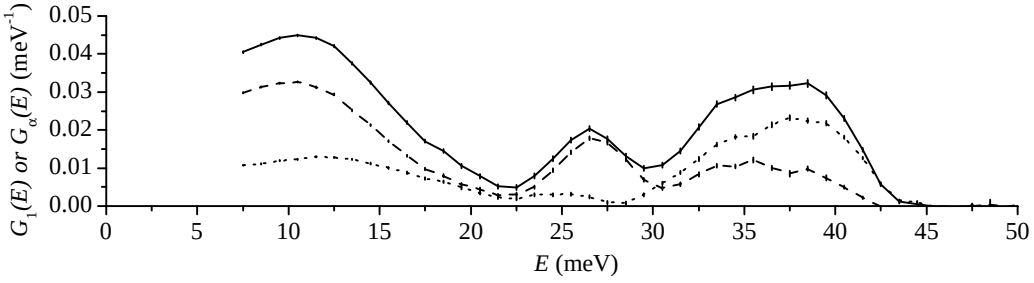

Figure 6-37: The functions $G_1(E) = G_{\mathrm{Ge}}(E) + G_{\mathrm{Se}}(E)$ (solid curve), $G_{\mathrm{Ge}}(E)$ (dotted curve) and $G_{\mathrm{Se}}(E)$ (dashed curve) for GeSe_2 calculated in the "silver medal" approximation using the SVD matrix for experiment 2.

to $G_1(E)$ from Ge and Se are weighted approximately by their atomic concentrations. From approximately 21 to 30 meV, Se atoms contribute almost exclusively, whereas above 30 meV the contributions from Ge and Se receive a roughly equally weighting. These three ranges correspond to 0 to 17 meV, 17 to 26 meV and 26 to 40 meV in the simulations.

Comparison with simulation data

Figures 6-32 and 6-33 show a systematic shift in E between experiment and the MD simulations made by Giacomazzi *et al.* [35] for the $G_1(E)$ function calculated in the "bronze medal" approximation and for the $G_\alpha(E)$ functions calculated in the "silver medal" approximation. This shift is often seen in MD simulations [37, 177]. However, the features in the density of states are in agreement as shown in figure 6-38, where the E axis for the simulated data has been scaled by a factor of 1.15 to bring the simulated data into better agreement with the experimental data.

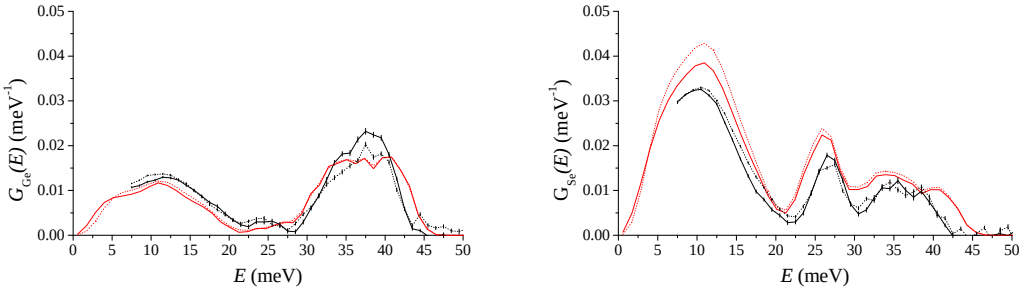

(a) $G_{\mathrm{Ge}}(E)$ *(b)* $G_{\mathrm{Se}}(E)$

Figure 6-38: Comparison of the partial vibrational density of states obtained in the "silver medal" approximation for (a) $G_{\mathrm{Ge}}(E)$ or (b) $G_{\mathrm{Se}}(E)$ from the MD simulations made by Giacomazzi *et al.* [35] with the E axis scaled by a factor of 1.15 (red) with the results from experiments 2 and 3 obtained using the SVD matrix (equation 5.6) (black) at a temperature of 5 K (solid curves) or 292 K (broken curves).

One small area of disagreement between simulation and experiment is the presence in the experimental data of a peak at ≈ 25 meV in $G_{\mathrm{Ge}}(E)$. This feature is present in $G_{\mathrm{Ge}}(E)$ calculated for all three measurements taken at $E_i \simeq 60$ meV (figure 6-31 (d)). In Raman and infrared scattering studies of $GeSe_2$ [157, 158, 160, 178, 179], separate peaks found at 24.944 and 27.151 meV are attributed to the symmetric stretching modes of corner and edge sharing tetrahedra, respectively. The potentials used for the MD simulations result in a fraction $N_{\mathrm{Ge}}(\mathrm{ES})/N_{\mathrm{Ge}}(\mathrm{CS}) = 47\%$ where $N_{\mathrm{Ge}}(\mathrm{ES})$ and $N_{\mathrm{Ge}}(\mathrm{CS})$ are the number of edge and corner sharing tetrahedra in the glass, respectively [141]. The value of $N_{\mathrm{Ge}}(\mathrm{ES})/N_{\mathrm{Ge}}(\mathrm{CS})$ found from a neutron diffraction experiment made using the method of isotopic substitution, such that the full set of partial structure factors could be obtained, is 83(16) % [136, 139]. While the energy resolution in the present study does not allow two distinct peaks to be resolved, the presence of the small peak in $G_{\mathrm{Ge}}(E)$ may result from a larger number of edge sharing tetrahedra when compared to simulations.

It is difficult to compare the $G_1(Q,E)$ functions for experiment and simulation on an absolute scale due to the systematic shift in E. However, qualitatively these functions agree for $G_1(Q,E)$ calculated for $^{\mathrm{N}}\mathrm{Ge}^{\mathrm{N}}\mathrm{Se}_2$ in the "bronze medal" approximation (see figure 6-27) and the partial $G_\alpha(Q,E)$ functions calculated in the "silver medal" approximation using the SVD matrix for both experiments 2 and 3 (see figure 6-28), within a scaling factor.

For the MD simulations, the motion of the Se atoms is further broken down into rocking, bending and stretching motions as shown in figure 6-39. Rocking motions

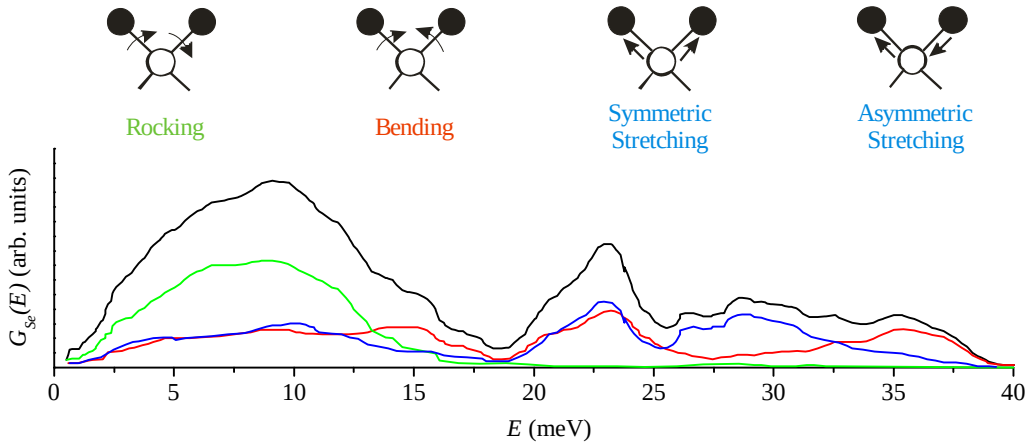

Figure 6-39: (top) Schematic of the bending, stretching and rocking motions, reproduced from ref. [180]. Open and filled circles represent Ge and Se atoms respectively. (bottom) The $G_{\mathrm{Se}}(E)$ function from the MD simulations made by Giacomazzi *et al.* [35] (solid black curve) separated into contributions from rocking (solid green curve), bending (solid red curve) and stretching (solid blue curve) motions.

only contribute to the lower band where $E < 17$ meV (corresponding to $E < 21$ meV in the experimental data), while the middle band is due to stretching and bending motions having equal weightings. The upper band for $E > 25$ meV (corresponding to $E > 29$ meV in the experimental data) consists of two broad peaks at ≈ 26 meV for stretching motions and ≈ 36 meV for bending motions (corresponding to ≈ 34 meV and ≈ 39 meV in the experimental data, respectively). This view is supported by the peak assignments from Raman and infrared experiments [155]. Here, the bending direction is taken along the bisector of the Ge-Se-Ge angle, the rocking direction is normal to the Ge-Se-Ge bridge and the stretching direction is orthogonal to the previous two as illustrated in the top of figure 6-39.

Comparison with other experiments

The $G_1(E)$ function calculated in the "bronze medal" approximation using the sample of $^{\mathrm{N}}\mathrm{Ge}^{\mathrm{N}}\mathrm{Se}_2$ is in good agreement, within the resolution broadening, with other available neutron scattering experiments made by Walter *et al.* [51], Sinclair *et al.* [164] and Cappelletti *et al.* [130] (see figure 6-30).

The measured vibrational density of states, with an interpretation provided by the simulations of Giacomazzi *et al.* [35], is consistent with the other bands identified in Raman spectra [134] that are centred on 17.98, 22.32 and 30.62 meV. These are assigned to Se bending, the Ge-Ge bond and Se stretching motions, respectively. The vibrational density of states in the present study was not measured with a high enough resolution to observe these features as sharp peaks as has been seen in other neutron scattering studies [155].

6.8 Conclusion

The total dynamical structure factors have been successfully measured for samples of $^{\mathrm{N}}\mathrm{Ge}^{\mathrm{N}}\mathrm{Se}_2$, $^{70}\mathrm{Ge}^{\mathrm{N}}\mathrm{Se}_2$ and $^{73}\mathrm{Ge}^{76}\mathrm{Se}_2$ in two different experiments. Further measurements were made at an incident energy of 29.9(1) meV to obtain the elastic scattering at higher resolution for the $^{\mathrm{N}}\mathrm{Ge}^{\mathrm{N}}\mathrm{Se}_2$ sample. These measurements were used to find the mean squared displacement as a function of temperature by comparing the total and elastic scattering as described in section 6.3.5 at temperatures between 10 K and 280 K. The mean squared displacement increases from 0.006(3) to 0.0375(60) $\mathrm{Å}^2$, while the first peak position shifts from 10.31(10) to 10.70(10) meV as the temperature increases from 10 to 280 K.

The method for estimating the multiple scattering was successfully implemented, with results that agree with expectations for the low temperature measurement. The method for calculating the multiple phonon scattering described in section 4.1.4 was successfully used for both the low and room temperature (292 K) data as judged by good agreement between both datasets after the correction was made (see figure 6-31). In the case of the room temperature measurements, multiple phonon scattering was very large.

The results were of good enough precision for the "silver medal" approximation to be used to calculate the partial vibrational density of states in each case. The results for MERLIN experiments 2 and 3 and the MARI experiment are in good agreement with each other, and the calculation of $G_1(E)$ in the "bronze medal" approximation for $^{\mathrm{N}}\mathrm{Ge}^{\mathrm{N}}\mathrm{Se}_2$ is in good agreement with the experimental data taken from refs [51, 130, 164] and the simulations taken from ref. [35]. The results from the "silver medal"

approximation are in good agreement with the simulated data, within a shift in E.

The current study shows that the density of states features two peaks at ≈ 9.8 and ≈ 26.5 meV, and a broad feature above 34 meV. The first peak has contributions from Ge and Se atoms roughly weighted by their atomic concentrations, the second peak has contributions mostly from Se while the third region has roughly equal contributions from Ge and Se. With the aid of the simulations, these regions were associated with local rocking, bending and stretching motions of the Se atoms in tetrahedral structural motifs.

7. Vibrational Density of States of GeO_2 Glass Using the MARI Spectrometer

7.1 Introduction

As discussed in chapter 5, the development of models for glassy materials depends on good experimental data with which to test their accuracy. For the $GeSe_2$ system investigated in chapters 5 and 6, the extreme incoherent approximation was valid for the natural isotopic abundance. In the case where the masses and scattering lengths are different, $G_1(E)$ calculated in this way can deviate significantly from the true density of states $Z(E)$ [181]. For example, in the case of SiO_2, the difference is as much as 20% of the measured density of states [182]. It is therefore necessary to either combine simulations with experimental data to modify the measured density of states (as discussed in [181, 182]) or to measure the full partial vibrational density of states as discussed in section 2.2.3. For the latter, the method of isotope substitution in neutron spectroscopy can be used.

GeO_2 glass fulfills the conditions whereby both chemical species of natural isotopic abundance have different scattering lengths and masses. The ^{N}Ge and O coherent scattering lengths are 8.185(20) and 5.803(4) fm [113], while their atomic weights are 72.64 and 15.9995 g, respectively, where N denotes the natural isotopic abundance. However, there is a large scattering length contrast between the Ge isotopes, where $b(^{70}\mathrm{Ge})$ and $b(^{73}\mathrm{Ge})$ are 10.0(1) and 5.02(4) fm, respectively. This makes GeO_2 a good candidate for isotope substitution experiments, such as the successful neutron diffraction experiments described in refs. [175, 183].

GeO_2 is part of a family of archetypical strong network glass forming systems which includes SiO_2 and BeF_2 [184]. Many models have been used to simulate the properties of these glasses [36, 37, 44, 131, 162, 185–190]. Data are also available for the differential scattering cross sections of $^{N}GeO_2$, $^{70}GeO_2$ and $^{73}GeO_2$ [175] and for the

vibrational density of states of $^{N}GeO_2$ in the extreme incoherent ("bronze medal") approximation [191, 192]. The partial vibrational density of states would, therefore, provide additional information to test the simulations and help in analysing previous experimental results.

In this chapter, the method of isotope substitution in neutron spectroscopy is used to measure the partial vibrational density of states of GeO_2 in the "silver medal" approximation. Using the MARI spectrometer (see section 3.2.1), two experiments were done, the first using an incident neutron energy of 48.3 meV and the second using an incident neutron energy of 173.6 meV. In the first experiment, the resolution of the elastic line was good enough that an estimate of the elastic differential scattering cross section could be obtained. This was used to calculate the Debye-Waller factor. In the second experiment, the vibrational density of states of GeO_2 was obtained over its full range using the Debye-Waller factor that was found in the first experiment.

The chapter is organised as follows. In section 7.2 the experimental procedure is presented. In section 7.3 the results of the experiment done using an incident neutron energy of 48.3 meV are presented and the Debye-Waller factor is calculated. In section 7.4 the data analysis procedure for the experiment done using an incident neutron energy of 173.6 meV is given, where at each stage the total vibrational density of states $G(E)$ is calculated within the extreme incoherent ("bronze medal") approximation and the results are presented before and after each correction to show their effect. Corrections are made for the empty can scattering including beam attenuation and intensity renormalisation (section 7.4.3), multiple scattering (section 7.4.4), and multiple phonon scattering (section 7.4.5). The matrices used to calculated the partial dynamical structure factors are presented in section 7.5.

In section 7.6 the results are given in the "bronze medal" and "silver medal" approximations. They are compared with the *ab initio* simulations made using a GGA functional for GeO_2 by Giacomazzi *et al.* [36, 37, 44] (model I from ref. [36]) as well as the classical MD simulations of Marrocchelli *et al.* [38], where a dipole-polarizable-ion model [193, 194] was used. Finally the efficacy of the experimental and data analysis procedures is discussed in section 7.7 and conclusions are drawn in section 7.8.

7.2 Experimental Method

7.2.1 Sample Preparation

Three isotopically enriched glassy samples were prepared in an identical way. Approximately 2 g of $^{N}GeO_2$ (99.9999 %, Alfa Aesar), $^{70}GeO_2$ (with a Ge isotopic abundance of 97.71 % ^{70}Ge, 2.23 % ^{72}Ge, 0.02 % ^{73}Ge, 0.03 % ^{74}Ge, 0.01 % ^{76}Ge, Isoflex) or

$^{73}GeO_2$ (with an Ge isotopic abundance of 0.04 % ^{70}Ge, 2.84 % ^{72}Ge, 96.07 % ^{73}Ge, 1.03 % ^{74}Ge, 0.02 % ^{76}Ge, Isoflex) powder was dried in a Pt (10 % Rh) crucible for 2 h at 200 °C. The powder was then melted in air at 1400 °C for 30 min after which the crucible was placed on a liquid nitrogen cooled brass block and doused with liquid nitrogen. The crucible was subsequently warmed to room temperature using a heat gun, to avoid condensation of atmospheric water, and the clear glass was then removed as large shards (with a small surface area) and stored in an Ar filled glovebox to prevent contamination by atmospheric water.

For each experiment, the large shards of GeO_2 glass were placed in a He glovebox, ground into a coarse powder using a mortar and pestle, and then loaded into or unloaded from aluminium foil packets. After use in each experiment (where all experiments were done under vacuum or a He atmosphere), the samples were sealed in glass bottles in an argon filled glovebox and placed inside a bomb. Any contamination by water could lead to a change in e.g. the diffraction patterns.

The properties of the isotopically enriched samples that are relevant to the present neutron scattering experiments are given in table 7.1. It is assumed that the samples have a number density equal to the room temperature value for the $^{N}GeO_2$ sample, which is 0.0629(1) Å^{-3} [175].

	$^{N}GeO_2$	$^{70}GeO_2$	$^{73}GeO_2$
$\overline{M}$ (g)	34.8629	33.9900	34.9678
M_{Ge} (g)	72.5900	69.9712	72.9047
M_O (g)	15.9994	15.9994	15.9994
$\left\langle \bar{b}^2 \right\rangle$ (barn)	0.4478(11)	0.5560(7)	0.3128(14)
$\bar{b}_{Ge}$ (fm)	8.185(2)	9.965(10)	5.15(4)
$\bar{b}_O$ (fm)	5.803(4)	5.803(4)	5.803(4)

Table 7.1: Specific parameters for the isotopically enriched samples that were measured using the MARI spectrometer at the ISIS pulsed neutron source where $\overline{M}$ is the average atomic mass for the sample, M_α is the average atomic mass of an atom of chemical species α, $\bar{b}_\alpha$ is the average coherent scattering length of chemical species α and $\left\langle \bar{b}^2 \right\rangle = \sum c_\alpha \bar{b}_\alpha^2$ is the mean square coherent scattering length. The scattering lengths were calculated using the values taken from reference [113]. N denotes the natural isotopic abundance.

7.2.2 Neutron Spectroscopy Measurements

Two experiments (summarised in table 7.2) were done on the MARI spectrometer at the ISIS Pulsed Neutron Source in Didcot (see section 3.2.1). The first experiment was done using neutrons with an incident energy of 48.3(1) meV selected by a Fermi chopper spinning at a frequency of 200 Hz and the second experiment was done using neutrons

with an incident energy of 173.6(1) meV selected by a Fermi chopper spinning with a frequency of 350 Hz. In both experiments, a "Gd" type Fermi chopper was used. This transmits a high intensity of neutrons with low energy resolution and selects an almost monochromatic incident beam of neutrons centred on the incident neutron energy. For this configuration, the MCHOP software [168] was used to give the estimated incident neutron flux and full width at half maximum (FWHM) in energy of the elastic line given in table 7.2. The energy resolution and detector coverage of the spectrometer under

Label	Experiment 1	Experiment 2
Incident energy (meV)	48.3(1)	173.6(1)
Temperature (K)	10	10
Fermi chopper freq. (Hz)	200	350
Est. incident flux (n s^{-1})	9040	11405
Est. FWHM of elastic line (meV)	1.94	7.57

Table 7.2: Instrument configurations for the MARI spectrometer used for experiments 1 and 2. The FWHM of the elastic line and incident flux were estimated using the MCHOP [168] software.

these conditions is shown in figure 7-1 for the measurements made with $E_i = 48.3$ meV and in figure 7-2 for the measurements made with $E_i = 173.6$ meV. The samples

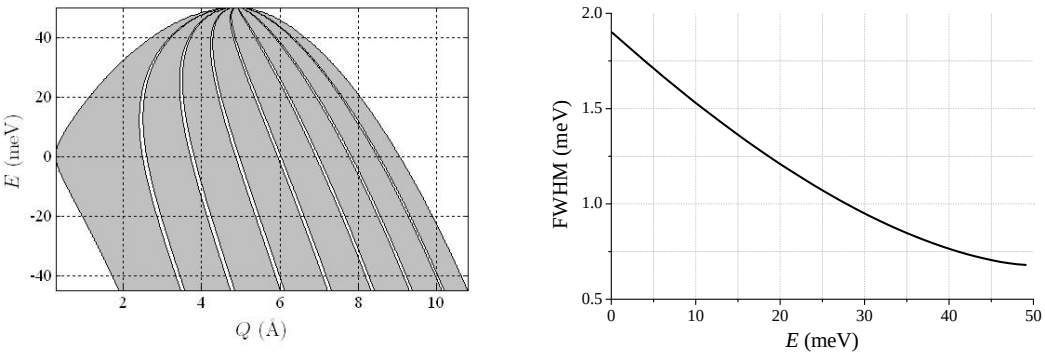

(a) *(b)*

Figure 7-1: (a) The kinematically allowed region and (b) the energy resolution full width at half maximum (FWHM) calculated using the MCHOP program [168] for the GeO_2 experiment done using the MARI spectrometer using an incident energy of 48.3(1) meV and Fermi chopper frequency of 200 Hz. In (a) the accessible Q-E space is shaded in grey i.e. there are gaps between the different detector groups (see section 3.2.1).

(masses given in table 7.3) were loaded in the same way as in the experiment described in section 5.2.2. The GeO_2 powder was loaded into packets made from 0.013(1) mm thick aluminium foil in a He filled glovebox. Each loaded sample was wrapped around

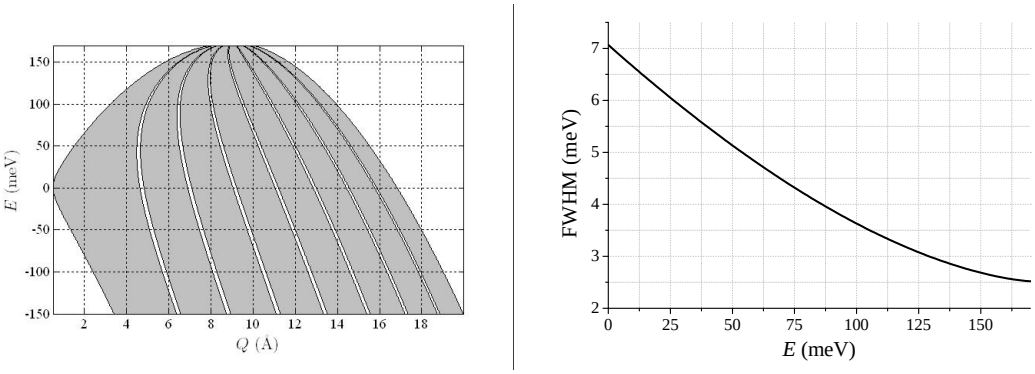

(a) *(b)*

Figure 7-2: (a) The kinematically allowed region and (b) the energy resolution full width at half maximum (FWHM) calculated using the MCHOP program [168] for the GeO_2 experiment done using the MARI spectrometer using an incident energy of 173.6(1) meV and Fermi chopper frequency of 350 Hz. In (a) the accessible Q-E space is shaded in grey i.e. there are gaps between the different detector groups (see section 3.2.1).

Sample	Sample Mass (g)	Proton Charge (μA h)
$^{N}GeO_2$	3.8298(1)	4512.9
$^{70}GeO_2$	1.9181(1)	6353.4
$^{73}GeO_2$	1.9318(1)	5026
Empty Can A	N/A	3884.5
Empty Can B	N/A	4768.8

Table 7.3: The mass of sample used together with the charge of protons that was incident on the spallation target during each measurement made using neutrons with an incident energy of 173.6(1) meV. The latter is proportional to the number of neutrons that were incident on the sample during that measurement. The $^{N}GeO_2$ sample and Empty Can A were also used in the first experiment done using an incident energy of 48.3 meV.

the inside surface of a cylindrical aluminium can of thickness 0.10(1) mm and diameter of 42 mm to form an annular sample geometry. A 1 mm thick cadmium plate was used to cover the top of the can and provide shielding. The can was then attached to a "candle stick" and the assembly was placed into a CCR in the neutron beam. The CCR was purged with He gas three times, then a pressure of 26 mbar of He gas was let into the sample chamber for heat exchange with the CCR. The samples were cooled to 10(1) K. The incident beam profile was square with a height of 35.0 mm and width of 50.0 mm centred on the foil packet such that the entire sample was illuminated by neutrons.

Using an incident neutron energy of 48.3(1) meV, two measurements were taken under identical conditions for a sample of $^{\mathrm{N}}GeO_2$ in an aluminium foil packet and an empty Al foil packet for a period of time until a proton charge of 2780 or 2098.3 μA h were reached, respectively. A further measurement for a short amount of time was made at room temperature using vanadium.

Due to practical difficulties, two experiments (A and B) had to be made at different times for the measurements using an incident neutron energy of 173.6(1) meV. In experiment A, three measurements were made for a sample of $^{\mathrm{N}}GeO_2$ in an Al foil packet and an empty foil packet in can A; and vanadium. The sample and empty can used in experiment A were the same as those used in experiment 1. In experiment B, four measurements were made under identical conditions for samples of $^{70}GeO_2$, and $^{73}GeO_2$ in an Al foil packet, an empty Al foil packet in can B and vanadium. Both experiments, made at an incident energy of 173.6(1) meV, are hereafter treated as a single experiment, where the corrections for $^{\mathrm{N}}GeO_2$ are made using empty can A and vanadium measurement A, and the corrections for $^{70}GeO_2$ and $^{73}GeO_2$ are made using empty can B and vanadium measurement B. The different measurements are summarised in table 7.3.

A further measurement was made using a solid annular vanadium sample at room temperature for detector calibration using an incident beam containing a wide range of neutron energies (i.e. a so-called white beam).

7.3 The Debye-Waller Factor

The Debye-Waller factor was found from experiment 1, which was made using an incident neutron energy of 48.3(1) meV. In these measurements, the resolution function broadened elastic peak is sharper and thus there is a smaller contribution from inelastic scattering.

7.3.1 Width of the Elastic Line

The elastic line resolution broadening is described in section 5.3.1. Figure 7-3 shows, for the vanadium sample, the broadening of the elastic line due to the effect of the energy resolution function of the instrument for an incident energy of 48.3(1) meV. A range of $-7 \leq E \leq 6$ meV was selected by eye to define the extent of the elastic line where the limits are shown in figure 7-3 as dotted lines. An assumption is made that all of the scattering inside this range is elastic. Therefore, an integral over this peak will represent the elastic differential scattering cross section.

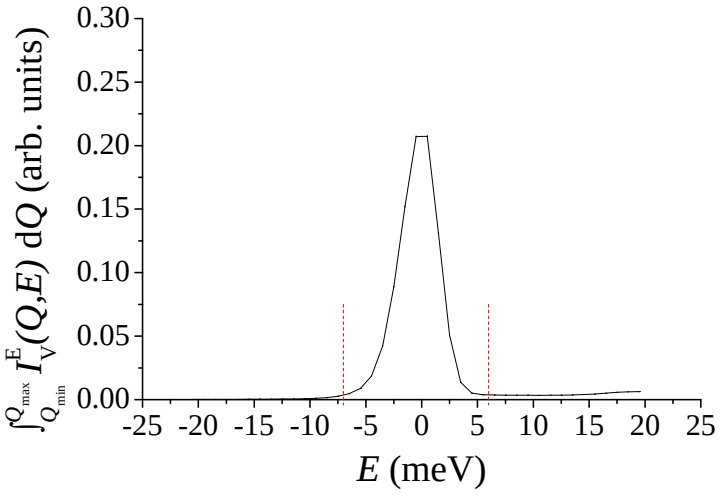

Figure 7-3: The width of the elastic line due to energy resolution broadening from the monochromatic vanadium measurement represented by the function $\int_{Q_{\min}}^{Q_{\max}} I_{\mathrm{E}}^{\mathrm{V}}(Q,E)\,\mathrm{d}Q$ where, for each value of E, $Q_{\min}$ and $Q_{\max}$ are the minimum and maximum Q values that can be measured. Dotted lines indicate the energy transfer range for which the measured intensity is mostly elastic. The data have been normalised such that the integral under the curve is unity.

7.3.2 Background Subtraction with Attenuation Correction and Renormalisation

The normalised sample-in-can scattered intensity $I_{\mathrm{sc}}^{\mathrm{E}}(Q,E)$ and empty can scattered intensity $I_{\mathrm{c}}^{\mathrm{E}}(Q,E)$ were measured for the $^{\mathrm{N}}GeO_2$ sample. The scattered intensity for the sample $I_{\mathrm{s}}(Q,E)$ was found by using equation (4.6) which, for convenience, is re-written here:

$$I_{\mathrm{s}}(Q,E) = \frac{m}{A_{\mathrm{sc,sc}}(Q,E)}\left(I_{\mathrm{sc}}^{\mathrm{E}}(Q,E) - I_{\mathrm{c}}^{\mathrm{E}}(Q,E)\right)\,, \tag{7.1}$$

where $A_{\mathrm{sc,sc}}(Q,E)$ is the attenuation coefficient (figure 7-4) found by treating the sample-in-can as a single annular sample with effective parameters for $^{\mathrm{N}}GeO_2$ given

in table 7.4 and m is a renormalisation constant.

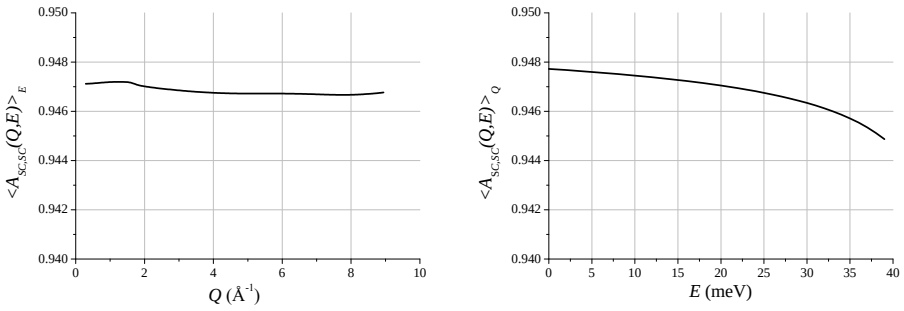

(a) Q Dependence *(b)* E Dependence

Figure 7-4: The attenuation coefficients $A_{\mathrm{sc,sc}}(Q,E)$ for a sample of $^{\mathrm{N}}\mathrm{Ge}^{\mathrm{N}}\mathrm{O}_2$ averaged (a) over energies between 0 and 30 meV and (b) over all Q values. The coefficients were calculated using the parameters for $^{\mathrm{N}}\mathrm{GeO}_2$ given in table 7.4.

At low Q, the effect of the Debye-Waller factor is small and $\mathrm{d}\sigma/\mathrm{d}\Omega|_{\mathrm{el}} \approx \mathrm{d}\sigma/\mathrm{d}\Omega$. Therefore, m was chosen by eye such that the first peak in $\mathrm{d}\sigma/\mathrm{d}\Omega|_{\mathrm{el}} = \int_{E_{\mathrm{min}}}^{E_{\mathrm{max}}} I_{\mathrm{s}}(Q,E)\mathrm{d}E$ at $Q \approx 1.5$ Å^{-1} agreed with $\mathrm{d}\sigma/\mathrm{d}\Omega$ from a diffraction experiment made on the D4C diffractometer at the Institut Laue-Langevin (ILL) by Salmon *et al.* [175], where E_{min} and E_{max} are -7 and 6 meV, respectively (see figure 7-5). The value of m thus obtained is 0.99. There are still Al Bragg peaks present in $I_{\mathrm{s}}(Q,E)$, although the effect is not as

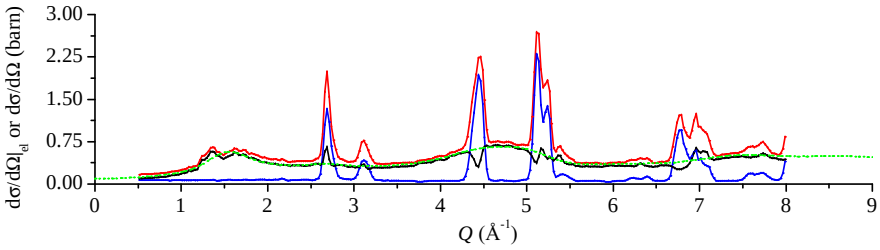

Figure 7-5: The elastic differential scattering cross section $\mathrm{d}\sigma/\mathrm{d}\Omega|_{\mathrm{el}}$ for a sample of $^{\mathrm{N}}\mathrm{GeO}_2$ calculated for the sample-in-can $\int_{E_{\mathrm{min}}}^{E_{\mathrm{max}}} I_{\mathrm{sc}}^{\mathrm{E}}(Q,E)\mathrm{d}E$ (solid red curve), empty can $\int_{E_{\mathrm{min}}}^{E_{\mathrm{max}}} I_{\mathrm{c}}^{\mathrm{E}}(Q,E)\mathrm{d}E$ (solid blue curve) and corrected sample $\int_{E_{\mathrm{min}}}^{E_{\mathrm{max}}} I_{\mathrm{s}}(Q,E)\mathrm{d}E$ (solid black curve) intensities, where E_{min} and E_{max} are -7 and 6 meV, respectively. The datasets are compared to the total scattering cross section $\mathrm{d}\sigma/\mathrm{d}\Omega$ from a diffraction experiment by Salmon *et al.* [175] where $\mathrm{d}\sigma/\mathrm{d}\Omega = F(Q) + \sigma_{\mathrm{self}}/4\pi$ (broken green curve).

bad as found for the $GeSe_2$ samples described in section 5.3.3.

7.3.3 Fitting the Debye-Waller Factor

In equation (2.62) the $F(Q)$ function deduced from the elastic scattering is given by

$$F(Q) = \left.\frac{\mathrm{d}\sigma}{\mathrm{d}\Omega}\right|_{\mathrm{el}} - e^{-2\overline{W}(Q)} \sum_{\alpha=1}^{n} c_\alpha(\bar{b}_\alpha^2 + b_{\mathrm{inc},\alpha}^2) \,, \tag{7.2}$$

where $\sum_{\alpha=1}^{n} c_\alpha(\bar{b}_\alpha^2 + b_{\mathrm{inc},\alpha}^2) = 0.4526$ barn is the self scattering limit. $\overline{W}(Q)$ was chosen such that $F(Q)$ given by equation (7.2) and $F(Q)$ from a diffraction experiment made by Salmon *et al.* [63] were in as close agreement as possible at high Q (see figure 7-6). The Debye-Waller factor thus found gave $2\overline{W}(Q)/Q^2 = \langle u^2 \rangle /3 = 0.0015(10)$ Å^2. In

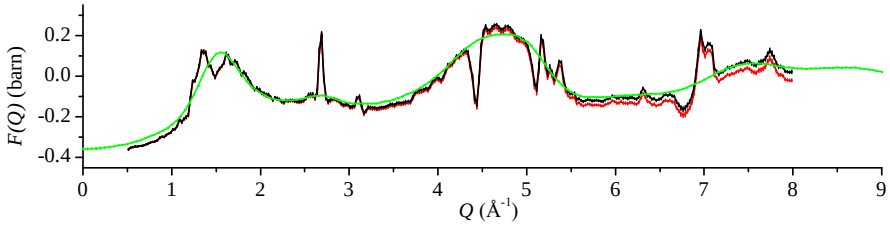

Figure 7-6: The $F(Q)$ functions for $^{\mathrm{N}}\mathrm{GeO}_2$ calculated using $F(Q) = \int_{E_{\min}}^{E_{\max}} I_{\mathrm{s}}(Q,E)\mathrm{d}E - \sum_\alpha^n c_\alpha(\bar{b}_\alpha^2 + b_{\mathrm{inc},\alpha}^2)$ (solid red curve), $F(Q) = \int_{E_{\min}}^{E_{\max}} I_{\mathrm{s}}(Q,E)\mathrm{d}E - \sum_\alpha^n c_\alpha(\bar{b}_\alpha^2 + b_{\mathrm{inc},\alpha}^2)\exp\left(-2\overline{W}(Q)\right)$ (solid black curve) and from the diffraction experiment by Salmon *et al.* [175] (solid green curve), where $E_{\min}$ and $E_{\max}$ are -7 and 6 meV, respectively, while $\overline{W}(Q) = Q^2 \langle u^2 \rangle /3$ with $\langle u^2 \rangle /3$ given in table 6.4.

figure 7-7 the value for $\langle u^2 \rangle /3$ is plotted together with values of $\langle u^2 \rangle /3$ for Ge and O in GeO_2 as found from the *ab initio* MD simulations made by Giacomazzi *et al.* [34].

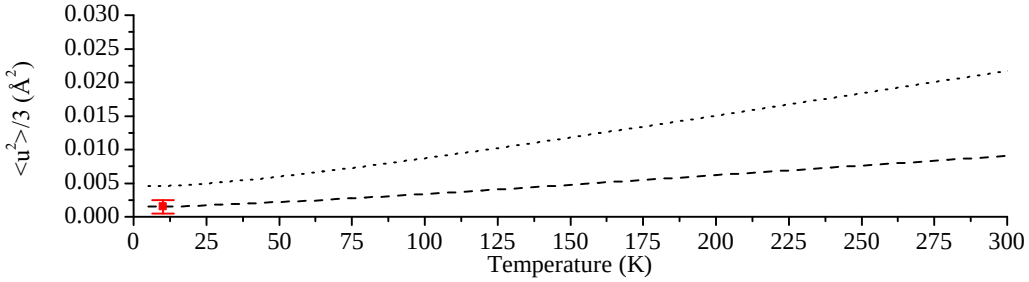

Figure 7-7: Temperature dependence of the mean squared displacement $\langle u^2 \rangle /3$ found for Ge (dashed line) and O (dotted line) from *ab initio* MD simulations by Giacomazzi *et al.* [34] compared to the average $\langle u^2 \rangle /3$ value found in the current work (closed red square).

7.4 The Vibrational Density of States of GeO_2

Data taken at the incident energy of 173.6 meV were used to find the vibrational density of states of GeO_2. The data analysis procedure for these measurements follows the general correction procedure described in section 4.1.

7.4.1 Width of the Elastic Line

The width of the elastic line is discussed in section 5.3.1. Figure 7-8a shows, for a vanadium sample, the broadening of the elastic line due to the effect of the energy resolution of the instrument. A range of $-20 \leq E \leq 16$ meV was selected by eye to define the extent of the elastic line where the limits are shown in figure 7-8a as dotted lines. Outside of this range, scattering is deemed to be fully inelastic. The range is

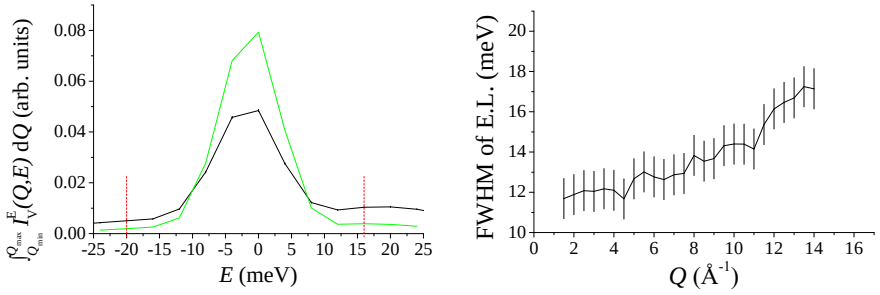

(a) *(b)*

Figure 7-8: (a) The width due to energy resolution broadening of the elastic peak from the monochromatic vanadium measurement as represented by the function $\int_{Q_{\min}}^{Q_{\max}} I_{\mathrm{V}}^{\mathrm{E}}(Q,E)\,\mathrm{d}Q$, where for each value of E, $Q_{\min}$ and $Q_{\max}$ are the minimum and maximum Q values that can be measured (solid black curve) or $Q_{\max}$ is fixed at 6 Å^{-1} (solid green curve) to show how the inelastic scattering increases with Q value. Dotted lines indicate the energy transfer range for which the scattered intensity is mostly elastic at all Q values. Data have been normalised such that the integral under the curve is unity. (b) The Q dependence of the FWHM of the elastic line (E.L.) found empirically from the monochromatic vanadium measurement.

harder to distinguish at this incident energy than in the experiments made at lower incident energies (e.g. section 7.3.1) because inelastic scattering from the vanadium is larger. This arises from the higher values of Q that are accessible (up to ≈ 16 Å^{-1}), where the inelastic scattering has a Q^2 dependence (see section 2.2.1).

The range over which the elastic line is broadened is dependent on Q. The FWHM of the elastic line found empirically using the monochromatic measurement on the vanadium sample are shown in figure 7-8b. The FWHM increases from 11.7(10) to 17.1(10) meV over the range in Q from 1.5 to 14 Å^{-1}. These values differ significantly from that found using the MCHOP software [168] of 7.75 meV.

7.4.2 Bose-Einstein Occupation Factor

The Bose-Einstein occupation factor was calculated using equation (2.14) for the experimental temperature of 10 K and is given in figure 7-9. The plot shows that inelastic scattering for $E < 0$ will be very small such that only inelastic scattering for $E > 0$ will be considered.

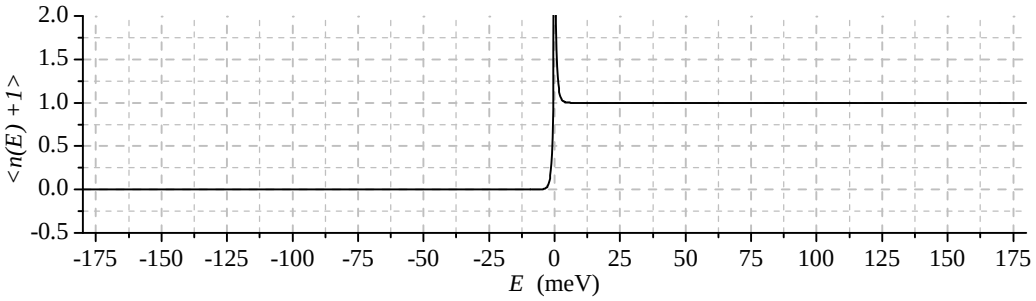

Figure 7-9: The Bose-Einstein occupation factor calculated using equation (2.14) for a temperature of 10 K.

7.4.3 Background Subtraction with Attenuation Corrections and Renormalisation

The normalised sample-in-can scattered intensity $I^{\mathrm{E}}_{\mathrm{sc}}(Q,E)$ and empty can scattered intensity $I^{\mathrm{E}}_{\mathrm{c}}(Q,E)$ were measured for each sample. The scattered intensity $I_{\mathrm{s}}(Q,E)$ for each sample was calculated by using equation (7.1), where the attenuation coefficients $A_{\mathrm{sc,sc}}(Q,E)$ (figure 7-10) were found by treating the sample-in-can as a single annular sample with effective parameters given in table 7.4 and the renormalisation constant m was found to be 0.96, 0.93 or 1.03 for the measurements on $^{\mathrm{N}}GeO_2$, $^{70}GeO_2$ and $^{73}GeO_2$, respectively. In figure 7-11 integrals of intensities are given for the sample-in-

	$^{\mathrm{N}}Ge^{\mathrm{N}}O_2$	$^{70}Ge^{\mathrm{N}}O_2$	$^{73}Ge^{\mathrm{N}}O_2$
Inner Radius (cm)	2.065	2.0736	2.0739
Outer Radius (cm)	2.1	2.1	2.1
Eff. Number Density ($\mathrm{\AA}^{-3}$)	0.0620	0.0616	0.0615
Eff. Total Scattering Cross Section (barn)	4.24(1)	4.21(5)	2.94(5)
Eff. Abs. Cross Section at 2200 ms^{-1} (barn)	0.560(9)	0.602(3)	2.48(6)

Table 7.4: Parameters used to calculate $A_{\mathrm{sc,sc}}(Q,E)$. The parameters for each pseudo sample were calculated using neutron scattering and absorption cross sections taken from ref. [113], a GeO_2 number density of 0.0629 $\mathrm{\AA}^{-3}$ [195] and an Al number density of 0.06026 $\mathrm{\AA}^{-3}$ [165].

can measurement $\int_{E_{\min}}^{E_{\max}} I^E_{sc}(Q,E)\mathrm{d}E$, empty can measurement $\int_{E_{\min}}^{E_{\max}} I^E_{c}(Q,E)\mathrm{d}E$ and

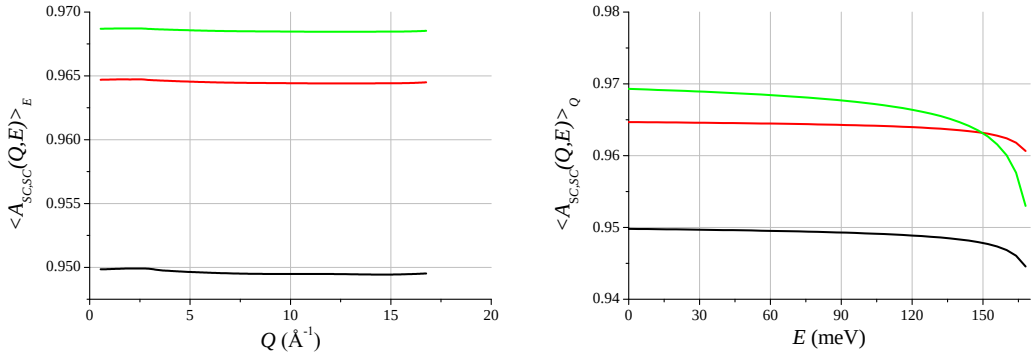

(a) Q Dependence *(b)* E Dependence

Figure 7-10: The attenuation coefficients $A_{\mathrm{sc,sc}}(Q,E)$ for samples of $^{\mathrm{N}}GeO_2$ (solid black curve) $^{70}GeO_2$ (solid red curve) and $^{73}GeO_2$ (solid green curve) averaged (a) over energies between 0 and 145 meV or (b) over all Q values. The coefficients were calculated using the parameters taken from table 7.4. The maximum energy for the vibrational density of states is $\sim$ 150 meV (see e.g. figure 7-14).

corrected sample scattering $\int_{E_{\mathrm{min}}}^{E_{\mathrm{max}}} I_s(Q,E)\mathrm{d}E$, where E_{min} and E_{max} are the minimum ($\geq$ -150 meV) and maximum ($\leq$ 150 meV) energies which were measured at a given Q value. These integrals represent the differential scattering cross sections and are presented to show the effect that scattering from the can has on the sample-in-can measurements. The differential scattering cross sections from Salmon *et al.* [175] that were used to find m are also plotted in figure 7-11. Some Al Bragg peaks remain in $I_{\mathrm{s}}(Q,E)$. The effect of the background, attenuation and renormalisation corrections on the $G(E)$ function is shown in figure 7-12 for the $^{\mathrm{N}}GeO_2$ sample where the appropriate values for $^{\mathrm{N}}GeO_2$ have been taken from table 7.1 and used in equation (2.45).

7.4.4 Multiple Scattering Correction

The approximate method used to calculate the multiple scattering contributions to the inelastic part of the $I_{\mathrm{s}}(Q,E)$ functions is given in section 4.1.3. The incoherent approximation given by $I_{\mathrm{s}}(Q,E) = I_{\mathrm{ms}}(E) + B(E)Q^2\exp(-2\overline{W}(Q))$ (equation (4.7)) could not be fitted directly to the $I_{\mathrm{s}}(Q,E)$ functions at each measured E value due to a large statistical error. As explained in section 6.4.4, the multiple scattering contribution to $G(E)$ for cold samples roughly follows the density of states. Therefore, for the multiple scattering contribution, $I_{\mathrm{ms}}(E)$ was estimated by using the expression

$$I_{\mathrm{ms}}(E) = C_{\mathrm{ms}}G_{\mathrm{uncor}}(E)\frac{\langle n(E)+1\rangle}{E}\ , \tag{7.3}$$

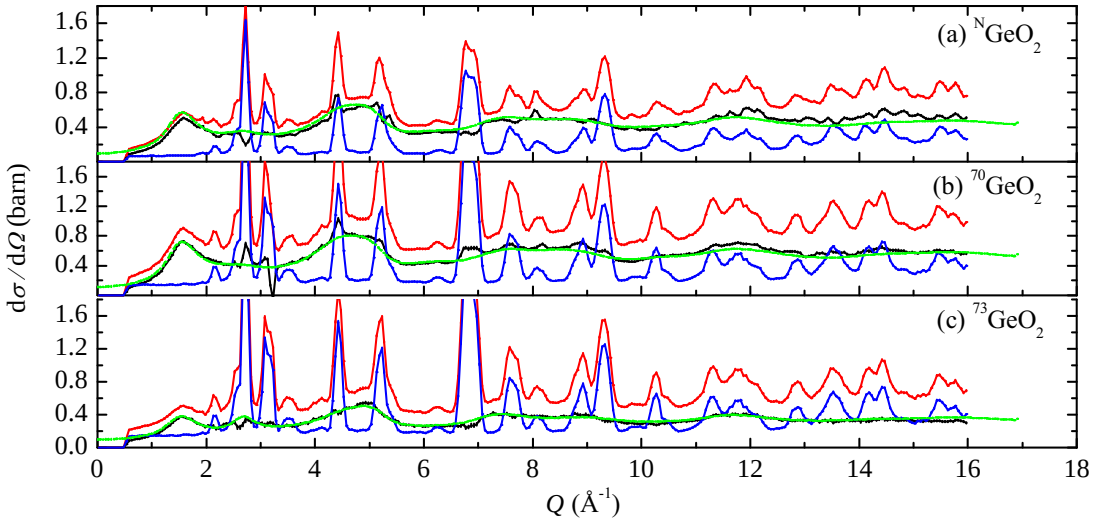

Figure 7-11: The differential scattering cross section $\mathrm{d}\sigma/\mathrm{d}\Omega$ for samples of (a) $^{\mathrm{N}}\mathrm{GeO}_2$, (b) $^{70}\mathrm{GeO}_2$ and (c) $^{73}\mathrm{GeO}_2$ calculated using the sample-in-can $\int_{E_{\min}}^{E_{\max}} I_{sc}^{\mathrm{E}}(Q,E)\mathrm{d}E$ (solid red curve), empty can $\int_{E_{\min}}^{E_{\max}} I_{c}^{\mathrm{E}}(Q,E)\mathrm{d}E$ (solid blue curve), and corrected sample $\int_{E_{\min}}^{E_{\max}} I_{\mathrm{s}}(Q,E)\mathrm{d}E$ (solid black curve) intensities, where $E_{\min}$ and $E_{\max}$ are the minimum (≥ -150 meV) and maximum (≤ 150 meV) energies that were measured at a given Q value. Also plotted is $\mathrm{d}\sigma/\mathrm{d}\Omega = F(Q) + \sigma_{\mathrm{self}}/4\pi$ from the diffraction experiment by Salmon *et al.* [175] (solid green curve).

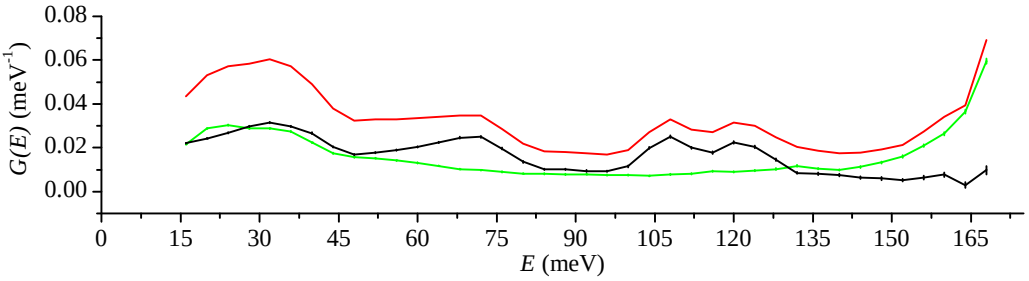

Figure 7-12: $G(E)$ for the $^{\mathrm{N}}\mathrm{GeO}_2$ sample calculated in the "bronze medal" approximation from $I_{\mathrm{sc}}^{\mathrm{E}}(Q,E)$ for the sample-in-can (solid red curve), from $I_{\mathrm{c}}^{\mathrm{E}}(Q,E)$ for the empty can (solid green curve), and from $I_{\mathrm{s}}(Q,E)$ for the sample after correction for the empty can scattering, attenuation and renormalisation (solid black curve) . No correction for the multiple scattering or multiple phonon scattering has been applied.

where $G_{\mathrm{uncor}}(E)$ is the density of states calculated without the correction for multiple scattering or multiple phonon scattering and C_{ms} is a constant which was selected using the method described in section 5.3.4. The fits to the $I_{\mathrm{s}}(Q,E)$ functions were compared to the $I_{\mathrm{s}}(Q,E)$ functions by integrating over several broad ranges in E, an example of which is given in figure 7-13.

The coherent dynamical structure factor is given by $S_{\mathrm{c}}(Q,E) = I_{\mathrm{s}}(Q,E) - I_{\mathrm{ms}}(E)$ (see equation (4.9)). Using equations (2.44) and (2.45) for the "bronze medal" approximation, the $G(E)$ functions that were calculated for the three samples using the appropriate values from table 7.1 and either $I_{\mathrm{s}}(Q,E)$, $S_{\mathrm{c}}(Q,E)$ or $I_{\mathrm{ms}}(E)$ are given in figure 7-14.

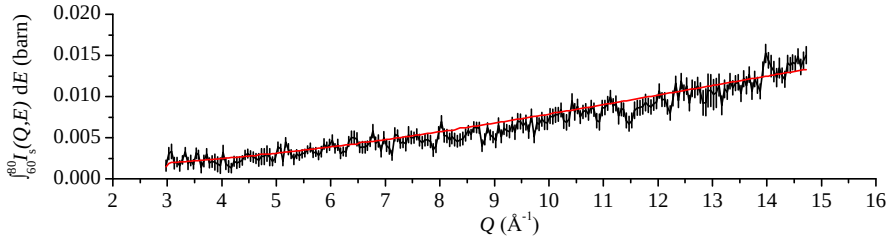

Figure 7-13: $I_{\mathrm{s}}(Q,E)$ for the $^{70}GeO_2$ sample (solid black curve) and a fit to the data using $I_{\mathrm{s}}(Q,E) = I_{\mathrm{ms}}(E) + B(E)Q^2\exp\left(-2\overline{W}(Q)\right)$ (solid red curve), where $I_{\mathrm{ms}}(E)$ is defined in equation (7.3). To improve the statistics, the functions have been integrated over the energy transfer range from 60 to 80 meV.

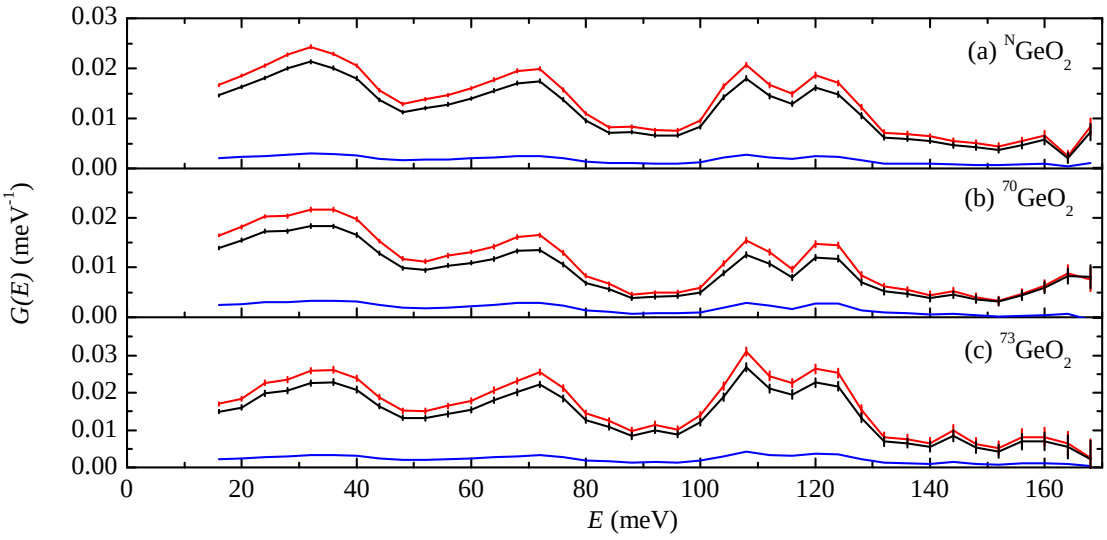

Figure 7-14: $G(E)$ calculated in the "bronze medal" approximation for samples of (a) $^{N}GeO_2$, (b) $^{70}GeO_2$ or (c) $^{73}GeO_2$ using $I_{\mathrm{s}}(Q,E)$ (solid red curve), $I_{\mathrm{ms}}(E)$ (solid blue curve), or $S_{\mathrm{c}}(Q,E) = I_{\mathrm{s}}(Q,E) - I_{\mathrm{ms}}(E)$ (solid black curve) and the values taken from table 7.1.

7.4.5 Multiple Phonon Correction

To assist in the calculation of the multiple phonon corrections, $G(E)$ was calculated from $S_c(Q,E)$ using equations (2.44) and (2.45) with the appropriate values given in table 7.1. The Debye model [172] was used in the region which could not be measured (below 16 meV) due to broadening of the elastic scattered intensity. In the Debye model, $G(E) \propto E^2$ and the constant of proportionality was chosen such that the Debye model fit coincided with the first measured data point beyond the region of the elastic peak.

The multiple phonon correction, $S_{mp}(Q,E)$, was then calculated up to the 5^{th} phonon term using the method described in section 4.1.4. The vibrational density of states calculated from $S_c(Q,E)$ without the multiple phonon correction $G(E)$, the multiple phonon contribution to the vibrational density of states $G_{mp}(E)$ and the single phonon vibrational density of states $G_1(E) = G(E) - G_{mp}(E)$ are plotted in figure 7-15. The single phonon dynamical structure factor was found from the expression $S_1(Q,E) =$

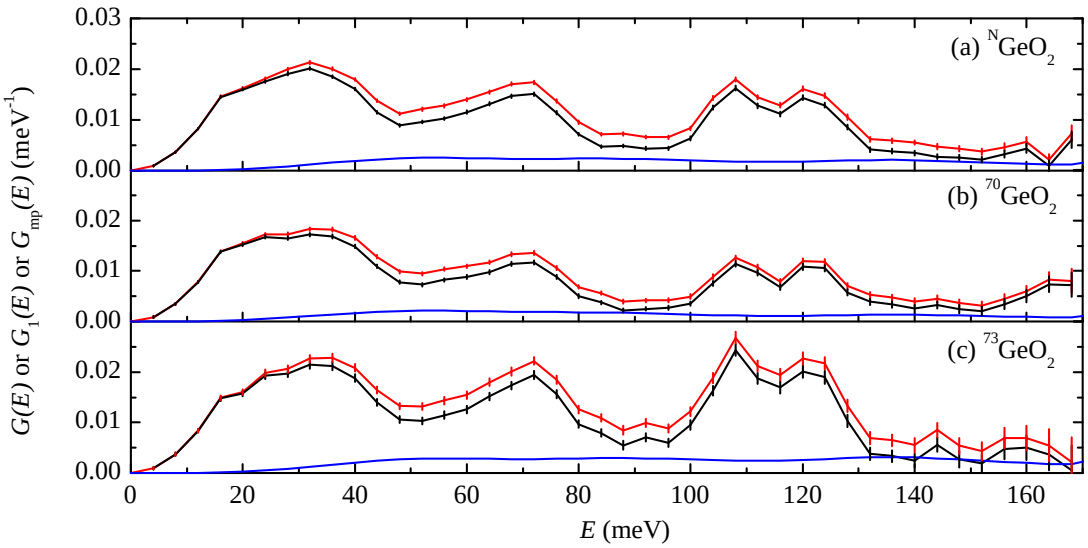

Figure 7-15: $G(E)$ calculated in the "bronze medal" approximation from $S_c(Q,E)$ without the multiple phonon correction (solid red curve), the calculated multiple phonon correction to the vibrational density of states $G_{mp}(E)$ (solid blue curve) and the single phonon vibrational density of states $G_1(E) = G(E) - G_{mp}(E)$ (solid black curve) for samples of (a) $^{N}GeO_2$, (b) $^{70}GeO_2$ or (c) $^{73}GeO_2$.

$S_c(Q,E) - S_{mp}(Q,E)$ (equation (4.22)). An example of the dynamical structure factor thus obtained is given in figure 7-16 for the $^{N}GeO_2$ sample, where $S_c(Q,E)$, $S_1(Q,E)$ and $S_{mp}(Q,E)$ are integrated over two energy transfer ranges of (a) 20 to 40 meV or (b) 100 to 130 meV. In all cases the empty can, attenuation, renormalisation and multiple

scattering corrections have been made.

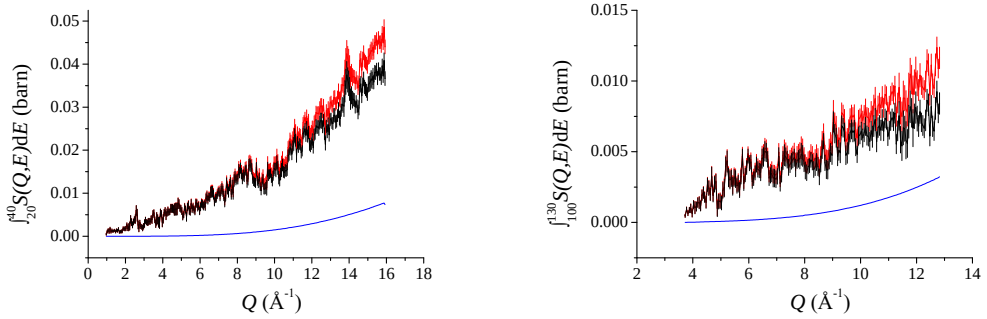

(a) 20 to 40 meV

(b) 100 to 130 meV

Figure 7-16: The $S_{\mathrm{c}}(Q,E)$ function (solid red curve), the multiple phonon contribution $S_{\mathrm{mp}}(Q,E)$ (solid blue curve) and the single phonon contribution calculated using $S_1(Q,E) = S_{\mathrm{c}}(Q,E) - S_{\mathrm{mp}}(Q,E)$ (solid black curve) for the $^{\mathrm{N}}GeO_2$ sample, where each function has been integrated over an energy transfer range of (a) 20 to 40 meV or (b) 100 to 130 meV. In all cases the empty can, attenuation, renormalisation and multiple scattering corrections have been made.

7.5 "Silver Medal" Calculations

Once the data had been fully corrected, the "silver medal" results were calculated. Three different matrices were used as described in section 2.2.4 where, using the values given in table 7.1, for the $^{\mathrm{N}}GeO_2$ and $^{70}GeO_2$ samples

$$\begin{pmatrix} S'_{\mathrm{GeGe}}(Q,E) \\ S'_{\mathrm{OO}}(Q,E) \end{pmatrix} = \begin{pmatrix} -201.5221 & 201.5221 \\ 135.8768 & -88.3653 \end{pmatrix} \begin{pmatrix} {}_{\mathrm{N}}S_1\,(Q,E) \\ {}_{70}S_1\,(Q,E) \end{pmatrix}, \tag{7.4}$$

for the $^{\mathrm{N}}GeO_2$ and $^{73}GeO_2$ samples

$$\begin{pmatrix} S'_{\mathrm{GeGe}}(Q,E) \\ S'_{\mathrm{OO}}(Q,E) \end{pmatrix} = \begin{pmatrix} 178.7686 & -178.7686 \\ -30.8767 & 78.3881 \end{pmatrix} \begin{pmatrix} {}_{\mathrm{N}}S_1\,(Q,E) \\ {}_{73}S_1\,(Q,E) \end{pmatrix} \tag{7.5}$$

and for the $^{70}GeO_2$ and $^{73}GeO_2$ samples

$$\begin{pmatrix} S'_{\mathrm{GeGe}}(Q,E) \\ S'_{\mathrm{OO}}(Q,E) \end{pmatrix} = \begin{pmatrix} 94.7323 & -94.7323 \\ -16.3620 & 63.8735 \end{pmatrix} \begin{pmatrix} {}_{70}S_1\,(Q,E) \\ {}_{73}S_1\,(Q,E) \end{pmatrix}. \tag{7.6}$$

In these matrices, ${}_xS_1(Q,E)$ denotes the single phonon total dynamical structure factor, measured for a sample of $^{x}GeO_2$, where $x = \mathrm{N}, 70$ or 73 and N denotes the natural

isotopic abundance.

Using the method of singular value decomposition [173], the following matrix for a set of "silver medal" results was also used, where the data taken from all three isotopically enriched samples contribute to the final result

$$\begin{pmatrix} S'_{\mathrm{GeGe}}(Q,E) \\ S'_{\mathrm{OO}}(Q,E) \end{pmatrix} = \begin{pmatrix} 3.77418 & 92.73233 & -96.50650 \\ 14.21998 & -23.89742 & 57.18893 \end{pmatrix} \begin{pmatrix} {}_{\mathrm{N}}S_1(Q,E) \\ {}_{70}S_1(Q,E) \\ {}_{73}S_1(Q,E) \end{pmatrix}. \tag{7.7}$$

The partial vibrational density of states, $G_\alpha(E)$ were calculated using equations (2.38) and (2.39) with Debye-Waller factors of $W_{\mathrm{Ge}}(Q) = W_{\mathrm{O}}(Q) = \overline{W}(Q) = 0.0015Q^2$. The results are given in figure 7-17. There is a significant difference between $G_{\mathrm{Ge}}(E)$ ob-

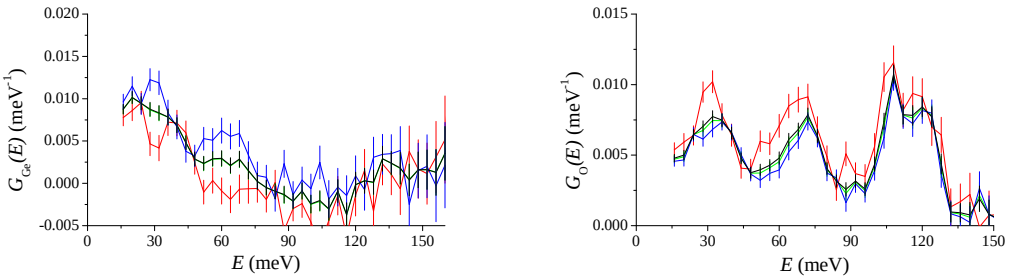

(a) $G_{\mathrm{Ge}}(E)$ *(b)* $G_{\mathrm{O}}(E)$

Figure 7-17: The partial vibrational density of states obtained in the "silver medal" approximation for (a) $G_{\mathrm{Ge}}(E)$ or (b) $G_{\mathrm{O}}(E)$ calculated using equation (7.4) (solid red curve), equation (7.5) (solid green curve), equation (7.6) (solid blue curve) or equation (7.7) (solid black curve).

tained using each of the four different matrices in the "silver medal" approximation (see figure 7-17), particularly for the two results that made use of the data measured for the $^{\mathrm{N}}GeO_2$ sample. The result for which the $^{\mathrm{N}}GeO_2$ measurement has a positive weighting in the matrix (equation (7.5)) consistently overestimates $G_{\mathrm{Ge}}(E)$, while the result for which the $^{\mathrm{N}}GeO_2$ measurement has a negative weighting in the matrix (equation (7.4)) consistently underestimates $G_{\mathrm{Ge}}(E)$ when compared to the result which does not feature data taken for the $^{\mathrm{N}}GeO_2$ sample (using equation (7.6)). This deviation is particularly evident for the features at $E \approx 30, 62$ and 104 meV. The measurement on the $^{\mathrm{N}}GeO_2$ sample was taken at a different time to the measurements made using the $^{70}GeO_2$ and $^{73}GeO_2$ samples, so there may be small differences in the setup and background scattering. If this has not been subtracted properly, then small effects that might otherwise cancel in the "silver medal" approximation will instead remain. All

results for $G_{\mathrm{Ge}}(E)$ in the "silver medal" approximation feature unexplained, unphysical negative values above $E \approx 80$ meV. Meanwhile, all of the results for $G_{\mathrm{O}}(E)$ in the "silver medal" approximation are in good agreement, with the exception of the result obtained using samples with the lowest scattering length contrast (equation (7.4)).

The *ab initio* MD simulations made by Giacomazzi *et al.* [36] show that for GeO_2, the "silver medal" approximation gives $G_\alpha(E)$ functions that are close to the true partial vibrational density of states $Z_\alpha(E)$ (see figure 7-18).

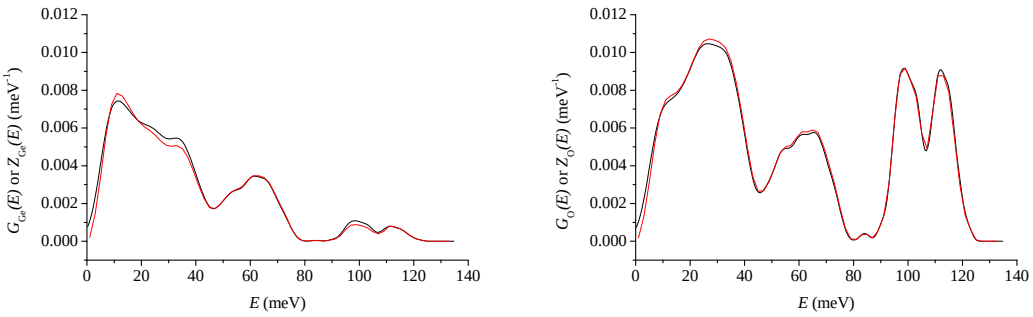

(a) $G_{\mathrm{Ge}}(E)$ or $Z_{\mathrm{Ge}}(E)$ *(b)* $G_{\mathrm{O}}(E)$ or $Z_{\mathrm{O}}(E)$

Figure 7-18: Comparison of the contributions from (a) Ge and (b) O to the true vibrational density of states of GeO_2 (solid black curves) and the vibrational density of states calculated in the "silver medal" approximation (solid red curves) obtained from the *ab initio* MD simulations by Giacomazzi *et al.* [36].

7.6 Results

7.6.1 Generalised Vibrational Density of States

The generalised single phonon vibrational density of states $G_1(Q, E)$ for the $^{\mathrm{N}}GeO_2$ sample (figure 7-19) and generalised single phonon partial vibrational density of states $G_\alpha(Q, E)$ from the SVD matrix (equation (7.7)) (figure 7-20) were calculated by using equations (2.44) and (2.38), respectively. To improve the statistics, integrals of these functions were taken over three ranges of energy representing the three peaks in $G_1(E)$ (see e.g. figure 7-22). The first peak is from 16 to 44 meV, the second peak is from 56 to 84 meV and the third peak is from 100 to 132 meV. The generalised vibrational density of states $G_1(Q, E)$ for a sample of $^{\mathrm{N}}GeO_2$ and the generalised partial vibrational density of states $G_\alpha(Q, E)$ calculated by Giacomazzi *et al.* from *ab initio* MD simulations [34] are also plotted in figures 7-19 and 7-20. The integration ranges chosen for the simulation data are different to those for the experimental data because there

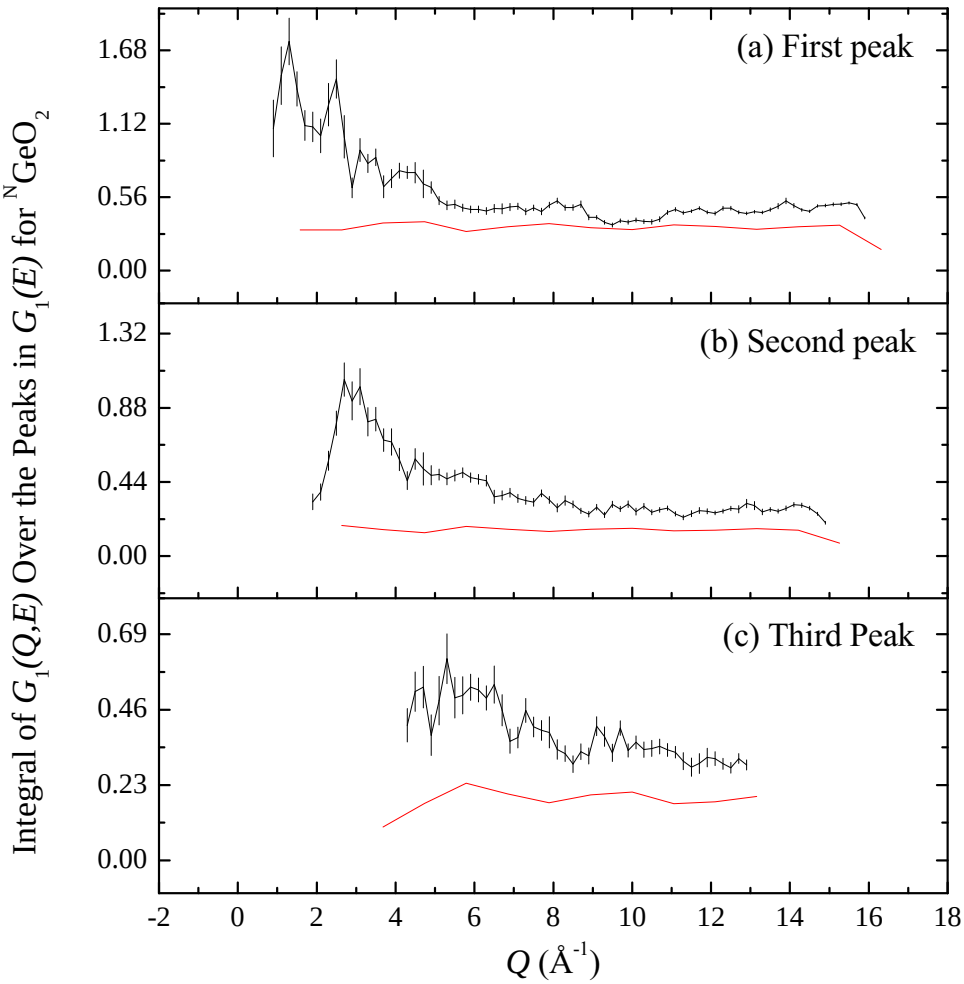

Figure 7-19: The integral of $G_1(Q, E)$ over (a) the first peak, or (b) the second peak, or (c) the third peak in $G_1(E)$ for a sample of $^{N}GeO_2$. The curves correspond to those obtained from the present experimental study (solid black curves) and from the *ab initio* MD simulations done by Giacomazzi *et al.* [34] (solid red curves). The limits for the integrals are given in the text.

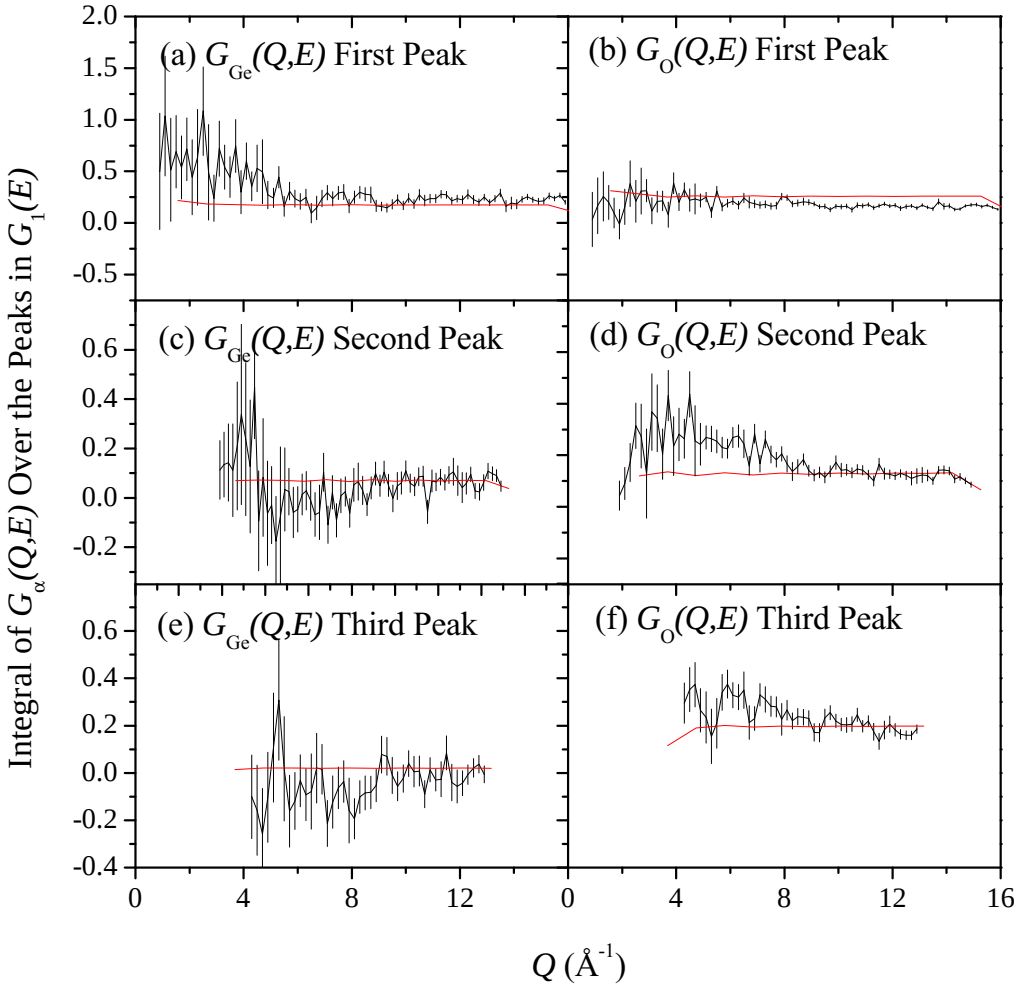

Figure 7-20: The integral of either $G_{\mathrm{Ge}}(Q,E)$ or $G_{\mathrm{O}}(Q,E)$ over (a) and (b) the first peak, or (c) and (d) the second peak, or (e) and (f) the third peak in $G_1(E)$, respectively, obtained from the present experimental study (solid black curves) or from the *ab initio* MD simulations done by Giacomazzi *et al.* [34] (solid red curves). $G_{\mathrm{Ge}}(E)$ and $G_{\mathrm{O}}(E)$ have been calculated in the "silver medal" approximation using the SVD matrix in equation 7.7. The limits for the integrals are given in the text.

is a relative shift of the peaks in $G_1(E)$ as demonstrated in figure 7-22. Ranges that cover the same peaks were therefore used for the *ab initio* MD results, in this case 10 to 38 meV for the first peak, 48 to 77 meV for the second peak and 90 to 122 meV for the third peak.

7.6.2 Single Phonon Vibrational Density of States

The results in the "bronze medal" approximation for the samples of $^{N}GeO_2$, $^{70}GeO_2$ and $^{73}GeO_2$ are compared in figure 7-21. In figure 7-22 a comparison is made between

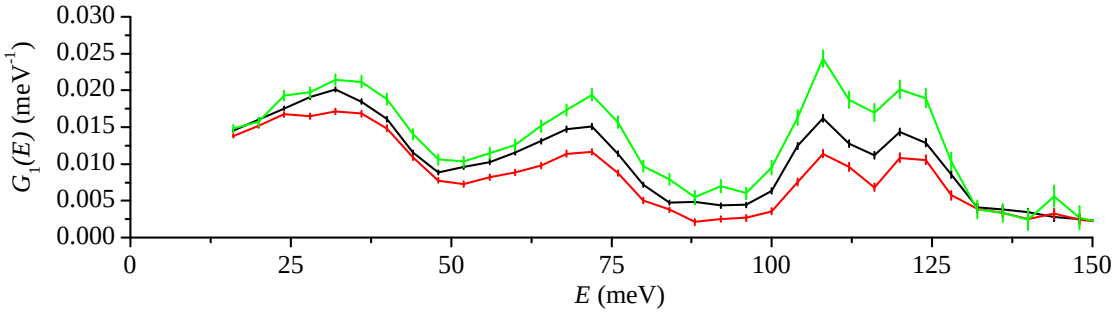

Figure 7-21: The fully corrected single phonon vibrational density of states $G_1(E)$ calculated using the "bronze medal" approximation for samples of $^{N}GeO_2$ (solid black curve), $^{70}GeO_2$ (solid red curve) and $^{73}GeO_2$ (solid green curve).

the $G_1(E)$ functions calculated for $^{N}GeO_2$ using the "bronze medal" approximation in the present work, the experimental results of Galeener *et al.* [192] and Pilla *et al.* [191], the *ab initio* MD simulation results of Giacomazzi *et al.* [36, 37, 44], and the exact vibrational density of states $Z(E)$ calculated from classical MD simulations by Marrocchelli *et al.* [38]. In figure 7-23, $G_1(E)$ calculated in the "bronze medal" approximation for $^{N}GeO_2$ is compared with $G_1(E) = G_{Ge}(E) + G_O(E)$ calculated in the "silver medal" approximation using the SVD matrix for both the present study and the MD simulations made by Giacomazzi *et al.* [36]. Finally, in figure 7-24, the $G_\alpha(E)$ functions calculated in the "silver medal" approximation using the SVD matrix (equation (7.7)) are compared to the $G_\alpha(E)$ functions calculated in the "silver medal" approximation from the *ab initio* simulation data.

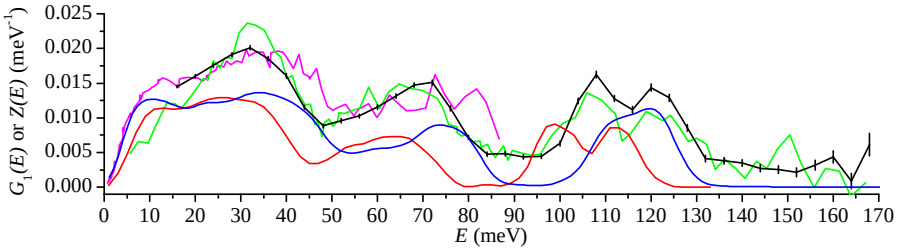

Figure 7-22: The single phonon density of states $G_1(E)$ calculated using the "bronze medal" approximation for a sample of $^{N}GeO_2$ as obtained in the present work (solid black curve), from a study using the IN4 time of flight spectrometer at the Institut Laue-Langevin, France at ambient temperature with an incident neutron energy of 16.9 meV in neutron energy gain mode by Pilla *et al.* [191] (solid magenta curve), from a study made at ambient temperature using the neutron Be filter spectroscopy method at the PLUTO reactor of the Atomic Energy Research Establishment, UK by Galeener *et al.* [192] (solid green curve). The other experimental results were not measured on an absolute scale and have been scaled to best fit with the present work. The experimental data are compared to the *ab initio* MD simulations made by Giacomazzi *et al.* [36] (solid red curve) and the exact vibrational density of states $Z(E)$ from the classical MD simulations made by Marrocchelli *et al.* [38] (solid blue curve).

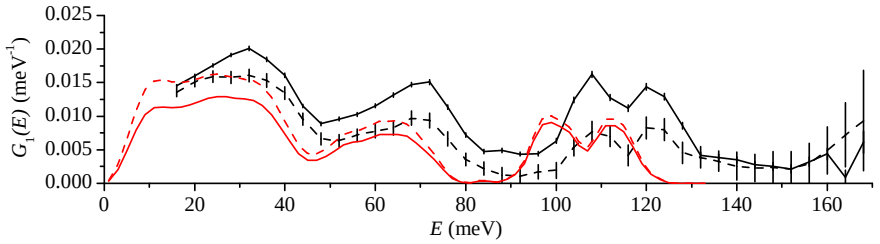

Figure 7-23: $G_1(E)$ obtained using either the "bronze medal" approximation for the $^{N}GeO_2$ sample (solid curves) or from the expression $G_1(E) = G_{Ge}(E) + G_O(E)$ for the "silver medal" SVD results (broken curves). The functions are obtained from the present study (black) and the *ab initio* MD simulations made by Giacomazzi *et al.* [36] (red).

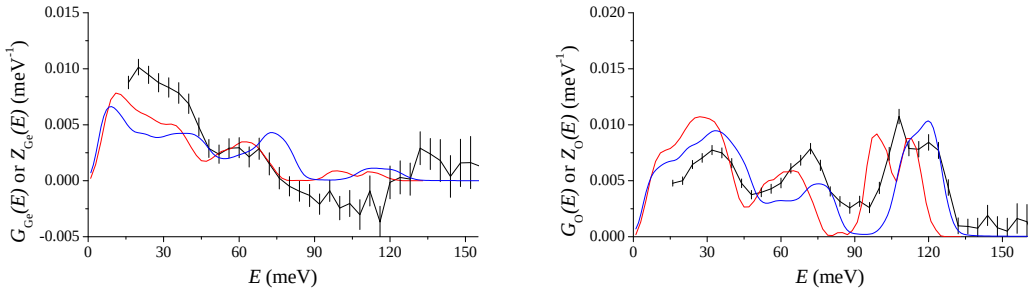

(a) *(b)*

Figure 7-24: Comparison of the partial vibrational density of states $G_\alpha(E)$ calculated in the "silver medal" approximation using the SVD matrix (equation 7.7) (solid black curves) with those calculated from the *ab initio* MD simulations made by Giacomazzi *et al.* [36] (solid red curves) and the exact partial vibrational density of states $Z_\alpha(E)$ calculated from the classical MD simulations made by Marrocchelli *et al.* [38] (solid blue curves) for (a) Ge or (b) O.

7.7 Discussion

There is a significant discrepancy in scaling between $G_1(E)$ calculated for $^{N}GeO_2$ in the "bronze medal" approximation from the current work and $G_1(E)$ calculated from the *ab initio* MD simulations of Giacomazzi *et al.* [36, 37, 44] (figure 7-22). This is despite there being good agreement between the measured differential scattering cross sections and the results found from a diffraction study by Salmon *et al.* [175] (figure 7-11). The simulations were made using the "bronze medal" approximation so this difference cannot be attributed to the approximations that were made in obtaining $G_1(E)$ from the experimental data. The origin of this discrepancy is unknown. The previous measurements of $G_1(E)$ made by Pilla *et al.* [191] and Galeener *et al.* [192] were presented on an arbitrary scale, while the classical MD simulations made by Marrocchelli *et al.* [38] did not take into account the experimental approximations and so their scales cannot be directly compared to the present work.

The "silver medal" results found using the SVD matrix (equation (7.7)) are in qualitative agreement with the *ab initio* MD simulations made by Giacomazzi *et al.* [36, 37, 44] and the classical MD simulations made by Marrocchelli *et al.* [38], except for the unphysical negative values of $G_{Ge}(E)$ in the experimental data. There is a systematic shift in E of the vibrational density of states between the experimental data and the simulations of Giacomazzi *et al.* [36, 37, 44]. Similar systematic shifts in the vibrational density of states are found from *ab initio* MD models of the crystalline phases of GeO_2 [196]. When this shift is taken into account, by scaling the E axis of the results obtained from the simulations made by Giacomazzi *et al.* [36, 37, 44] by a factor of 1.1, then the sum of the "silver medal" results in the present study $G_1(E) = G_{Ge}(E) + G_O(E)$ is in excellent agreement with the simulations (see figure 7-25). The simulations

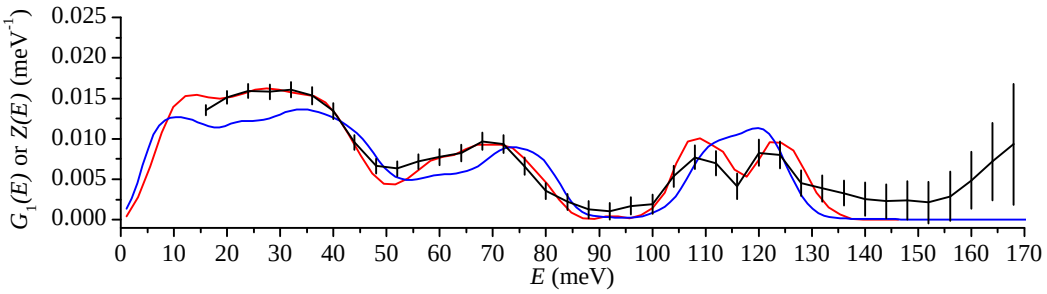

Figure 7-25: $G_1(E)$ obtained from the expression $G_1(E) = G_{Ge}(E) + G_O(E)$ for the present study (black), the *ab initio* simulations made by Giacomazzi *et al.* [36], where the E axis has been scaled by 1.1 (solid red curve) and the true vibrational density of states $Z(E)$ obtained from MD simulations by Marrocchelli *et al.* [38] (solid blue curve).

of Marrocchelli *et al.* [38] show only one peak in $G_O(E)$ at $E > 90$ meV instead

of two as found in the present study and in the simulations made by Giacomazzi *et al.* [36, 37, 44]. This peak splitting is seen in both GeO_2 and SiO_2 from experiments using optical spectroscopy or neutron scattering [192, 197, 198] and has been attributed to a splitting in energy of the local symmetric and asymmetric stretching modes of the tetrahedral units (see the top of figure 6-39 for a representation of these modes). For a detailed explanation focused on SiO_2 see refs. [162, 199, 200], while for GeO_2 see ref. [44].

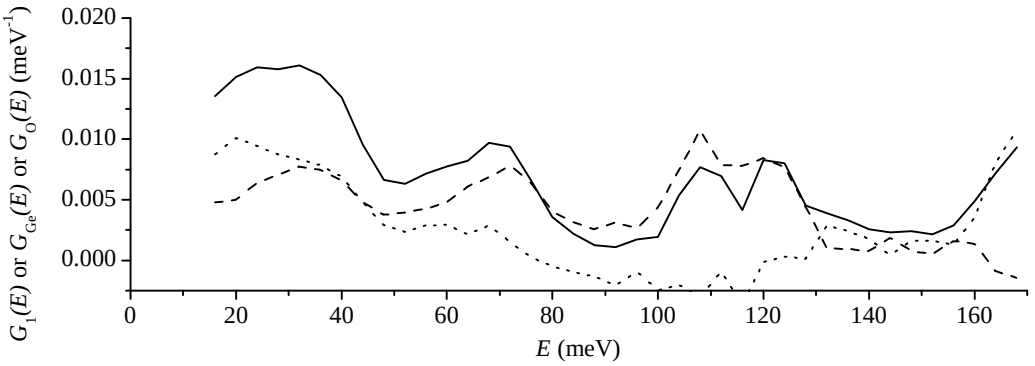

Figure 7-26: $G_1(E) = G_{Ge}(E) + G_O(E)$ (solid curve), $G_{Ge}(E)$ (dotted curve) and $G_O(E)$ (dashed curve) calculated in the "silver medal" approximation using the SVD matrix (equation (7.7)). Error bars have been omitted for clarity of presentation.

There are four distinct peaks in $G_1(E)$. In the first peak at 31.52(5) meV the weighting of the Ge and O contributions to the full vibrational density of states is approximately 1:1 (see figure 7-26). In the second peak at 70.37(5) meV the weighting is approximately the same as the atomic concentrations of 1/3 and 2/3 for Ge and O respectively. The third and fourth peaks at 108.09(5) and 120.73(5) meV have contributions mainly from the O atoms. This indicates that the motions of Ge and O is highly correlated for modes with energies up to approximately 95 meV (90 meV in the *ab initio* simulated data), above which the motion of the heavier Ge atoms become less important [36]. In addition, the *ab initio* MD simulations made by Giacomazzi [36, 37, 44] and the classical MD simulations made by Marrocchelli *et al.* [38] show that for GeO_2 there are three bands of energy related to different types of motion (examples are given at the top of figure 6-39). In the simulations by Giacomazzi *et al.* [36] the lower band up to $\approx$ 47 meV is due to O rocking motions, the middle band from $\approx$ 47 to 87 meV is due to O bending motions and the upper band, above $\approx$ 87 meV, is mostly due to O stretching motions. These bands correspond to ranges of 0 to 47, 47 to 95 and 95 to 145 meV in the experimental data, respectively.

The vibrational spectra of GeO_2 and SiO_2 [198] have similar modes as seen in infrared and Raman scattering studies [123, 201–205], although there is a shift between

the spectra that is attributed to the difference in mass between Si and Ge [202]. A similar scenario is found for the vibrational density of states measured by neutron spectroscopy in the "bronze medal" approximation (figure 7-27). In table 7.5, the

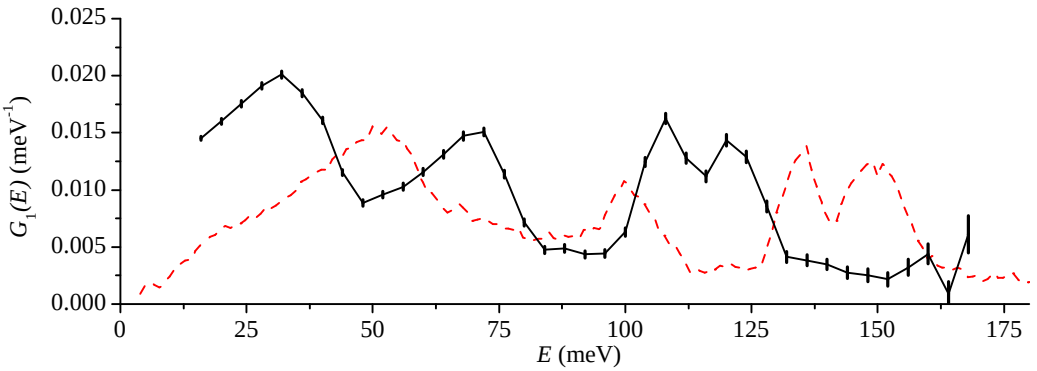

Figure 7-27: Comparison of $G_1(E)$ calculated in the "bronze medal" approximation for GeO_2 (solid black curve) and for SiO_2 measured on the MARI spectrometer by Haworth *et al.* [182] (broken red curve). The data are for samples of natural isotopic abundance.

positions of the four peaks in $G_1(E)$ are presented, as found from $G_1(E)$ calculated for $^{N}GeO_2$ in the "bronze medal" approximation in the present work and as found in the most recent measurements on SiO_2 made by Haworth *et al.* [182]. Also shown are the peak positions found from the sum of the "silver medal" results, which exhibit a small shift relative to the "bronze medal" results. The bands of energy for the O motions in

	GeO_2 position (meV)		SiO_2 position (meV)	Shift (meV)
	Bronze	Silver	Bronze	
First Peak	31.52(5)	32.48(5)	53.3(2)	21.78
Second Peak	70.37(5)	69.10(5)	102.2(2)	31.83
Third Peak	108.09(5)	108.94(5)	135.8(2)	27.71
Fourth Peak	120.73(5)	121.78(5)	150.3(2)	29.57

Table 7.5: The positions of the first four peaks in $G_1(E)$ for GeO_2 and SiO_2 calculated in the "bronze medal" approximation. Shift denotes the position of the GeO_2 peak subtracted from the position of the SiO_2 peak. Also given are the peak positions of the first four peaks in the "silver medal" approximation where $G_1(E) = G_{Ge}(E) + G_O(E)$. The peak positions for SiO_2 are taken from ref. [182].

SiO_2 correspond to rocking (from 0 to $\approx$ 70 meV), bending (from $\approx$ 70 to $\approx$ 120 meV) and stretching (above $\approx$ 120 meV) motions as found from the *ab initio* MD simulations made by Pasquarello *et al.* [200].

7.8 Conclusion

The partial vibrational density of states have been measured in the "silver medal" approximation for the GeO_2 system, where the extreme incoherent ("bronze medal") approximation does not give a good approximation to the true vibrational density of states. The partial vibrational density of states obtained in the present study show qualitative agreement with results obtained from the *ab initio* MD simulations made by Giacomazzi *et al.* [36, 37, 44] and the classical MD simulations made by Marrocchelli *et al.* [38]. The partial vibrational density of states calculated from MD simulations made by Giacomazzi *et al.* [36, 37, 44] exhibit a shift in E but contain features corresponding to those of the experimental data while the classical MD simulations made by Marrocchelli *et al.* [38] do not exhibit this shift but do not reproduce the correct high E behaviour.

Similar to the other inelastic neutron scattering experiments described in this thesis (chapters 5 and 6), the quality of the final results is limited by the ability to measure accurate single phonon dynamical structure factors for three isotopically enriched samples. These limitations include the ability to subtract unwanted scattering from sources other than the sample, the accuracy of the multiple scattering and multiple phonon corrections. For instance, there are unphysical negative values of $G_{\mathrm{Ge}}(E)$ in regions for which the *ab initio* MD simulations of Giacomazzi *et al.* [36, 37, 44] and the classical MD simulations of Marrocchelli *et al.* [38] indicate that $G_{\mathrm{Ge}}(E) \approx 0$. Further investigations are required to solve these issues.

Despite the limitations of the correction procedure, the measured functions agree well with other neutron spectroscopy experiments [191, 192]. The technique requires further development but already leads to results that can be reliably compared to simulations. Simulations can then be used to calculate quantities that are difficult to access experimentally such as the intermediate range ordering or properties of materials under conditions that currently cannot be accessed by experiment (e.g. under pressure [206]). The technique of isotopic substitution in neutron spectroscopy adds to the suite of experimental methods that can be used to test simulations.

8. Changes in the Structure of GeO_2 Glass with Pressure Using the PEARL Diffractometer

8.1 Introduction

Understanding the structure of silicates under pressure is important for understanding geological processes because they form the most abundant materials in the Earth's crust [39, 207, 208]. The first step for understanding the properties of silicates is to understand the structure of silica (SiO_2) and other similar network glass formers. SiO_2 is a "strong" network forming glass similar to GeO_2 and BeF_2 [184]. SiO_2 and GeO_2 share several structural and chemical characteristics and are often regarded as analogues [123, 209]; although some differences do exist in the intermediate range ordering [210]. The structures of both GeO_2 and SiO_2 (figure 8-1) are based on an open arrangement of tetrahedral motifs connected at their corners with a large mean inter-tetrahedral angle of $\gtrsim 132^\circ$ [12, 175, 192, 211–213]. This structure undergoes significant transformations with increasing pressure [40, 123, 215–225]. In SiO_2, there is a transformation in the local ordering from 4-fold coordinated tetrahedra to 6-fold coordinated octahedra at pressures up to 50 GPa [125, 215, 219, 221, 225–228]. GeO_2 has analogous structural transformations but at much lower pressures as found from a variety of spectroscopic [216, 217, 229–231], x-ray diffraction [110, 220, 223, 232] and neutron diffraction [39, 40] studies. This makes GeO_2 a material that is more amenable to *in situ* high pressure neutron diffraction experiments, where the range of pressures that can be reached is limited.

The use of X-rays with small diamond anvil cells [233, 234] and established data correction procedures [235] allows for the investigation of SiO_2 under pressures from ambient to above 50 GPa. However, for neutron diffraction experiments, current studies on amorphous solids have reached only ≈ 9 GPa due to the necessary use of a Paris-Edinburgh press as described in section 3.4.

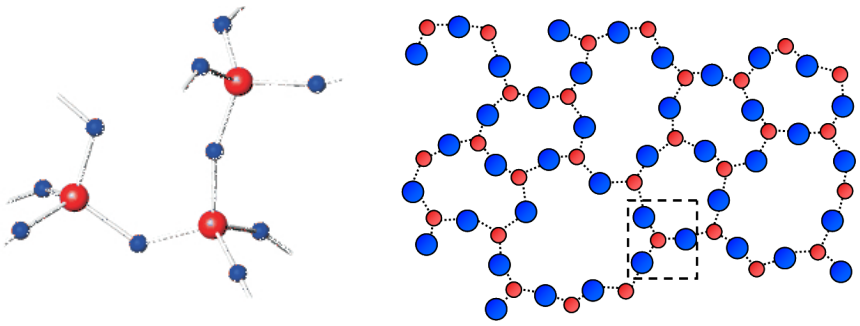

(a) *(b)*

Figure 8-1: The structure of AO_2, where A is either Ge or Si. Atoms of chemical species A are represented in red and atoms of chemical species O are represented in blue for (a) a 3-Dimensional representation from reference [214] and (b) a 2-Dimensional projection of the structure. The broken box in (b) surrounds the tetrahedral structural motif, where one O atom is out of the plane of the image and is not shown.

Neutron diffraction is complimentary to x-ray diffraction as it leads to different weighting factors for the $S_{\alpha\beta}(Q)$ functions in the measured $F(Q)$ pattern. Also, with high quality data, the method of isotopic substitution in neutron diffraction [5, 175, 236] can be used with many glasses to obtain the $S_{\alpha\beta}(Q)$ and $g_{\alpha\beta}(Q)$ functions that describe fully the pair distribution of atoms of species β around atoms of species α. While this is a technique that is well developed for ambient conditions, for examples see references [14, 173, 237, 238], no such experiments have yet been done at high pressures. Therefore, neutron scattering experiments would add greatly to the structural information already available from x-ray diffraction. To achieve the high quality data required, the experimental method and data analysis procedure must first be perfected.

The method of measuring the structure of amorphous solids using neutron diffraction at high pressures is constantly under development to improve both the quality of data and the limit of the highest pressure that can be reached. Some of the first studies on GeO_2 were done at pressures below 5 GPa with high statistical and systematic errors [220]. More recently, successful experiments yielding high quality data have been done for pressures $\lesssim 9$ GPa by using Boron-Nitride (BN) anvils with a Paris-Edinburgh press [40, 239, 240]. To reliably obtain pressures higher than ≈9 GPa, sintered diamond anvils must be used. In this case, there is significantly higher scattering from the anvils with large diamond Bragg scattering and absorption edge effects. This leads to severely contaminated diffraction patterns. Indeed, the first neutron diffraction experiments on samples of amorphous SiO_2 [72] could not measure the total structure factor $F(Q)$ to a good enough accuracy to calculate reliable total pair distribution functions $G(r)$. However, pressures of ≈ 25 GPa were reached for the first time.

In this chapter, new *in situ* neutron diffraction results on the structure of GeO_2 at

pressures up to ≈ 17 GPa are presented. These experiments were done on the PEARL diffractometer at the ISIS pulsed neutron source. Improvements were made to the incident beam collimation and shielding of the sintered diamond anvils. In addition, the new normalisation and background correction procedure described by Drewitt [39] was improved. Measurements were made on GeO_2 samples up to pressures of 8.5 GPa and 17.5 GPa using single and double toroid sintered diamond anvils respectively. A data analysis procedure, described in section 4.2, was developed that allowed the total pair distribution function $G(r)$ to be measured with sufficient accuracy that coordination numbers and nearest neighbour distances could be calculated for the first time. This represents significant progress in neutron diffraction from amorphous solids under high pressure conditions. As well as being an important material to study, GeO_2 is a good material to test the efficacy of the new procedure; the structure is well known under ambient conditions [175] and high quality experiments are available from neutron diffraction at pressures up to ≈ 9 GPa [40], x-ray diffraction at pressures up to ≈ 16 GPa [220, 223] and Extended X-ray Absorption Fine Structure (EXAFS) spectroscopy experiments at pressures up to ≈ 44 GPa [222, 224]. Simulations are also available to compare with the experimental results [241]. The pressure range used in our experiments covers a regime where there is a substantial progression from a tetrahedral to an octahedral glass.

The experimental procedure, steps in the data analysis procedure and the resultant $F(Q)$ and $G(r)$ functions are presented as well as the coordination numbers, nearest neighbour distances and peak positions. Where possible, the results from this experiment are compared to previous measurements.

8.2 Experimental Procedure

8.2.1 Sample Preparation

Glassy samples were prepared by first drying ≈ 5 g of GeO_2 powder (99.9999 %, Alfa Aesar), contained in a Pt (10 % Rh) crucible, for 2 h at 200 °C. The powder was then melted in air at 1600 ° C for 20-30 min after which the crucible was placed on a liquid nitrogen cooled brass block and doused with liquid nitrogen. The crucible was subsequently warmed to room temperature using a heat gun, to avoid condensation of atmospheric water, and the clear glass was then removed as a single piece and stored either in a desiccator or argon filled glovebox and used to make GeO_2 pellets as below.

The high pressure experiments used sintered diamond anvils having either a single or double toroid profile as described in section 3.4. Both geometries correspond to samples that have a cylindrical core with a spherical cap placed on each flat surface

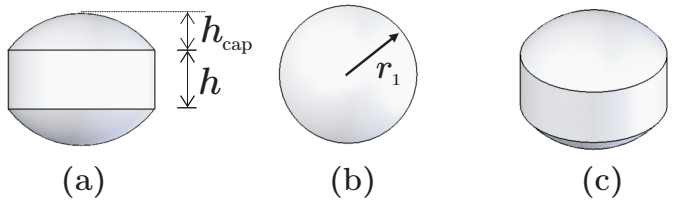

Figure 8-2: The geometry of the single and double toroid sample pellets in (a) side view, (b) top view and (c) 3-dimensional view.

(figure 8-2). The sample volume is then given by

$$V_{\text{pellet}} = 2V_{\text{cap}} + V_{\text{cyl}} = \frac{1}{3}\pi h_{\text{cap}}\left(3r_1^2 + h_{\text{cap}}^2\right) + \pi r_1^2 h \quad , \tag{8.1}$$

where V_{cap} is the volume of a cap section, V_{cyl} is the volume of the cylindrical section, r_1 is the radius of the cylindrical section and the base of the cap, h_{cap} is the height of the cap and h is the height of the cylinder. For the single toroid geometry $r_1 = 3.0$ mm, $h_{\text{cap}} = 1.5$ mm, $h = 1.6$ mm and the sample volume is $V_{\text{pellet}} = 91.2$ mm^3. In the case of the double toroid geometry $r_1 = 2.0$ mm, $h_{\text{cap}} = 1$ mm, $h = 1.6$ mm and the sample volume is $V_{\text{pellet}} = 33.7$ mm^3. Pellets of GeO_2 were made with masses as close as possible to the ideal mass for the corresponding volume as calculated by using a density of 3.643 g cm^3 [175]. The ideal mass of GeO_2 is 0.33218 g for single toroid anvils and 0.12284 g for double toroid anvils, respectively.

The GeO_2 sample for the single toroid anvil experiments was in the form of a pellet of pre-compacted finely powdered glass. The glass was compacted in a press using a load of 8 tns. The GeO_2 samples for the double toroid anvil experiments were in the form of solid pieces that had been shaped to the correct geometry using a rotary tool and polished using diamond paste. Vanadium samples for both geometries were made by compacting the correct mass of either vanadium foil or powder under a load of 1 tns into the pellet shape. The mass of vanadium required was found using a density of 6.110 g cm^{-3} [165] to be 0.55714 g for single toroid anvils and 0.20603 g for double toroid anvils. A summary of the actual masses of the pellets used in the experiments is given in table 8.1.

8.2.2 Neutron Diffraction Experiments

The high pressure experiments were done at room temperature using the PEARL diffractometer. The experimental setup for this diffractometer, which used the Paris-Edinburgh press in transverse geometry, is given in section 3.3.1. The single and double toroid sintered diamond anvils were in a V3 or V4 variant Paris-Edinburgh

Pellet	Sample	Type	Mass (g)	Geometry
1	GeO_2	powder	0.22(1)	ST
2	GeO_2	solid	0.12146(5)	DT
3	GeO_2	solid	0.1220(1)	DT
4	GeO_2	solid	0.1234(1)	DT
A	V	powder	0.390(1)	ST
B	V	foil	0.2061(5)	DT
C	V	foil	0.1961(5)	DT
D	V	foil	0.2012(5)	DT

Table 8.1: Summary of the samples made for GeO_2 experiments done on the PEARL instrument. ST indicates a single toroid geometry, DT indicates a double toroid geometry. The pellets of GeO_2 are distinguished by numbers and the pellets of V are distinguished by letters such that they may be referred to later in the text.

press [68, 242] with piston areas of 100 cm^2 and 102 cm^2, respectively. Background scattering was reduced by three methods. First, the incident beam was collimated by using a BN and Gd tube arrangement. The Gd tube was inserted into the anvil on the breach of the press with an outer diameter of 3.5 mm and wall thickness of 0.06 mm. Second, the anvils were shielded by neutron absorbing Cd. Third, for the single toroid experiment, a Gd foil of thickness 25 μm was used between the gaskets and the anvils to provide further shielding at the sample position.

For the empty gasket measurement, an empty gasket was placed between the anvils in the press and a load of 2 tns was first applied to hold the assembly in place. The press was then lowered into the neutron beam and centred. A measurement was made for $\approx$ 1 day. For each sample measurement, the sample was placed between the anvils and a small load of 2 tns was applied to hold the assembly in place. The assembly was then lowered into the neutron beam and centred. The load applied to the anvils via the pistons of the press was slowly increased using a hydraulic oil pump until the desired load was reached. While increasing the pressure, the system was allowed to equilibrate for $\approx$ 5 min at regular intervals (approximately after every 10 tns of additional load applied). As the anvils compress, the centre of the sample changes position in the beam. Therefore, for each measurement the assembly was moved using a motorised system and the sample was centred in the beam by eye. A neutron diffraction pattern was then collected over a period of approximately 1 day. After each measurement was made, the load was either increased to make a further measurement at a new pressure point or slowly released and the sample removed such that all pressure points were approached from below. For each measurement on a sample of GeO_2, a smaller load was applied to a sample of V and a measurement taken for a short time. The load applied to the sample of V was then increased in small increments, taking a measurement each

GeO_2 Load (tns)	V Load (tns)	Anvils	GeO_2 Pellet	V Pellet	P (GPa)
2	20	ST	1	A	0
2	20	DT	2	B	0
50	70	ST	1	A	4.5(5)
100	110	ST	1	A	8.5(5)
75	35	DT	3	C	8.5(5)
100	45	DT	3	C	11.5(5)
120	85	DT	2	B	14.5(5)
140	100	DT	4	D	17.5(5)

Table 8.2: Measurements made using single toroid (ST) or double toroid (DT) anvils, where P is the pressure at the sample position found using the calibration curve in figure 4-7 and the pellets are defined in table 8.1.

time, until the ratio of $I_{sc}(Q)/I_{vc}(Q)$ was flat and as free from diamond Bragg peaks as possible (see section 4.2). A full measurement was then taken for use in the data analysis procedure. The measurements made using the single and double toroid anvils are summarised in table 8.2.

8.3 Data Analysis

The data analysis procedure described in section 4.2 was used to obtain $F(Q)$ functions. The $F(0) = -0.387$ barn limit was found by fitting a diffraction pattern taken at ambient by Salmon *et al.* [175] with $F(Q) = aQ^2 + F(0)$, where a is a constant, to the lowest four data points at $Q = 0.4, 0.45, 0.5$ and 0.55 Å^{-1} as indicated in figure 8-3. The dependence of $F(Q)$ at low Q is discussed by Salmon [243]. The density of GeO_2 at the pressures attained was found using work done by Hong *et al.* who made an *in-situ* study [110] (see figure 8-4). These values are in agreement with other studies by Tsiok *et al.* [245], Smith *et al.* [244], and Mei *et al.* [223] over extended pressure ranges. The work of Hong *et al.* [110], Smith *et al.* [244] and Tsiok *et al.* [245] indicate an increase of the gradient $\mathrm{d}\rho/\mathrm{d}P$ at about 4.5 GPa and the data sets of Hong *et al.* [110] and Mei *et al.* [223] show a decrease of this gradient at higher pressures with the former indicating a transition at $\approx$ 10 GPa. The values of density used in the present study are given in table 8.4.

The initial $F^{(0)}(Q)$ function was found for each pressure point using the correction factors C_s, C_V and W (see equation (4.28)) are listed in table 8.3 . $W_2F^{(0)}(Q)$, where W_2 is the re-scaling factor, is shown with the $F(Q)$ function in figure 8-5 for the single toroid anvil measurements and in figure 8-6 for the double toroid anvil measurements

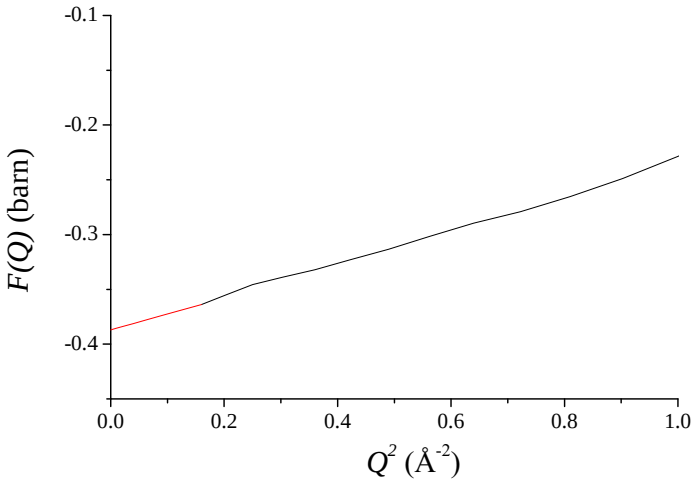

Figure 8-3: Extrapolation of the $F(Q)$ function measured on the D4C diffractometer for a sample of GeO_2 by Salmon *et al.* [175] plotted against Q^2. The $F(Q)$ function (solid black curve) is fitted, assuming a Q^2 dependence, to the first four data points and an extrapolation was made to $Q = 0$ (solid red curve). This procedure was used to find $F(0) = -0.387$ barn.

P (GPa)	Anvils	C_s	C_V	W	W_2
0	ST	0.94	0.74	0.45	1.05
0	DT	0.67	0.60	0.39	1.05
4.5	ST	0.56	0.45	0.44	1.80
8.5	ST	0.30	0.20	0.44	2.10
8.5	DT	0.2	0.2	0.44	1.70
11.5	DT	0.2	0.2	0.45	1.70
14.5	DT	0.2	0.3	0.38	1.80
17.5	DT	0.15	0.15	0.46	2.30

Table 8.3: Correction factors for GeO_2 experiments done using single toroid (ST) and double toroid (DT) anvils. C_s and C_V are the multiplication factors for the empty gasket diffraction pattern which is subtracted from the sample and vanadium diffraction patterns, respectively, W is the initial normalisation constant and W_2 is the re-scaling factor as described in section 4.2.

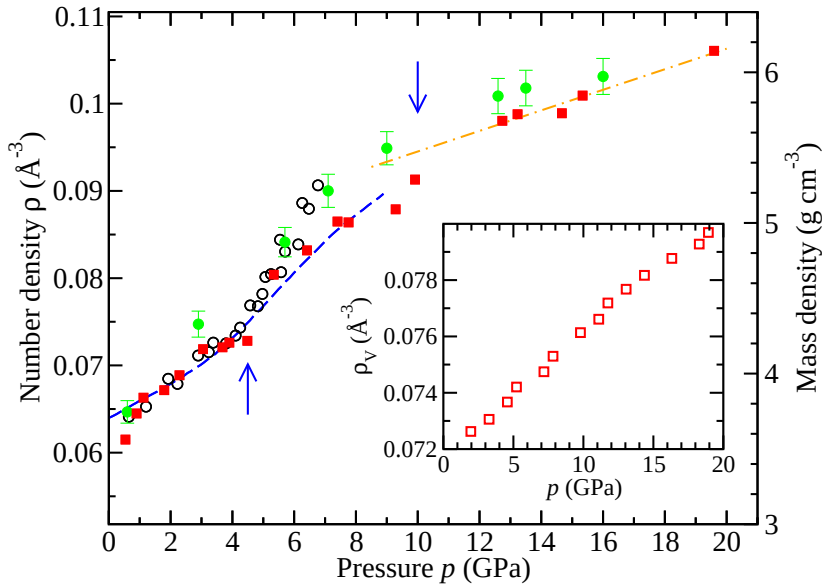

Figure 8-4: The number density ρ and corresponding mass density for GeO_2 glass as measured on compression from the *in situ* studies of Hong *et al.* [110] (■, no pressure transmitting medium), Smith *et al.* [244] (○, 1:1 mixture of pentane and isopentane used as a pressure transmitting medium), Tsiok *et al.* [245] (dashed (blue) curve, 4:1 mixture of methanol:ethanol used as a pressure transmitting medium with a coated glass sample to avoid reaction with this medium) and Mei *et al.* [223] (● with vertical error bars, He pressure transmitting medium). The dashed (orange) curve is drawn through the Hong *et al.* [110] data points at higher pressures as a guide for the eye and the vertical arrows mark the approximate pressures where there is a change in the gradient $\mathrm{d}\rho/\mathrm{d}P$. The inset gives the number density of vanadium ρ_V as measured on compression from the *in situ* x-ray diffraction study of Nakamoto *et al.* [111] at room temperature (□, He pressure transmitting medium).

to show the effect of the slope removal and Lorentzian fitting procedure. In each case the Lorentzian function that was fitted at low Q has been highlighted. Also plotted in figures 8-5 and 8-6 are the back Fourier transforms of the $G(r)$ functions after the majority of the unphysical low-r oscillations have been removed, and these are found to be in excellent agreement with the $F(Q)$ functions. The efficacy of the semi-empirical data analysis procedure was tested by comparing both the $F(Q)$ (figure 8-7) and $G(r)$ (figure 8-8) functions from this study to those found in experiments on samples of GeO_2 at similar pressures up to $\lesssim$9 GPa using the D4C diffractometer at the Institut Laue-Langevin in Grenoble, France. The ambient pressure $F(Q)$ functions found using the PEARL diffractometer for both single and double toroid anvils are in good agreement, within the statistical errors, with high quality data taken by Salmon *et al.* [175] in a standard vanadium can. The measurement in single toroid anvils at a pressure of 4.5 GPa is in good agreement with $F(Q)$ measured at a similar pressure (4.9(5) GPa) by Drewitt *et al.* [40]. Similarly, the measurements taken for both single and double toroid anvils at a pressure of 8.5(5) GPa are in good agreement with $F(Q)$ measured at the same pressure by Drewitt *et al.* [40]. The experiment by Drewitt *et al.* [40] was done using single toroid BN anvils and a direct scattering geometry, wherein the scattered beam is measured in the same plane as the incident beam. The BN in the anvils provides shielding from unwanted scattering and higher quality patterns can be measured. In these experiments, the low Q region can be measured successfully due to the geometry; however, the highest pressure that can be reliably attained using BN anvils is $\approx$ 8.5 GPa.

Peak Positions and Coordination Numbers

Peak positions in $F(Q)$ and $G(r)$ were obtained by fitting a parabola $f_{\mathrm{par}}(x) = ax^2 + bx + c$ to the highest 3 data points, where a, b and c are constants, x is the independent variable (Q or r). The peak position is then defined by the equation $\mathrm{d}f_{\mathrm{par}}(x)/\mathrm{d}(x) = 0$, such that $x_{\mathrm{peak}} = -b/(2a)$.

The mean coordination number of O around Ge, $\overline{n}^{\mathrm{O}}_{\mathrm{Ge}}$, is given by the integral of $g_{\mathrm{GeO}}(r)$ over the first peak. An isotopic substitution experiment by Salmon *et al.* [175], whereby the full set of partial pair distribution functions $g_{\alpha\beta}(r)$ as given in equation (2.53) were measured, shows that only $g_{\mathrm{GeO}}(r)$ contributes to $G(r)$ in the region of the first peak. Therefore, in this region, equation (2.53) can be rearranged to show that

$$g_{\mathrm{GeO}}(r) = \frac{1}{2c_{\mathrm{Ge}}c_{\mathrm{O}}\overline{b}_{\mathrm{Ge}}\overline{b}_{\mathrm{O}}}(G(r) - G(0))\,, \tag{8.2}$$

where $c_{\mathrm{Ge}} = 1/3$ and $c_{\mathrm{O}} = 2/3$ are the atomic fractions of Ge and O, while $\overline{b}_{\mathrm{Ge}}$ and $\overline{b}_{\mathrm{O}}$ are the coherent neutron scattering lengths of Ge and O, respectively. Substituting

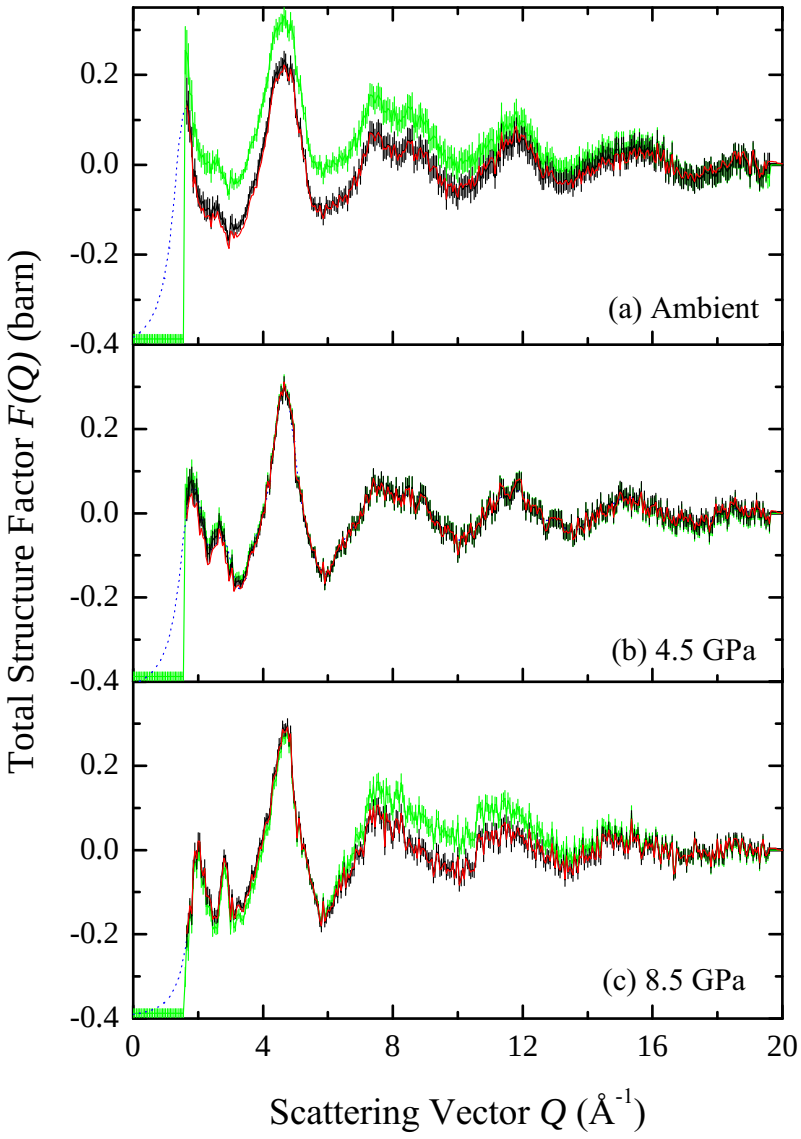

Figure 8-5: Plots showing the measured $F(Q)$ functions for glassy GeO_2 in single toroid anvils at the indicated pressures. The curves correspond to the function $W_2F^{(0)}(Q)$ as calculated by using equation (4.28) (solid green curve), the $F(Q)$ function after slope removal and rescaling (solid black curve), the fitted Lorentzian function at low Q (broken blue curve) and the back Fourier transform of the $G(r)$ functions after removal of the majority of unphysical low r oscillations (solid red curve).

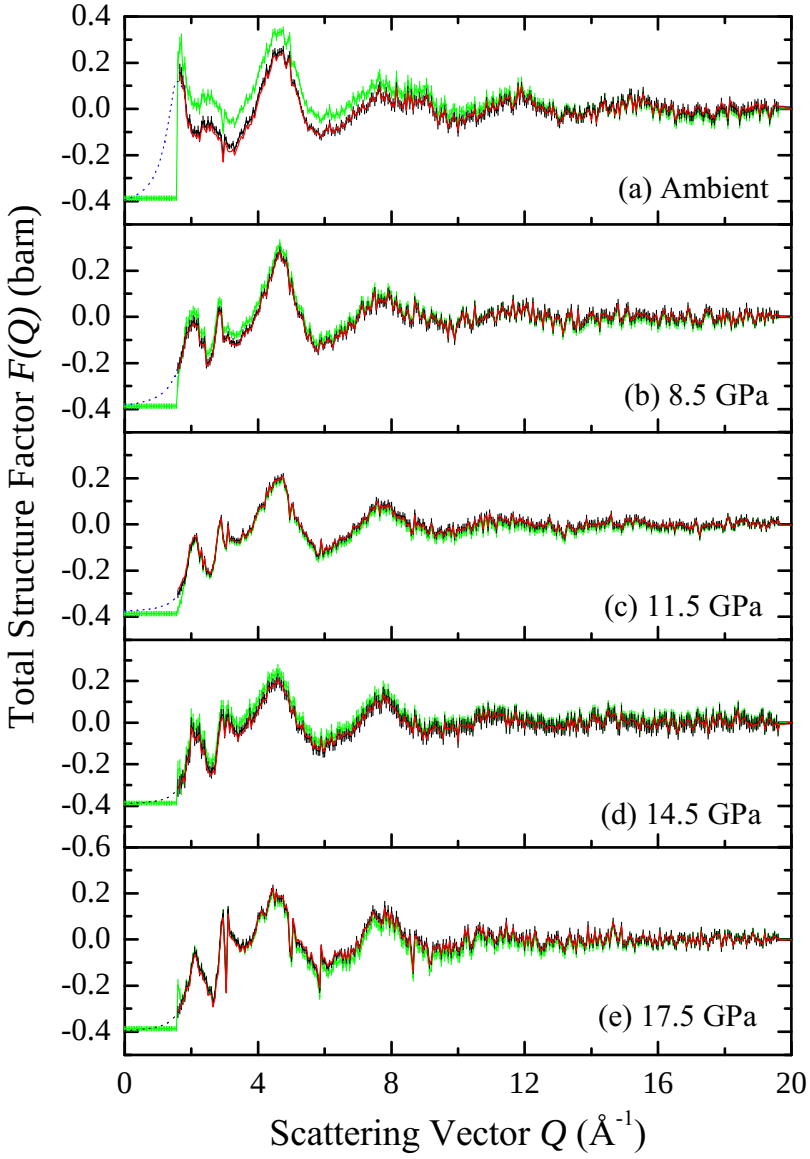

Figure 8-6: Plots showing the measured $F(Q)$ functions for glassy GeO_2 in double toroid anvils at the indicated pressures. The curves correspond to the function $W_2F^{(0)}(Q)$ as calculated by using equation (4.28) (solid green curve), the $F(Q)$ function after slope removal and rescaling (solid black curve), the fitted Lorentzian function at low Q (broken blue curve) and the back Fourier transform of the $G(r)$ functions after removal of the majority of unphysical low r oscillations (solid red curve).

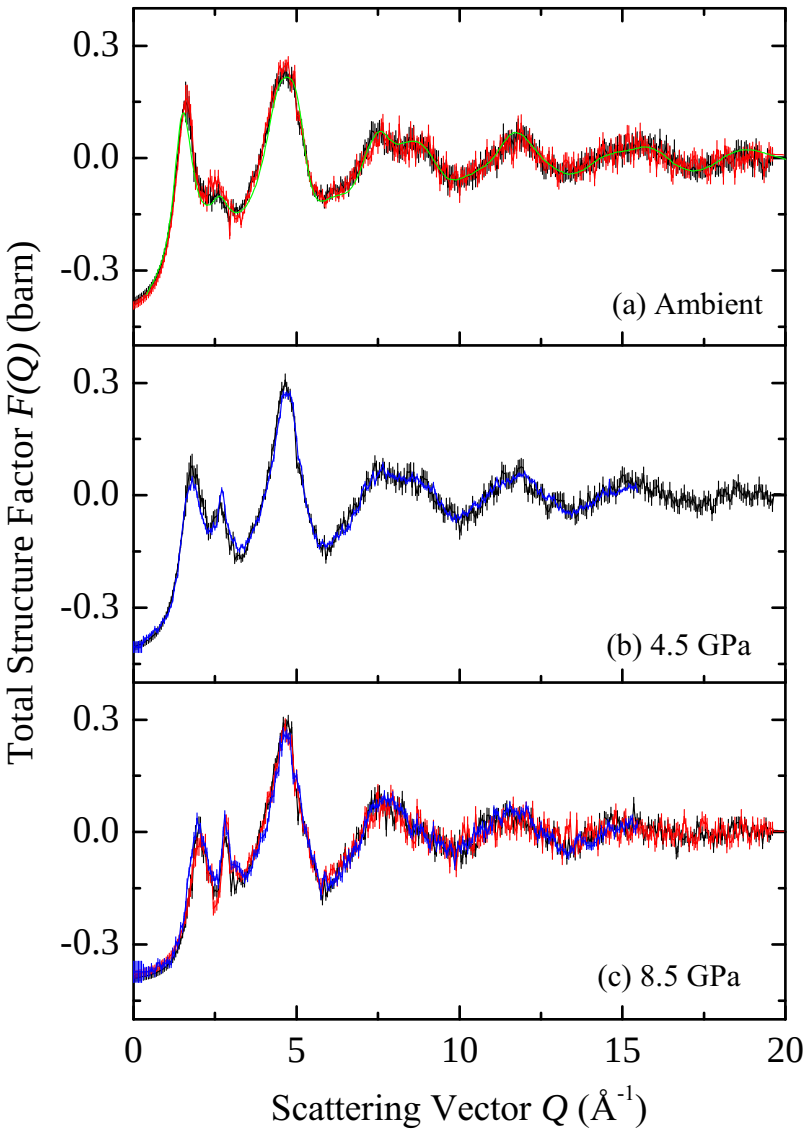

Figure 8-7: The total structure factors $F(Q)$ measured for GeO_2 glass in this study using single toroid anvils (solid black curves) for pressures of (a) ambient, (b) 4.5(5) GPa or (c) 8.5(5) GPa; or using double toroid anvils (solid red curves) for pressures of ambient and 8.5(5) GPa as plotted in panels (a) and (c), respectively. Also plotted in panels (b) and (c) are the results from Drewitt *et al.* [40] for pressures of 4.9(5) GPa and 8.5(5) GPa, respectively (solid blue curves); and in panel (a), the data taken in a cylindrical vanadium can by Salmon *et al.* [175] (solid green curve)

.

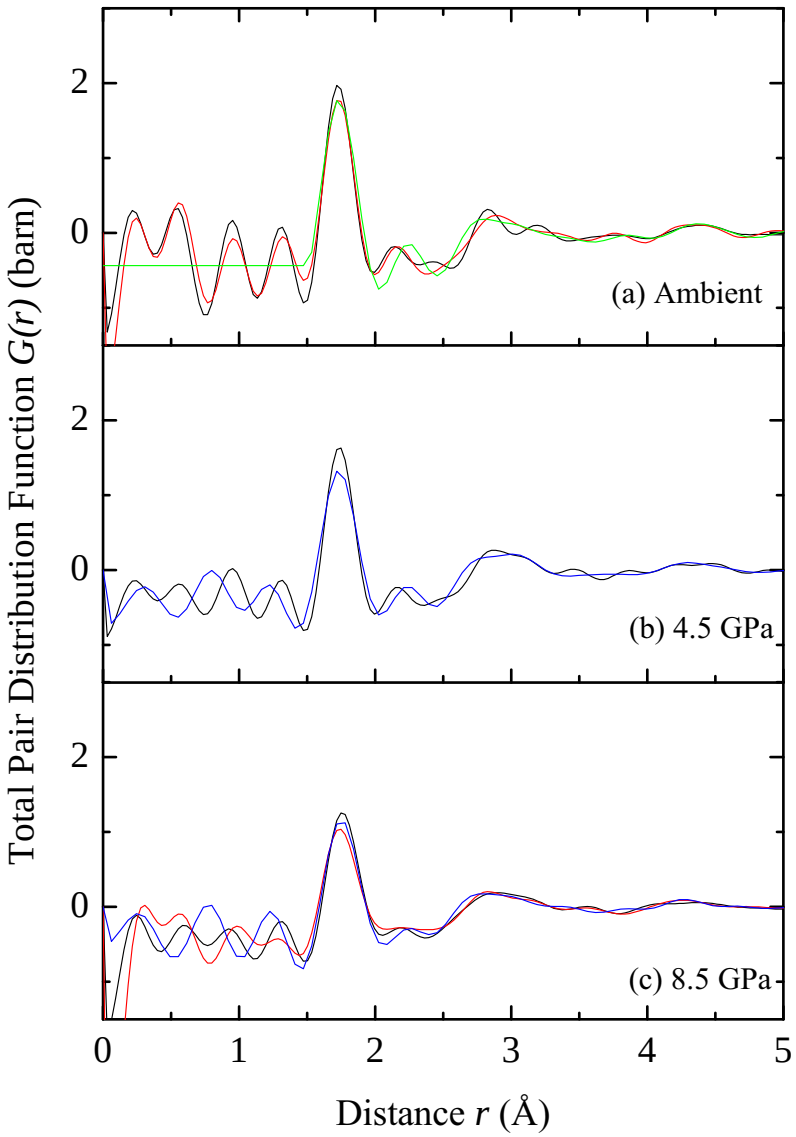

Figure 8-8: The total pair distribution functions $G(r)$ measured for GeO_2 glass in this study using single toroid anvils (solid black curves) for pressures of (a) ambient, (b) 4.5(5) GPa or (c) 8.5(5) GPa; or using double toroid anvils (solid red curves) for pressures of ambient and 8.5(5) GPa as plotted in panels (a) and (c), respectively. Also plotted in panels (b) and (c) are the results from Drewitt *et al.* [40] for pressures of 4.9(5) GPa and 8.5(5) GPa, respectively (solid blue curves); and in panel (a), the data taken in a cylindrical vanadium can by Salmon *et al.* [175] (solid green curve)

.

equation (8.2) into equation (2.55) gives the average Ge-O coordination number as

$$\overline{n}^{\mathrm{O}}_{\mathrm{Ge}} = 4\pi\rho c_{\mathrm{O}} \int_{r_1}^{r_2} r^2 g_{\mathrm{GeO}}(r)\,\mathrm{d}r = \frac{2\pi\rho}{c_{\mathrm{Ge}}\bar{b}_{\mathrm{Ge}}\bar{b}_{\mathrm{O}}} \int_{r_1}^{r_2} r^2 (G(r) - G(0))\,\mathrm{d}r\,, \tag{8.3}$$

where ρ is the atomic number density. In practice, defining the first peak over which to integrate is problematic for diffraction experiments when $F(Q)$ has high statistical noise and is not measured over a wide range in Q, leading to Fourier transform artefacts. Often, as is demonstrated in figure 8-9, the peak must be extrapolated to $G(r) = G(0)$ on the high-r side. Two methods were considered to calculate the coordination number.

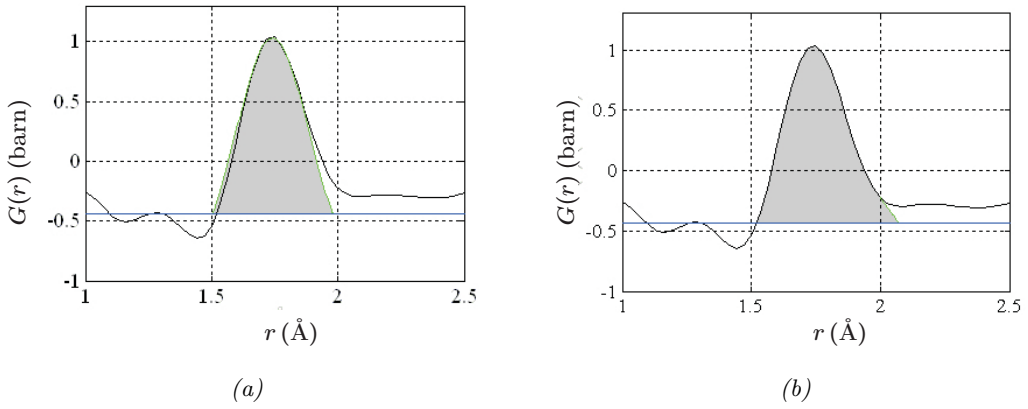

Figure 8-9: The first peak in $G(r)$ (solid black curves) for a sample of GeO_2 under a load of 75 tns in double toroid anvils (corresponding to a pressure of 8.5 GPa). Two methods were considered to find the area under the peak (a) by fitting a Gaussian shape centred at the peak position (solid green curve) and (b) by fitting a straight line (solid green curve) to the final few points and extrapolating it to the $G(0)$ limit (shown by the solid blue line). An integral (the grey area) is then taken between these two r-space points where the revised peak in $G(r)$ crosses $G(0)$.

Firstly, $G(r)$ was fitted with a Gaussian shape in the region of the peak. The Gaussian shape was centred on the position of the peak in r as calculated using the method described above and the fitted Gaussian curve was used as $G(r)$ in equation (8.3), with r_1 and r_2 set as the values for which the peak crosses $G(0)$. Secondly, the first peak was extrapolated to $G(r) = G(0)$ by fitting the four highest r values (judged by eye) with a straight line and extrapolating this to $G(r) = G(0)$. For all pressure points, the Gaussian fit used in the first method did not coincide well with the $G(r)$ function (figure 8-9a) and so the second method was used to find the coordination numbers reported here in table 8.4.

Pressure (GPa)	Type	ρ (Å^{-3})	Q_{FSDP} (Å^{-1})	Q_{PP} (Å^{-1})	r_{GeO} (Å)	$\overline{n}^{\mathrm{O}}_{\mathrm{Ge}}$	r_2/r_{GeO}
Ambient	ST	0.0629(3)	1.63(5)	2.51(3)	1.73(2)	4.0(2)	1.636
Ambient	DT	0.0629(3)	1.59(5)	2.56(3)	1.73(2)	3.9(2)	1.671
4.5(5)	ST	0.0761(9)	1.86(3)	2.73(3)	1.74(2)	4.2(2)	1.649
8.5(5)	ST	0.0868(9)	2.01(3)	2.82(3)	1.76(2)	4.7(2)	1.642
8.5(5)	DT	0.0868(9)	2.06(3)	2.90(3)	1.75(2)	4.5(2)	1.617
11.5(5)	DT	0.0951(9)	2.14(3)	2.87(3)	1.78(2)	4.8(2)	1.545
14.5(5)	DT	0.0987(9)	2.18(3)	3.07(3)	1.81(2)	5.0(2)	1.492
17.5(5)	DT	0.1031(9)	2.17(3)	3.06(3)	1.82(2)	5.5(2)	1.462

Table 8.4: Parameters describing the pressure dependence of the structure of GeO_2 glass as obtained from the neutron diffraction experiments using the PEARL diffractometer with either single toroid (ST) or double toroid (DT) sintered diamond anvils. The number density ρ of the glass [110] is given together with the position Q_{FSDP} of the first sharp diffraction peak, the position Q_{PP} of the principal peak, the Ge-O bond distance r_{GeO} taken from the position of the first peak in $G(r)$, the mean Ge-O coordination number $\overline{n}^{\mathrm{O}}_{\mathrm{Ge}}$, and the ratio r_2/r_{GeO} where r_2 is the position of the second peak in $G(r)$.

8.4 Results

In table 8.4 a series of peak positions and properties of the system for the measured pressures are given. The positions are given of the first and second peaks in $F(Q)$, referred to as the first sharp diffraction peak (FSDP) with position Q_{FSDP} and principal peak (PP) with position Q_{PP}, respectively, which relate to the intermediate and extended range ordering in the system [63, 243]. Also given is the position of the first peak in $G(r)$, which is the mean nearest neighbour bond distance r_{GeO}, and the ratio of the position of the second peak to the position of the first peak r_2/r_{GeO}. Finally, the atomic number density ρ and the mean coordination number $\overline{n}_{\mathrm{GeO}}$ are listed.

The measured $F(Q)$ functions are given in figures 8-10 and 8-11 for the single toroid and double toroid experiments, respectively. These are compared with the $F(Q)$ functions obtained from the molecular dynamics (MD) simulations of Marrocchelli *et al.* [241]. A spline fit was made to the neutron diffraction data to smooth the high frequency noise and it is the spline fits that were used as $F(Q)$ in equation (2.53) to obtain the $G(r)$ functions given in figures 8-12 and 8-13 for the single and double toroid experiments, respectively. Also plotted in figures 8-12 and 8-13 are the $F(Q)$ functions calculated by Fourier transforming the $G(r)$ from Marrocchelli *et al.* [241], truncating $F(Q)$ at $Q = 19.6$ Å^{-1} (i.e. the maximum Q for which $F(Q)$ was measured on PEARL) and back Fourier transforming to give the $G(r)$ functions that are compared to the present work.

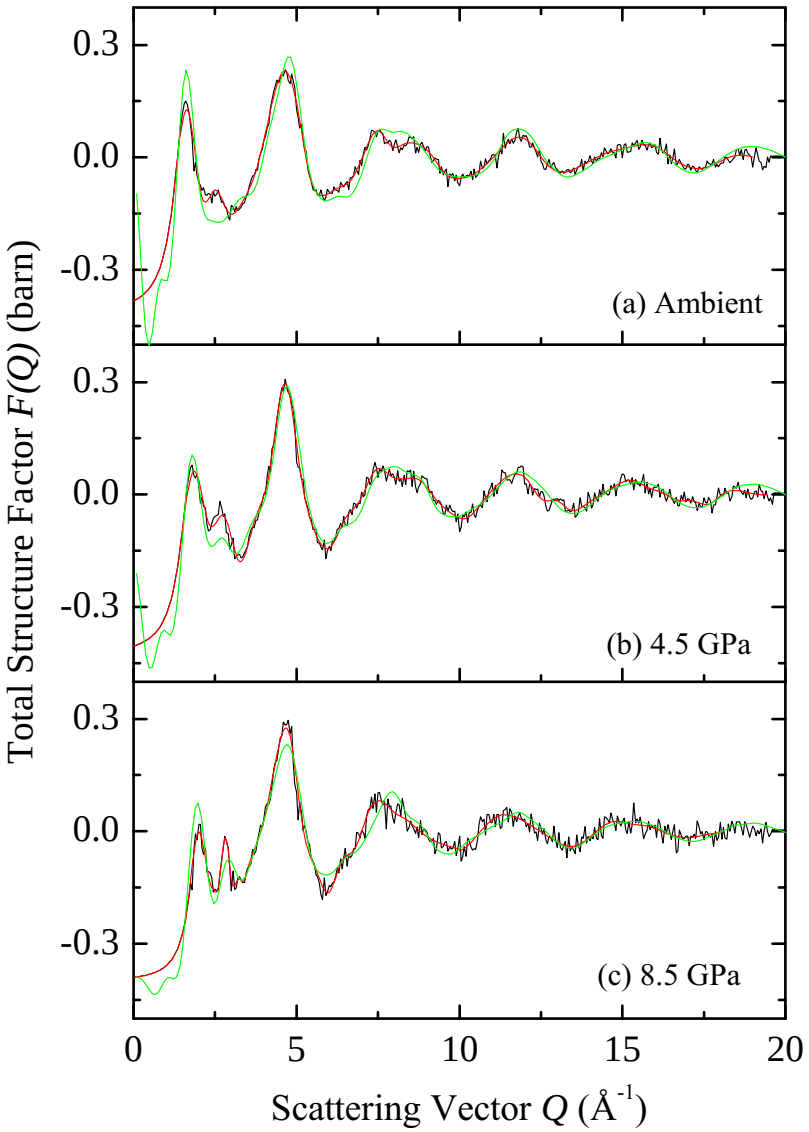

Figure 8-10: The pressure dependence of the $F(Q)$ functions measured at the stated pressures for the experiment done using single toroid anvils (solid black curves), and the spline fits to the $F(Q)$ data as extrapolated to small Q values by using a Lorentzian function (see the text) (solid red curves). The data are compared with $F(Q)$ found from the MD simulation study of Marrocchelli *et al.* [241] made at the same number density as the experimental results (solid green curves).

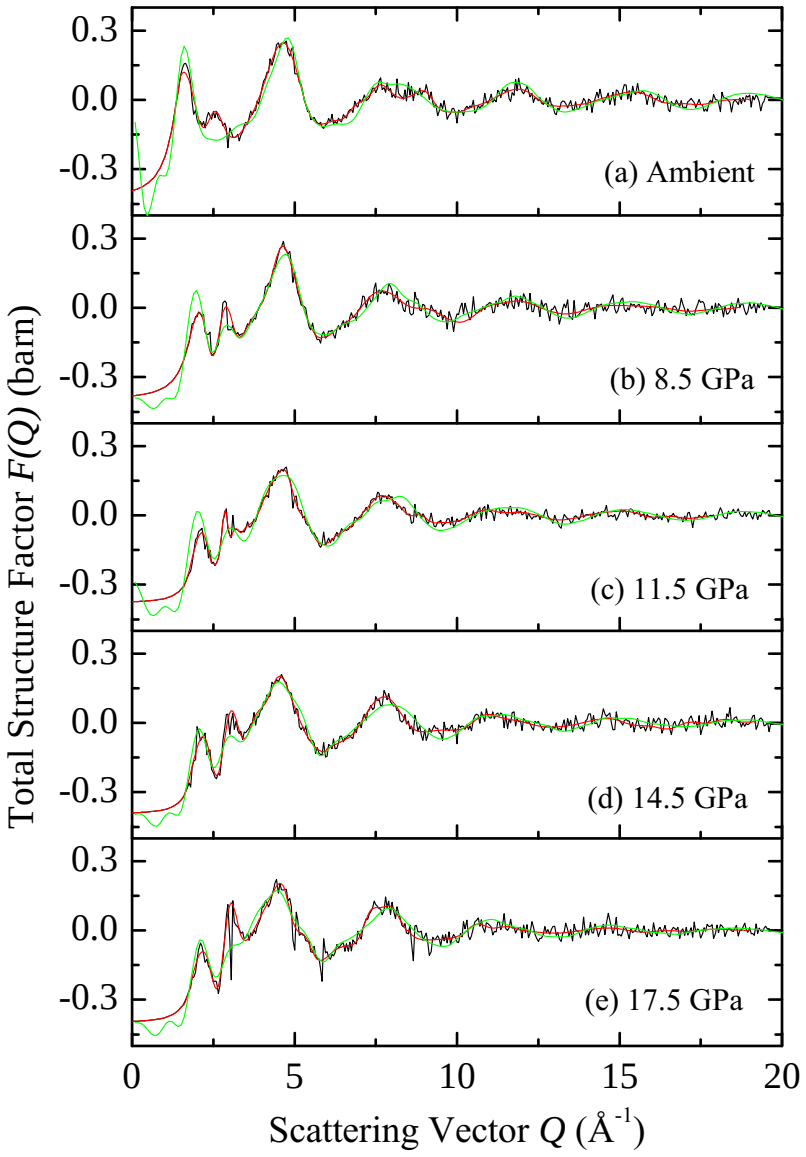

Figure 8-11: The pressure dependence of the $F(Q)$ functions measured at the stated pressures for the experiment done using double toroid anvils (solid black curves), and the spline fits to the $F(Q)$ data as extrapolated to small Q values by using a Lorentzian function (see the text) (solid red curves). The data are compared with $F(Q)$ found from the MD simulation study of Marrocchelli *et al.* [241] made at the same number density as the experimental results (solid green curves).

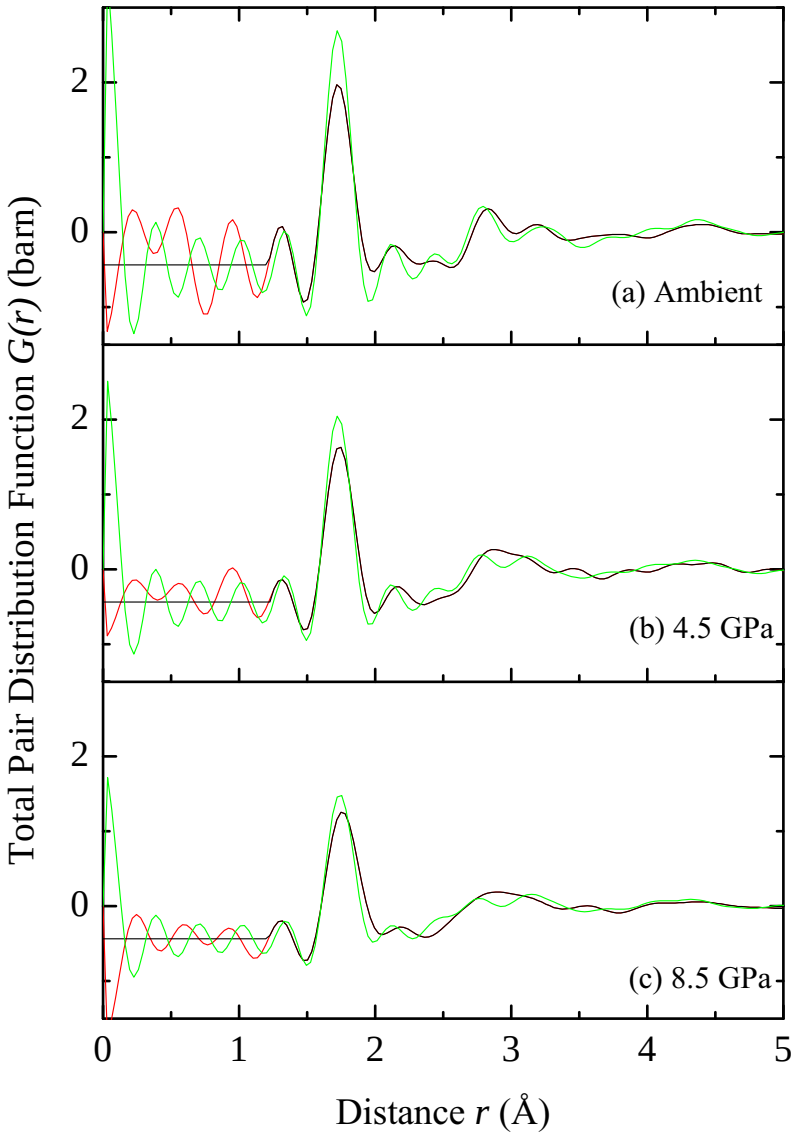

Figure 8-12: The pressure dependence of the $G(r)$ functions measured at the stated pressures calculated from the spline fitted $F(Q)$ function shown in figure 8-10 for the experiments done using single toroid anvils (solid black curves) compared with the $G(r)$ functions found from the MD simulation study of Marrocchelli *et al.* [241] made at the same densities (solid green curves). The latter were obtained by fourier transforming the $F(Q)$ functions truncated at 19.6 $Å^{-1}$. The solid red curve shows the unphysical low-r oscillations obtained for the neutron diffraction results.

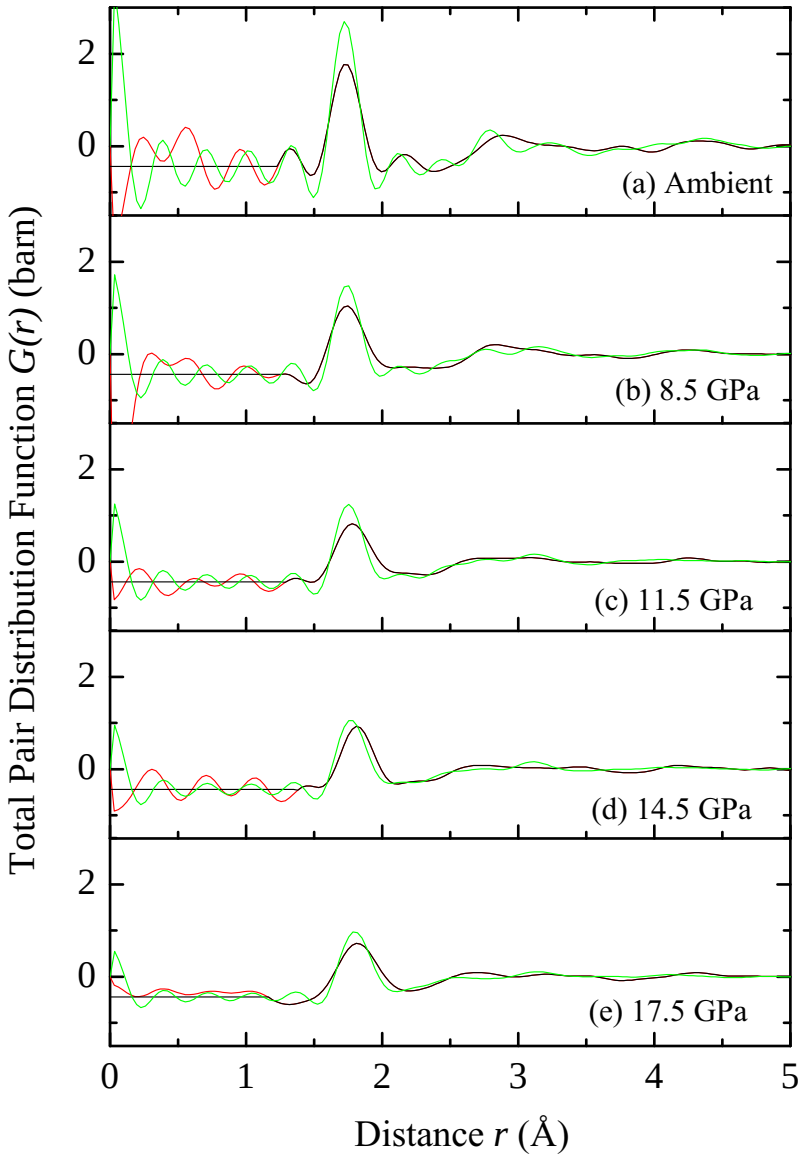

Figure 8-13: The pressure dependence of the $G(r)$ functions measured at the stated pressures calculated from the spline fitted $F(Q)$ function shown in figure 8-11 for the experiments done using double toroid anvils (solid black curves) compared with the $G(r)$ functions found from the MD simulation study of Marrocchelli *et al.* [241] made at the same densities (solid green curves). The latter were obtained by fourier transforming the $F(Q)$ functions truncated at 19.6 $Å^{-1}$. The solid red curve shows the unphysical low-r oscillations obtained for the neutron diffraction results.

8.5 Discussion

The FSDP is indicative of intermediate range ordering of periodicity given by $2\pi/Q_{\mathrm{FSDP}}$, where Q_{FSDP} is the position of the peak. There is an associated correlation length given by the inverse of the peak width [63, 246]. Similarly, the PP is related to extended range ordering with periodicity given by $2\pi/Q_{\mathrm{PP}}$. The increase in the Q_{FSDP} and Q_{PP} values with increasing pressure indicates a decrease of the periodicity associated with the intermediate and extended range ordering. The increase in Q_{FSDP} is more or less linear with pressure until a pressure of ≈ 10 GPa is reached, when there is a change in the gradient $\mathrm{d}Q_{\mathrm{FSDP}}/\mathrm{d}p$ as shown in figure 8-14. This is in agreement with the neutron diffraction study by Drewitt *et al.* [40], the MD simulation study by Marrocchelli *et al.* [241] and the x-ray diffraction studies by Hong *et al.* [110] and Guthrie *et al.* [220]. There is, however, some disagreement with the study made using x-ray diffraction by

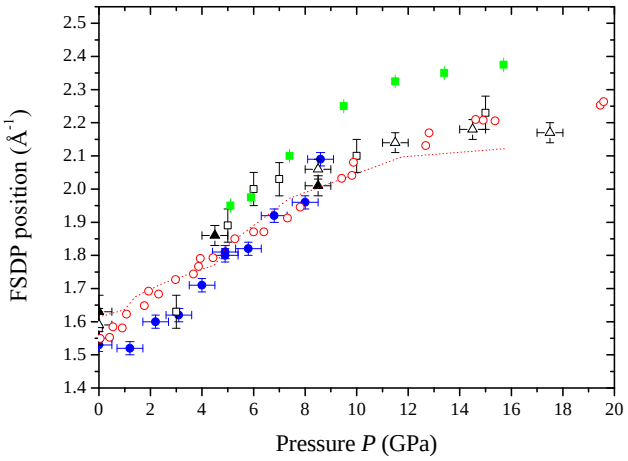

Figure 8-14: The pressure dependence of the position of the first sharp diffraction peak in $F(Q)$, Q_{FSDP}, as measured in the present work by using neutron diffraction with either single (▲) or double (△) toroid anvils. The results are compared to those obtained from the previous neutron diffraction experiments of Drewitt *et al.* [40] (●) and the x-ray diffraction experiments of Hong *et al.* [110] (○) Guthrie *et al.* [220] (□) and Mei *et al.* [223] ((■)). The dotted (red) line shows the simulation results of Marrocchelli *et al.* [241].

Mei *et al.* [223], where the peak position is consistently higher than in the current study, particularly at pressures > 8 GPa. This may be explained by the fact that, unlike the other experiments, the x-ray diffraction study by Mei *et al.* [223] was made using helium as a pressure transmitting medium to promote hydrostatic conditions. The opposite effect has been observed in SiO_2, whereby He enters voids in the glass structure and decreases the compressibility [247, 248]; it would be interesting to further investigate

the effect of He on GeO_2. The change in gradient at $\approx$ 10 GPa also corresponds to a modification in the main features observed with increasing pressure in x-ray absorption near-edge spectroscopy (XANES) and extended x-ray absorption fine structure (EXAFS) spectroscopy experiments on GeO_2 glass [224]. The main contribution to the FSDP comes from Ge-Ge correlations [63]. The movement of this peak to higher Q with pressure indicates that the Ge atoms at the centre of the structural motifs are moving closer together with pressure as expected.

The first peak in $G(r)$ broadens with increasing pressure and shifts position (r_{Ge}) in table 8.4) to larger r values after a threshold of ≈4.5(5) GPa has been reached. This is accompanied by an increase with pressure of the average coordination number of O around Ge from $\overline{n}^{\mathrm{O}}_{\mathrm{Ge}} = 4.2(2)$ at 4.5(5) GPa to $\overline{n}^{\mathrm{O}}_{\mathrm{Ge}} = 5.5(2)$ at 17.5(5) GPa. Meanwhile, the ratio r_2/r_{GeO} decreases with pressure, consistent with a decrease of $r_{\mathrm{OO}}/r_{\mathrm{GeO}}$ where r_{OO} is the first peak in $g_{\mathrm{OO}}(r)$, from the value of $\sqrt{8/3}$ expected for tetrahedral GeO_4 motifs to the value of $\sqrt{2}$ expected for octahedral GeO_6 motifs [104]. The pressure dependences of $\overline{n}^{\mathrm{O}}_{\mathrm{Ge}}$ and r_{GeO} are in good agreement with the MD simulations of Marrocchelli *et al.* [241] and are in excellent agreement with the neutron diffraction studies of Drewitt *et al.* [40] as shown in figure 8-15b. There is some dis-

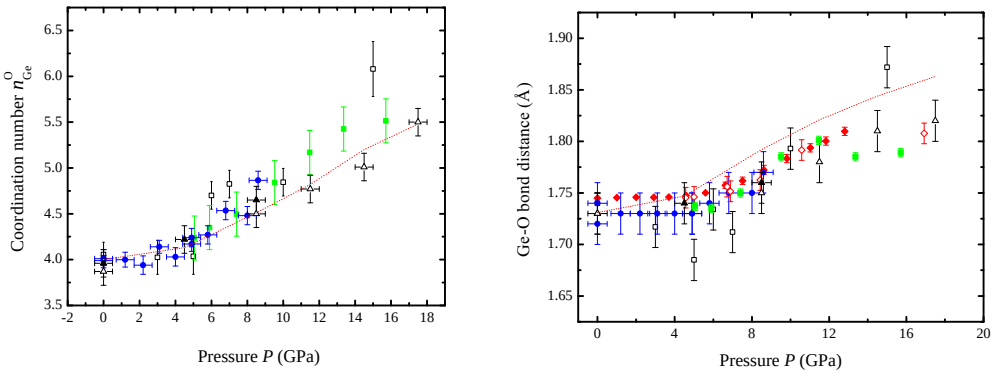

(a) *(b)*

Figure 8-15: The pressure dependence of (a) the mean coordination number $\overline{n}^{\mathrm{O}}_{\mathrm{Ge}}$ and (b) The Ge-O bond distance r_{GeO} for GeO_2 glass as measured in the present work by using neutron diffraction with either single (▲) or double (△) toroid anvils. The values for $\overline{n}^{\mathrm{O}}_{\mathrm{Ge}}$ were obtained by integrating over the first peak in $G(r)$ (see equation (8.3)). The results are compared to those obtained from the previous neutron diffraction experiments of Drewitt *et al.* [40] (●), the x-ray diffraction experiments of Guthrie *et al.* [220] (□) and Mei *et al.* [223] ((■)) and the EXAFS experiments of Vaccari *et al.* [222] (♦) and Baldini *et al.* [224] ◊. The dotted red lines show the results of the simulations by Marrocchelli *et al.* [241].

agreement at higher pressures between the values of $\overline{n}^{\mathrm{O}}_{\mathrm{Ge}}$ obtained in the present study and those obtained in the x-ray diffraction studies of Mei *et al.* [223] and Guthrie *et*

al. [220]. There is agreement between the present study and the Extended X-ray Absorption Fine Structure (EXAFS) spectroscopy experiments of Vaccari *et al.* [222] and Baldini *et al.* [224] in the values of r_{GeO}. The threshold value of ≈ 5 GPa corresponds to a change in the pressure dependence of the principal peak position in the Raman spectrum of GeO_2 glass [110]. There is no indication of an abrupt change in the Ge-O bond length at pressures between 6.6 and 8.0 GPa, as reported in a previous EXAFS experiment [216] nor of a plateau region between 6 and 10 GPa where $\overline{n}^{\mathrm{O}}_{\mathrm{Ge}} \approx 5$ [220]. The majority of the experimental results illustrated in figure 8-15a indicate that a pressure in excess of 18 GPa is necessary in order to form a fully octahedral glass for which $\overline{n}^{\mathrm{O}}_{\mathrm{Ge}} = 6$. Recent EXAFS results suggest that the latter is achieved when the pressure is about 30 GPa [224].

In the simulations by Marrocchelli *et al.* [241], the interaction potentials included dipole polarisation effects and were parameterised by using first principles calculations and not by using empirical methods [38]. The aim of the new potentials was to develop an accurate description of the interactions, going beyond classical pairwise interaction potentials, which have limited accuracy. The simulations compare well with experiments on the structural and vibrational properties of GeO_2 under ambient conditions. The dynamical properties of simulated liquid GeO_2 at high temperatures also agree well with experiment [38]. The limitations associated with glass formation under pressure in MD simulations meant that the equation of state for GeO_2 glass was not reproduced in the simulations and the data of Marrocchelli *et al.* [241] were presented as a function of density. The density was converted to pressure using the calibration curve given by Hong *et al.* [110] in figure 8-4. As shown in figures 8-10 to 8-13 the molecular dynamics simulations reproduce the main features of the measured $F(Q)$ and $G(r)$ functions although, at the highest pressure points, there is a tendency to underestimate the sharpness of the principal peak in $F(Q)$ and the first peak position in $G(r)$. The MD results do, however, show a growing asymmetry of the first peak in $g_{\mathrm{GeO}}(r)$ with increasing pressure and the weighted peak position $\langle r_{\mathrm{GeO}} \rangle = \int \mathrm{d}r r g_{\mathrm{GeO}}(r) / \int \mathrm{d}r g_{\mathrm{GeO}}(r)$ follows the neutron diffraction results as shown in figure 8-15b. The simulations also show a threshold pressure of ≈ 5 GPa below which the Ge-O bond length and coordination number remain constant (figure 8-15) and where compaction occurs via a change in the intermediate range order as reflected by the pressure dependence of Q_{FSDP} shown in figure 8-14. At pressures greater than this threshold, the simulation results for the Ge-O bond length and coordination number again follow the neutron diffraction data and there is a reduction in $\mathrm{d}Q_{\mathrm{FSDP}}/\mathrm{d}P$ starting around 8 GPa (figure 8-14). The pressure range from about 5 to 8 GPa corresponds to a mass density increase from about 4.5 to 5.05 g cm^{-3} and, according to the molecular dynamics results, this corresponds to a regime where the predominant conversion mechanism is from four-fold to

five-fold coordinated Ge atoms. For densities greater that 5.25 g cm^{-3} ($P \approx 10$ GPa) six-fold coordinated Ge atoms start to appear in appreciable concentrations (≈ 10 %). As demonstrated by Salmon *et al.* [104], the MD simulation results presented here agree better with the experimental data than results obtained from other simulations of GeO_2 glass using either molecular dynamics and the Oeffner-Elliott interaction potentials [122, 209, 249–251] or first principles molecular dynamics [252].

8.6 Conclusion

Neutron diffraction was used to measure, for the first time, the structure of GeO_2 glass at pressures up to 17.5(5) GPa with a Paris-Edinburgh press and sintered diamond anvils of either single toroid or double toroid geometry. The semi-empirical methodology that has been developed leads to structure factors that are largely free from diamond Bragg peaks and its validity has been verified by comparison with the data available from other neutron diffraction experiments at pressures up to ≈ 8.5 GPa. The measured neutron structure factors are the highest quality ever obtained above ≈ 9 GPa which offers the opportunity for studying the detailed structure of glassy and liquid materials by using neutron diffraction at pressures up to ≈ 18 GPa. The new results for GeO_2 glass are consistent with the existence of four principal densification mechanisms. At pressures up to a threshold of ≈ 5 GPa the density increases through a change in the connectivity of GeO_4 tetrahedra [40]. At pressures larger than this threshold, there is a steady increase in the Ge-O bond length and coordination number in contrast with an early EXAFS study [222] but in agreement with more recent neutron and x-ray diffraction and EXAFS experiments [224]. The rate of change of the intermediate range order, as measured by the pressure dependence of Q_{FSDP}, decreases once the pressure exceeds ≈ 10 GPa and the Ge-O coordination number $\overline{n}^{\mathrm{O}}_{\mathrm{Ge}} > 4.5$. According to the molecular dynamics studies of Marrocchelli *et al.* [241], the pressure range from 5 to ≈ 10 GPa corresponds to a regime where GeO_4 units are replaced predominantly by GeO_5 units and, at pressures beyond ≈ 10 GPa, appreciable concentrations of GeO_6 units begin to form. Eventually, at about 30 GPa, the transformation to a predominantly octahedral glass is achieved and densification proceeds via compression of the Ge-O bond [224]. The onset of two of these densification regimes correspond to observable changes in the pressure dependence of the bulk number density of the glass ρ which shows an increase in $\mathrm{d}\rho/\mathrm{d}P$ at ≈ 5 GPa followed by a decrease in $\mathrm{d}\rho/\mathrm{d}P$ at ≈ 10 GPa (figure 8-4). The work presented in this chapter is also reported in reference [104].

9. Structure of SiO_2 and B_2O_3 Glass Under Pressure

9.1 Introduction

In section 8, the neutron diffraction method was used to measure accurate diffraction patterns of a glass for the first time at pressures > 8.5 GPa using the PEARL diffractometer at ISIS. In the current chapter, two experiments are described which use the same method to measure the neutron diffraction patterns of two other archetypical network glass forming systems - SiO_2 and B_2O_3. Under ambient conditions, these glasses have rather different open network structures and are therefore of fundamental interest for understanding transformations under pressure [211, 253–262].

In the case of the SiO_2 (figure 9-1a), the structure under ambient conditions is analogous to that of GeO_2. The network is made from 4-fold coordinated tetrahedral SiO_4 motifs connected at their corners [263, 264]. However, unlike GeO_2, SiO_2 does not exhibit any change to the structural motif in the pressure range from ambient to 20 GPa as discussed in chapter 8. However, there is an increase in density with pressure in this region [219, 221] and evidence from x-ray scattering indicates that there is a significant re-arrangement of the tetrahedra on an intermediate length scale [225, 265]. This is a view that is supported by the results obtained from simulations [228, 253, 266–268] (where a useful summary is given in by Huang *et al.* [253]), a combined energy dispersive x-ray diffraction / sound velocity experiment [269] and light scattering techniques [215, 226, 270]. A transformation is also seen in samples recovered from pressures above 9 GPa [265, 271, 272]. Thus far, the only *in situ* neutron diffraction experiment made on SiO_2 at pressures above 9 GPa has not yielded total structure factors of good enough quality to obtain the total pair distribution function $G(r)$ [72].

In the case of B_2O_3, the network under ambient conditions (figure 9-1b) is made from corner sharing planar BO_3 trigonal motifs that can link to form highly ordered so-called B_3O_6 boroxol rings [274]. There is some debate over the fraction of BO_3 motifs that form B_3O_6 units in the glass [275] with authors claiming fractions from 0

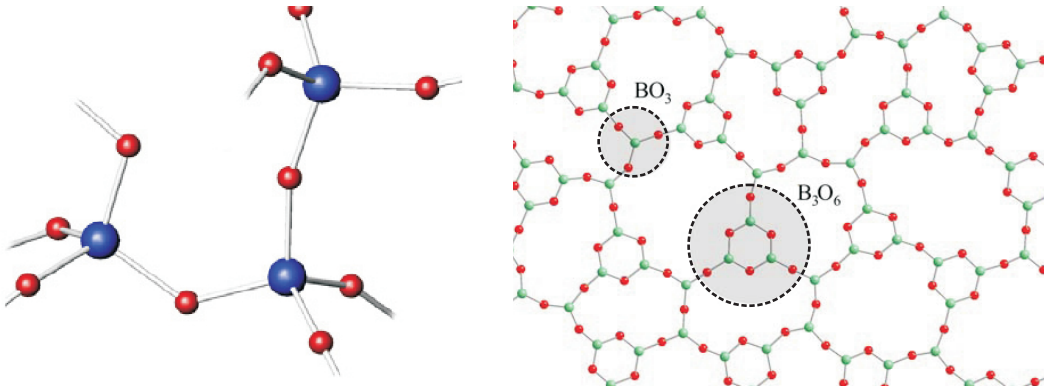

Figure 9-1: The structure of (a) SiO_2 under ambient conditions adapted from ref. [214] and (b) B_2O_3 under ambient conditions from ref. [273]. The blue atoms represent Si, the green B and the red atoms O.

to 80 %. A useful summary is given in ref. [276].

It has been proposed, using molecular dynamics (MD) simulations that few rings exist and that the Raman active vibrational mode often associated with boroxol rings can instead be assigned to the breathing modes of BO_3 units [277]. This view was supported by a reverse Monte-Carlo (RMC) analysis of neutron and x-ray diffraction data [278] where, if the model had more than 30 % boroxol rings, the data could not be fitted in a self-consistent way. Results using the empirical potential structure refinement (EPSR) method with neutron and x-ray diffraction data suggest that diffraction experiments are insensitive to the fraction of boroxol rings [275].

However, the consensus from many experimental techniques is that the fraction of boroxol rings is between 70 and 80 % [256, 279]. These experiments include ^{17}O and ^{11}B NMR [280–283], Raman spectroscopy [284–286], x-ray diffraction [287] and neutron scattering (both spectroscopy and diffraction) [288, 289]. It is worth noting that in ref. [289] it was found that matrix element effects enhance by as much as 40 times the peak in the vibrational density of states associated with boroxol ring structures as measured by Raman scattering [289]. This demonstrates the usefulness of complementary inelastic neutron scattering measurements for which the vibrational modes receive an equal weighting.

It is difficult to simulate the B_2O_3 structure because the number of atoms that can be used in the most accurate simulations is too small and the simulated quench rate is too fast for rings to form [290]. The most recent simulations try to take into account these problems and show that the fraction of boroxol rings is around 70 % [276, 290, 291].

The mechanisms by which the B_2O_3 glass network collapses under pressure are of

great interest due to the planar arrangement of the BO_3 units and the presence of the aforementioned boroxol rings [254, 292, 293]. Current *in situ* experiments using x-ray diffraction [292], Raman scattering [294], Brillouin scattering [295, 296] and inelastic x-ray scattering [297] indicate that boroxol rings break up in the pressure range from ambient to 6 GPa and that there are transformations of the structural units in the region of 6-15 GPa. In this pressure regime, the 3-fold coordinated trigonal units transform to 4-fold coordinated tetrahedra. This view is supported by *ab initio* MD simulations made by Brazhkin *et al.* [292], although the pressure dependence in the simulations does not correspond to experiment. Neutron diffraction experiments under pressure are not yet available, although unpublished data have been taken using the D4C diffractometer at the Institut Laue-Langevin, France by Salmon *et al.* [298] up to pressures of 9 GPa. Data above 9 GPa are presented in the present work.

The present chapter is organised as follows. In section 9.2 the experimental procedure is presented, where samples of SiO_2 and B_2O_3 were measured under pressures up to 17.5 GPa. The data analysis procedure is presented in section 9.3 using the method described in section 4.2. In section 9.4 the results are presented alongside new simulations of SiO_2 made by Wilson [213]. Results are discussed in section 9.5, where coordination numbers, bond distances and first sharp diffraction peak positions are given. Where possible, these values are compared to other experiments and simulations. Finally, conclusions are drawn in section 9.6.

9.2 Experimental Procedure

9.2.1 Sample Preparation

For the SiO_2 sample, a commercially available 5 mm diameter fused silica rod (Goodfellow 99.9 %) was roughly shaped into a pellet suitable for double toroid anvil geometry (see figure 8-2) by using a rotary tool.

In the case of B_2O_3 a fresh glassy sample was made that was isotopically enriched with 99.65 wt% ^{11}B, because ^{N}B has a large neutron absorption cross section (767 barn at a neutron wavelength 1.798 Å, compared to 0.0055(33) barn for ^{10}B) [113]. Glassy $^{11}B_2O_3$ was made by first heating $\approx$ 5 g of $^{11}B_2O_3$ powder (Ceradyne, inc.), contained in a Pt (10 % Rh) crucible, for 2 h at 200 °C. The powder was then melted in air at 1000 °C for 45 min. The viscous liquid was poured in air into the bottom part of a mould made from P20 tool steel (figure 9-2) and the top part closed. The glass quickly solidified before the mould could be fully closed, resulting in a pellet with one well shaped spherical cap and a cylindrical part, but a badly shaped "upper" spherical cap. The "upper" spherical cap was ground into the correct shape using a rotary tool

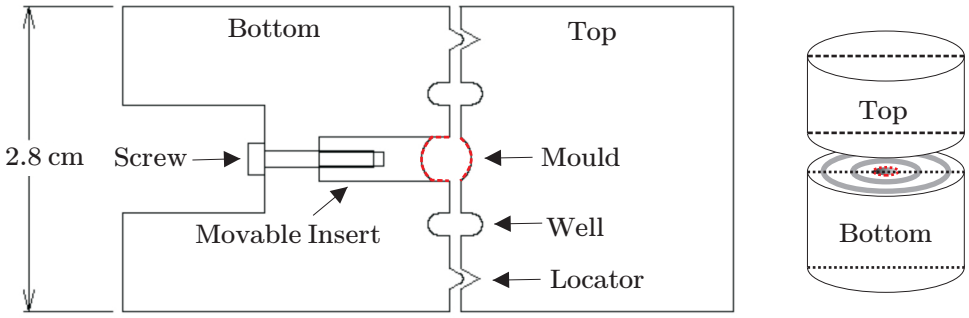

Figure 9-2: (left) Cross section of the double toroid stainless steel mould designed to make pellets for double toroid anvil geometry (see figure 8-2) (drawn on its side). The glass forming liquid is poured into the centre. A locator ensures that the top and bottom parts are in alignment when the mould is closed. A well helps to accommodate any superfluous liquid so that the two halves can quickly be pushed together. After the liquid has solidified, an insert is moved with a screw to remove the glass pellet. (right) A three dimensional representation of the mould. The dotted black lines indicate the cross section corresponding to the figure on the left hand side.

in an Ar filled glovebag.

The pellets of SiO_2 and B_2O_3 were made with masses as close as possible to the ideal mass for the corresponding volume (see section 8.2.1). Using densities of 2.2101 [175] and 1.7911 g cm^3 [299], these ideal masses were found to be 0.074183 and 0.06036 g, respectively. The actual masses of the pellets that were used are given in table 9.1. Between fabrication and the diffraction experiments, the silica pellet was left in air, while the B_2O_3 pellet was placed in a bomb in an Ar filled glovebox to prevent any contamination by moisture in the air.

Sample	Pellet	Mass (g)
SiO_2	1	0.0638(2)
B_2O_3	2	0.06093(5)
V	A	0.1981
V	B	0.2020(2)

Table 9.1: Summary of the samples made for the SiO_2 and B_2O_3 experiments done on the PEARL instrument. The sample pellets are distinguished by numbers and the vanadium pellets are distinguished by letters such that they may be referred to later in the text.

9.2.2 Neutron Diffraction Experiments

The high pressure experiments were made at room temperature using the PEARL diffractometer. The experimental setup for this diffractometer, which used the Paris-

Edinburgh press in transverse geometry, is given in section 3.3.1. Double toroid sintered diamond anvils were held in a V4 variant Paris-Edinburgh press [68, 242] with a piston area of 102 cm^2. Background scattering was reduced by two methods. First, the incident beam was collimated by using a BN and Gd tube arrangement. The Gd tube was inserted into the anvil on the breach of the press with an outer diameter of 3.5 mm and wall thickness of 0.06 mm. Second, the anvils were shielded by neutron absorbing Cd.

For the empty gasket measurement, an empty gasket was placed between the anvils of the press and a load of 2 tns was first applied to hold the assembly in place. The press was then lowered into the neutron beam and centred. A measurement was made for ≈ 1 day. The sample of SiO_2 was placed between the anvils and a small load of 2 tns was again applied. The assembly was then lowered into the neutron beam and centred. The load applied to the anvils via the pistons of the press was slowly increased using a hydraulic oil pump until the desired load was reached. While increasing the pressure, the system was allowed to equilibrate for ≈ 5 min at regular intervals (approximately after every 10 tns of additional load applied). As the anvils compress, the centre of the sample changes position in the beam. Therefore, for each measurement the assembly was moved using a motorised system and the sample was centred in the beam by eye. A neutron diffraction pattern was collected over a period of approximately 1 day. After each measurement was made, the load was increased to make a further measurement at a new pressure point. For each measurement on the SiO_2 sample, a smaller load was applied to the pellet of V labelled "A" and a measurement taken for a short time. The load applied to the V sample was then increased in small increments, taking a measurement each time, until the ratio of $I_{\mathrm{sc}}(Q)/I_{\mathrm{vc}}(Q)$ was flat and as free from diamond Bragg peaks as possible (see section 4.2). A full measurement was then taken for use in the data analysis procedure. A similar procedure was then used to apply pressure to the pellet of B_2O_3, where the pressure was matched to the vanadium measurements such that the ratio $I_{\mathrm{sc}}(Q)/I_{\mathrm{vc}}(Q)$ was flat and as free from diamond Bragg peaks as possible, with the exception of a measurement that was made for a load of 75 tns. A run was therefore made on a second V pellet (labelled "B"). It was found that the V pellet "A" measured at 2 tns could not be used to correct the SiO_2 data taken at 2 tns so a measurement was made at a pressure of 20 tns using pellet "B". The pressure on V pellet "B" was then increased until the $I_{\mathrm{sc}}(Q)/I_{\mathrm{vc}}(Q)$ function was as flat as possible for the 75 tns B_2O_3 measurement. The measurements are summarised in table 9.2.

Sample	Sample Load (tns)	V Load (tns)	V Pellet	P (GPa)
SiO_2	2	20	B	0.0(1)
SiO_2	75	100	A	8.5(5)
SiO_2	120	120	A	14.5(5)
B_2O_3	2	2	A	0.0(1)
B_2O_3	75	55	B	8.5(5)
B_2O_3	110	100	A	13.0(5)
B_2O_3	140	120	A	17.5(5)

Table 9.2: Measurements made using double toroid anvils, where P is the pressure at the sample position found using the calibration curve in figure 4-7 and the pellets are defined in table 9.1.

9.3 Data Analysis

The data analysis procedure described in section 4.2 was used to obtain $F(Q)$ functions for the two samples. The $F(0)$ limit (-0.2232 and -0.2379 barn for SiO_2 and B_2O_3, respectively) was found by fitting diffraction patterns, taken at ambient on the D4C diffractometer at the Institut Laue-Langevin by Salmon *et al.* [298]. The function $F(Q) = aQ^2 + F(0)$, where a is a constant, was fitted to the lowest four data points at $Q = 0.4, 0.45, 0.5$ and 0.55 Å^{-1} for SiO_2 or at $Q = 0.3, 0.35, 0.4$ and 0.45 Å^{-1} for B_2O_3 (figure 9-3). The density of SiO_2 at the pressures attained was found by using the *in*

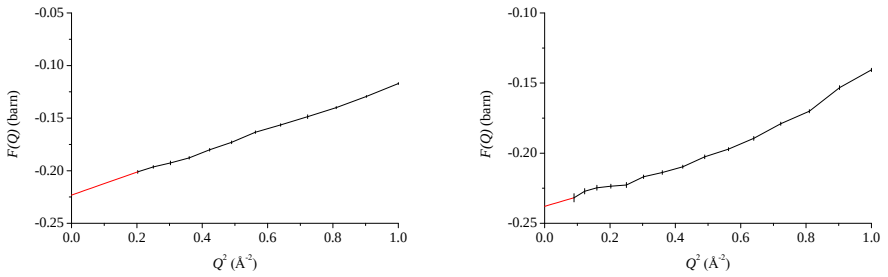

(a) SiO_2 *(b)* B_2O_3

Figure 9-3: Extrapolation of the $F(Q)$ function measured by Salmon *et al.* [298] for a sample of (a) SiO_2 or (b) B_2O_3 (solid black curves). The first four datapoints are fitted assuming a Q^2 dependence and an extrapolation made to $Q = 0$ (solid red curves). This procedure was used to find $F(0) = -0.2232$ and -0.2379 barn for samples of SiO_2 and B_2O_3, respectively .

situ measurements of Sato and Funamori [221] and Mead *et al.* [219] (figure 9-4 (a)). In both of these experiments, a diamond anvil cell was used and the change in volume of the sample measured as a function of pressure. The density of B_2O_3 was found using the

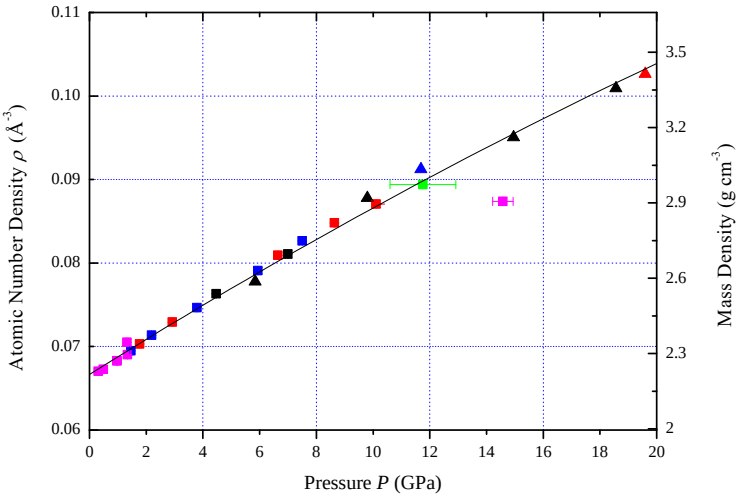

(a) SiO_2

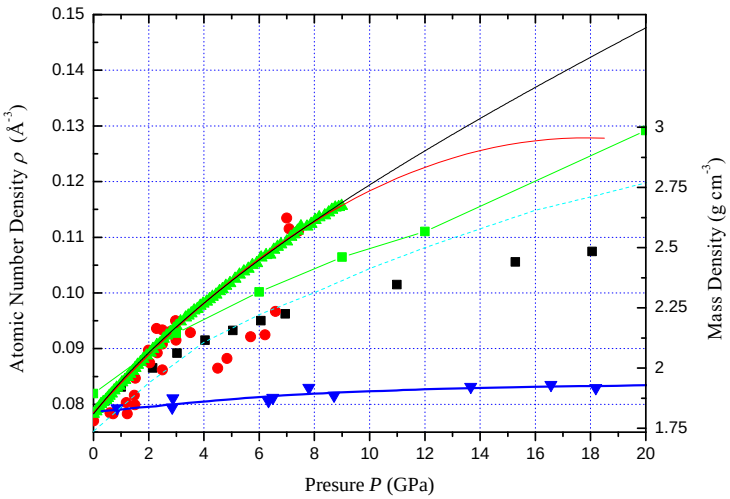

(b) B_2O_3

Figure 9-4: (a) The density of SiO_2 measured by Sato and Funamori in compression using a diamond anvil cell [221] in three separate runs, run 1 (▲), run 2 (▲) and run 3 (▲); and the density of SiO_2 measured by Mead *et al.* [219] using optical measurements of the strain for a sample within a diamond anvil cell in five separate runs, run 1 (■), run 2(■), run 3 (■), run 4 (■), run 5 (■). (b) The density of B_2O_3 from Brazhkin *et al.* as measured using volumetric measurements on a small sample in a single toroid cell with a methanol-ethanol pressure transmitting medium [292] (▲), using a similar method in a previous study (●) [299], or calculated from simulations (joined ■) [292]; the values found from the sound velocity measurements of Huang *et al.* [300] (■); the uniaxial measurements on a thin disk of B_2O_3 by Bridgman [255] (▼); and the simulations made by Takada *et al.* [301] (broken cyan curve). The red and black curves are a second order polynomial and a third order Birch-Murnaghan equation of state [302] fitted to the ▲ datapoints, respectively. The blue curve is fitted to the ▼ datapoints and is taken from ref. [255].

latest *in situ* measurements made by Brazhkin *et al.* [292] on the volume changes of a sample in a methanol-ethanol pressure transmitting medium held between single toroid anvils (figure 9-4 (b)). For pressures above 9 GPa, an extrapolation was made using a second order polynomial fitted to the data by Brazhkin *et al.* [292] and the values used are taken from this curve. Also presented is a fit of a third order Birch-Murnaghan equation of state given by [302]

$$P = \frac{3B_0}{2}\left[\left(\frac{V}{V_0}\right)^{-7/3} - \left(\frac{V}{V_0}\right)^{-5/3}\right]\left[1 + \frac{3}{4}\left(B_1 - 4\right)\left(\left(\frac{V}{V_0}\right)^{-2/3} - 1\right)\right], \qquad (9.1)$$

were V is the volume and V_0 is the volume under ambient conditions. The best fit was found with parameters $B_0 = 12.31(7)$ GPa and $B_1 = 3.28(3)$, where B_0 is the bulk modulus under ambient conditions. The experimental bulk modulus is $B_0 = 13.8$ GPa [245]. The Birch-Murnaghan equation is an approximation that is often used for equations of state (see e.g. equation (1) in ref. [303]). The values of Brazhkin *et al.* [292] agree qualitatively with previous *in situ* measurements made by Brazhkin *et al.* [299]; but disagree with values found from the sound velocity measurements made by Huang *et al.*, which underestimate the density as discussed in ref. [300], early uniaxial measurements on a small disc of sample made by Bridgman [255], and the values found from simulations made by Takada *et al.* [301] and Brazhkin *et al.* [292]. The densities used in the present study are given in table 9.4.

The functions $W_2F^{(0)}(Q)$ and $F(Q)$ that were found for each sample and pressure point using the correction factors listed in table 9.3 are plotted in figure 9-5 for SiO_2 and figure 9-6 for B_2O_3 to show the effect of the slope removal and Lorentzian fitting procedure. In each case the Lorentzian function that was fitted at low Q has been highlighted. Also plotted in figures 9-5 and 9-6 are the back Fourier transforms of the $G(r)$ functions after the majority of the unphysical low-r oscillations have been removed. These are found to be in excellent agreement with the $F(Q)$ functions, with the exception of the ambient B_2O_3 measurement.

The efficacy of the semi-empirical data analysis procedure was tested by comparing both the $F(Q)$ (figure 9-7) and $G(r)$ (figure 9-8) functions from this study to those found in experiments on samples of SiO_2 or B_2O_3 at similar pressures $\lesssim 9$ GPa by Salmon *et al.* using the D4C diffractometer at the Institut Laue-Langevin in Grenoble, France with single toroid boron-nitride anvils in a Paris-Edingburgh press [298]. The $G(r)$ functions from Salmon *et al.* were calculated using $F(Q)$ functions truncated at a Q value of 19.6 Å^{-1} corresponding to the maximum Q measured on PEARL. The small disagreements between $F(Q)$ measured by Salmon *et al.* [298] and the present work for SiO_2 can be explained by the different resolution functions of the two

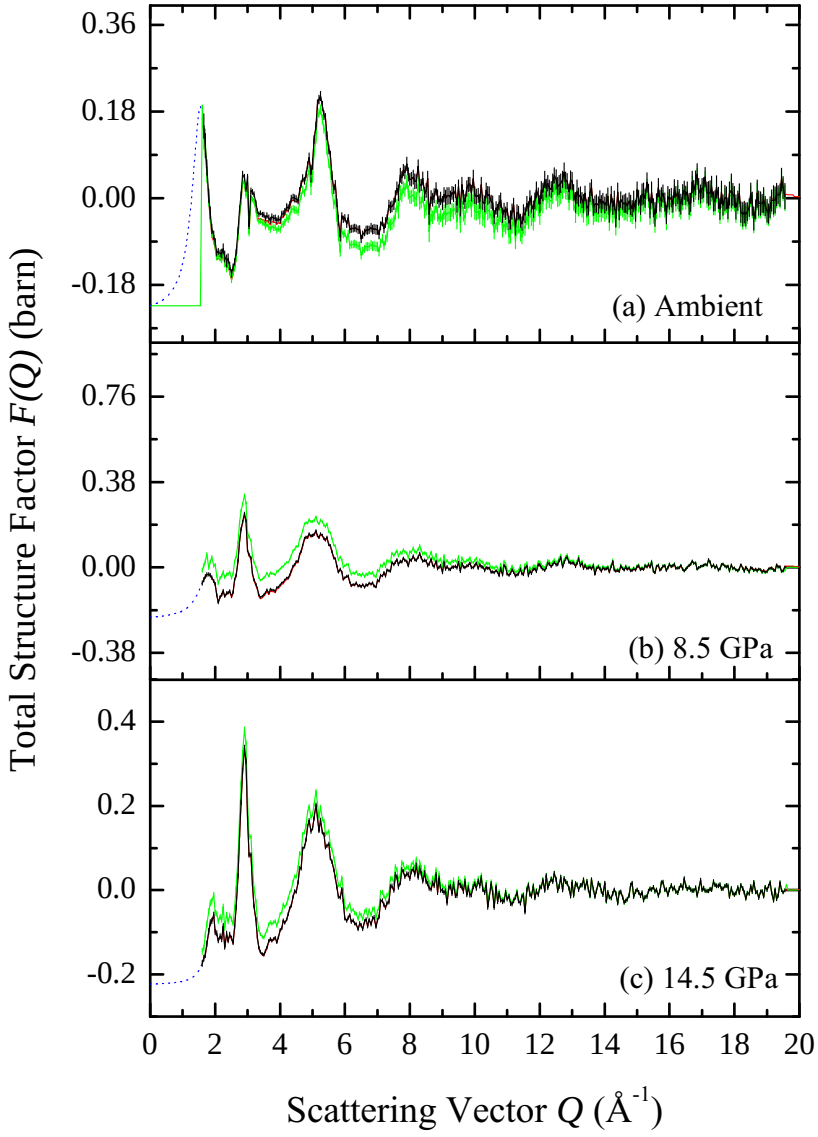

Figure 9-5: For measurements of the SiO_2 sample in double toroid anvils at the indicated pressures, the function $W_2F^{(0)}(Q)$ as calculated by using equation (4.28) (solid green line), the $F(Q)$ function after slope removal, rescaling and fitting a Lorentzian function at low Q (solid black line), and the back Fourier transform of the $G(r)$ function after removal of the majority of unphysical low r oscillations (solid red curve). The solid red curves are often hidden due to excellent agreement with the solid black curves.

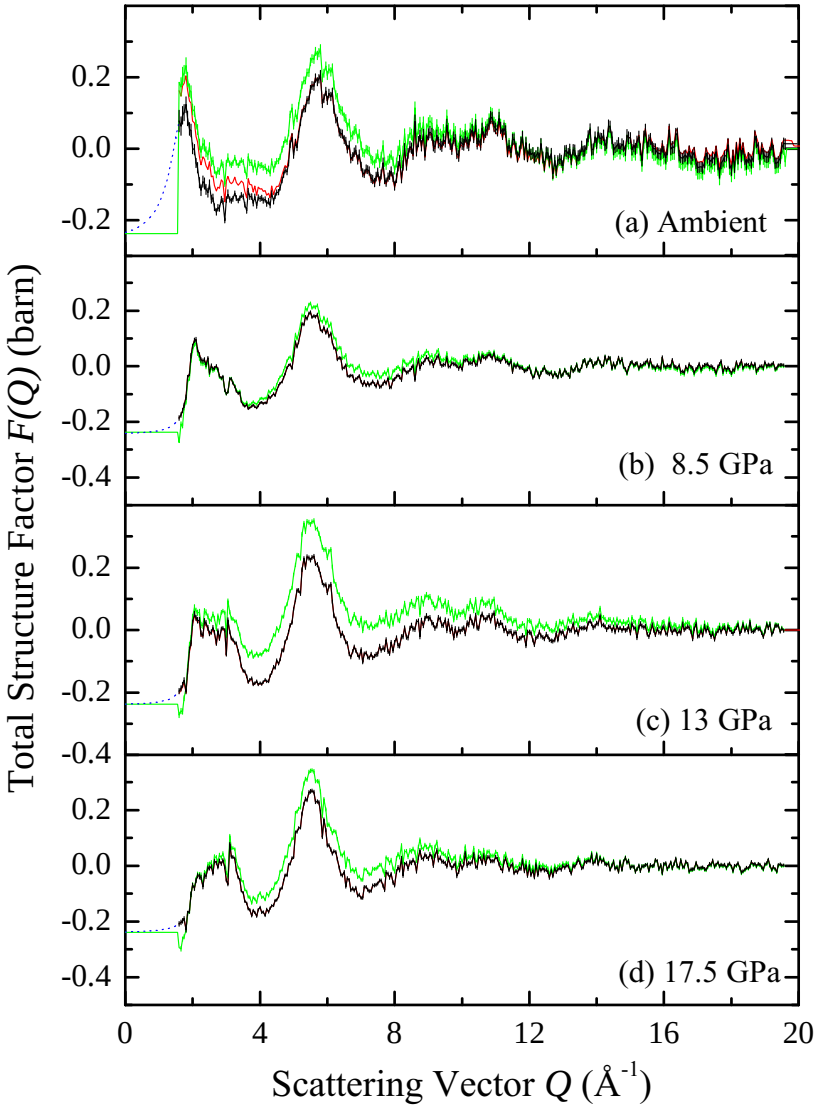

Figure 9-6: For measurements of the B_2O_3 sample in double toroid anvils at the indicated pressures, the function $W_2F^{(0)}(Q)$ as calculated by using equation (4.28) (solid green line), the $F(Q)$ function after slope removal, rescaling and fitting a Lorentzian function at low Q (solid black line), and the back Fourier transform of the $G(r)$ function after removal of the majority of unphysical low r oscillations (solid red curve). The solid red curves are often hidden due to excellent agreement with the solid black curves

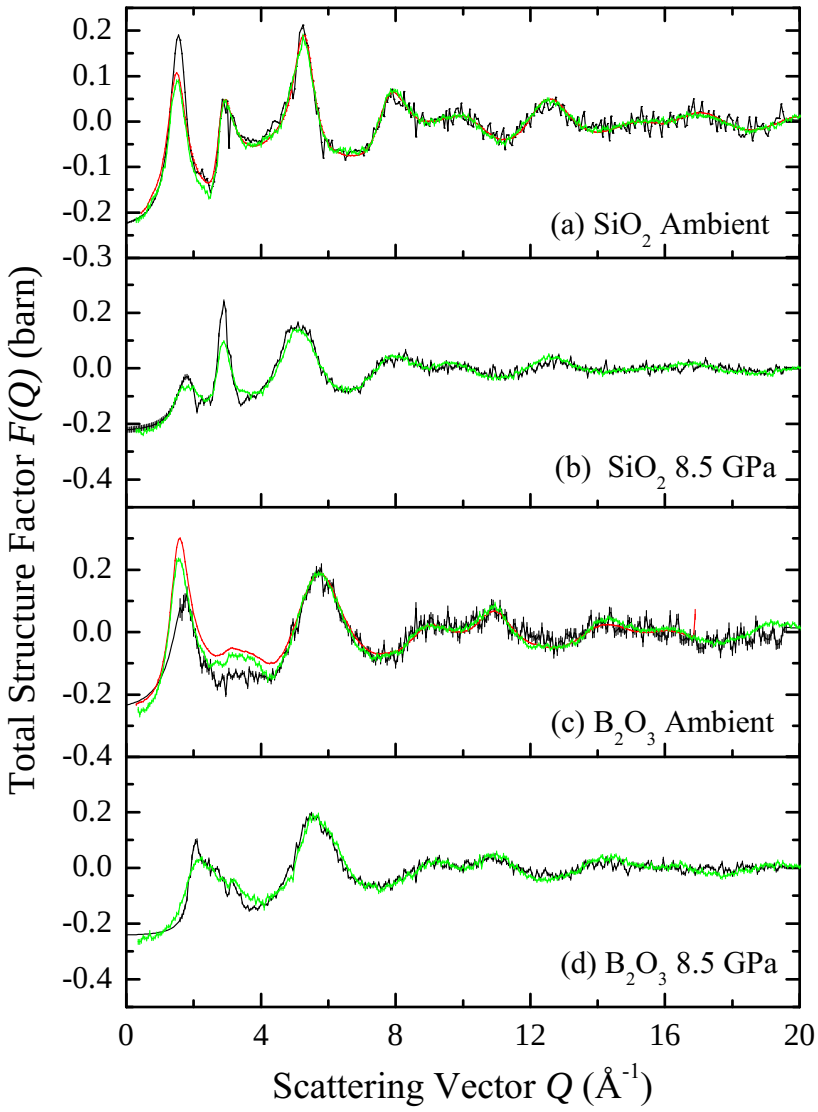

Figure 9-7: The total structure factors $F(Q)$ measured for samples of (a) SiO_2 under ambient pressure, (b) SiO_2 under a pressure of 8.5 GPa, (c) B_2O_3 under ambient pressure and (d) B_2O_3 under a pressure of 8.5 GPa from the present study (solid black curves). The datasets are compared to measurements made using the D4C diffractometer using boron-nitride anvils [298, 304] (solid green curves) either under ambient conditions in (a) and (c) or under a pressure of 8.1 GPa in (b) and (d), or to measurements made using the D4C diffractometer with the sample held in a standard vanadium container [298] (solid red curves in (a) and (c)).

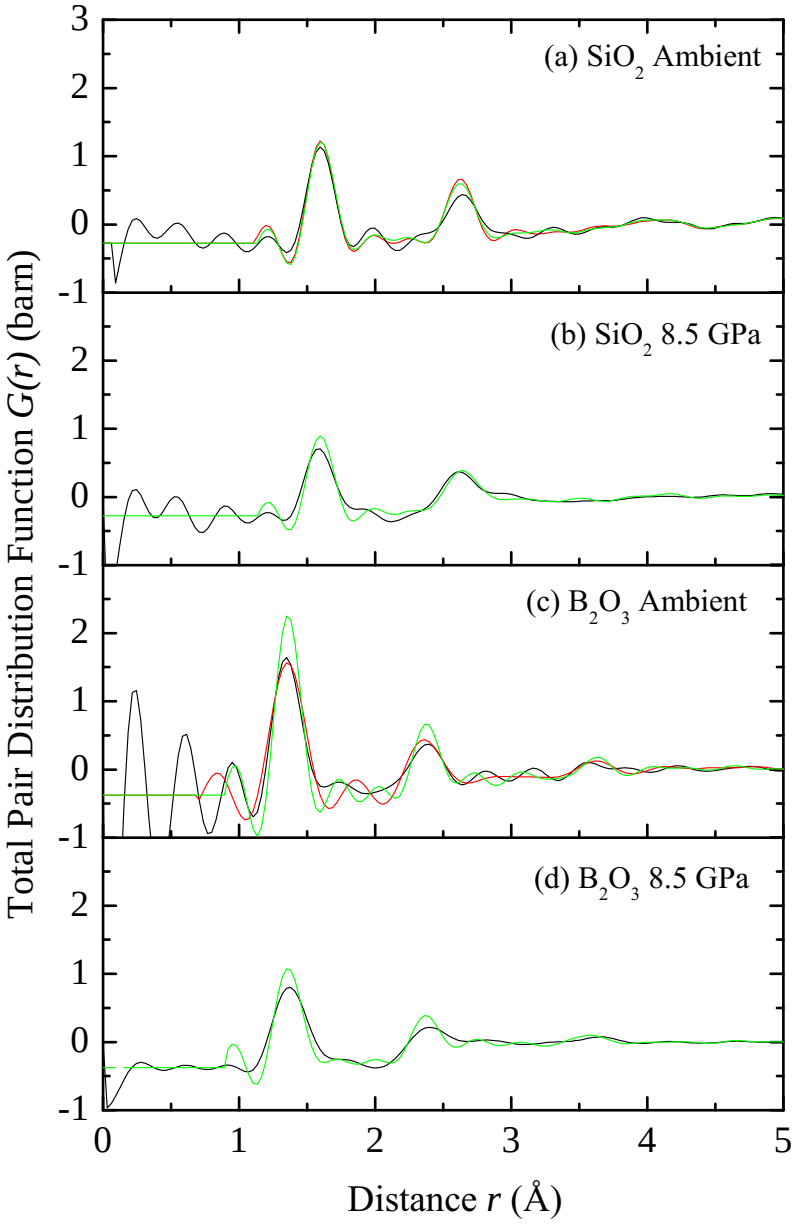

Figure 9-8: The total pair distribution functions $G(r)$ measured for samples of (a) SiO_2 under ambient pressure, (b) SiO_2 under a pressure of 8.5 GPa, (c) B_2O_3 under ambient pressure and (d) B_2O_3 under a pressure of 8.5 GPa from the present study (solid black curves). The datasets are compared to measurements made using the D4C diffractometer using boron-nitride anvils [298, 304] (solid green curves) either under ambient conditions in (a) and (c) or under a pressure of 8.1 GPa in (b) and (d), or to measurements made using the D4C diffractometer with the sample held in a standard vanadium container [298] (solid red curves in (a) and (c)).

P (GPa)	C_s	C_v	W	W_2
SiO_2 Measurements				
Ambient	0.83	0.92	0.32	1.25
8.5	0.30	0.20	0.30	2.00
14.5	0.20	0.15	0.285	2.40
B_2O_3 Measurements				
Ambient	0.72	0.63	0.35	1.30
8.5	0.25	0.20	0.32	1.75
13	0.20	0.20	0.33	1.95
17.5	0.15	0.15	0.34	2.00

Table 9.3: The correction factors for the SiO_2 and B_2O_3 experiments made using double toroid anvils. C_s and C_v are the multiplication factors for the empty gasket diffraction pattern which is subtracted from the sample and vanadium diffraction patterns, respectively. W is the initial normalisation constant and W_2 is the re-scaling factor as described in section 4.2.

instruments. The resolution of PEARL is $\Delta Q/Q \simeq 0.85\%$, while the resolution of D4C is $\Delta Q/Q \simeq 3\%$ [39]. The resolution function has a significant effect in the region of sharp peaks at low Q [49]. The small disagreement between the $F(Q)$ functions measured by Salmon *et al.* [298] and the present work for B_2O_3 at ambient pressure could be explained by the high compressibility of the B_2O_3 glass. The compressibility of B_2O_3 is 0.07246 GPa^{-1} [292], which compares to the compressibility of SiO_2 of 0.02396 GPa^{-1} [245]. This means that even small pressures can change the structure of the glass. The load of 2 tns applied to hold the sample in place may have had the effect of compressing the sample. The smaller height and shift to higher Q of the first sharp diffraction peak (FSDP) at $\approx 2\text{Å}^{-1}$ is consistent with the sample being under a higher pressure [225, 292, 304], such that the intermediate range ordering has changed [63]. At a pressure of 8.5 GPa, $F(Q)$ measured for the B_2O_3 sample is in better agreement with the neutron diffraction experiments made by Salmon *et al.* [298].

9.4 Results

In table 9.4 several parameters describing the structures of SiO_2 and B_2O_3 are given for the measured pressures. The positions are given for the first and second peaks in $F(Q)$, referred to as the first sharp diffraction peak (FSDP) with position Q_{FSDP} and principal peak (PP) with position Q_{PP} which relate to the intermediate and extended range ordering in the system [63, 243], respectively. In the case of the B_2O_3 experiment, the FSDP and PP have merged for the higher pressure measurements and cannot be distinguished. Also given is the position of the first peak in $G(r)$, which corresponds

to the mean nearest neighbour Si-O or B-O bond distance denoted by r_{SiO} or r_{BO}, respectively, and the ratio of the position of the second peak to the position of the first peak r_2/r_{SiO} and r_2/r_{BO}. Finally, the atomic number density ρ and the mean Si-O or B-O coordination number, denoted by $\overline{n}^{\mathrm{O}}_{\mathrm{Si}}$ and $\overline{n}^{\mathrm{O}}_{\mathrm{B}}$ respectively, are listed. The measured

Pressure (GPa)	ρ (Å^{-3})	Q_{FSDP} (Å^{-1})	Q_{PP} (Å^{-1})	$r_{(\mathrm{Si,B})\mathrm{O}}$ (Å)	$\overline{n}^{\mathrm{O}}_{(\mathrm{Si,B})}$	$r_2/r_{(\mathrm{Si,B})\mathrm{O}}$
			SiO_2 Measurements			
Ambient	0.066(1)	1.55(2)	2.90(2)	1.60(2)	4.0(1)	1.652
8.5(5)	0.085(1)	1.78(2)	2.90(2)	1.59(2)	4.0(1)	1.652
14.5(5)	0.095(1)	1.93(2)	2.90(2)	1.59(2)	4.0(1)	1.647
			B_2O_3 Measurements			
Ambient	0.0785(1)	N/A	N/A	1.35(2)	3.0(1)	1.773
8.5(5)	0.1145(1)	N/A	N/A	1.37(2)	3.3(1)	1.750
13(5)	0.1166(1)	N/A	N/A	1.40(2)	3.7(1)	1.735
17.5(5)	0.1279(1)	N/A	N/A	1.41(2)	3.9(1)	1.704

Table 9.4: Parameters describing the pressure dependence of the structure of SiO_2 and B_2O_3 glasses as obtained from the neutron diffraction experiments using the PEARL diffractometer with double toroid sintered diamond anvils. The number densities ρ of the glasses [219, 228, 293] are given together with the position Q_{FSDP} of the first sharp diffraction peak, the position Q_{PP} of the principal peak, the Si-O or B-O bond distance $r_{(\mathrm{Si,B})\mathrm{O}}$ taken from the position of the first peak in $G(r)$, the mean Si-O or B-O coordination number $\overline{n}^{\mathrm{O}}_{(\mathrm{Si,B})}$, and the ratio $r_2/r_{(\mathrm{Si,B})\mathrm{O}}$ where r_2 is the position of the second peak in $G(r)$.

$F(Q)$ functions are given in figures 9-9 and 9-10 for the SiO_2 and B_2O_3 experiments, respectively. The results for SiO_2 are compared with the $F(Q)$ functions obtained from new classical molecular dynamics (MD) simulations made by Wilson [305] using the potentials of Tangney [306] obtained from *ab initio* force field calculations. The simulations were made at the same densities as found for the experimental results from figure 9-4. The neutron diffraction data were spline fitted to smooth the high frequency noise and Fourier transformed using equation (2.53) to obtain the $G(r)$ functions given in figures 9-11 and 9-12 for the SiO_2 and B_2O_3 experiments, respectively.

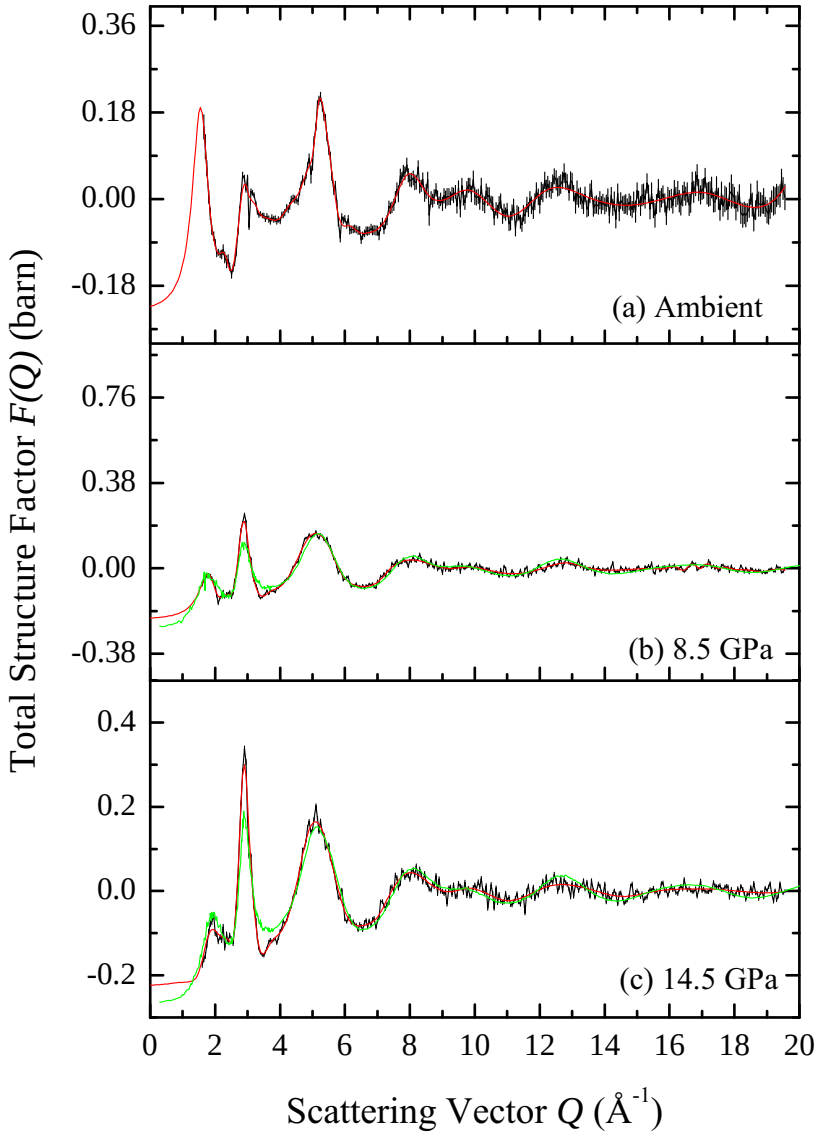

Figure 9-9: The pressure dependence of the $F(Q)$ functions measured for SiO_2 at the stated pressures using a Paris-Edingburgh press with double toroid sintered diamond anvils (solid black curves). Spline fits to the data are given by solid red curves. The datasets are compared to the MD simulations made by Wilson [305, 306] (solid green curves).

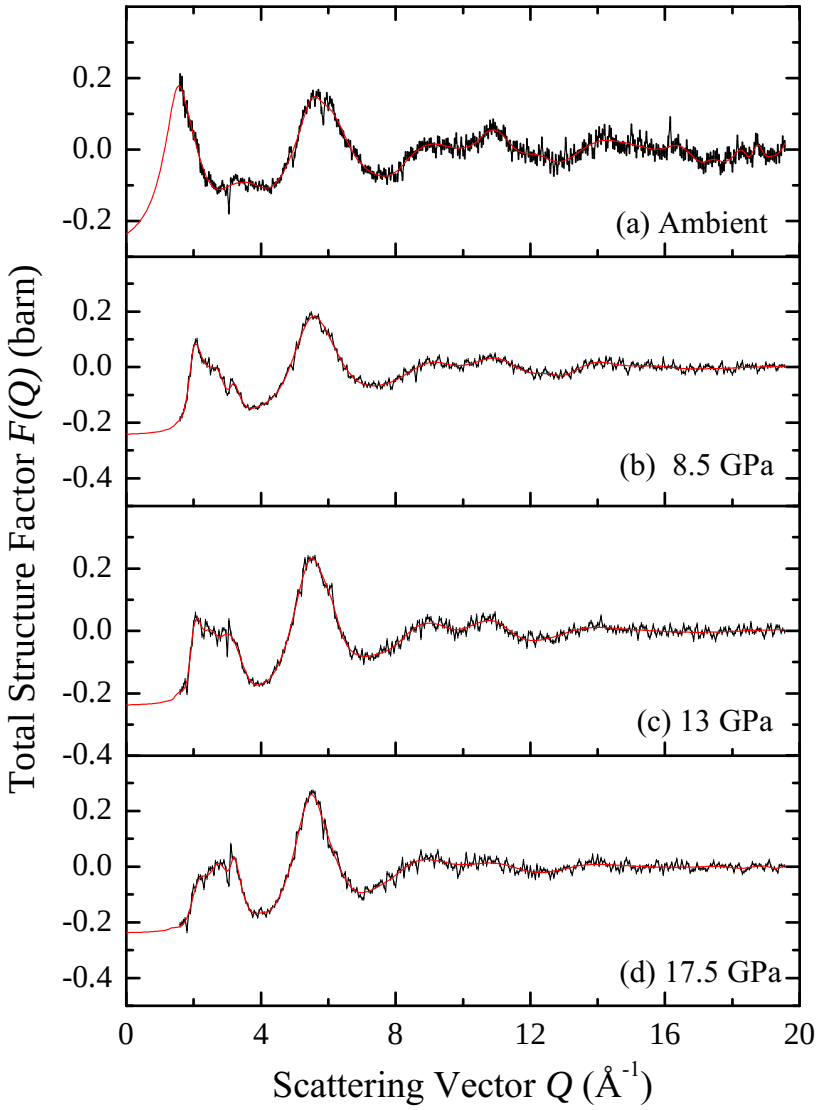

Figure 9-10: The pressure dependence of the $F(Q)$ functions measured for B_2O_3 at the stated pressures using a Paris-Edingburgh press with double toroid sintered diamond anvils (solid black curves). Spline fits to the data are given by solid red curves.

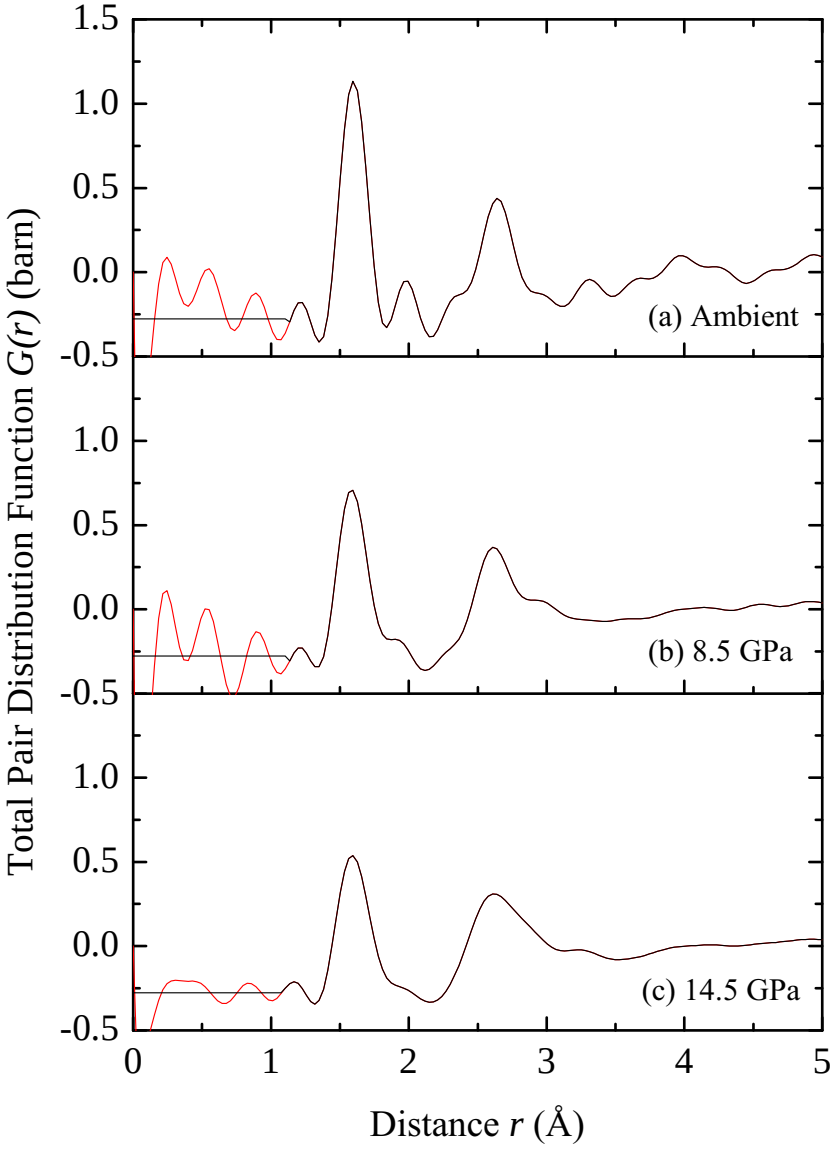

Figure 9-11: The pressure dependence of the $G(r)$ functions for SiO_2 at the stated pressures as obtained by using the spline fitted $F(Q)$ functions shown in figure 9-9 (solid black curves). The solid red curves show the extent of the unphysical low-r oscillations.

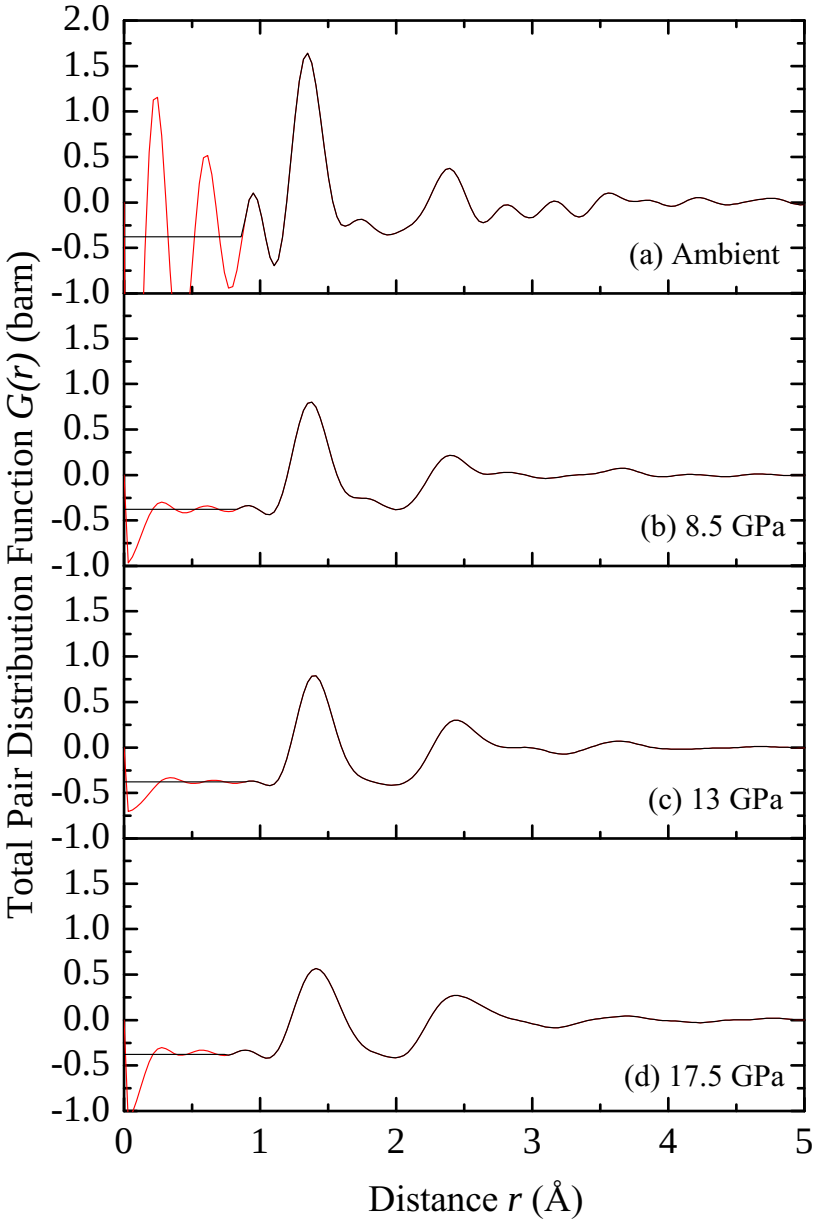

Figure 9-12: The pressure dependence of the $G(r)$ functions for B_2O_3 at the stated pressures as obtained by using the spline fitted $F(Q)$ functions shown in figure 9-10 (solid black curves). The solid red curves show the extent of the unphysical low-r oscillations.

9.5 Discussion

9.5.1 Silica Experiment

The FSDP is indicative of intermediate range order as discussed in section 8.5, and the pressure dependence of its position is plotted in figure 9-13. These data are compared to the positions found from the experiments made on the D4C diffractometer by Salmon *et al.* [298]; the x-ray diffraction experiments made using a diamond anvil cell by Benmore *et al.* [225], Meade *et al.* [219], Sato *et al.* [221], and Sato and Funamori [228]; the x-ray diffraction experiments made using a cubic multi-anvil apparatus by Inamura *et al.* [265], where measurements taken below 9 GPa were made with a different variant of the apparatus to those taken above 11 GPa [265]; and the MD simulations made by Huang *et al.* [307] (broken red curve). The MD simulations were made using a charge-transfer three-body potential, which was developed to describe the charge redistribution upon breaking and forming bonds, and were made at a temperature of 500 K. The results from the various studies are in agreement, although more datapoints are required between pressures of 10 and 15 GPa where there appears to be a change in the gradient $\mathrm{d}Q_{\mathrm{FSDP}}/\mathrm{d}P$ at $\approx$ 10 GPa. This observation is to some extent reproduced by the simulations made by Huang *et al.* [307], while the MD simulations of Wilson [305] do not have datapoints in this region of pressure.

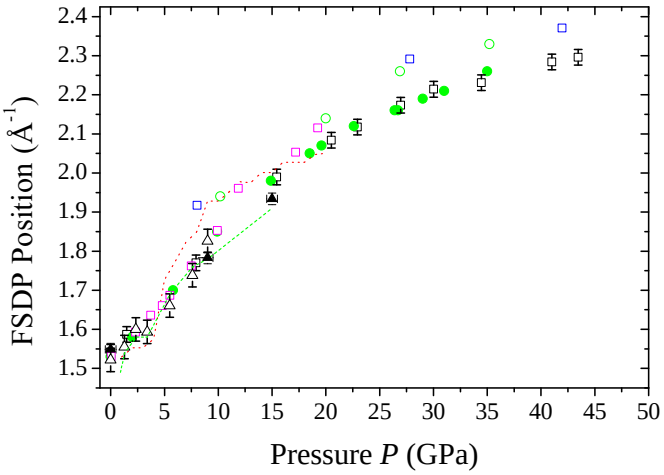

Figure 9-13: The pressure dependence of the position of the first sharp diffraction peak in $F(Q)$, Q_{FSDP}, for the samples of SiO_2 as measured in the present work by using neutron diffraction (▲). The results are compared to those obtained from the neutron diffraction experiments made on the D4C diffractometer by Salmon *et al.* [298] (△), the x-ray diffraction experiments made by Benmore *et al.* [225] (□), Meade *et al.* [219] (□), Inamura *et al.* [265] (□), Sato *et al.* [221] (●), and Sato and Funamori [228] (○); and molecular dynamics simulations made by Huang *et al.* [307] (broken red curve) and Wilson [305, 306] (broken green curve).

The most recent MD simulations made by Wilson [305] (figure 9-9) provide $F(Q)$ functions that are in good agreement with the current data in the region of the FSDP. The $F(Q)$ functions in the region of the PP are not in such good agreement, where the $F(Q)$ functions from simulation are lower than the experimental data. However, the same trend is observed, whereby the FSDP shrinks as the PP rises with increasing pressure. This indicates a change in the intermediate and extended range ordering of the system, consistent with the picture of a re-ordering of tetrahedra [225, 307].

The first and second peaks in $G(r)$ broaden with increasing pressure but do not change position (see figure 9-11), while the Si-O coordination number does not change from the value of 4 at pressures below 14.5 GPa. This is in accordance with neutron diffraction experiments made on the D4C diffractometer by Salmon *et al.* [298]; x-ray diffraction experiments made using a diamond anvil cell by Benmore *et al.* [225], Meade *et al.* [219], Sato *et al.* [221], and Sato and Funamori [228]; and MD simulations made by Huang *et al.* [307] and Tse *et al.* [308] (figure 9-14). The latter were made using two body potentials constructed by using the *ab initio* approach of van Beest *et al.* [309].

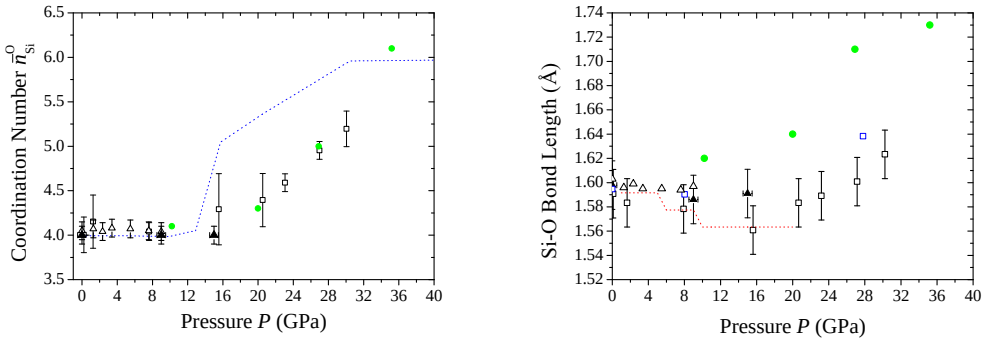

(a) *(b)*

Figure 9-14: The pressure dependence of (a) the mean coordination number $\overline{n}^{O}_{Si}$ and (b) the Si-O bond distance r_{SiO} for SiO_2 glass as measured in the present work by using neutron diffraction (▲); the neutron diffraction measurements made on the D4C diffractometer by Salmon *et al.* [298] (△); the x-ray diffraction experiments made by Benmore *et al.* [225] (□), Sato *et al.* [228] (●), and Meade *et al.* [219] (□); and the molecular dynamics simulations of Tse *et al.* [308] (broken blue curve), and Huang *et al.* [307] (broken red curve). The values for $\overline{n}^{O}_{Si}$ from the present study were obtained by integrating over the first peak in $G(r)$ (see equation (8.3)).

At the present time, for pressures higher than ≈ 20 GPa, a diamond anvil cell must be used and only x-ray studies can be made due to the small sample volume. Such studies [219, 225, 228, 265] indicate a gradual change in coordination number, which begins at a pressure of 20 GPa, and where the structural motifs become fully octahedral at a pressure of ≈ 36 GPa. By comparison, in GeO_2 (see chapter 8), a

similar transformation from a tetrahedral to an octahedral glass occurs between 5 and 30 GPa.

9.5.2 Boron Oxide Experiment

In the case of B_2O_3, the FSDP merges with the principal peak and a broad feature is formed in $F(Q)$ at the high pressures measured in the present study (figure 9-10) such that the positions of these peaks cannot be distinguished. The ratio of weighting factors for the contributions of $S_{BB}(Q)$:$S_{OO}(Q)$:$S_{BO}(Q)$ to $F(Q)$ are 0.17444:0.33912:0.48643 for neutron diffraction and 0.10917:0.62882:0.26201 for x-ray diffraction at $Q = 0$. The $F(Q)$ functions measured for neutrons are therefore more heavily weighted towards the B-O correlations, while the $F(Q)$ functions measured for x-rays are more heavily weighted towards the O-O correlations. The FSDP is more separated from the principal peak in the x-ray structure factors (see figure 9-15) due to this difference in weighting factors. The x-ray diffraction study by Brazhkin *et al.* [292] shows that the FSDP moves

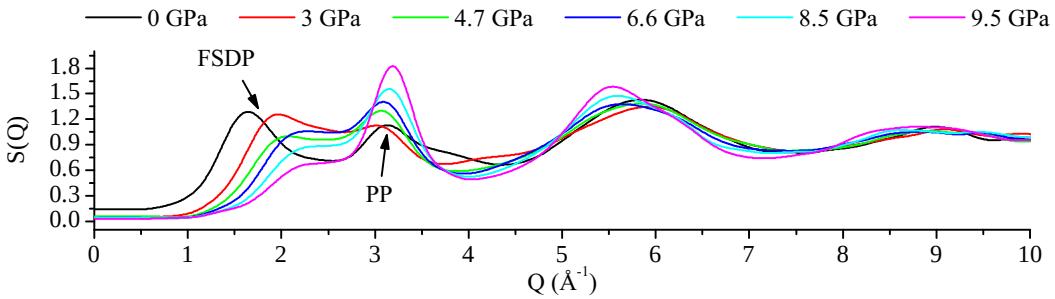

Figure 9-15: The pressure dependence of the structure factor for B_2O_3 glass as measured by x-ray diffraction by Brazhkin *et al.* using a multi-anvil press [292].

to higher Q with increasing pressure and eventually merges with the PP at a pressure of about 9.5 GPa. The PP shows an accompanying increase in intensity with increasing pressure. In the present study, this behaviour continues with pressures increasing up to 17.5 GPa.

The position of the first peak in the $G(r)$ functions (figure 9-12), which is attributed to the B-O correlations, increases with pressure. Other experimental studies [292, 297, 298] show that this increase begins at a pressure of $\approx$ 8 GPa (see figure 9-16), i.e. at pressures below $\approx$ 8 GPa, the B-O bond distance does not change from its ambient value. The bond distance then increases steadily from 1.35 to 1.41 Å between a pressure of 8.5 and 17.5 GPa.

The coordination numbers found in the present work (see figure 9-17a) are in good agreement, within the experimental error, with those obtained from the inelastic x-ray experiments of Lee *et al.* made using a diamond anvil cell [297]. In these experiments,

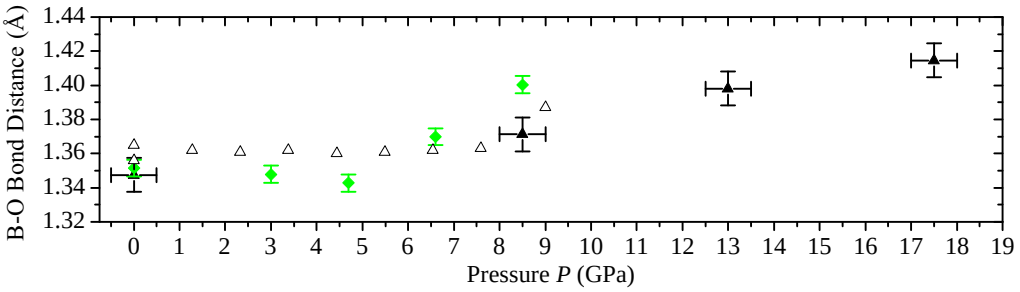

Figure 9-16: The B-O bond distance r_{BO} for B_2O_3 glass as measured in the present work by using neutron diffraction (▲). The results are compared to the neutron diffraction measurements made on the D4C diffractometer by Salmon *et al.* [298] (△); and the x-ray diffraction experiments made by Brazhkin *et al.* [292] (♦).

the fractions of 3-fold and 4-fold coordinated boron atoms were found as a function of pressure, allowing the mean coordination numbers to be calculated. The present results also agree with the unpublished neutron diffraction results of Salmon *et al.* [298] and the x-ray diffraction results made by Brazhkin *et al.* using a multi-anvil press [292]. The coordination numbers calculated from the present study disagree with the first principles MD simulations made by Brazhkin *et al.* [292] and Takada *et al.* [301]. These simulations also give a variation of the density with pressure that is not in agreement with experiment (see figure 9-4). Better agreement between the coordination numbers found from experiment and from simulation is obtained by plotting the datasets as a function of density (see figure 9-17b). In this representation, the simulations made by Brazhkin *et al.* [292] and Takada *et al.* [301] are also in good agreement with each other. The experimental data show that there is an increase in the B-O coordination number with pressure beginning at ≈ 8 GPa. The inelastic x-ray results of Lee *et al.* [297] indicate a sudden transition of the mean coordination number from 3 to 3.47 in the region of 7 to 8 GPa. However, the present study and the study of Brazhkin *et al.* [292] support a more gradual increase in coordination number with pressure, accompanied by a gradual increase in the B-O bond distance.

The experimental data are consistent with two densification mechanisms as described by Brazhkin *et al.* [292] and reproduced in figure 9-18. First, there is a rearrangement of the BO_3 trigonal motifs and a breakup of B_3O_6 boroxol rings at pressures up to ≈ 8 GPa. Second, above 8 GPa there is continuation of this rearrangement accompanied by a gradual transition of the structural motifs from 3-fold trigonal BO_3 to 4-fold tetrahedral BO_4 units. The pressure at which the glass becomes fully tetrahedral is not well established, though the inelastic x-ray scattering study of Lee *et al.* [297] indicate that full transformation occurs above ≈ 23 GPa.

The comparison of the experimental and simulation results show that an accurate

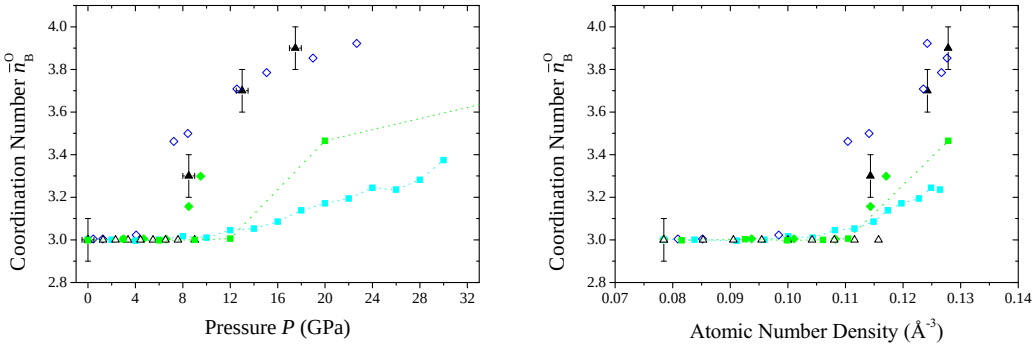

Figure 9-17: The mean coordination number $\overline{n}_B^O$ of B_2O_3 as a function of (a) pressure and (b) density as measured in the present work by using neutron diffraction (▲). The results are compared to the neutron diffraction measurements made on the D4C diffractometer by Salmon *et al.* [298] (△); the x-ray diffraction experiments made by Brazhkin *et al.* [292] (♦); the inelastic x-ray experiments made by Lee *et al.* [297] (◊); and the molecular dynamics simulations made by Brazhkin *et al.* [292] (joined ■) and Takada *et al.* [301] (joined ■). The values for $\overline{n}_B^O$ from the present work were obtained by integrating over the first peak in $G(r)$ (see equation (8.3)).

Figure 9-18: A schematic of the network collapse for B_2O_3 for simulated pressures of (a) ambient, (b) 20 GPa and (c) 200 GPa reproduced from figure 2 in ref. [292]. The quantitative pressure dependence does not correspond to experiments.

simulation of B_2O_3 under pressure is difficult. New simulations are needed and further experiments, such as x-ray diffraction, are required to fully resolve the densification mechanisms for B_2O_3. Further *in situ* measurements are also needed for the density of B_2O_3 at pressures above 9 GPa to ensure that the correct coordination numbers are calculated from the neutron scattering experiments.

9.6 Conclusions

Reliable total structure factors $F(Q)$ have for the first time been measured for glassy SiO_2 and B_2O_3 at pressures above 9 GPa using neutron diffraction. The pressure dependence of the measured FSDP position, Si-O and B-O coordination numbers and Si-O and B-O bond distances are in agreement with other experiments.

In the case of SiO_2, the principal densification mechanism in the region of ambient pressure to 15 GPa is a change in the intermediate range ordering of the tetrahedra. This is indicated by changes in both the FSDP and PP in the $F(Q)$ functions. The data were compared with the new MD simulations made by Wilson [305, 306] which show promising preliminary results. The combination of experimental techniques and simulations will shed light on the re-arrangement of the tetrahedral network of this fundamentally important glass.

In the case of B_2O_3, densification occurs through two mechanisms for pressures up to 17.5 GPa. From ambient pressure to $\approx$ 8 GPa, there is a rearrangement of the trigonal motifs (see figures 9-18a and 9-18b reproduced from figure 2 in ref. [292]). Above 8 GPa, the number of 4 fold coordinated tetrahedral motifs increases (see figure 9-18b and 9-18c), resulting in an increase of the mean coordination number. The growth in coordination number is accompanied by an increase in the mean B-O bond distance to accommodate the additional O atoms. The available MD simulations do not agree well with the experimental results due to the difficulty in simulating the boroxol ring structures.

The densification mechanisms for the archetypical glasses studied in this thesis, namely GeO_2 (see chapter 8), SiO_2, and B_2O_3 have some similar features. In the low pressure regime, the structural motifs and their connectivity do not change, but there is a reorganisation of the intermediate range ordering. At higher pressures, a second densification mechanism arises where a change in the nature of the structural motifs involves an increase in the coordination number. This second densification mechanism occurs above threshold pressures of $\approx$ 5, 20, and 9 GPa, for GeO_2, SiO_2, and B_2O_3, respectively. The nature of the changes to the intermediate range ordering is not directly accessible from the experimental data. To understand the full nature of these mechanisms a combined experimental and simulation approach must be used.

10. Overall Conclusions

In this thesis, two new neutron scattering techniques have been presented for measuring glasses on the atomic level: the method of isotope substitution in neutron spectroscopy and the method of neutron diffraction at pressures above 9 GPa. The network glasses $GeSe_2$, GeO_2, SiO_2 and B_2O_3 were studied by these methods. The main results and future directions are discussed below.

The technique of isotope substitution in neutron spectroscopy was developed by first measuring a sample of $GeSe_2$ using the MARI spectrometer (chapter 5). $GeSe_2$ was chosen because it is a difficult glass to simulate (due to the close electronegativity of the Ge and Se atoms) and the scattering lengths of the isotopes of Ge and Se make it a good candidate for this type of experiment. The full generalised single phonon vibrational density of states $G_1(Q,E)$ and single phonon vibrational density of states $G_1(E)$ were measured in the "bronze medal" approximation for samples of $^{\mathrm{N}}\mathrm{Ge}^{\mathrm{N}}\mathrm{Se}_2$, $^{70}\mathrm{Ge}^{\mathrm{N}}\mathrm{Se}_2$ and $^{73}\mathrm{Ge}^{76}\mathrm{Se}_2$ at a temperature of 20 K. The measurements also allowed the partial generalised single phonon vibrational density of states $G_{\mathrm{Ge}}(Q,E)$ and $G_{\mathrm{Se}}(Q,E)$ and the partial single phonon vibrational density of states $G_{\mathrm{Ge}}(E)$ and $G_{\mathrm{Se}}(E)$ to be obtained in the "silver medal" approximation. There were large statistical errors and scattering from sources other than the sample was relatively high, so two further experiments were made using the MERLIN neutron spectrometer (chapter 5). In the MERLIN experiments, $G_1(Q,E)$ and $G_1(E)$ were measured in the "bronze medal" approximation for samples of $^{\mathrm{N}}\mathrm{Ge}^{\mathrm{N}}\mathrm{Se}_2$, $^{70}\mathrm{Ge}^{\mathrm{N}}\mathrm{Se}_2$ and $^{73}\mathrm{Ge}^{76}\mathrm{Se}_2$; and $G_{\mathrm{Ge}}(Q,E)$, $G_{\mathrm{Se}}(Q,E)$, $G_{\mathrm{Ge}}(E)$ and $G_{\mathrm{Se}}(E)$ were obtained in the "silver medal" approximation at low temperature (5 K) and room temperature (292 K). The density of states features two peaks at ≈ 9.8, ≈ 26.5 meV with a broad feature above 34 meV. The first peak has contributions from Ge and Se atoms roughly weighted by their atomic concentrations, the second peak has contributions mostly from Se while the third feature has roughly equal contributions from Ge and Se. The mean squared atomic displacement and first peak in $G_1(E)$ were also measured for a sample of $^{\mathrm{N}}\mathrm{Ge}^{\mathrm{N}}\mathrm{Se}_2$ in the "bronze medal" approximation as a function of temperature. The mean squared displacement increases from 0.006 to 0.0375 $\mathrm{\AA}^2$, while the first peak position shifts from 10.31(10) to 10.70(10) meV as the

temperature increases from 10 to 280 K. Methods for subtracting multiple scattering and multiple phonon scattering were developed and the agreement between different instruments and different temperatures indicate that these methods worked well. Thus, the method of isotope substitution in neutron spectroscopy has proved to be a valuable technique for extracting the partial vibrational density of states.

In chapter 7, the method of isotope substitution in neutron spectroscopy was used to measure the vibrational density of states of GeO_2. The full generalised single phonon vibrational density of states $G_1(Q, E)$ and single phonon vibrational density of states $G_1(E)$ were measured in the "bronze medal" approximation for samples of $^{\mathrm{N}}GeO_2$, $^{70}GeO_2$ and $^{73}GeO_2$ at a temperature of 10 K. The "bronze medal" approximation does not, however, give a good approximation to the true vibrational density of states for this glass due to the large difference in scattering lengths and masses of the Ge and O atoms. The partial generalised single phonon vibrational density of states $G_{\mathrm{Ge}}(Q, E)$ and $G_{\mathrm{O}}(Q, E)$ and the partial single phonon vibrational density of states $G_{\mathrm{Ge}}(E)$ and $G_{\mathrm{O}}(E)$ were calculated in the "silver medal" approximation. For this glass, there are four distinct peaks in the vibrational density of states at 32.48(5), 69.10(5), 108.94(5) and 121.78(5) meV. The first peak has roughly equal contributions from Ge and O atoms, the second peak has Ge and O contributions that are roughly weighted by their atomic concentrations, while the third and fourth peaks have contributions almost exclusively from O atoms. With the aid of the simulations, the first peak can be associated mostly with rocking motions, the second peak is associated with bending motions and the third and fourth peaks are associated mostly with stretching motions. The density of states measured for a sample of $^{\mathrm{N}}GeO_2$ in the "bronze medal" approximation is similar to that measured for SiO_2 but with a shift in energy scale, where the various peak positions are shifted by values between 21.78 and 31.83 meV depending on the peak. Further investigations using a different instrument are required to resolve two issues - a large difference in scaling of the "bronze medal" results between the data and simulation and unphysical negative values in $G_{\mathrm{Ge}}(E)$.

In chapter 8, reliable total structure factors $F(Q)$ were measured for the first time by neutron diffraction for a glassy sample, chosen to be GeO_2, at pressures above 9 GPa. A semi-empirical data correction procedure was used. This procedure was found to be effective as proven by good agreement with the diffraction results obtained using different apparatus and a different data correction method. The $F(Q)$ functions were fourier transformed to obtain reliable total pair distribution functions $G(r)$, allowing the Ge-O coordination numbers and bond distances to be measured. The new results for GeO_2 glass are consistent with the existence of four principal densification mechanisms. At pressures up to a threshold of ≈ 5 GPa the density increases through a reorganisation of the corner shared GeO_4 tetrahedra. At pressures larger than this threshold, there

is a steady increase in the Ge-O bond length and coordination number. The rate of change of the intermediate range order, as measured by the pressure dependence of the position of the first sharp diffraction peak in $F(Q)$, decreases once the pressure exceeds ≈ 10 GPa. Eventually, at about 30 GPa, the transformation to a predominantly octahedral glass is achieved and densification proceeds via compression of the Ge-O bond.

Finally, in chapter 9, the $F(Q)$ functions were presented for SiO_2 and B_2O_3 at pressures between ambient and 17.5 GPa. The $F(Q)$ functions were Fourier transformed to obtain $G(r)$ functions, allowing the Si-O and B-O coordination numbers and bond distances to be measured. In the case of SiO_2, the principle densification mechanism in the region of ambient pressure to 15 GPa is a reogranisation of the SiO_4 tetrahedra on an intermediate length scale. This is indicated by changes in the FSDP in the $F(Q)$ functions. The data can be interpreted with the aid of simulations, for which preliminary results show good agreement with the experimental data. In the case of B_2O_3, densification occurs through two mechanisms at pressures < 17.5 GPa. From ambient pressure to ≈ 8 GPa, there is a rearrangement of the trigonal motifs. Above 8 GPa, the number of BO_4 tetrahedral motifs increases. This is accompanied by an increase in the mean B-O bond distance to accommodate the additional O atoms. The available MD simulations do not agree well with the experimental results due to the difficulty in simulating boroxol ring structures. In both SiO_2 and B_2O_3, further work is required using simulations to fully understand the densification mechanisms.

The results presented in this thesis show that experimental data can be used with molecular dynamics simulations to provide insights into the nature of glasses at the atomic scale. The techniques and data analysis procedures that have been developed provide new, more detailed information to test models. The technique of isotope substitution in neutron spectroscopy can be used to measure other glassy samples for which appropriate isotopes are available. It could also be used to measure the partial vibrational density of states of the isotopically substituted chemical species in multi-component glasses (e.g. Ag in Ag-$GeSe_2$). The method of isotope substitution can also be extended to high pressure studies using the PEARL instrument, allowing the full set of partial structure factors to be obtained for a glass at pressures up to 17.5 GPa. Both of the methods developed in this thesis allow a wide variety of glasses to be explored by measuring either their vibrational density of states or their structural changes at high pressures.

Appendix A

A.1 The Inclusion of Incoherent Scattering in Calculating the Vibrational Density of States

In section 2.2 the vibrational density of states was found for the case of coherent neutron scattering. In the following, an account is given that includes the effect of incoherent scattering.

The double differential scattering cross section for a system of N scattering centres is given by (see equation (2.4) [9]

$$\frac{1}{N}\frac{\mathrm{d}^2\sigma}{\mathrm{d}\Omega \mathrm{d}E_f} = \frac{1}{N}\frac{k_f}{k_i}\frac{1}{2\pi\hbar}\int_{-\infty}^{\infty}\mathrm{d}t e^{-i\omega t}\sum_{\mathrm{i}=1}^{N}\sum_{\mathrm{j}=1}^{N}\overline{b_\mathrm{i}b_\mathrm{j}}\left\langle e^{-i\mathbf{Q}\cdot\mathbf{R}_\mathrm{i}(0)}e^{i\mathbf{Q}\cdot\mathbf{R}_\mathrm{j}(t)}\right\rangle \quad , \tag{A.1}$$

where the brackets $\langle\cdots\rangle$ denote a thermal average, the quantity $\overline{b_\mathrm{i}b_\mathrm{j}}$ is the value of $b_\mathrm{i}b_\mathrm{j}$ averaged over random nuclear spin orientations and isotope distributions, while b_i and b_j are the scattering lengths of nuclei i and j, respectively. $\mathbf{R}_\mathrm{i}(0)$ and $\mathbf{R}_\mathrm{j}(t)$ are the positions of particles i at time $t = 0$ and j at time t, respectively. $\omega = E/\hbar$ is an angular frequency where E is the energy transfer in a scattering event.

The double differential cross section can be expressed in terms of a total structure factor such that

$$\frac{1}{N}\frac{\mathrm{d}^2\sigma}{\mathrm{d}\Omega \mathrm{d}E_f} = \frac{k_f}{k_i}S(\mathbf{Q},E) \tag{A.2}$$

and $S(\mathbf{Q},E)$ is given by [41]

$$S(\mathbf{Q},E) = \frac{1}{N}\frac{1}{2\pi\hbar}\int_{-\infty}^{\infty}\mathrm{d}t\, e^{-i\omega t}\sum_{\mathrm{i}=1}^{N}\sum_{\mathrm{j}=1}^{N}\overline{b_\mathrm{i}b_\mathrm{j}}\left\langle e^{-i\mathbf{Q}\cdot\mathbf{R}_\mathrm{i}(0)}e^{i\mathbf{Q}\cdot\mathbf{R}_\mathrm{j}(t)}\right\rangle . \tag{A.3}$$

In a solid, nuclei move around well defined equilibrium positions, $\mathbf{R}_\mathrm{i}$, such that $\mathbf{R}_\mathrm{i}(t) = \mathbf{R}_\mathrm{i} + \mathbf{u}_\mathrm{i}(t)$, where $\mathbf{u}_\mathrm{i}(t)$ is a time dependent displacement. If the displacements are small, then the harmonic approximation can be used and equation (A.3) is re-written as [41]

$$\begin{aligned} S(\mathbf{Q},E) =& \frac{1}{N}\sum_{\mathrm{i}=1}^{N}\sum_{\mathrm{j}=1}^{N}\overline{b_\mathrm{i}b_\mathrm{j}}\left\langle e^{\left(-i\mathbf{Q}\cdot(\mathbf{R}_\mathrm{i}-\mathbf{R}_\mathrm{j})\right)}\right\rangle e^{-(W_\mathrm{i}(Q)+W_\mathrm{j}(Q))} \\ &\times\frac{1}{2\pi\hbar}\int_{-\infty}^{\infty}\mathrm{d}t\, e^{-i\omega t}e^{\left\langle(\mathbf{Q}\cdot\mathbf{u}_\mathrm{i}(0))(\mathbf{Q}\cdot\mathbf{u}_\mathrm{j}(t))\right\rangle} \quad , \end{aligned} \tag{A.4}$$

where $W_\mathrm{i}(Q) = \frac{1}{6}\left\langle u_\mathrm{i}^2\right\rangle Q^2$ and $W_\mathrm{j}(Q) = \frac{1}{6}\left\langle u_\mathrm{j}^2\right\rangle Q^2$ are the Debye-Waller factors for nuclei i and j while $\left\langle u_\mathrm{i}^2\right\rangle$ and $\left\langle u_\mathrm{j}^2\right\rangle$ are the mean square displacements of nuclei i and

j, respectively. The final term in equation (A.4) can be Taylor expanded as a power series such that

$$e^{\langle(\mathbf{Q}\cdot\mathbf{u}_{\mathrm{i}}(0))(\mathbf{Q}\cdot\mathbf{u}_{\mathrm{j}}(t))\rangle} = \sum_{p=0}^{\infty} \frac{1}{p!} \langle(\mathbf{Q}\cdot\mathbf{u}_{\mathrm{i}}(0))(\mathbf{Q}\cdot\mathbf{u}_{\mathrm{j}}(t))\rangle^{p} \quad , \tag{A.5}$$

where $p = 0, 1, 2, \ldots$. Substituting equation (A.5) into equation (A.4) gives

$$\begin{aligned} S(\mathbf{Q},E) =& \frac{1}{N} \sum_{\mathrm{i}=1}^{N} \sum_{\mathrm{j}=1}^{N} \overline{b_{\mathrm{i}} b_{\mathrm{j}}} \left\langle e^{\left(-i\mathbf{Q}\cdot(\mathbf{R}_{\mathrm{i}}-\mathbf{R}_{\mathrm{j}})\right)} \right\rangle e^{-(W_{\mathrm{i}}(Q)+W_{\mathrm{j}}(Q))} \\ & \times \frac{1}{2\pi\hbar} \int_{-\infty}^{\infty} \mathrm{d}t\, e^{-i\omega t} \sum_{p=0}^{\infty} \frac{1}{p!} \langle(\mathbf{Q}\cdot\mathbf{u}_{\mathrm{i}}(0))(\mathbf{Q}\cdot\mathbf{u}_{\mathrm{j}}(t))\rangle^{p} \quad . \end{aligned} \tag{A.6}$$

In this series, $p = 0$ represents the cross section for elastic scattering, $p = 1$ represents the cross section for all of the one phonon processes while $p > 2$ represents the cross section for p phonon (multiple phonon) processes.

A.1.1 Single Phonon Scattering

The single phonon contribution to the coherent dynamical structure factor (the case when $p = 1$ in equation (A.6)) is given by the sum of contributions from events that create phonons, $S_{+1}(\mathbf{Q},E)$, and from events that annihilate phonons $S_{-1}(\mathbf{Q},E)$, so that $S_1(\mathbf{Q},E) = S_{+1}(\mathbf{Q},E) + S_{-1}(\mathbf{Q},E)$, where $S_1(\mathbf{Q},E)$ is the single phonon coherent total dynamical structure factor. The general motion of each of N quantised simple harmonic oscillators in 3 dimensions due to single phonon processes can be described by the superposition of $3N$ allowed normal modes [11, pp. 139] such that for the case when $E = E_i - E_f > 0$

$$\begin{aligned} S_{+1}(\mathbf{Q},E) =& \frac{1}{N} \frac{\hbar^2}{2} \sum_{\mathrm{i}=1}^{N} \sum_{\mathrm{j}=1}^{N} \overline{b_{\mathrm{i}} b_{\mathrm{j}}} \left\langle e^{-i\mathbf{Q}\cdot(\mathbf{R}_{\mathrm{i}}-\mathbf{R}_{\mathrm{j}})} \right\rangle e^{-(W_{\mathrm{i}}(Q)+W_{\mathrm{j}}(Q))} \\ & \times \sum_{\nu=1}^{3N} \frac{(\mathbf{Q}\cdot\mathbf{e}_{\mathrm{i}}^{\nu})^{*}(\mathbf{Q}\cdot\mathbf{e}_{\mathrm{j}}^{\nu})}{(M_{\mathrm{i}}M_{\mathrm{j}})^{1/2}E_{\nu}} \langle n(E_{\nu})+1\rangle\, \delta(E-E_{\nu}) \end{aligned} \tag{A.7}$$

and for the case when $E = E_i - E_f < 0$

$$\begin{aligned} S_{-1}(\mathbf{Q},E) =& \frac{1}{N} \frac{\hbar^2}{2} \sum_{\mathrm{i}=1}^{N} \sum_{\mathrm{j}=1}^{N} \overline{b_{\mathrm{i}} b_{\mathrm{j}}} e^{-i\mathbf{Q}\cdot(\mathbf{R}_{\mathrm{i}}-\mathbf{R}_{\mathrm{j}})} e^{-(W_{\mathrm{i}}(Q)+W_{\mathrm{j}}(Q))} \\ & \times \sum_{\nu=1}^{3N} \frac{(\mathbf{Q}\cdot\mathbf{e}_{\mathrm{i}}^{\nu})^{*}(\mathbf{Q}\cdot\mathbf{e}_{\mathrm{j}}^{\nu})}{(M_{\mathrm{i}}M_{\mathrm{j}})^{1/2}E_{\nu}} \langle n(E_{\nu})\rangle\, \delta(E+E_{\nu}) \quad , \end{aligned} \tag{A.8}$$

where M_{i} and M_{j} are the masses of nuclei i and j respectively. $\mathbf{e}_{\mathrm{i}}^{\nu}$ and $\mathbf{e}_{\mathrm{j}}^{\nu}$ are the displacement vectors of the i^{th} and j^{th} nucleus in the ν^{th} normal mode , respectively, $E_{\nu} = \hbar\omega_{\nu}$ is the energy of mode ν, $\langle n_{\nu}(E)\rangle$ and $\langle n_{\nu}(E)+1\rangle$ are the Bose-Einstein occupation factors given by

$$\langle n(E_{\nu})\rangle = \frac{1}{e^{E_{\nu}/(k_B T)} - 1} \tag{A.9}$$

and

$$\langle n(E_{\nu}) + 1\rangle = \frac{e^{E_{\nu}/(k_B T)}}{e^{E_{\nu}/(k_B T)} - 1} \quad , \tag{A.10}$$

where k_B is Boltzmann's constant and T is the absolute temperature. The delta functions ensure that the only contributions to the summations in equations (A.7) and (A.8) are when $E = E_{\nu}$ and $E = -E_{\nu}$, respectively. Also, for the case when $E < 0$, using the symmetry of the delta function it follows that $\delta(E+E_{\nu}) = \delta(-(E+E_{\nu})) = \delta(|E|-E_{\nu})$. In addition

$$\langle n(-E)\rangle = \frac{1}{e^{-E/(k_B T)} - 1} = \frac{e^{E/(k_B T)}}{1 - e^{E/(k_B T)}} = -\langle n(E)+1\rangle \ , \tag{A.11}$$

such that $\langle n(-E)\rangle/(-E) = \langle n(E)+1\rangle/E$. Hence it follows that equation (A.8) can be re-written as

$$\begin{aligned} S_{-1}(\mathbf{Q},E) =& \frac{1}{N}\frac{\hbar^2}{2}\sum_{\mathrm{i}=1}^{N}\sum_{\mathrm{j}=1}^{N}\overline{b_{\mathrm{i}}b_{\mathrm{j}}}e^{-i\mathbf{Q}\cdot(\mathbf{R}_{\mathrm{i}}-\mathbf{R}_{\mathrm{j}})}e^{-(W_{\mathrm{i}}(Q)+W_{\mathrm{j}}(Q))} \\ & \times \sum_{\nu=1}^{3N}\frac{(\mathbf{Q}\cdot\mathbf{e}_{\mathrm{i}}^{\nu})^*(\mathbf{Q}\cdot\mathbf{e}_{\mathrm{j}}^{\nu})}{(M_{\mathrm{i}}M_{\mathrm{j}})^{1/2}E}\langle n(E)+1\rangle\,\delta(|E|-E_{\nu}) \quad . \end{aligned} \tag{A.12}$$

Since $E > 0$ (thus $E = |E|$) in equation (A.7), equations (A.7) and (A.12) can both be expressed in the same equation valid for all $E \neq 0$ such that

$$\begin{aligned} S_1(\mathbf{Q},E) =& \frac{1}{N}\frac{\hbar^2 Q^2}{2}\sum_{\mathrm{i}=1}^{N}\sum_{\mathrm{j}=1}^{N}\overline{b_{\mathrm{i}}b_{\mathrm{j}}}\left\langle e^{-i\mathbf{Q}\cdot(\mathbf{R}_{\mathrm{i}}-\mathbf{R}_{\mathrm{j}})}\right\rangle e^{-(W_{\mathrm{i}}(Q)+W_{\mathrm{j}}(Q))} \\ & \times \frac{\langle n(E)+1\rangle}{E}\sum_{\nu=1}^{3N}\frac{(\hat{\mathbf{Q}}\cdot\mathbf{e}_{\mathrm{i}}^{\nu})^*(\hat{\mathbf{Q}}\cdot\mathbf{e}_{\mathrm{j}}^{\nu})}{(M_{\mathrm{i}}M_{\mathrm{j}})^{1/2}}\delta(|E|-E_{\nu}) \ , \end{aligned} \tag{A.13}$$

where $Q = |\mathbf{Q}|$ and $\hat{\mathbf{Q}} = \mathbf{Q}/(|\mathbf{Q}|)$. Equation (A.7) is recovered from equation (A.13) when $E > 0$ and equation (A.8) is recovered from equation (A.13) when $E < 0$.

A.1.2 The Extreme Incoherent Approximation

In the extreme incoherent approximation, no distinction is made between (e.g. the chemical) identity of the nuclei such that equation (A.13) becomes

$$S_1(\mathbf{Q},E) = \frac{1}{N}\frac{\hbar^2Q^2}{2\overline{M}}\left\langle\overline{b^2}\right\rangle e^{-2\overline{W}(Q)}\sum_{\mathrm{i}=1}^{N}\sum_{\mathrm{j}=1}^{N}\left\langle e^{-i\mathbf{Q}\cdot(\mathbf{R}_\mathrm{i}-\mathbf{R}_\mathrm{j})}\right\rangle \times \frac{\langle n(E)+1\rangle}{E}\sum_{\nu=1}^{3N}(\hat{\mathbf{Q}}\cdot\mathbf{e}_\mathrm{i}^{\nu})^*(\hat{\mathbf{Q}}\cdot\mathbf{e}_\mathrm{j}^{\nu})\delta(|E|-E_\nu) \quad . \tag{A.14}$$

All nuclei are described by the same mean square scattering length, which is taken to be

$$\left\langle\overline{b^2}\right\rangle = \sum_{\alpha=1}^{n}\overline{b_\alpha^2} = \sum_{\alpha=1}^{n}c_\alpha\left(b_{\mathrm{coh},\alpha}^2+b_{\mathrm{inc},\alpha}^2\right) , \tag{A.15}$$

the same mass, which is taken to be

$$\overline{M} = \sum_{\alpha=1}^{n}c_\alpha M_\alpha , \tag{A.16}$$

and the same Debye-Waller factor, which is taken to be

$$\overline{W}(Q) = \sum_{\alpha=1}^{n}c_\alpha W_\alpha(Q) . \tag{A.17}$$

In equations (A.15), (A.16) and (A.17), α denotes a chemical species, n denotes the number of chemical species while c_α, $\overline{b}_\alpha$, M_α and $W_\alpha(Q)$ are the atomic fraction, mean scattering length, mean mass and mean Debye-Waller factor for chemical species α, respectively. For convenience, the coherent scattering lengths $\overline{b}_{\mathrm{coh},\alpha}^2 = 4\pi\overline{b}_\alpha^2$ and incoherent scattering lengths $\overline{b}_{\mathrm{inc},\alpha}^2 = \left(\overline{b_\alpha^2}-\overline{b}_\alpha^2\right)$ of chemical species α have been used.

The incoherent approximation is then made, whereby only the contribution from terms where i = j (i.e. terms involving the same nucleus) within the sum made in equation (A.14) are considered such that

$$S_1(\mathbf{Q},E) = \frac{1}{N}\frac{\hbar^2Q^2}{2\overline{M}}\left\langle\overline{b^2}\right\rangle e^{-2\overline{W}(Q)}\frac{\langle n(E)+1\rangle}{E}\sum_{\mathrm{i}=1}^{N}\sum_{\nu=1}^{3N}|\hat{\mathbf{Q}}\cdot\mathbf{e}_\mathrm{i}^{\nu}|^2\delta(|E|-E_\nu) \quad . \tag{A.18}$$

If $\hat{\mathbf{Q}}$ is averaged over all directions (which is the case for an homogeneous, isotropic solid such as most glasses) then

$$\left\langle|\hat{\mathbf{Q}}\cdot\mathbf{e}_\mathrm{i}^{\nu}|^2\right\rangle = \frac{1}{3}\left\langle|\mathbf{e}_\mathrm{i}^{\nu}|^2\right\rangle \quad . \tag{A.19}$$

If the *total* vibrational density of states, $Z(E)$, is defined to be the fraction of states between E and $E + \mathrm{d}E$ then

$$Z(E) = \frac{1}{3N} \sum_{\mathrm{i}=1}^{N} \sum_{\nu=1}^{3N} \left\langle |\mathbf{e}_{\mathrm{i}}^{\nu}|^2 \right\rangle \delta(|E| - E_\nu) = \frac{1}{3N} \sum_{\nu=1}^{3N} \delta(|E| - E_\nu) \quad . \tag{A.20}$$

It follows that $Z(E)$ is an even function, $\int Z(E)\mathrm{d}E = 1$ for $E > 0$, and that equation (A.18) can be expressed in the extreme incoherent approximation as

$$S_1(Q, E) = \frac{\hbar^2 Q^2}{2\overline{M}} \left\langle \overline{b^2} \right\rangle e^{-2\overline{W}(Q)} \frac{\langle n(E) + 1 \rangle}{E} Z(E) \quad . \tag{A.21}$$

A.1.3 The Incoherent Approximation

For a two component system of chemical species A and X, equation (A.13) can be rewritten as the sum of partial dynamical structure factors $S_{\alpha\beta}(\mathbf{Q}, E)$ ($\alpha = A, X$, $\beta = A, X,$) such that

$$S_1(\mathbf{Q}, E) = \overline{b_A^2} S_{AA}(\mathbf{Q}, E) + \overline{b_X^2} S_{XX}(\mathbf{Q}, E) + 2\overline{b}_A \overline{b}_X S_{AX}(\mathbf{Q}, E) \quad , \tag{A.22}$$

where $\overline{b_\alpha^2} = b_{\mathrm{coh},\alpha}^2 + b_{\mathrm{inc},\alpha}^2$, and $\overline{b}_\alpha = b_{\mathrm{coh},\alpha}$. $S_{\alpha\beta}(\mathbf{Q}, E)$ represents the correlations between nuclei of chemical species α and nuclei of chemical species β and is given by

$$\begin{aligned} S_{\alpha\beta}(\mathbf{Q}, E) =& \frac{1}{N} \frac{\hbar^2 Q^2}{2} \sum_{\alpha\mathrm{i}=1}^{N_\alpha} \sum_{\beta\mathrm{j}=1}^{N_\beta} e^{-(W_{\alpha\mathrm{i}}(Q) + W_{\beta\mathrm{j}}(Q))} \left\langle e^{-i\mathbf{Q}\cdot(\mathbf{R}_{\alpha\mathrm{i}} - \mathbf{R}_{\beta\mathrm{j}})} \right\rangle \\ & \times \frac{\langle n(E) + 1 \rangle}{E} \sum_{\nu=1}^{3N} \frac{(\hat{\mathbf{Q}} \cdot \mathbf{e}_{\alpha\mathrm{i}}^{\nu})^* (\hat{\mathbf{Q}} \cdot \mathbf{e}_{\beta\mathrm{j}}^{\nu})}{(M_{\alpha\mathrm{i}} M_{\beta\mathrm{i}})^{1/2}} \delta(|E| - E_\nu) \quad , \end{aligned} \tag{A.23}$$

where N_α and N_β are the number of nuclei in the system of chemical species α and β, while $\alpha\mathrm{i}$ and $\beta\mathrm{j}$ denote nuclei of chemical species α and β, respectively.

The incoherent approximation is then made, whereby only terms involving $\alpha\mathrm{i} = \beta\mathrm{j}$ (i.e. terms involving the same nuclei) contribute to the sum in equation (A.23) such that $S_{\alpha\beta}(Q, E) = 0$ for $\alpha \neq \beta$ and

$$S_{\alpha\alpha}(\mathbf{Q}, E) = \frac{1}{N} \frac{\hbar^2 Q^2}{2M_\alpha} e^{-2W_\alpha(Q)} \frac{\langle n(E) + 1 \rangle}{E} \sum_{\alpha\mathrm{i}=1}^{N_\alpha} \sum_{\nu=1}^{3N} |\hat{\mathbf{Q}} \cdot \mathbf{e}_{\alpha\mathrm{i}}^{\nu}|^2 \delta(|E| - E_\nu) \quad , \tag{A.24}$$

where M_α and $W_\alpha(Q)$ are the mean mass and Debye-Waller factor for atoms of chemical species α, respectively. If $\hat{\mathbf{Q}}$ is averaged over all directions (which is the case for an

homogeneous, isotropic solid such as most glasses) then

$$\left\langle |\hat{\mathbf{Q}} \cdot \mathbf{e}_{\alpha \mathrm{i}}^{\nu}|^2 \right\rangle = \frac{1}{3} \left\langle |\mathbf{e}_{\alpha \mathrm{i}}^{\nu}|^2 \right\rangle \quad . \tag{A.25}$$

The partial vibrational density of states for a given chemical species α is defined as the fraction of modes with energy between E and $E + \mathrm{d}E$ such that

$$Z_{\alpha}(E) = \frac{1}{3N} \sum_{\alpha \mathrm{i}=1}^{N_{\alpha}} \sum_{\nu=1}^{3N} \left\langle |\mathbf{e}_{\alpha \mathrm{i}}^{\nu}|^2 \right\rangle \delta(|E| - E_{\nu}) \quad , \tag{A.26}$$

where $Z_{\alpha}(E)$ is the partial vibrational density of states, defined such that $\int Z_{\alpha}(E) \mathrm{d}E = c_{\alpha}$. Therefore equation (A.24) becomes

$$S_{\alpha\alpha}(Q, E) = \frac{\hbar^2 Q^2}{2M_{\alpha}} e^{-2W_{\alpha}(Q)} \frac{\langle n(E) + 1 \rangle}{E} Z_{\alpha}(E) \quad . \tag{A.27}$$

The total vibrational density of states is given by $Z(E) = Z_{\mathrm{A}}(E) + Z_{\mathrm{X}}(E)$.

A.2 First Order Difference Functions

The "silver medal" results presented in this thesis (see section 2.2.4) can be shown to be equivalent to an application of the first order difference method (see e.g. [175]). If two experiments are made on a two component system that differ only in the isotopic compositions of the elements, then the $S(Q,E)$ functions that are measured can be represented by

$$S(Q,E) = b_1^2 S_{11}(Q,E) + b_2^2 S_{22}(Q,E) + 2b_1 b_2 S_{12}(Q,E) \tag{A.28}$$

$$S'(Q,E) = {}'b_1^2 S_{11}(Q,E) + {}'b_2^2 S_{22}(Q,E) + 2\,{}'b_1 {}'b_2 S_{12}(Q,E)\,, \tag{A.29}$$

where $S(Q,E)$ and $S'(Q,E)$ are the measured total dynamical structure factors, while b_α and ${}'b_\alpha$ are the scattering lengths of chemical species α for the isotope compositions used in experiments 1 and 2, respectively. $S_{\alpha\beta}(Q,E)$ denotes a partial dynamical structure factor for chemical species α and β. Two first order difference functions can be defined by

$$\Delta S(Q,E) = \frac{1}{b_1^2\,{}'b_2^2 - b_2^2\,{}'b_1^2}\left({}'b_2^2 S(Q,E) - b_2^2 S'(Q,E)\right) \tag{A.30}$$

and

$$\Delta S'(Q,E) = \frac{1}{b_1^2\,{}'b_2^2 - b_2^2\,{}'b_1^2}\left(b_1^2 S'(Q,E) - {}'b_1^2 S(Q,E)\right)\,. \tag{A.31}$$

By substituting equations (A.28) and (A.29) into equations (A.30) and (A.31) it can be shown that

$$\Delta S(Q,E) = S_{11}(Q,E) + \frac{2b_2\,{}'b_2}{b_1\,{}'b_2 + b_2\,{}'b_1} S_{12}(Q,E) \tag{A.32}$$

and

$$\Delta S'(Q,E) = S_{22}(Q,E) + \frac{2b_1\,{}'b_1}{b_1\,{}'b_2 + {}'b_1 b_2} S_{12}(Q,E)\,. \tag{A.33}$$

In the incoherent approximation, the contributions from $S_{12}(Q,E)$ are neglected such that equations (A.32) and (A.33) become

$$\Delta S(Q,E) = S_{11}(Q,E) \tag{A.34}$$

and

$$\Delta S'(Q,E) = S_{22}(Q,E)\,, \tag{A.35}$$

respectively.

In the "silver medal" approach using the incoherent approximation (see section 2.2.4),

the contributions from $S_{12}(Q,E)$ are neglected and a matrix can be made where

$$\mathbf{A} = \begin{pmatrix} b_1^2 & b_2^2 \\ {}'b_1^2 & {}'b_2^2 \end{pmatrix}, \tag{A.36}$$

such that equations (A.28) and (A.29) can be described in matrix notation by

$$\begin{pmatrix} S\left(Q,E\right) \\ S'\left(Q,E\right) \end{pmatrix} = \mathbf{A} \begin{pmatrix} S_{11}(Q,E) \\ S_{22}(Q,E) \end{pmatrix} \tag{A.37}$$

and therefore

$$\begin{pmatrix} S_{11}(Q,E) \\ S_{22}(Q,E) \end{pmatrix} = \mathbf{A}^{-1} \begin{pmatrix} S\left(Q,E\right) \\ S'\left(Q,E\right) \end{pmatrix}. \tag{A.38}$$

The inversion of the 2 by 2 matrix $\mathbf{A}$ can be done using Cramers rule [310] giving

$$\mathbf{A}^{-1} = \frac{1}{b_1^2\,{}'b_2^2 - b_2^2\,{}'b_1^2} \begin{pmatrix} -{}'b_2^2 & b_2^2 \\ -{}'b_1^2 & b_1^2 \end{pmatrix}. \tag{A.39}$$

By substituting equation A.39 into equation A.38 and expanding the matrices, it follows that

$$S_{11}(Q,E) = \frac{1}{b_1^2\,{}'b_2^2 - b_2^2\,{}'b_1^2} \left({}'b_2^2 S(Q,E) - b_2^2\,S'(Q,E)\right) \tag{A.40}$$

$$S_{22}(Q,E) = \frac{1}{b_1^2\,{}'b_2^2 - b_2^2\,{}'b_1^2} \left(b_1^2\,S'(Q,E) - {}'b_1^2 S(Q,E)\right). \tag{A.41}$$

Within the coherent approximation, equations (A.34) and (A.35) show that $S_{11}(Q,E) = \Delta S(Q,E)$ and $S_{22}(Q,E) = \Delta S'(Q,E)$. In this case, equations (A.40) and (A.41) found using the "silver medal" approach are equivalent to equations (A.30) and (A.31) using the first order difference approach, respectively.

Bibliography

[1] K. Thyagarajan and A. K. Ghatak. *Fibre Optic Essentials*. Wiley, New York, 2007.

[2] R. Zallen. *The Physics of Amorphous Solids*. John Wiley and Sons, New York, 1983.

[3] S. R. Elliott. *Physics of Amorphous Materials*. Longman Group UK, Essex, 2nd. edition, 1990.

[4] N. E. Cusack. *The Physics of Structurally Disordered Matter: An Introduction*. IOP Publishing, Bristol, 1987.

[5] H. E. Fischer, A. C. Barnes, and P. S. Salmon. Neutron and x-ray diffraction studies of liquids and glasses. *Reports on Progress in Physics*, 69:233, 2006.

[6] G. N. Greaves and S. Sen. Inorganic glasses, glass-forming liquids and amorphizing solids. *Advances in Physics*, 56:1, 2007.

[7] P. W. Anderson. Viewpoint: The future. *Science*, 267:1615, 1995.

[8] L. Huang, F. Yuan, and Q. Zhao. Designing glasses with tunable structure and properties by computer simulation. In *Materials Research Society Symposium Proceedings*, volume 1229, page 19, 2010.

[9] G. L. Squires. *An Introduction to the Theory of Thermal Neutron Scattering*. Cambridge University Press, Cambridge, 1978.

[10] A. C. Wright, B. A. Shakhmatkin, and N. M. Vedishcheva. The chemical structure of oxide glasses: A concept consistent with neutron scattering studies? *Glass Physics and Chemistry*, 27:97, 2001.

[11] M. T. Dove. *Introduction to Lattice Dynamics*. Cambridge Topics in Mineral Physics and Chemistry. Cambridge University Press, Cambridge, 1993.

[12] A. C. Wright, G. Etherington, J. A. E. Desa, R. N. Sinclair, G. A. N Connell, and J. C. Mikkelsen Jr. Neutron amorphography. *Journal of Non-Crystalline Solids*, 49(1-3):63, 1982.

[13] W. H. Zachariasen. The atomic arrangement in glass. *Journal of American Chemistry Society*, 54:3841, 1932.

[14] P. S. Salmon. Structure of liquids and glasses in the Ge-Se binary system. *Journal of Non-Crystalline Solids*, 353(32-40):2959, 2007.

[15] D. L. Price, S. C. Moss, R. Reijers, M-L. Saboungi, and S. Susman. Intermediate-range order in glasses and liquids. *Journal of Physics: Condensed Matter*, 1(5):1005, 1989.

[16] P. F. McMillan. Polyamorphic transformations in liquids and glasses. *Journal of Materials Chemistry*, 14:1506, 2004.

[17] C. Massobrio. Nanostructural units in disordered network-forming materials and the origin of intermediate range order. In C. Massobrio, H. Bulou, and C. Goyhenex, editors, *Advances in the Atomic-Scale Modeling of Nanosystems and Nanostructured Materials*, volume 795 of *Lecture Notes in Physics*, page 343. Springer Berlin / Heidelberg, 2010.

[18] M. P. Allen and D. J. Tildesley. *Computer Simulation of Liquids*. Clarendon, Oxford, 1989.

[19] R. Car and M. Parrinello. Unified approach for molecular dynamics and density-functional theory. *Physical Review Letters*, 55:2471, 1985.

[20] W. Kohn. Nobel lecture: Electronic structure of matter-wave functions and density functionals. *Reviews of Modern Physics*, 71:1253, 1999.

[21] R. O. Jones and O. Gunnarsson. The density functional formalism, its applications and prospects. *Reviews of Modern Physics*, 61:689, 1989.

[22] P. Hohenberg and W. Kohn. Inhomogeneous electron gas. *Physical Review*, 136:B864, 1964.

[23] W. Kohn and L. J. Sham. Self-consistent equations including exchange and correlation effects. *Physical Review*, 140:A1133, 1965.

[24] J. Hafner. Ab-initio simulations of materials using VASP: Density-functional theory and beyond. *Journal of Computational Chemistry*, 29(13):2044, 2008.

[25] J. P. Perdew and A. Zunger. Self-interaction correction to density-functional approximations for many-electron systems. *Physical Review B*, 23:5048, 1981.

[26] J. P. Perdew. Density-functional approximation for the correlation energy of the inhomogeneous electron gas. *Physical Review B*, 33:8822, 1986.

[27] J. P. Perdew, M. Ernzerhof, and K. Burke. Rationale for mixing exact exchange with density functional approximations. *The Journal of Chemical Physics*, 105(22):9982, 1996.

[28] A. D. Becke. A new mixing of Hartree-Fockand local density-functional theories. *The Journal of Chemical Physics*, 98(2):1372, 1993.

[29] K. Kim and K. D. Jordan. Comparison of density functional and MP2 calculations on the water monomer and dimer. *The Journal of Physical Chemistry*, 98(40):10089, 1994.

[30] P. J. Stephens, F. J. Devlin, C. F. Chabalowski, and M. J. Frisch. *Ab initio* calculation of vibrational absorption and circular dichroism spectra using density functional force fields. *The Journal of Physical Chemistry*, 98(45):11623, 1994.

[31] C. Massobrio, F. Cleri, and R. Kozubski. Computer simulation of disordered structures and nanosystems: An atomic-scale view. *Solid State Sciences*, 12(2):155, 2010.

[32] C. Massobrio, M. Micoulaut, and P. S. Salmon. Impact of the exchange-correlation functional on the structure of glassy $GeSe_2$. *Solid State Sciences*, 12(2):199, 2010.

[33] J. E. Enderby, D. M. North, and P. A. Egelstaff. The partial structure factors of liquid Cu-Sn. *Phylosophical Magazine*, 14(131):961, 1966.

[34] L. Giacomazzi. Neutron partial vibrational density of states of v-$GeSe_2$ and v-GeO_2. Private Communication, 2011.

[35] L. Giacomazzi, C. Massobrio, and A. Pasquarello. First-principles investigation of the structural and vibrational properties of vitreous $GeSe_2$. *Physical Review B*, 75(17):174207, 2007.

[36] L. Giacomazzi, P. Umari, and A. Pasquarello. Vibrational spectra of vitreous germania from first-principles. *Physical Review B*, 74(15):155208, 2006.

[37] L. Giacomazzi, P. Umari, and A. Pasquarello. Medium-range structural properties of vitreous germania obtained through first-principles analysis of vibrational spectra. *Physical Review Letters*, 95(7):075505, 2005.

[38] D. Marrocchelli, M. Salanne, P. A. Madden, C. Simon, and P. Turq. The construction of a reliable potential for GeO_2 from first principles. *Molecular Physics*, 107(4-6):443, 2009.

[39] J. W. E. Drewitt. *Structure of Copper Halide Melts, Rare Earth Chalcogenide Glasses and Glassy Germania at High Pressure*. PhD thesis, University of Bath, 2009.

[40] J. W. E. Drewitt, P. S. Salmon, A. C. Barnes, S. Klotz, H. E. Fischer, and W. A. Crichton. Structure of GeO_2 glass at pressures up to 8.6 GPa. *Physical Review B*, 81:014202, 2010.

[41] D. L. Price and J. M. Carpenter. Scattering function of vitreous silica. *Journal of Non-Crystalline Solids*, 92:153, 1987.

[42] J. M. Carpenter and D. L. Price. Correlated motions in glasses studied by coherent inelastic neutron scattering. *Physical Review Letters*, 54(5):441, 1985.

[43] G. E. Bacon. *Neutron Diffraction*. Clarendon, Oxford, 1975.

[44] L. Giacomazzi and A. Pasquarello. Vibrational spectra of vitreous SiO_2 and vitreous GeO_2 from first principles. *Journal of Physics: Condensed Matter*, 19(41):415112, 2007.

[45] L. Giacomazzi, C. Massobrio, and A. Pasquarello. Vibrational properties of vitreous $GeSe_2$ with the Becke-Lee-Yang-Parr density functional. *Journal of Physics: Condensed Matter*, 23(29):295401, 2011.

[46] E. Fabiani, A. Fortana, and U. Buchenau. Neutron scattering study of the vibrations in vitreous silica and germania. *The Journal of Chemical Physics*, 128:244507, 2008.

[47] D. F. R. Mildner and A. C. Wright. Neutron elastic diffraction and its potential use in structural studies of amorphous solids. *Journal of Non-Crystalline Solids*, 42(1-3):97, 1980.

[48] G. Placzek. The scattering of neutrons by systems of heavy nuclei. *Physical Review*, 86(3):377, 1952.

[49] P. S. Salmon, I. Petri, P. H. K. de Jong, P. Verkerk, H. E. Fischer, and W. S. Howells. Structure of liquid lithium. *Journal of Physics: Condensed Matter*, 16:195, 2004.

[50] T. E. Faber and J. M. Ziman. A theory of the electrical properties of liquid metals. *Philosophical Magazine*, 11(109):153, 1965.

[51] U. Walter, D. L. Price, S. Susman, and K. J. Volin. Network dynamics of chalcogenide glasses. I. Germanium diselenide. *Physical Review B*, 37(8):4232, 1988.

[52] S. W. Lovesey. *Theory of Neutron Scattering from Condensed Matter*, volume 1. Oxford University Press, Oxford, 1986.

[53] CCLRC Rutherford Appleton Laboratory. *ISIS 2006: The ISIS Facility Annual Report*. CCLRC Media Services, 2006.

[54] J. M. Carpenter. Pulsed spallation neutron sources for slow neutron scattering. *Nuclear Instruments and Methods*, 145:91, 1977.

[55] C. G. Windsor. *Pulsed Neutron Scattering*. Taylor and Francis, London, 1981.

[56] P. C. H. Mitchell, S. F. Parker, A. J. Ramirez-Cuesta, and J. Tomkinson. *Vibrational Spectroscopy with Neutrons*. Series on Neutron Techniques and Applications. World Scientific Publishing, Singapore, 2005.

[57] M. Arai, A. D. Taylor, S. M. Bennington, and Z. A. Bowden. MARI - a new spectrometer for liquid and amorphous materials. In W. S. Howells and A. K. Soper, editors, *Deveolopments in the Physics of Fluids*, pages F321–F328. Adam Hilger, Bristol, 1992.

[58] Image downloaded from `http://www.isis.stfc.ac.uk/instruments/mari/mari-picture7948.gif`, July 2010.

[59] N. Rhodes. Private communication, November 2011.

[60] R. I. Bewley, R. S. Eccleston, K. A. McEwen, S. M. Hayden, M. T. Dove, S. M. Bennington, J. R. Treadgold, and R. L. S. Coleman. MERLIN, a new high count rate spectrometer at ISIS. *Physica B*, 385-386:1029, 2006.

[61] Image downloaded from `http://www.isis.stfc.ac.uk/instruments/pearl/`, July 2010.

[62] S. R. Elliott. Origin of the first sharp diffraction peak in the structure factor of covalent glasses. *Physical Review Letters*, 67:711, 1991.

[63] P. S. Salmon. The structure of tetrahedral network glass forming systems at intermediate and extended length scales. *Journal of Physics: Condensed Matter*, 19:455208, 2007.

[64] S. Klotz, J. M. Besson, G. Hamel, R. J. Nelmes, J. S. Loveday, W. G. Marshall, and R. M. Wilson. Neutron powder diffraction at pressures beyond 25 GPa. *Applied Physics Letters*, 66(14):1735, 1995.

[65] S. Klotz, G. Hamel, and J. Frelat. A new type of compact large-capacity press for neutron and x-ray scattering. *High Pressure Research*, 24(1):219, 2004.

[66] L. G. Khvostantsev, V. N. Slesarev, and V. V. Brazhkin. Toroid type high-pressure device: history and prospects. *High Pressure Research*, 24(3):371, 2004.

[67] L. G. Khvostantsev and V. N. Slesarev. Large-volume high-pressure devices for physical investigations. *Physics-Uspekhi*, 51(10):1059, 2008.

[68] J. M. Besson and R. J. Nelmes. New developments in neutron-scattering methods under high pressure with the Paris-Edinburgh cells. *Physica B: Condensed Matter*, 213:31, 1995.

[69] C. L. Bull, M. Guthrie, S. Klotz, J. Philippe, T. Strässle, R. J. Nelmes, J. S. Loveday, and G. Hamel. Toroidal anvils for single-crystal neutron studies. *High Pressure Research*, 25(4):229, 2005.

[70] C. L. Bull, M. Guthrie, R. J. Nelmes, J. S. Loveday, K. Komatsu, H. Hamidov, and M. J. Gutmann. Time-of-flight single-crystal neutron diffraction to 10 GPa and above. *High Pressure Research*, 29(4):780, 2009.

[71] J. M. Besson, R. J. Nelmes, G. Hamel, J. S. Loveday, G. Weill, and S. Hull. Neutron powder diffraction above 10 GPa. *Physica B: Condensed Matter*, 180 - 181(2):907, 1992.

[72] M. Wilding, M. Guthrie, C. L. Bull, M. G. Tucker, and P. F. McMillan. Feasibility of *in situ* neutron diffraction studies of non-crystalline silicates up to pressures of 25 GPa. *Journal of Physics: Condensed Matter*, 20(24):244122, 2008.

[73] S. Klotz. Private communication, September 2010.

[74] T. G. Perring. *High Energy Magnetic Excitations in Hexagonal Colbalt.* PhD thesis, Cavendish Laboratory, Cambridge, 1989.

[75] J. Mayers. The use of vanadium as a scattering standard for pulsed source neutron spectrometers. *Nuclear Instruments and Methods*, 221:609, 1984.

[76] J. Mayers. Contribution of inelastic scattering to the vanadium differential scattering cross section; implications for the calibration of neutron spectrometers.

Nuclear Instruments and Methods in Physics Research Section A, 281(3):654, 1989.

[77] J. D. Champion, P. Amin, F. A. Akeroyd, T. G. Perring, and D. A. J. Whittaker. Libisis wiki (`www.libisis.org`). ISIS Pulsed Neutron Source, Harwell, U.K., 2008.

[78] R. Osborne, R. S. Eccleston, S. M. Bennington, and B. G. B. Kitchener. Data reduction on HET and MARI. Internal Report, ISIS pulsed neutron source, Harwell, UK, 1995.

[79] H. H. Paalman and C. J. Pings. Numerical evaluation of x-ray absorption factors for cylindrical samples and annular sample cells. *Journal of Applied Physics*, 33(8):2635, 1962.

[80] A. K. Soper and P. A. Egelstaff. Multiple scattering and attenuation of neutrons in concentric cylinders. *Nuclear Instruments and Methods*, 178(2-3):415, 1980.

[81] P. F. J. Poncet. Inelastic scattering from a liquid sample contained within a cylindrical container: Subtraction and attenuation corrections. Internal Report 77P0139S, Institut Laue-Langevin, 1977.

[82] C. J. Carlile. Spectrum correction factors for sample holder and self-shielding effects for planar samples in thermal neutron scattering studies. Technical Report RL-74-103, Rutherford Appleton Laboratory, 1974.

[83] P. Damay and A. Idrissi. Evaluation of self-attenuation parameters for neutron and x-ray scattering using a direct method. Application to slabs, cylinders and samples of any shape. *Physica B: Physics of Condensed Matter*, 382:71, 2006.

[84] G. H. Vineyard. Multiple scattering of neutrons. *Physical Review*, 96(1):93, 1954.

[85] V. F. Sears. Slow-neutron multiple scattering. *Advances in Physics*, 24(1):1, 1975.

[86] J. R. D. Copley. Monte Carlo calculation of multiple scattering effects in thermal neutron scattering experiments. *Computer Physics Communications*, 7:289, 1974.

[87] E. Johnson and L. Robinson. Neutron multiple scattering and absorption factors. *Review of Scientific Instruments*, 60(11):3447, 1989.

[88] J. Dawidowski, F. J. Bermejo, and J. R. Granada. Efficient procedure for the evaluation of multiple scattering and multiphonon corrections in inelastic neutron-scattering experiments. *Physical Review B*, 58(2):706, 1998.

[89] S. E. McLain, D. T. Bowron, A. C. Hannon, and A. K. Soper. GUDRUN: A computer program developed for analysis of neutron diffraction data. Technical report, ISIS Facility, Rutherford Appleton Laboratory, 2009. Available From: www.isis.rl.ac.uk/disordered/DMGroup/.

[90] M. W. Johnson. Discus: A computer program for the calculation of multiple scattering effects in inelastic neutron scattering experiments. Internal Report AERE-R7682, U.K.A.E.A, 1974.

[91] J. R. D. Copley. Monte Carlo calculation of multiple scattering effects in thermal neutron scattering experiments: Modification to slab geometry. *Computer Physics Communications*, 9(1):59, 1975.

[92] J. R. D. Copley. Monte Carlo calculations of multiple scattering effects in thermal neutron scaterring experiments: Modification to horizontal cylinder geometry. *Computer Physics Communications*, 9(1):64, 1975.

[93] J. R. D. Copley. Monte Carlo calculation of multiple scattering effects in thermal neutron scattering experiments: Improved computation of elastic coherent scattering intensities. *Computer Physics Communications*, 21(3):431, 1981.

[94] R. Stewart. Private communication, 2010.

[95] S. M. Bennington. Neutron school: MARI data analysis - multiple scattering and multi-phonon scattering. Unpublished Report, ISIS Pulsed Neutron Source, 2009.

[96] E. A. Goremychkin and R. Osborn. Crystal-field excitations in $CeCu_2Si_2$. *Physical Review B*, 47:14280, 1993.

[97] A. C. Hannon, M. Arai, R. N. Sinclair, and A. C. Wright. A dynamic correlation function for amorphous solids. *Journal of Non-Crystalline Solids*, 150(1-3):239, 1992.

[98] M. Arai, A. C. Hannon, A. D. Taylor, A. C. Wright, R. N. Sinclair, and D. L. Price. High resolution S(Q, E) measurement on g-SiO_2. *Physica B: Condensed Matter*, 180-181(2):779, 1992.

[99] J.-B. Suck and H. Rudin. Vibrational dynamics of metallic glasses studied by neutron inelastic scattering. In H. Beck and H. J. Gantherödt, editors, *Glassy Metal II*, volume 53 of *Topics in Applied Physics*, page 217. Springer Berlin / Heidelberg, 1983.

[100] J.-B. Suck. Inelastic neutron scattering applied to the investigation of collective excitations in topologically disordered matter. *Condensed Matter Physics*, 11(1):7, 2008.

[101] A. Sjölander. On 2-phonon processes in neutron diffraction against crystals. *Arkiv För Fysik*, 13(3):215, 1958.

[102] J. Dawidowski, F. J. Bermejo, R. Fayos, R. Fernandex Perea, S. M. Bennington, and A. Criado. Coherent neutron scattering response from glassy glycerol. *Physical Review E*, 53:5079, 1996.

[103] J. Dawidowski, G. J. Cuello, M. M. Koza, J. J. Blostein, G. Aurelio, A. Fernández Guillermet, and P. G. Donato. Analysis of multiple scattering and multiphonon contributions in inelastic neutron scattering experiments. *Nuclear Instruments and Methods in Physics Research B*, 195(3-4):389, 2002.

[104] P. S. Salmon, J. W. E. Drewitt, D. A. J. Whittaker, A. Zeidler, K. Wezka, C. L. Bull, M. G. Tucker, M. C. Wilding, M. Guthrie, and D. Marrocchelli. High pressure neutron diffraction study of GeO_2 glass up to 17.5 GPa. Submitted to Physical Review B, 2012.

[105] W. G. Marshall and D. J. Francis. Attainment of near-hydrostatic compression conditions using the Paris-Edinburgh cell. *Journal of Applied Crystallography*, 32:122, 2002.

[106] J. M. Brown. The NaCl pressure standard. *Journal of Applied Physics*, 86:5801, 1999.

[107] R. J. Hemley, A. P. Jephcoat, H. K. Mao, C. S. Zha, L. W. Finger, and D. E. Cox. Static compression of H_2O-ice to 128 GPa (1.28 Mbar). *Nature*, 330:737, 1987.

[108] D. Martinez-Garcia, Y. Le Godec, M. Mazouar, G. Syfosse, J. P. Itié, and J. M. Besson. Equations of state of MgO at high pressure and temperature. *High Pressure Research*, 18(1-6):339, 2000.

[109] A. Le Bail, H. Duroy, and J. L. Fourquet. Ab-initio structure determination of $LiSbWO_6$ by x-ray powder diffraction. *Materials Research Bulletin*, 23(3):447, 1988.

[110] X. Hong, G. Shen, V. B. Prakapenka, M. Newville, M. L. Rivers, and S. R. Sutton. Intermediate states of GeO_2 glass under pressures up to 35 GPa. *Physical Review B*, 75:104201, 2007.

[111] Y. Nakamoto, K. Takemura, M. Ishizuka, K. Shimizu, and T. Kikegawa. Equation of state for vanadium under hydrostatic conditions. In *Joint 20th AIRAPT (International Association for the Advancement of High Pressure Science and Technology) - 43rd EHPRG (European High Pressure Research Group) meeting*, Karlsruhe, Germany, June 27 - July 1 2005.

[112] M. A. Howe, R. L. McGreevy, and W. S. Howells. The analysis of liquid structure data from time-of-flight neutron diffractometry. *Journal of Physics: Condensed Matter*, 1(22):3433, 1989.

[113] V. F. Sears. Neutron scattering lengths and cross sections. *Neutron News*, 3(3):27, 1992.

[114] P. S. Salmon and L. Jian. The relation between the melt topology and glass-forming ability for liquid Ge-Se alloys. *Journal of Physics: Condensed Matter*, 6:1449, 1994.

[115] A. P. Sokolov, A. Kishuk, M. Soltwisch, and D. Quitmann. Medium-range order in glasses: Comparison of Raman and diffraction measurements. *Physical Review Letters*, 69:1540, 1992.

[116] M. Matsubara, M. Celino, P. S. Salmon, and C. Massobrio. Atomic scale modelling of materials: A prerequisite for any multi-scale approach to structural and dynamic properties. *Solid State Phenomena*, 139:141, 2008.

[117] Z. H. Stachurski. On structure and properties of amorphous materials. *Materials*, 4(9):1564, 2011.

[118] G. Malavasi, M. Menziani, A. Pedone, B. Civalleri, M. Corno, and P. Ugliengo. A computational multiscale strategy to the study of amorphous materials. *Theoretical Chemistry Accounts: Theory, Computation, and Modeling*, 117:933, 2007.

[119] G. Malavasi, A. Pedone, and M. C. Menziani. Towards a quantitative rationalization of multicomponent glass properties by means of molecular dynamics simulations. *Molecular Simulation*, 32(12-13):1045, 2006.

[120] A. N. Cormack and Y. Cao. Molecular dynamics simulation of silicate glasses. *Molecular Engineering*, 6:183, 1996.

[121] R. Vuilleumier, N. Sator, and B. Guillot. Computer modeling of natural silicate melts: What can we learn from *ab initio* simulations. *Geochimica et Cosmochimica Acta*, 73(20):6313, 2009.

[122] M. Micoulaut, Y. Guissani, and B. Guillot. Simulated structural and thermal properties of glassy and liquid germania. *Physical Review E*, 73(3):031504, 2006.

[123] M. Micoulaut, L. Cormier, and G. S. Henderson. The structure of amorphous, crystalline and liquid GeO_2. *Journal of Physics: Condensed Matter*, 18:R753, 2006.

[124] F. Shimojo, S. Munejiri, K. Hoshino, and Y. Zempo. Temperature dependence of the atomic structure of liquid As_2Se_3 : *ab initio* molecular dynamics simulations. *Journal of Physics: Condensed Matter*, 12(28):6161, 2000.

[125] D. M. Teter, R. J. Hemley, G. Kresse, and J. Hafner. High pressure polymorphism in silica. *Physical Review Letters*, 80(10):2145, 1998.

[126] D. Rodney, A. Tanguy, and D. Vandembroucq. Modeling the mechanics of amorphous solids at different length scale and time scale. *Modelling and Simulation in Materials Science and Engineering*, 19(8):083001, 2011.

[127] M. Cobb and D. A. Drabold. *Ab initio* molecular-dynamics study of liquid $GeSe_2$. *Physical Review B*, 56(6):3054, 1997.

[128] M. Hawlitzky, J. Horbach, S. Ispas, M. Krack, and K. Binder. Comparative classical and *ab initio* molecular dynamics study of molten and glassy germanium dioxide. *Journal of Physics: Condensed Matter*, 20(28):285106, 2008.

[129] D. A. Drabold and J. Li. Approximate *ab initio* simulations of amorphous silicon and glassy chalcogenides. *Current Opinion in Solid State & Materials Science*, 5(6):509, 2001.

[130] R. L. Cappelletti, M. Cobb, D. A. Drabold, and W. A. Kamitakahara. Neutron-scattering and *ab-initio* molecular-dynamics study of vibrations in glassy $GeSe_2$. *Physical Review B*, 52(13):9133, 1995.

[131] J. K. Christie, S. N. Taraskin, and S. R. Elliott. Vibrational behavior of a realistic amorphous-silicon model. *Journal of Non-Crystalline Solids*, 353(22-23):2272, 2007.

[132] D. A. Drabold. Topics in the theory of amorphous materials. *The European Physical Journal B - Condensed Matter and Complex Systems*, 68:1, 2009.

[133] C. Massobrio and A. Pasquarello. Short and intermediate range order in amorphous $GeSe_2$. *Physical Review B*, 77(14):144207, 2008.

[134] P. Boolchand. *Insulating and Semiconducting Glasses*. World Scientific, Singapore, 2000.

[135] A. Feltz. *Amorphous Inorganic Materials and Glasses*. Wiley-VCH, New York, 1993.

[136] P. S. Salmon and I. Petri. Structure of glassy and liquid $GeSe_2$. *Journal of Physics: Condensed Matter*, 15:S1509, 2003.

[137] S. Susman, K. J. Volin, D. G. Montague, and D. L. Price. The structure of vitreous and liquid $GeSe_2$: a neutron diffraction study. *Journal of Non-Crystalline Solids*, 125(1-2):168, 1990.

[138] A. Feltz, M. Pohle, H. Steil, and G. Herms. Glass formation and properties of chalcogenide systems XXXI. RDF studies on the structure of vitreous GeS_2 and $GeSe_2$. *Journal of Non-Crystalline Solids*, 69(2-3):271, 1985.

[139] I. Petri, P. S. Salmon, and H. E. Fischer. Defects in a disordered world: The structure of glassy $GeSe_2$. *Physical Review Letters*, 84(11):2413, 2000.

[140] S. C. Moss and D. L. Price. *Physics of Disordered Materials*. Plenum, New York, 1985.

[141] P. Vashishta, R. K. Kalia, G. A. Antonio, and I. Ebbsjö. Atomic correlations and intermediate-range order in molten and amorphous $GeSe_2$. *Physical Review Letters*, 62(14):1651, 1989.

[142] O. Uemura, Y. Sagara, and T. Satow. The neutron diffraction study of amorphous $GeSe_2$. *Physica Status Solidi (a)*, 32(2):K91, 1975.

[143] O. Uemura, Y. Sagara, D. Muno, and T. Satow. The structure of liquid As_2Se_3 and $GeSe_2$ by neutron diffraction. *Journal of Non-Crystalline Solids*, 30(2):155, 1978.

[144] P. H. Fuoss, P. Eisenberger, W. K. Warburton, and A. Bienenstock. Application of differential anomalous x-ray scattering to structural studies of amorphous materials. *Physical Review Letters*, 46(23):1537, 1981.

[145] P. H. Fuoss and A. Fischer-Colbrie. Structure of a-$GeSe_2$ from x-ray scattering measurements. *Physical Review B*, 38:1875, 1988.

[146] A. Fischer-Colbrie and P. H. Fuoss. X-ray scattering studies of intermediate-range order in amorphous $GeSe_2$. *Journal of Non-Crystalline Solids*, 126(1-2):1, 1990.

[147] J. C. Phillips. Topology of covalent non-crystalline solids I: Short-range order in chalcogenide alloys. *Journal of Non-Crystalline Solids*, 34(2):153, 1979.

[148] S. Hosokawa, W-C. Pilgrim, J. F. Berar, and S. Kohara. Recent developments of anomalous x-ray scattering for non-crystalline materials with help of reverse Monte Carlo modeling: The example of $GeSe_2$ glass. *Physica Status Solidi (a)*, 208(11):2544, 2011.

[149] M. Kibalchenko, J. R. Yates, C. Massobrio, and A. Pasquarello. Structural composition of first-neighbor shells in $GeSe_2$ and $GeSe_4$ glasses from a first-principles analysis of NMR chemical shifts. *The Journal of Physical Chemistry C*, 115(15):7755, 2011.

[150] V. Petkov and D. Le Messurier. Atomic-scale structure of $GeSe_2$ glass revisited: a continuous or broken network of Ge-$(Se_{1/2})_4$ tetrahedra? *Journal of Physics: Condensed Matter*, 22(11):115402, 2010.

[151] Q. Mei, C. J. Benmore, R. T. Hart, E. Bychkov, P. S. Salmon, C. D. Martin, F. M. Michel, S. M. Antao, P. J. Chupas, P. L. Lee, S. D. Shastri, J. B. Parise, K. Leinenweber, S. Amin, and J. L. Yarger. Topological changes in glassy $GeSe_2$ at pressures up to 9.3 GPa determined by high-energy x-ray and neutron diffraction measurements. *Physical Review B*, 74:014203, 2006.

[152] J. C. Mauro and A. K. Varshneya. Multiscale modeling of $GeSe_2$ glass structure. *Journal of the American Ceramic Society*, 89(7):2323, 2006.

[153] L. F. Gladden, S. R. Elliott, R. N. Sinclair, and A. C. Wright. A neutron inelastic scattering study of intermediate range order and low energy excitations in vitreous Ge_xSe_{1-x} alloys. *Journal of Non-Crystalline Solids*, 106:120, 1988.

[154] R. A. Barrio, F. L. Galeener, E. Martinez, and R. J. Elliott. Regular ring dynamics in AX_2 tetrahedral glasses. *Physical Review B*, 48(21):15672, 1993.

[155] P. Boolchand, R. N. Enzweiler, R. L. Cappelletti, W. A. Kamitakahara, Y. Cai, and M. F. Thorpe. Vibrational thresholds in covalent networks. *Solid State Ionics*, 39(1-2):81, 1990.

[156] J. R. Magaña and J. S. Lannin. Raman scattering and structural order in liquid $GeSe_2$. *Journal of Non-Crystalline Solids*, 59(2):1055, 1983.

[157] N. Kumagai, J. Shirafuji, and Y. Inuishi. Raman and infrared studies on vibrational properties of Ge-Se glasses. *Journal of the Physical Society of Japan*, 42(4):1262, 1977.

[158] P. Tronc, M. Bensoussan, A. Brenac, and C. Sebenne. Optical-absorption edge and Raman scattering in Ge_xSe_{1-x} glasses. *Physical Review B*, 8(12):5947, 1973.

[159] T. Atake, R. Abe, K. Honda, H. Kawaji, H. B. Johnsen, and S. Stölen. Heat capacities of glassy and crystalline $GeSe_2$. *Journal of Physics and Chemistry of Solids*, 61(9):1373, 2000.

[160] R. J. Nemanich, S. A. Solin, and G. Lucovsky. First evidence for vibrational excitations of large atomic clusters in amorphous semiconductors. *Solid State Communications*, 21(3):273, 1977.

[161] S. Sugai. Stochastic random network model in Ge and Si chalcogenide glasses. *Physical Review B*, 35:1345, 1987.

[162] P. N. Sen and M. F. Thorpe. Phonons in AX_2 glasses: From molecular to band-like modes. *Physical Review B*, 15(8):4030, 1977.

[163] P. F. McMillan. Structural studies of silicate glasses and melts: applications and limitations of Raman spectroscopy. *American Mineralogist*, 69(7-8):622, 1984.

[164] R. N. Sinclair, A. C. Wright, A. G. Clare, and A. C. Hannon. An inelastic neutron scattering study of tetrahedral connectivity in vitreous Ge_xSe_{1-x}. In *XIX International Congress on Glass*, volume 43C of *Glass Technology*, page 191, Edinburgh, 2001.

[165] G. W. C. Kaye and T. H. Laby. *Tables of physical and chemical constants.* Longman, London, UK, 15th edition, 1993.

[166] P. Vashishta, Rajiv K. Kalia, and I. Ebbsjö. Structural correlations and phonon density of states in gese2: A molecular-dynamics study of molten and amorphous states. *Physical Review B*, 39(9):6034, 1989.

[167] R. Azoulay, H. Thibierge, and A. Brenac. Devitrification characteristics of Ge_xSe_{1-x} glasses. *Journal of Non-Crystalline Solids*, 18:33, 1975.

[168] J. D. Champion, F. A. Akeroyd, P. Amin, T. G. Perring, and D. A. J. Whittaker. *Homer User Manual.* Unpublished Report, ISIS Pulsed Neutron Source, 2008.

[169] C.-K. Loong, S. Ikeda, and J. M. Carpenter. The resolution function of a pulsed-source neutron chopper spectrometer. *Nuclear Instruments and Methods in Physics Research A*, 260(2-3):381, 1987.

[170] C.-K. Loong, J. M. Carpenter, and S. Ikeda. A parametric formulation of the resolution function of a pulsed-source chopper spectrometer. Number XII in ICANS, 1993. (unpublished).

[171] S. Ikeda and J. M. Carpenter. Wide-energy-range, high-resolution measurements of neutron pulse shapes of polyethylene moderators. *Nuclear Instruments and Methods in Physics Research A*, 239(3):536, 1985.

[172] C. Kittel. *Introduction to Solid State Physics*. John Wiley & Sons, Ltd., London, 4th edition, 1971.

[173] A. Zeidler, P. S. Salmon, R. A. Martin, T. Usuki, P. E. Mason, G. J. Cuello, S. Kohara, and H. E. Fischer. Structure of liquid and glassy $ZnCl_2$. *Physical Review B*, 82:104208, 2010.

[174] P. A. G. O'Hare and A. Zywocinski. Thermodynamics of (germanium + selenium): a review and critical assessment. *Journal of Chemical Thermodynamics*, 28:459, 1996.

[175] P. S. Salmon, A. C. Barnes, R. A. Martin, and G. J. Cuello. Structure of glassy GeO_2. *Journal of Physics: Condensed Matter*, 19(41):415110, 2007.

[176] A. Pasquarello. Private Communication, Feb 2012.

[177] M. Cobb, D. A. Drabold, and R. L. Cappelletti. *Ab initio* molecular-dynamics study of the structural, vibrational, and electronic properties of glassy $GeSe_2$. *Physical Review B*, 54(17):12162, 1996.

[178] G. Lucovsky, R. J. Nemanich, S. A. Solin, and R. C. Keezer. Coordination dependent vibrational properties of amorphous semiconductors alloys. *Solid State Communications*, 17(12):1567, 1975.

[179] P. M. Bridenbaugh, G. P. Espinosa, J. E. Griffiths, J. C. Phillips, and J. P. Remeika. Microscopic origin of the companion A_1 Raman line in glassy $Ge(S,Se)_2$. *Physical Review B*, 20:4140, 1979.

[180] H. Aguiar, J. Serra, P. González, and B. León. Structural study of sol-gel silicate glasses by IR and Raman spectroscopies. *Journal of Non-Crystalline Solids*, 355(8):475, 2009.

[181] S. N. Taraskin and S. R. Elliott. Connection between the true vibrational density of states and that derived from inelastic neutron scattering. *Physical Review B*, 55:117, 1997.

[182] R. Haworth, G. Mountjoy, M. Corno, P. Ugliengo, and R. J. Newport. Probing vibrational modes in silica glass using inelastic neutron scattering with mass contrast. *Physical Review B*, 81(6):060301, 2010.

[183] D. L. Price, M-L. Saboungi, and A. C. Barnes. Structure of vitreous germania. *Physical Review Letters*, 81(15):3207, 1998.

[184] C. A. Angell. Formation of glasses from liquids and biopolymers. *Science*, 267(5206):1924, 1995.

[185] De N. Tafen and D. A. Drabold. Models and modeling schemes for binary IV-VI glasses. *Physical Review B*, 71(5):054206, 2005.

[186] A. Takada. New geometrical modelling of B_2O_3 and SiO_2 glass structures. *Physics and Chemistry of Glasses*, 50(3):219, 2009.

[187] A. Takada and A. N. Cormack. Computer simulation models of glass structure. *Physics and Chemistry of Glasses B*, 49(3):127, 2008.

[188] E. Duval, A. Boukenter, and T. Achibat. Vibrational dynamics and the structure of glasses. *Journal of Physics: Condensed Matter*, 2(51):10227, 1990.

[189] J. Peralta, G. Gutiarrez, and J. Rogan. Structural and vibrational properties of amorphous GeO_2 : a molecular dynamics study. *Journal of Physics: Condensed Matter*, 20(14):145215, 2008.

[190] M. F. Thorpe and F. L. Galeener. Network dynamics. *Physical Review B*, 22(6):3078, 1980.

[191] O. Pilla, A. Fontana, S. Caponi, F. Rossi, G. Viliani, M. A. Gonzalez, E. Fabiani, and C. P. E. Varsamis. Vibrational dynamic of 'strong' glasses: the case of v-SiO_2 and v-GeO_2. *Journal of Non-Crystalline Solids*, 322(1-3):53, 2003.

[192] F. L. Galeener, A. J. Leadbetter, and M. W. Stringfellow. Comparison of the neutron, Raman, and infrared vibrational spectra of vitreous SiO_2, GeO_2, and BeF_2. *Physical Review B*, 27(2):1052, 1983.

[193] M. J. Castiglione, M. Wilson, and P. A. Madden. Polarization effects in the simulation of lead (II) fluoride. *Journal of Physics: Condensed Matter*, 11(46):9009, 1999.

[194] M. J. Castiglione, M. Wilson, P. A. Madden, and C. P. Grey. Ion mobility in α-PbF_2 : a computer simulation study. *Journal of Physics: Condensed Matter*, 13(1):51, 2001.

[195] A. J. Leadbetter and A. C. Wright. Diffraction studies of glass structure: II. the structure of vitreous germania. *Journal of Non-Crystalline Solids*, 7:37, 1972.

[196] T. P. Mernagh and L. Liu. Temperature dependence of Raman spectra of the quartz- and rutile-types of GeO_2. *Physics and Chemistry of Minerals*, 24:7, 1997.

[197] F. L. Galeener and P. N. Sen. Theory for the first-order vibrational spectra of disordered solids. *Physical Review B*, 17(4):1928, 1978.

[198] F. L. Galeener and G. Lucovsky. Longitudinal optical vibrations in glasses: GeO_2 and SiO_2. *Physical Review Letters*, 37(22):1474, 1976.

[199] J. Sarnthein, A. Pasquarello, and R. Car. Origin of the high-frequency doublet in the vibrational spectrum of vitreous SiO_2. *Science*, 275(5308):1925, 1997.

[200] A. Pasquarello, J. Sarnthein, and R. Car. Dynamic structure factor of vitreous silica from first principles: Comparison to neutron-inelastic-scattering experiments. *Physical Review B*, 57(22):14133, 1998.

[201] Y. S. Bobovich and T. P. Tolub. Raman spectra of alkali-germanate glasses. *Optika i Spektroskopiya*, 5:210213, 1958.

[202] G. S. Henderson, D. R. Neuville, B. Cochain, and L. Cormier. The structure of GeO_2-SiO_2 glasses and melts: A Raman spectroscopy study. *Journal of Non-Crystalline Solids*, 355(8):468, 2009.

[203] P. V. Teredesai, D. T. Anderson, N. Hauser, K. Lantzky, and J. L. Yarger. Infrared spectroscopy of germanium dioxide (GeO_2) glass at high pressure. *Physics and Chemistry of Glasses*, 46(4):345, 2005.

[204] G. S. Henderson, G. M. Bancroft, and M. E. Fleet. Raman spectra of gallium and germanium substituted silicate glasses: Variations in intermediate range order. *American Mineralogist*, 70:946, 1985.

[205] F. Rossi, G. Baldi, S. Caponi, R. Dal Maschiod, A. Fontanaac, L. Orsinghera, and M. Zanattaa. The vibrational dynamics of GeO−2 at the glass transition: a Raman and Brillouin scattering study. *Philosophical Magazine*, 91:1910, 2011.

[206] G. Gutiérrez, E. Menéndez-Proupin, C. Loyola, J. Peralta, and S. Davis. Computer simulation study of amorphous compounds: structural and vibrational properties. *Journal of Materials Science*, 45:5124, 2010.

[207] A. M. Dziewonski and D. L. Anderson. Preliminary reference earth model. *Physics of the Earth and Planetary Interiors*, 25:297, 1981.

[208] J. S. Monroe, R. Wincander, and R. Hazlet. *Physical Geology: Exploring the Earth*. Brooks/Cole, Kentucky, 6th edition, 2006.

[209] R. D. Oeffner and S. R. Elliott. Interatomic potential for germanium dioxide empirically fitted to an *ab initio* energy surface. *Physical Review B*, 58(22):14791, 1998.

[210] S. Kohara and K. Suzuya. Intermediate-range order in vitreous SiO_2 and GeO_2. *Journal of Physics: Condensed Matter*, 17(5):S77, 2005.

[211] A. C. Wright, A. G. Clare, D. I. Grimley, and R. N. Sinclair. Neutron-scattering studies of network glasses. *Journal of Non-Crystalline Solids*, 112(1-3):33, 1989.

[212] M. G. Tucker, D. A. Keen, M. T. Dove, and K. Trachenko. Refinement of the Si-O-Si bond angle distribution in vitreous silica. *Journal of Physics: Condensed Matter*, 17(5):S67, 2005.

[213] M. Wilson and P. S. Salmon. Network topology and the fragility of tetrahedral glass-forming liquids. *Physical Review Letters*, 103:157801, 2009.

[214] A. C. Hannon, D. Di Martino, L. F. Santos, and R. M. Almeida. Ge-O coordination in cesium germanate glasses. *Journal of Physics and Chemistry B*, 111:3342, 2007.

[215] Q. Williams and R. Jeanloz. Spectroscopic evidence for pressure-induced coordination changes in silicate glasses and melts. *Science*, 239(4842):902, 1988.

[216] J. P. Itié, A. Polian, G. Calas, J. Petiau, A. Fontaine, and H. Tolentino. Pressure-induced coordination changes in crystalline and vitreous GeO_2. *Physical Review Letters*, 63:398, 1989.

[217] D. J. Durben and G. H. Wolf. Raman spectroscopic study of the pressure-induced coordination change in GeO_2 glass. *Physical Review B*, 43:2355, 1991.

[218] M. Madon, Ph. Gillet, Ch. Julien, and G. D. Price. A vibrational study of phase transitions among the GeO_2 polymorphs. *Physics and Chemistry of Minerals*, 18:7, 1991.

[219] C. Meade, R. J. Hemley, and H. K. Mao. High-pressure x-ray diffraction of SiO_2 glass. *Physical Review Letters*, 69:1387, 1992.

[220] M. Guthrie, C. A. Tulk, C. J. Benmore, J. Xu, J. L. Yarger, D. D. Klug, J. S. Tse, H-K. Mao, and R. J. Hemley. Formation and structure of a dense octahedral glass. *Physical Review Letters*, 93(11):115502, 2004.

[221] T. Sato and N. Funamori. Sixfold-coordinated amorphous polymorph of SiO_2 under high pressure. *Physical Review Letters*, 101:255502, 2008.

[222] M. Vaccari, G. Aquilanti, S. Pascarelli, and O. Mathon. A new EXAFS investigation of local structural changes in amorphous and crystalline GeO_2 at high pressure. *Journal of Physics: Condensed Matter*, 21(14):145403, 2009.

[223] Q. Mei, S. Sinogeikin, G. Shen, S. Amin, C. J. Benmore, and K. Ding. High-pressure x-ray diffraction measurements on vitreous GeO_2 under hydrostatic conditions. *Physical Review B*, 81(17):174113, 2010.

[224] M. Baldini, G. Aquilanti, H-k. Mao, W. Yang, G. Shen, S. Pascarelli, and W. L. Mao. High-pressure EXAFS study of vitreous GeO_2 up to 44 GPa. *Physical Review B*, 81:024201, 2010.

[225] C. J. Benmore, E. Soignard, S. A. Amin, M. Guthrie, S. D. Shastri, P. L. Lee, and J. L. Yarger. Structural and topological changes in silica glass at pressure. *Phsyical Review B*, 81:054105, 2010.

[226] R. J. Hemley, H. K. Mao, P. M. Bell, and B. O. Mysen. Raman spectroscopy of SiO_2 glass at high pressure. *Physical Review Letters*, 57:747, 1986.

[227] B. Champagnon, C. Martinet, M. Boudeulle, D. Vouagner, C. Coussa, T. Deschamps, and L. Grosvalet. High pressure elastic and plastic deformations of silica: *In situ* diamond anvil cell Raman experiments. *Journal of Non-Crystalline Solids*, 354:569, 2008.

[228] T. Sato and N. Funamori. High-pressure structural transformation of SiO_2 glass up to 100 GPa. *Physical Review B*, 82:184102, 2010.

[229] S. Sugai and A. Onodera. Medium-range order in permanently densified SiO_2 and GeO_2 glass. *Physical Review Letters*, 77:4210, 1996.

[230] C. H. Polsky, K. H. Smith, and G. H. Wolf. Effect of pressure on the absolute Raman scattering cross section of SiO_2 and GeO_2 glasses. *Journal of Non-Crystalline Solids*, 248(2-3):159, 1999.

[231] T. Deschamps, C. Martinet, D. de Ligny, J. L. Bruneel, and B. Champagnon. Correlation between Boson peak and anomalous elastic behavior in GeO_2 glass: An *in situ* Raman scattering study under high-pressure. *The Journal of Chemical Physics*, 134(23):234503, 2011.

[232] S. Sampath, C. J. Benmore, K. M. Lantzky, J. Neuefeind, K. Leinenweber, D. L. Price, and J. L. Yarger. Intermediate-range order in permanently densified GeO_2 glass. *Physical Review Letters*, 90(11):115502, 2003.

[233] G. Shen, V. B. Prakapenka, M. L. Rivers, and S. R. Sutton. Structural investigation of amorphous materials at high pressures using the diamond anvil cell. *Review of Scientific Instruments*, 74(6):3021, 2003.

[234] E. Soignard, C. J. Benmore, and J. L. Yarger. A perforated diamond anvil cell for high-energy x-ray diffraction of liquids and amorphous solids at high pressure. *Review of Scientific Instruments*, 81(3):035110, 2010.

[235] Q. Mei, C. J. Benmore, E. Soignard, S. Amin, and J. L. Yarger. Analysis of high-energy x-ray diffraction data at high pressure: the case of vitreous As_2O_3 at 32 GPa. *Journal of Physics: Condensed Matter*, 19(41):415103, 2007.

[236] S. Biggin and J. E. Enderby. The structure of molten zinc chloride. *Journal of Physics C: Solid State Physics*, 14(22):3129, 1981.

[237] I. Petri, P. S. Salmon, and H. E. Fischer. Structure of molten GeSe by neutron diffraction: the Ge coordination environment. *Journal of Non-Crystalline Solids*, 250-252(2):405, 1999.

[238] I. T. Penfold and P. S. Salmon. Structure of covalently bonded glass-forming melts: A full partial-structure-factor analysis of liquid $GeSe_2$. *Physical Review Letters*, 67:97, 1991.

[239] S. Klotz, Th. Strässle, G. Rousse, G. Hamel, and V. Pomjakushin. Angle-dispersive neutron diffraction under high pressure to 10 GPa. *Applied Physics Letters*, 86(3):031917, 2005.

[240] A. Zeidler, J. W. E. Drewitt, P. S. Salmon, A. C. Barnes, W. A. Chrichton, S. Klotz, H. E. Fischer, C. J. Benmore, S. Ramos, and A. C. Hannon. Establishing the structure of GeS_2 at high pressures and temperatures: a combined approach using x-ray and neutron diffraction. *Journal of Physics: Condensed Matter*, 21:474217, 2009.

[241] D. Marrocchelli, M. Salanne, and P. A. Madden. High-pressure behaviour of GeO_2: a simulation study. *Journal of Physics: Condensed Matter*, 22(15):152102, 2010.

[242] J. M. Besson, Ph. Pruzan, S. Klotz, G. Hamel, B. Silvi, R. J. Nelmes, J. S. Loveday, R. M. Wilson, and S. Hull. Variation of interatomic distances in ice VIII to 10 GPa. *Physical Review B*, 49:12540, 1994.

[243] P. S. Salmon. Decay of the pair correlations and small-angle scattering for binary liquids and glasses. *Journal of Physics: Condensed Matter*, 18:11443, 2006.

[244] K. H. Smith, E. Shero, A. Chizmeshya, and G. H. Wolf. The equation of state of polyamorphic germania glass - a 2-domain description of the viscoelastic response. *Journal of Chemical Physics*, 102(17):6851, 1995.

[245] O. B. Tsiok, V. V. Brazhkin, A. G. Lyapin, and L. G. Khvostantsev. Logarithmic kinetics of the amorphous-amorphous transformations in SiO_2 and GeO_2 glasses under high pressure. *Physical Review Letters*, 80(5):999, 1998.

[246] P. S. Salmon. Real space manifestation of the first sharp diffraction peak in the structure factor of liquid and glassy materials. *Procedings of the Royal Society of London A*, 445:351, 1994.

[247] G. Shen, Q. Mei, V. B. Prakapenka, P. Lazor, S. Singogeikin, Y. Meng, and C. Park. Effect of helium on structure and compression behavior of SiO_2 glass. *Proceedings of the National Academy of Sciences*, 108:6004, 2011.

[248] T. Sato, N. Funamori, and T. Yagi. Helium penetrates into silica glass and reduces its compressibility. *Nature Communications*, 2:345, 2011.

[249] M. Micoulaut. Structure of densified amorphous gemanium dioxide. *Journal of Physics: Condensed Matter*, 16:L131, 2004.

[250] K. V. Shanavas, N. Garg, and S. M. Sharma. Classical molecular dynamics simulations of behavior of GeO_2 under high pressures and at high temperatures. *Physical Review B*, 73(9):094120, 2006.

[251] T. Li, S. Huang, and J. Zhu. The structure and void analysis of pressure-induced amorphous GeO_2: Molecular dynamics simulation. *Chemical Physics Letters*, 471:253, 2009.

[252] X. F. Zhu and L. F. Chen. First-principles molecular dynamics simulations of the structure of germanium dioxide under pressures. *Physica B*, 404:4178, 2009.

[253] L. Huang, M. Durandurdu, and J. Kieffer. Transformation pathways of silica under high pressure. *Nature Materials*, 5:977, 2006.

[254] V. V. Brazhkin and A. G. Lyapin. High-pressure phase transformations in liquids and amorphous solids. *Journal of Physics: Condensed Matter*, 15(36):6059, 2003.

[255] P. W. Bridgman and I. Simon. Effects of very high pressures on glass. *Journal of Applied Physics*, 24(4):405, 1953.

[256] A. C. Wright, R. N. Sinclair, D. I. Crimley, R. A. Hulme, N. M. Vedishcheva, B. A. Shakhmatkin, A. C. Hannon, S. A. Feller, B. M. Meyer, M. L. Royle, and

D. L. Wilkerson. Borate glasses, superstructural units and the random network theory 1. *Glass Physics and Chemistry*, 22(4):268, 1996.

[257] R. N. Sinclair and A. C. Wright. Neutron scattering from vitreous silica I. the total cross-section. *Journal of Non-Crystalline Solids*, 57(3):447, 1983.

[258] Takashi Uchino. Structure and properties of amorphous silica and its related materials: Recent developments and future directions. *Journal of the Ceramic Society of Japan*, 113:17, 2005.

[259] T. Loerting, V. V. Brazhkin, and T. Morishita. *Advances in Chemical Physics*, volume 143, chapter Multiple Amorphous-Amorphous Transitions, page 29. John Wiley & Sons, Inc., Hoboken, NJ, USA, 2009.

[260] M. C. Wilding, M. Wilson, and P. F. McMillan. Structural studies and polymorphism in amorphous solids and liquids at high pressure. *Chemical Society Reviews*, 35:964, 2006.

[261] D. R. Uhlmann, J. F. Hays, and D. Turnbull. Effect of high pressure on B_2O_3 - crystallisation densification and crystallisation anomaly. *Physics and Chemistry of Glasses*, 8(1):1, 1967.

[262] J. D. Mackenzie. High-pressure effects on oxide glasses: I, densification in rigid state. *Journal of the American Ceramic Society*, 46(10):461, 1963.

[263] Q. Mei, C. J. Benmore, S. Sen, R. Sharma, and J. L. Yarger. Intermediate range order in vitreous silica from a partial structure factor analysis. *Physical Review B*, 78:144204, 2008.

[264] A. C. Wright and R. N. Sinclair. Neutron scattering from vitreous silica: III. elastic diffraction. *Journal of Non-Crystalline Solids*, 76(2-3):351, 1985.

[265] Y. Inamura, Y. Katayama, W. Utsumi, and K. Funakoshi. Transformations in the intermediate-range structure of SiO_2 glass under high pressure and temperature. *Physical Review Letters*, 93:015501, 2004.

[266] L. W. Hobbs, C. E. Jesurum, V. Pulim, and B. Berger. Local topology of silica networks. *Philosophical Magazine A*, 78(3):679, 1998.

[267] W. Jin, R. K. Kalia, P. Vashishta, and J. P. Rino. Structural transformation in densified silica glass: A molecular-dynamics study. *Physical Review B*, 50:118, 1994.

[268] M. Benoit, S. Ispas, P. Jund, and R. Jullien. Model of silica glass from combined classical and *ab initio* molecular-dynamics simulations. *Condensed Matter Physics*, 13(4):631, 2000.

[269] Y. Kono, C. Park, T. Sakamaki, C. Kenny-Benson, G. Shen, and Y. Wang. Simultaneous structure and elastic wave velocity measurement of SiO_2 glass at high pressures and high temperatures in a Paris-Edinburgh cell. *Review of Scientific Instruments*, 83(3):033905, 2012.

[270] H. Fukui, M. Kanzaki, N. Hiraoka, and Y. Q. Cai. Coordination environment of silicon in silica glass up to 74 GPa: An x-ray Raman scattering study at the silicon *l* edge. *Physical Review B*, 78:012203, 2008.

[271] S. Susman, K. J. Volin, D. L. Price, M. Grimsditch, J. P. Rino, R. K. Kalia, P. Vashishta, G. Gwanmesia, Y. Wang, and R. C. Liebermann. Intermediate-range order in permanently densified vitreous SiO_2: A neutron-diffraction and molecular-dynamics study. *Physical Review B*, 43:1194, 1991.

[272] D. Wakabayashi, N. Funamori, T. Sato, and T. Taniguchi. Compression behavior of densified SiO_2 glass. *Physical Review B*, 84:144103, 2011.

[273] A. C. Hannon. Adrian C. Wright: glasses, neutrons, borates! *Physics and Chemistry of Glasses*, 51(1):40, 2010.

[274] J. Krogh-Moe. The structure of vitreous and liquid boron oxide. *Journal of Non-Crystalline Solids*, 1(4):269, 1969.

[275] A. K. Soper. Boroxol rings from diffraction data on vitreous boron trioxide. *Journal of Physics: Condensed Matter*, 23(36):365402, 2011.

[276] L. Huang and J. Kieffer. Thermomechanical anomalies and polyamorphism in B_2O_3 glass: A molecular dynamics simulation study. *Physical Review B*, 7:224107, 2006.

[277] A. H. Verhoef and H. W. den Hartog. A molecular dynamics study of B_2O_3 glass using different interaction potentials. *Journal of Non-Crystalline Solids*, 146:267, 1992.

[278] J. Swenson and L. Börjesson. Fraction of boroxol rings in vitreous boron trioxide. *Physical Review B*, 55(17):11138, 1997.

[279] A. C. Wright, N. M. Vedishcheva, and B. A. Shakhmatkin. Vitreous borate networks containing superstructural units: a challenge to the random network theory? *Journal of Non-Crystalline Solids*, 192-193:92, 1995.

[280] G. E. Jellison Jr., L. W. Panek, P. J. Bray, and G. B. Rouse Jr. Determinations of structure and bonding in vitreous B_2O_3 by means of B^{10}, B^{11}, and O^{17} NMR. *The Journal of Chemical Physics*, 66(2):802, 1977.

[281] R. E. Youngman, S. T. Haubrich, J. W. Zwanziger, M. T. Janicke, and B. F. Chmelka. Short-and intermediate-range structural ordering in glassy boron oxide. *Science*, 269(5229):1416, 1995.

[282] R.E. Youngman and J.W. Zwanziger. Multiple boron sites in borate glass detected with dynamic angle spinning nuclear magnetic resonance. *Journal of Non-Crystalline Solids*, 168(3):293, 1994.

[283] S. K. Lee, K. Mibe, Y. Fei, G. D. Cody, and B. O. Mysen. Structure of B_2O_3 glass at high pressure: A ^{11}B solid-state NMR study. *Physical Review Letters*, 94:165507, 2005.

[284] F. L. Galeener, G. Lucovsky, and J. C. Mikkelsen. Vibrational spectra and the structure of pure vitreous B_2O_3. *Physical Review B*, 22:3983, 1980.

[285] W. M. Risen Jr. Optical spectra of glasses. *Journal of Non-Crystalline Solids*, 76(1):97, 1985.

[286] C. F. Windisch Jr. and W. M. Risen Jr. Vibrational spectra of oxygen- and boron-isotopically substituted B_2O_3 glasses. *Journal of Non-Crystalline Solids*, 48(2-3):307, 1982.

[287] K. Suzuya, Y. Yoneda, S. Kohara, and N. Umesaki. High energy x-ray study of the structure of vitreous B_2O_3. *Physics and Chemistry of Glasses*, 41(5):282, 2000.

[288] A. C. Hannon, D. I. Grimley, R. A. Hulme, A. C. Wright, and R. N. Sinclair. Boroxol groups in vitreous boron oxide: new evidence from neutron diffraction and inelastic neutron scattering studies. *Journal of Non-Crystalline Solids*, 177:299, 1994.

[289] A. C. Hannon, A. C. Wright, J. A. Blackman, and R. N. Sinclair. The vibrational modes of vitreous B_2O_3: inelastic neutron scattering and moddeling studies. *Journal of Non-Crystalline Solids*, 182(1-2):78, 1995.

[290] P. Umari and A. Pasquarello. Fraction of boroxol rings in vitreous boron oxide from a first-principles analysis of Raman and NMR spectra. *Physical Review Letters*, 95:137401, 2005.

[291] G. Ferlat, T. Charpentier, A. P. Seitsonen, A. Takada, M. Lazzeri, L. Cormier, G. Calas, and F. Mauri. Boroxol rings in liquid and vitreous B_2O_3 from first principles. *Physical Review Letters*, 101:065504, 2008.

[292] V. V. Brazhkin, Y. Katayama, K. Trachenko, O. B. Tsiok, A. G. Lyapin, E. Atrtacho, M. Dove, G. Ferlat, Y. Inamura, and H. Saitoh. Nature of the structural transformations in B_2O_3 glass under high pressure. *Physical Review Letters*, 101:035702, 2008.

[293] V. V. Brazhkin, O. B. Tsiok, and Y. Katayama. Investigation of polyamorphism in compressed B_2O_3 glass by the direct measurement of the density. *Journal of Experimental and Theoretical Physics*, 89(5):244, 2009.

[294] M. Grimsditch, A. Polian, and A. C. Wright. Irreversible structural changes in vitreous B_2O_3 under pressure. *Physical Review B*, 54:152, 1996.

[295] J. Nicholas, S. Sinogeikin, J. Kieffer, and J. Bass. A high pressure Brillouin scattering study of vitreous boron oxide up to 57 GPa. *Journal of Non-Crystalline Solids*, 349:30, 2004.

[296] M. Grimsditch, R. Bhadra, and Y. Meng. Brillouin scattering from amorphous materials at high pressures. *Physical Review B*, 38:7836, 1988.

[297] S. K. Lee, P. J. Eng, H-K Mao, Y. Meng, M. Newville, M. Y. Hiu, and J. Shu. Probing of bonding changes in B_2O_3 glasses at high pressures with inelastic x-ray scattering. *Nature Materials*, 4:851, 2005.

[298] P. S. Salmon, A. Zeidler, K. Wezka, and H. E. Fischer. Data taken from experiments made on the D4C diffractometer at the Instituit Laue-Langevin, France (private communication). April 2012.

[299] V. V. Brazhkin, Y. Katayama, Y. Inamura, M. V. Kondrin, A. G. Lyapin, S. V. Popova, and R. N. Voloshin. Structural transformations in liquid, crystalline and glassy B_2O_3 under high pressure. *Journal of Experimental and Theoretical Physics*, 78:845, 2003.

[300] L. Huang, J. Nicholas, J. Keieffer, and J. Bass. Polyamorphic transitions in vitreous B_2O_3 under pressure. *Journal of Physics: Condensed Matter*, 20:075107, 2008.

[301] A. Takada. Molecular dynamics study of pressure induced structural changes in B_2O_3. *Physics and Chemistry of Glasses*, 45(2):156, 2004.

[302] F. Birch. Finite elastic strain of cubic crystals. *Physical Review*, 71:809, 1947.

[303] L. B. Skinner, C. J. Benmore, S. Antao, E. Soignard, S. A. Amin, E. Bychkov, E. Rissi, J. B. Parise, and J. L. Yarger. Structural changes in vitreous $gese_4$ under pressure. *The Journal of Physical Chemistry C*, 116(3):2212, 2012.

[304] K. Wezka. Private communication. March 2012.

[305] M. Wilson. Private communication. March 2012.

[306] P. Tangney and S. Scandolo. An *ab initio* parametrized interatomic force field for silica. *The Journal of Chemical Physics*, 117(19):8898, 2002.

[307] L. Huang, L. Duffréne, and J. Kieffer. Structural transitions in silica glass: thermo-mechanical anomalies and polyamorphism. *Journal of Non-Crystalline Solids*, 349:19, 2004.

[308] J. S. Tse, D. D. Klug, and Y. L. Page. High-pressure densification of amorphous silica. *Physical Review B*, 46(10):5933, 1992.

[309] B. W. H. van Beest, G. J. Kramer, and R. A. van Santen. Force fields for silicas and aluminophosphates based on *ab initio* calculations. *Physical Review Letters*, 64:1955, 1990.

[310] G. James, D. Burley, P. Dyke, J. Searl, D. Clements, and J. Wright. *Modern Engineering Mathematics*. Prentice Hall, NJ, USA, 2000.